Modeling of SiGeSn-based semiconductor heterostructures for optoelectronic applications

Dissertation

zur Erlangung des akademischen Grades

doctor rerum naturalium

(Dr. rer. nat.)

im Fach Physik

Spezialisierung: Theoretische Physik

eingereicht an der

Mathematisch-Naturwissenschaftlichen Fakultät

der Humboldt-Universität zu Berlin

von

M.Sc. Torsten Wendav

Präsidentin der Humboldt-Universität zu Berlin

Prof. Dr.-Ing. Dr. Sabine Kunst

Dekan der Mathematisch-Naturwissenschaftlichen Fakultät

Prof. Dr. Elmar Kulke

Gutachter:

1. Prof. Dr. Kurt Busch
2. Prof. Dr. Jörg Schulze
3. Prof. Dr. Giovanni Isella

Tag der mündlichen Prüfung: 22.06.2017

Ich erkläre, dass ich die Dissertation selbständig und nur unter Verwendung der von mir gemäß §7 Abs. 3 der Promotionsordnung der Mathematisch-Naturwissenschaftlichen Fakultät, veröffentlicht im Amtlichen Mitteilungsblatt der Humboldt-Universität zu Berlin Nr. 126/2014 am 18.11.2014 angegebenen Hilfsmittel angefertigt habe.

Weiterhin erkläre ich, dass ich mich nicht bereits anderwärts um einen Doktorgrad im Promotionsfach Physik beworben habe beziehungsweise einen entsprechenden Doktorgrad besitze.

Ich habe Kenntnis der dem Promotionsverfahren zugrunde liegenden Promotionsordnung der Mathematisch-Naturwissenschaftlichen Fakultät, veröffentlicht im Amtlichen Mitteilungsblatt der Humboldt-Universität zu Berlin Nr. 126/2014 am 18.11.2014.

Berlin, den 9. Februar 2017

To my parents

Acknowledgments

This thesis in its current form would not have been possible without the help from other people.

First of all, I want to thank Prof. Dr. Kurt Busch for offering the me the possibility to work on the topic of SiGeSn-based optoelectronics. Even after four years working on this topic, I am still very much excited about it. I enjoyed diving into band structure theory as much as into the theory of light-matter interaction in semiconductors.

Another aspect that made working on this project compelling to me was the opportunity to closely collaborate with the Institute of Semiconductor Engineering at the University of Stuttgart. I want to thank Prof. Dr. Jörg Schulze for offering me this opportunity.

Also, I want to thank Prof. Dr. Giovanni Isella for kindly agreeing to review my thesis and Prof. Dr. Cristoph T. Koch and PD Dr. Pasquale Pavone for completing my PhD committee.

For certain aspects of my thesis project, I was fortunate to have the support of a lot of very talented people. Related to the experiment-theory collaboration, I also want to thank Dr. Inga A. Fischer for helping me understand the experimental side of the SiGeSn investigation and taking the time to answer my numerous questions about experimental data. Moreover, I want to thank the other PhD students of the Institute of Semiconductor Engineering for the discussions (and the beers) during the PhD workshops and seminars in Stuttgart and Freudenstadt, in particular, Roman Körner, Erlend Rolseth, Stefan Bechler, Lion Augel, Martin Gollhofer, and Ahmed Elsayed.

My special thanks goes to Dr. Michele Virgilio. I really enjoyed the time we worked together on the effective mass model. I had been pocking around this topic for a while, but only with his detailed physical understanding things finally made sense. And most importantly, thank you for introducing me to Espresso con Panna.

For the work on the band alignment, I want to thank the group of Prof. Dr. Claudia Draxl. In particular, I want to thank PD Dr. Pasquale Pavone for his guidance and advice on how to approach the band alignment problem within the framework of density functional theory and Drs. Andris Gulans and Dmitrii Nabok for their patience in answering my questions related to the *exciting* code.

I also want to thank everybody from the Theoretical Optics & Photonics group. Working on this thesis would have been a lot less fun without you. In particular, I want to mention here my fellow (former) PhD students Dr. Julia F. M. Werra, Matthias Moeferdt, Dr. Christoph Martens, Dr. Tobias Sproll, Dr. Michael Schneider, Kathrin Herrmann, Dan-Nha Huynh, Thomas Kiel, Paris Varytis, and Marty Oelschläger.

Last but not least, I want to thank my family and friends for continuously supporting me. Without you I would not be standing where I am today.

Thank You!

Contents

List of Figures

Acronyms

μPL microphotoluminescence. 49, 50, 53, 54, 58, 95, 98

ADP absolute deformation potential. 66, 67, 86–88, 90–92

APW augmented plane waves. 68–71

BF-TEM bright field transmission electron spectroscopy. 96

CBM conduction band maximum. 61, 62, 64, 66, 75, 82

CBO conduction band offset. 61, 64, 66

CMOS complementary metal–oxide–semiconductor. 129

DFT density functional theory. 5, 9, 12–14, 24, 25, 60–62, 64, 66, 68, 75, 77, 85, 90, 91, 128

DP deformation potential. 67, 86, 87

EPM empirical pseudopotential method. 24–26, 30, 58, 105, 128

GGA general gradient approximation. 13, 91

HF hybrid exchange-correlation functional. 91

HR-TEM high resolution transmission electron spectroscopy. 96, 117

I interstitial. 68–70

LAPW linear augmented plane waves. 69, 70

LDA local density approximation. 11–13, 60, 61, 70, 75, 85, 91

lo local orbitals. 69, 70

MT muffin-tin. 68–70, 82, 83

NP no-phonon. 100, 101, 110, 112, 114, 115, 120–125, 128

PDOS projected density of states. 80, 82

PL photoluminescence. 30, 31, 35, 41, 43, 45, 54, 57, 58, 94, 98, 100, 101, 110, 112, 114–117, 120–125, 127, 128, 135

QCSE quantum-confined Stark effect. 3

QW quantum well. 61, 93–98, 101, 103–106, 108–110, 113–115, 117, 120–122, 124, 125, 128, 129

QWIP quantum well infrared photodetector. 129

RBS Rutherford backscattering spectrometry. 49, 50, 52–54, 57, 58

RSM reciprocal space map. 50, 52

SRH Shockley-Reed-Hall. 41

TB tight-binding. 24, 26, 27, 93, 114

TEM transmission electron microscopy. 95, 98, 124

VBM valence band maximum. 59–62, 64, 66, 67, 71–75, 77, 82, 83, 85–88, 90, 91

VBO valence band offset. 61, 64, 66, 67, 75, 77, 84–87, 90

VS virtual substrate. 49, 52

XRD x-ray diffraction. 34, 49, 50, 52, 53, 57, 58, 95, 97, 98, 117, 124, 135

Chapter 1

1 Introduction

In this chapter, we motivate the work presented within this thesis by introducing the current challenges in the design of integrated circuits and the need for faster on- and off-chip data transport. We introduce the idea of optical interconnects as an alternative to electrical interconnects and the SiGeSn material system as a candidate for the monolithic integration of optoelectronic devices into integrated circuits.

1.1 Motivation

In the last decades, a tremendous increase in computing power could be observed. This trend was primarily driven by the miniaturization of the transistors and is commonly described by Moore's law, which states that the number of transistors per unit area doubles approximately every 24 months [1]. However, as the size of transistors is reduced further, several technological challenges have to be addressed to sustain the trend. One of these challenges is the on- and off-chip wiring, which is realized through copper wires referred to as electrical interconnects. There are several short-comings associated to these electrical interconnects. One is the limitation of their bit-rate capacity. It can be shown that the bit-rate capacity B of a set of lines with total cross-sectional area A and length L is given by $B \simeq B_0 \frac{A}{L^2}$, where B_0 is a proportionality constant [2]. From this expression, it follows that once all space available for wiring is filled, the total bit rate is constant and cannot be improved. In contrast, the number of floating point operations performed on a chip scales with the number of transistors, which leads to a bottleneck between the rate of information processing and its distribution. Another limitation is the power consumption of electrical interconnects. Already today, power consumption due to the charging and discharging of the capacitance of the lines is the primary cause of the power dissipation in integrated circuits. With the overall power consumption of information and communication technology in the percents of the total electric power consumption, this becomes a growing concern [3]. Moreover, the dissipated energy has to be removed from the chip. Yet, the amount of heat that can be removed from a chip in a cost-effective manner is limited and for a lot of applications this limit has already been reached [4].

To increase the band width of electrical interconnects, it is possible to use amplifiers in order to improve the bit-rate capacity. However, this will also increase the power consumption as well as the heat production. For this reason, a replacement for the electrical interconnects is sought after. A promising alternative are optical interconnects.

1.2 Optical Interconnects

Optical interconnects consist of three active elements: a laser source, an electrooptical modulator that modulates the electric signal onto the laser beam, and a photodetector that converts the optical signal back into an electric signal. The transport of the optical signals happens either through free space or wave guides. Using optical instead of electrical interconnects has three main advantages:

- Reduced energy dissipation. The energy dissipation of electrical interconnects is the result of the charging and discharging of the capacitance of the interconnect itself. Consequently, optical interconnects might work more energy efficient than their electrical counterparts. At the same time, energy is required for the generation of light and for the conversion of the electrical signals into optical signals and vice versa. Calculations of the energy requirements for the replacement of electrical with optical interconnects have been performed [4–6].

- Higher interconnect density. Optical interconnects can carry substantial amounts of data with much smaller cable diameters than required for electrical interconnects. The reason for this is that optical fibers do not follow the same loss mechanism as electrical interconnects [3].

- Smaller signal delay. Decreasing the dimensions of an electrical interconnect increases the propagation time of electrical signals (latency). Optical interconnects potentially have a smaller latency then electrical interconnects, which is important in order to distribute data within a single clock cycle over the entire chip [7]. Moreover, optical interconnects can be used to distribute high quality clock signals in order to synchronize integrated circuits [8].

One possibility of accomplishing optoelectronic functionality for Si-based integrated circuits is by using the well established group-III/V semiconductor photonics technology [9]. Due to the missing/additional bond of group-III/V semiconductors in comparison to Si, they will act as dopants to Si and cannot be directly grown on Si without jeopardizing the electronic functionality of the integrated circuit. This can be circumvented by growing the electronic and photonic components on separate wafers and bonding the wafers to each other [10–12]. The disadvantage of wafer bonding is that the circuit design flexibility is restricted as a result of the strict separation between electronic and optical components. It is therefore desirable to directly integrate the optoelectronic devices into the current Si-based integrated electronic circuits - an approach referred to as *silicon photonics*.

1.3 Silicon Photonics: Current Challenges

Construction of optoelectronic devices based on Si poses two fundamental challenges. First of all, Si is an indirect-band-gap semiconductor (see Fig. 1.1). The conduction band minimum located at the six-fold degenerate Δ-valley (located roughly at 85% percent of the distance from the Γ- to the X-point) lies 2.3 eV lower in energy than the conduction band at the Γ-point. Light-emitting devices based on Si are therefore highly inefficient. Secondly, Si shows a weak Pockels, Kerr, and Franz-Keldysh effect [13]. This difficulty could be partially circumvented by using carrier injection and depletion for the modulation of the refractive index. However,

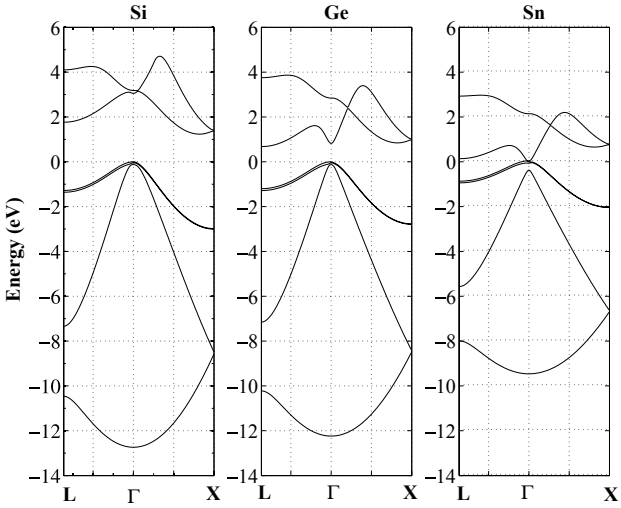

Figure 1.1: *Band structure of Si, Ge, and Sn for the Γ-L and Γ-X direction in the Brillouin zone according to [15]. Whereas the Si and Ge show an (indirect) band-gap, α-Sn is a semi-metal with a zero band-gap and an inverted band structure around the Γ-point. Spin-orbit coupling has been neglected in the calculation of the band structure.*

experimental studies indicate that device lengths of the order of 500 µm are required to accomplish the required phase shifts [14], which is much larger than the size of a transistor under current manufacturing standards.

The optoelectronic properties can be improved when Si is combined with Ge in a single device. Ge is also a group-IV semiconductor and as a result can be monolithically integrated into Si-based integrated circuits. Similar to Si, Ge is an indirect band-gap semiconductor (see Fig. 1.1). However, the direct band-gap is only 0.8 eV and therefore just 0.14 eV larger than the four-fold degenerate fundamental band-gap at the L-point. It was shown that using tensile strain, heavy n-type doping, and large currents for carrier injection, electrons accumulate in the conduction band minimum at the Γ-point, which opens up the possibility of using Ge as an active laser medium [16, 17]. Furthermore, experimental investigations have revealed that multiple quantum well structures consisting of alternating layers of pure Ge and SiGe alloys exhibit a strong quantum-confined Stark effect (QCSE) and based on this effect, efficient electrooptical modulators can be build [18]. In addition, due to the smaller direct band-gap, monolithically integrated Ge can also be used for efficient photodetection of infrared light [19, 20], which is the standard in optical telecommunication technology. However, one obstacle for the monolithical integration of Ge with Si is the fact that the lattice constant of Ge is roughly 4% larger than that of Si (see Tab. 1.1). As a result, it is very challenging to achieve the tensile strain required for lasing. Moreover, great care has to be taken when Ge is grown on top of Si as not all strain configurations lead to a stable growth. In order to circumvent these challenges, $Ge_{1-x-y}Si_xSn_y$ alloys have recently attracted great interest.

1.4 Optoelectronic Devices Based On $Ge_{1-x-y}Si_xSn_y$ Alloys

Similar to Si and Ge, Sn is also a group-IV element. Sn can assume two phases: α (nonmetallic form) and β (metallic form). α-Sn exhibits the same diamond crystal lattice as Si and Ge and,

Table 1.1: *Band-gaps of the elemental semiconductors Si, Ge, and Sn at the Γ-point E_g^Γ, the L-point E_g^L, and for the Δ-valley E_g^Δ at $T = 0\,\mathrm{K}$ [21]. Lattice constant a_L of all three elemental semiconductors [22].*

	E_g^Γ (eV)	E_g^L (eV)	E_g^Δ (eV)	a_L (nm)
Si	3.30	2.10	1.20	0.54307
Ge	0.81	0.70	0.90	0.56573
Sn	-0.41	0.12	0.91	0.64892

as a result, can be used to grow semiconducting $Ge_{1-x-y}Si_xSn_y$ alloys[1]. In contrast to Si and Ge, Sn is a semi-metal with a zero band-gap at the Γ-point (see Fig. 1.1). Furthermore, Sn has an inverted band structure at the Γ-point [23]. Normally, the conduction bands of group-IV materials at the Γ-point have antibonding character, while the valence bands have bonding character. This is, however, not true for Sn. The band below the highest valence band at the Γ-point is of antibonding nature while the lowest conduction band is of bonding nature (corresponding to the light hole band). For this reason, Sn is often referred to as a negative-band-gap semiconductor with a band-gap of $-0.41\,\mathrm{eV}$ at room-temperature [24]. Consequently, $Ge_{1-x-y}Si_xSn_y$ alloys are expected to exhibit a direct band-gap in certain compositional ranges. For the $Ge_{1-y}Sn_y$ alloys, experimental studies have already verified the indirect to direct cross-over to be in the range of $y = 0.12$ [25]. For $Ge_{1-x-y}Si_xSn_y$ alloys, it is not clear yet in which compositional range the alloy turns into a direct-band-gap semiconductor. Nonetheless, even if the ternary alloy is an indirect-band-gap semiconductor over a wide range of compositions, it is still an interesting material system. Particularly due to the fact that lattice constant and band-gap size decouple in ternary alloys, it may serve as natural barrier material in Ge/GeSiSn and GeSn/GeSiSn quantum well structures [W3, 26, 27].

The realization of optoelectronic devices based on $Ge_{1-x-y}Si_xSn_y$ alloys is demanding. A large number of aspects, like material composition, strain effects, and confinement energies of the charge carriers in heterostructures, have to be taken into account. In order to guide experimental efforts, theoretical calculations for the prediction of SiGeSn-based optoelectronic device properties are required. Various authors have already proposed optimized layouts of SiGeSn heterostructures for use as lasers, photodetectors, and optoelectronic modulators based on calculations performed within the framework of $\mathbf{k}\cdot\mathbf{p}$ theory or effective mass approximation [28–30]. Even though both methods are ideally suited to computationally optimize optoelectronic devices based on structures with a large parameter space, as is the case for the SiGeSn material system, the predictive power of these methods highly depends on the accuracy of the material parameters used as an input. While a great range of experimental and theoretical data is available on the binary alloys $Si_{1-x}Ge_x$ and $Ge_{1-y}Sn_y$ [31–37], much less is known about $Ge_{1-x-y}Si_xSn_y$ alloys and their heterostructures. Two needs arise from this observation. First of all, greater research has to be conducted on fundamental material parameters of the SiGeSn material system. As it is very demanding to do this experimentally for a great range of compositions, theoretical or theoretical-experimental approaches are required. Secondly, theoretical models describing the optoelectronic properties of entire devices that have predictive power for a wide range of structures and are also experimentally verified need to be developed. Within this thesis, we explore the SiGeSn material system in these two directions.

[1] In the following, we are only interested in α-Sn. For ease of reading, we will omit the α when referring to α-Sn from now on.

1.5 Thesis Outline

An essential step in the calculation of the optoelectronic properties of semiconductor bulk and heterostructures is to understand their underlying band structure. In Chap. 2, we introduce fundamental methods for calculating the band structure of semiconductors. We focus particularly on the description of the density functional theory (DFT) and $\mathbf{k}\cdot\mathbf{p}$ theory. In Chap. 3, we present a theoretical-experimental study of the compositional dependence of direct band-gap of the $Ge_{1-x-y}Si_xSn_y$ alloy, where we use $\mathbf{k}\cdot\mathbf{p}$ theory in order to extract the band-gap energies from photoluminescence measurements. In Chap. 4, we use DFT in order to determine the valence band offsets between the elemental semiconductors Si, Ge, and Sn. These are required for the calculation of the optical and optoelectronic properties of $Ge_{1-x-y}Si_xSn_y$-based heterostructures. In Chap. 5, we then turn our attention towards the simulation of the heterostructure based on $\mathbf{k}\cdot\mathbf{p}$ theory. As the parameters for the SiGeSn material system are not understood well enough to model complex structures, we limit ourselves to the simulation of a $Si_{1-x}Ge_x$/Si multiple quantum well structure. In particular, we focus on modeling the photoluminescence spectrum of such a structure and compare this with experimental measurements. In Chap. 6, we conclude our work by summarizing our findings and putting them into a wider perspective.

2 Chapter 2
Electronic Band-Structure Calculations

In order to understand the optoelectronic properties of bulk semiconductors and semiconductor heterostructures, we have to investigate their electronic band structure. It determines in a fundamental way how electrons can interact with photons. In this chapter, we review theoretical methods which can be used to calculate the electronic band structure of semiconductor bulk and heterostructures. In particular, we focus on density functional theory and the $\mathbf{k}\cdot\mathbf{p}$ *method, which are used throughout this thesis. At the end of this chapter, we provide a brief description of the fundamentals of the empirical pseudopotential and the tight-binding methods, which we frequently reference to.*

2.1 Many-Body Schrödinger Equation

In order to learn about the properties of a quantum-mechanical system, we need to determine its wavefunction by solving the Schrödinger equation. The non-relativistic and time-independent many-body Schrödinger equation of crystalline solids is given by

$$\left\{ -\sum_i \frac{\hbar^2}{2m_0}\nabla^2_{\mathbf{r}_i} - \sum_I \frac{\hbar^2}{2M_I}\nabla^2_{\mathbf{R}_I} + \frac{1}{2}\sum_{i\neq j}\frac{e^2}{4\pi\epsilon_0}\frac{1}{|\mathbf{r}_i-\mathbf{r}_j|} + \frac{1}{2}\sum_{I\neq J}\frac{e^2}{4\pi\epsilon_0}\frac{Z_I Z_J}{|\mathbf{R}_I-\mathbf{R}_J|} - \sum_{i,I}\frac{e^2}{4\pi\epsilon_0}\frac{Z_I}{|\mathbf{r}_i-\mathbf{R}_I|} \right\} \Psi_\eta = \mathcal{E}_\eta\,\Psi_\eta \tag{2.1}$$

where m_0 is the mass of the electron, $e > 0$ is the elementary charge, $\mathbf{r}_i$ is the coordinate of the i-th electron, and M_I, Z_I, and $\mathbf{R}_I$ are the mass, charge, and coordinate of the I-th nucleus, respectively. Furthermore, Ψ_η and E_η are the eigenfunction and eigenvalue of the η-th eigenstate. The terms given in the bracket can be identified, in this order, as

- the kinetic energy term of the electrons $T^{\mathrm{e}} = -\sum_i \frac{\hbar^2}{2m_0}\nabla^2_{\mathbf{r}_i}$,
- the kinetic energy term of the nuclei $T^{\mathrm{n}} = -\sum_I \frac{\hbar^2}{2M_I}\nabla^2_{\mathbf{R}_I}$,

- the electron-electron interaction $V^{\mathrm{ee}} = \frac{1}{2}\sum_{i\neq j}\frac{e^2}{4\pi\epsilon_0}\frac{1}{|\mathbf{r}_i-\mathbf{r}_j|}$,
- the nuclei-nuclei interaction $V^{\mathrm{nn}} = \frac{1}{2}\sum_{I\neq J}\frac{e^2}{4\pi\epsilon_0}\frac{Z_I Z_J}{|\mathbf{R}_I-\mathbf{R}_J|}$, and
- the electron-nuclei interaction $V^{\mathrm{ne}} = -\sum_{i,I}\frac{e^2}{4\pi\epsilon_0}\frac{Z_I}{|\mathbf{r}_i-\mathbf{R}_I|}$.

The many-body wavefunction $\Psi_\eta = \Psi_\eta(\{\mathbf{r}_i\},\{\mathbf{R}_I\})$ depends on all electron and nuclei coordinates. Since the number of particles in a typical solid is in the order of the Avogadro number, solving this equation is by no means trivial. Different levels of approximations are required in order to calculate eigenfunctions and eigenvalues.

2.1.1 Born-Oppenheimer-Approximation

One of the most fundamental approximations in solid-state physics is the assumption that the motion of electron and nuclei motion decouple. This step is justified due to the small mass of the electron in comparison to the nuclei ($m_0/M_I \simeq 10^{-4}$). Thus, electrons move much faster than the nuclei and follow any configurational change of the nuclei instantaneously by adopting the lowest state of energy. The electrostatic potential of the nuclei, parametrized by $\{\mathbf{R}_I\}$, can therefore be seen as an external potential to the electrons. Following this idea, a Schrödinger equation just for the electronic part ψ_ν of the total wavefunction Ψ_η can be formulated

$$\left[T^{\mathrm{e}} + V^{\mathrm{ee}} + V^{\mathrm{ne}} + V^{\mathrm{nn}}\right]\psi_\nu(r,R) = E_\nu(R)\,\psi_\nu(r,R), \tag{2.2}$$

where $R = \{\mathbf{R}_I\}$, $r = \{\mathbf{r}_i\}$, and E_ν is the eigenenergy of the electronic state ψ_ν. Here, we also include the nuclei-nuclei potential term V^{nn} in the electronic Hamiltonian as it is just a constant energy contribution. For any fixed nuclear configuration, the eigenfunctions ψ_ν form a complete basis set. The total wavefunction Ψ_η can then be expanded in terms of the electronic wavefunctions

$$\Psi_\eta(r,R) = \sum_\nu \chi_{\eta\nu}(R)\,\psi_\nu(r,R), \tag{2.3}$$

where $\chi_{\eta\nu}(R)$ are the respective expansion coefficients. We can solve for the expansion coefficients by taking Eq. (2.3), inserting it back into the original many-body Schrödinger equation (Eq. (2.1)), and multiplying from the left with ψ_κ:

$$\sum_\nu \left[E_\kappa\,\chi_{\eta\nu}\,\delta_{\kappa\nu} + \int\cdots\int \mathrm{d}r\,\psi_\kappa\,T^n\,\chi_{\eta\nu}\,\psi_\nu\right] = \mathcal{E}_\eta\,\chi_{\eta\kappa}. \tag{2.4}$$

The Born-Oppenheimer approximation is to neglect all off-diagonal terms in Eq. (2.4) that couple electronic wavefunctions of different quantum number to each other. It can be shown that this approximation is valid as long as the eigenenergies of the different electronic wavefunctions are reasonably separated. If this is the case, electrons follow the slow motion of ions without changing their eigenstates. For this reason, the Born-Oppenheimer approximation is also referred to as the *adiabatic* approximation. The equation that determines the wavefunctions of the nuclei is then given by

$$\left\{T^n - E_\nu(R)\right\}\chi_{\eta\nu}(R) = \mathcal{E}_\eta\,\chi_{\eta\nu}(R). \tag{2.5}$$

Therefore, the wavefunction of the electrons and the nuclei fully decouple and the total wavefunction is just the product of both. All methods that we will introduce in the following, will be based on this result.

Note that by neglecting the off-diagonal terms in Eq. (2.4), we ruled out any interaction between lattice dynamics (phonons) and electrons. As this interaction is believed to be small, however, it can for most systems of interest be reintroduced perturbatively, if required, which we will do in Chap. 5.

2.2 Density Functional Theory

We want to start out our discussion of band structure method by deriving the DFT. DFT is solely based on quantum-mechanical equations without the need for the introduction of material parameters. For this reason, it is often referred to as *ab initio* or first-principle method. We start our discussion of DFT by introducing the Hohenberg-Kohn theorems, which describe how Eq. (2.2) can be further simplified by rewriting it as a variational problem of the electronic charge density. These theorems are at the very core of DFT and laid the foundation for the formulation of modern DFT. Nevertheless, the Hohenberg-Kohn theorems leave open how this newly found variational problem can be solved efficiently. For this, we will introduce the Kohn-Sham ansatz. We will finish this section by discussing the correctional functional, which is part of the Kohn-Sham ansatz.

2.2.1 Hohenberg-Kohn Theorems

Even after the application of the Born-Oppenheimer approximation, we still have to deal with a many-body problem when solving for the electronic wavefunction. In 1964, Hohenberg and Kohn [38] proved two theorems that greatly simplified the many-body problem. At the heart of both theorems is the idea that for any system of N_e interacting particles in an external potential, as in Eq. (2.2), the many-body Schrödinger equation can be reformulated in terms of the ground state density $n_0(\mathbf{r})$ defined as

$$n_0(\mathbf{r}) = N_e \left[\prod_{i=2}^{N_e} \int \mathrm{d}\mathbf{r}_i \right] \left| \psi_0(\mathbf{r}, \mathbf{r}_2, \ldots, \mathbf{r}_{N_e}) \right|^2 . \tag{2.6}$$

In the first Hohenberg-Kohn theorem, they showed that for any system of interacting particles in an external potential, the external potential is determined uniquely, except for a constant, by the ground-state particle density $n_0(\mathbf{r})$. Since the external potential in turn determines the wavefunction of ground and excited states, all properties of the system are fully determined by the ground-state density.

The second Hohenberg-Kohn theorem states that for any external potential the energy of a system of interacting particles is a functional $F[n]$ of the density. The minimum of this functional is the ground-state energy of the system and therefore also corresponds to the ground-state density:

$$E_0 = F[n_0] \leq F[n]. \tag{2.7}$$

These theorems greatly simplify the electronic many-body problem. Instead of dealing with a wavefunction that encompasses $3N_e$ spatial degrees of freedom, Hohenberg and Kohn showed that all the information required to describe the many-body system is contained within the ground-state particle density, which is a function of only three spatial degrees of freedom.

2.2.2 Kohn-Sham Ansatz

Even though Hohenberg and Kohn greatly simplified the original many-body problem, their theorems do not provide information about the exact form of the energy functional $F[n]$. While today this functional is still unknown, a number of approaches have been developed that allow for an approximate solution of the problem. Among those, the Kohn-Sham ansatz proved to be very effective and, today, provides the basis for most *ab initio* or first-principles calculations of solids [39].

The central idea of the Kohn-Sham ansatz is to replace the Hamiltonian describing the interacting multi-particle problem with an easier auxiliary system based on a non-interacting system of electrons. The wavefunction of this easier auxiliary system is simply given by a Slater determinant of one-particle orbitals, the so-called Kohn-Sham orbitals $\varphi_i(\mathbf{r})$. The underlying assumption of Kohn and Sham is that the exact ground-state density of the original system coincides with the ground-state density of this auxiliary system. The auxiliary Hamiltonian for the Kohn-Sham orbitals $\varphi_i(\mathbf{r})$ is then simply given by

$$H_{\mathrm{KS}} = -\frac{\hbar^2}{2m_0}\nabla^2 + V_{\mathrm{KS}}(\mathbf{r}), \tag{2.8}$$

where the first term describes the one-particle kinetic energy and the second is an effective local potential, which we have to derive. The total electronic density $n_{\mathrm{KS}}(\mathbf{r})$ for an auxiliary system consisting of N_e non-interacting electrons can then be written as

$$n_{\mathrm{KS}}(\mathbf{r}) = \sum_{i=1}^{N_e} |\varphi_i(\mathbf{r})|^2. \tag{2.9}$$

In order to define the effective potential $V_{\mathrm{KS}}(\mathbf{r})$, we investigate the different contributions to the total-energy functional of the system in more detail. First, we can split the kinetic-energy term of the interacting multi-particle problem into two terms:

$$\langle\psi|T^{\mathrm{e}}|\psi\rangle = -\frac{\hbar^2}{2m_0}\sum_{i=1}^{N_e}\int \mathrm{d}\mathbf{r}\,\varphi_i(\mathbf{r})\,\nabla^2\varphi_i(\mathbf{r}) + T^{\mathrm{c}}[n] \equiv T^{\mathrm{s}}[n] + T^{\mathrm{c}}[n]. \tag{2.10}$$

Here, the first term (T^{s}) describes the kinetic energy of the independent electron system whereas the second term (T^{c}) includes all the corrections related to the fact that we are in truth dealing with interacting particles. A similar approach can be taken for the potential energy term related to the electron-electron interaction:

$$\langle\psi|V^{\mathrm{ee}}|\psi\rangle = \frac{1}{2}\frac{e^2}{4\pi\epsilon_0}\int \mathrm{d}\mathbf{r}\mathrm{d}\mathbf{r}'\,\frac{n(\mathbf{r})n(\mathbf{r}')}{\left|\mathbf{r}-\mathbf{r}'\right|} + E^{\mathrm{ncl}}[n] \equiv E^{\mathrm{H}}[n] + E^{\mathrm{ncl}}[n]. \tag{2.11}$$

Here, we separated out the classical Coulomb interaction of the electron density with itself, the Hartree energy E^H, from the non-classical contributions E^{ncl} that need to be included when dealing with a quantum system of individual interacting particles. For the full energy functional, in the formulation by Kohn and Sham, we can therefore write

$$F_{\mathrm{KS}}[n(\mathbf{r})] = T^{\mathrm{s}}[n] + E^{\mathrm{H}}[n] + E^{\mathrm{ne}}[n] + E^{\mathrm{nn}} + E_{\mathrm{XC}}[n], \tag{2.12}$$

where E^{ne} and E^{nn} are the potential energy related to the electron-nuclei interaction and the nuclei-nuclei interaction, respectively. E_{XC} is the sum of the terms T^{c} and E^{ncl} as defined

above and describes the difference between the fictitious independent-particle system and the interacting many-particle problem. The first four terms of the energy functional can be directly calculated. The exchange-correlation energy, on the other hand, is generally not known for systems of practical relevance. However, different approaches have been invented to approximate this term. We will come back to this point in Sec. 2.2.3. For now, we will assume that we found an expression for $E_{\mathrm{XC}}[n]$. The ground state energy of the Kohn-Sham system can then be found by minimizing the total energy with respect to the one-particle orbitals

$$\frac{\delta F_{\mathrm{KS}}}{\delta \varphi_i^*(\mathbf{r})} = \frac{\delta T^{\mathrm{s}}}{\delta \varphi_i^*(\mathbf{r})} + \left\{ \frac{\delta E^{\mathrm{ne}}}{\delta n(\mathbf{r})} + \frac{\delta E^{\mathrm{H}}}{\delta n(\mathbf{r})} + \frac{\delta E_{\mathrm{XC}}}{\delta n(\mathbf{r})} \right\} \frac{\delta n(\mathbf{r})}{\delta \varphi_i^*(\mathbf{r})} = 0. \tag{2.13}$$

The previous equation together with the method of Lagrangian multipliers that assures the orthonormality of the single particle orbitals, i. e. $\langle \varphi_i | \varphi_j \rangle = \delta_{ij}$, can be used to set up a variational problem. Using the definition of T^{s}, E^{H}, and $n(\mathbf{r})$ from Eqs. (2.10), (2.11), and (2.9), respectively, we find

$$\frac{\delta T^s}{\delta \varphi_i^*(\mathbf{r})} = -\frac{\hbar^2}{2m_0}\nabla^2 \varphi_i(\mathbf{r}); \quad \frac{\delta E^{\mathrm{H}}}{\delta n(\mathbf{r})} = \frac{e^2}{8\pi\epsilon_0} \int \mathrm{d}\mathbf{r}' \, \frac{n(\mathbf{r}')}{|\mathbf{r}-\mathbf{r}'|}; \quad \frac{\delta n(\mathbf{r})}{\delta \varphi_i^*(\mathbf{r})} = \varphi_i(\mathbf{r}). \tag{2.14}$$

The effective local potential of the auxiliary Hamiltonian is then given by

$$\begin{aligned} V_{\mathrm{KS}} &= -\sum_I \frac{e}{4\pi\epsilon_0} \frac{Z_I}{|\mathbf{r}-\mathbf{R}_I|} + \frac{e^2}{8\pi\epsilon_0} \int \mathrm{d}\mathbf{r}' \, \frac{n(\mathbf{r}')}{|\mathbf{r}-\mathbf{r}'|} + \frac{\delta E_{\mathrm{XC}}}{\delta n(\mathbf{r})} \\ &\equiv V^{\mathrm{ne}}(\mathbf{r}) + V^{\mathrm{H}}(\mathbf{r}) + V_{\mathrm{XC}}(\mathbf{r}). \end{aligned} \tag{2.15}$$

From Eq. (2.15), we observe that the Kohn-Sham potential is itself a functional of the charge density through the terms V^{H} and V_{XC}. Therefore, the Kohn-Sham equations have to be solved in a self-consistent manner. This is usually done by guessing an initial density $n(\mathbf{r})$, calculating the Kohn-Sham potential V_{KS}, solving for the Kohn-Sham orbitals $\varphi_i(\mathbf{r})$, and then updating the charge density. This self-consistent cycle is repeated until the density and the effective potential do not change their values to within a certain predefined error margin.

2.2.3 Approximation to the Exchange-Correlation Functional

A key ingredient to the Kohn-Sham ansatz described in the previous section, is the exchange-correlation functional $E_{\mathrm{XC}}[n]$. Even though this functional is not known for systems of practical relevance, great progress has been made to approximate this functional as a local or nearly local functional of the electron density [40, 41]. For the calculations described within this thesis, we will use the simplest, but often also most effective approximation that can be made: The local density approximation (LDA).

Local Density Approximation

Already in their pioneering paper, Kohn and Sham pointed out that the electron distribution of solids resembles in first approximation a homogeneous electron gas. In this approximation, also known as jellium model, it is assumed that electrons do not interact with each other and the potential energy due to the nuclei is simply a constant. For this system, the exchange-correlation energy is local in character and can be calculated by integrating the exchange-correlation energy

density $\varepsilon_{\mathrm{XC}}^{\mathrm{hom}}$, weighted by the density, over all space:

$$\begin{aligned} E_{\mathrm{XC}}[n] &= \int \mathrm{d}\mathbf{r}\; n(\mathbf{r})\;\; \varepsilon_{\mathrm{XC}}^{\mathrm{hom}}[\sigma]\Big|_{\sigma=n(\mathbf{r})} \\ &= \int \mathrm{d}\mathbf{r}\; n(\mathbf{r})\;\left(\varepsilon_{\mathrm{X}}^{\mathrm{hom}}[\sigma]\Big|_{\sigma=n(\mathbf{r})} + \varepsilon_{\mathrm{C}}^{\mathrm{hom}}[\sigma]\Big|_{\sigma=n(\mathbf{r})} \right), \end{aligned} \tag{2.16}$$

where we wrote the exchange-correlation energy density as a sum of the exchange and correlation contribution in the last line. The exchange contribution can be calculated analytically and is given by [42]

$$\varepsilon_{\mathrm{X}}^{\mathrm{hom}}(n) = -\frac{3}{4}\left(\frac{3}{\pi}\right)^{1/3} \frac{e^2 n^{1/3}}{4\pi\epsilon_0}. \tag{2.17}$$

For the correlation contribution an analytical expression has not been found. Nonetheless, using Monte Carlo simulations, parametrizations of the correlation energy density of the homogeneous electron gas as a function of the electron density have been developed. The calculations presented in this thesis are based on the formulation of LDA by Perdew and Zunger [43].

The assumption that the electron distribution in a solid resembles that of a homogeneous electron gas is a very rough approximation. As a consequence of this and other approximations, some properties of solids are not described correctly by the Kohn-Sham approach. We briefly discuss the limitations of the Kohn-Sham approach in the next section.

2.2.4 Limitations of the Kohn-Sham Ansatz

A well-known limitation of the Kohn-Sham approach is the underestimation of the band-gaps of semiconductors. As a rule of thumb, the Kohn-Sham-based DFT in combination with the LDA underestimate the band-gap of semiconductors by about 40 % [44, 45]. The band-gap E_{g} of a semiconductor with N electrons is defined as the difference between the ionization potential I and the electron affinity A[1]

$$E_{\mathrm{g}} = I - A. \tag{2.20}$$

For a non-interacting system of electrons, the band-gap E_{g} simply corresponds to the difference between the energy ϵ_{N+1} and ϵ_N of the lowest unoccupied and the highest occupied Kohn-Sham orbitals:

$$E_{\mathrm{g}}^{\mathrm{KS}} = \epsilon_{N+1} - \epsilon_N, \tag{2.21}$$

where we used the superscript KS to remind us that $E_{\mathrm{g}}^{\mathrm{KS}}$ is the band-gap according to the Kohn-Sham approach. However, for an interacting electron system the relationship is more complicated. It can be shown that the band-gap E_{g} for an interacting electron system and the Kohn-Sham band-gap $E_{\mathrm{g}}^{\mathrm{KS}}$ are related by [46]

$$E_{\mathrm{g}} = E_g^{\mathrm{KS}} + \Delta_{\mathrm{XC}}, \tag{2.22}$$

[1] The ionization potential is defined as the energy required for removing a single electron from the highest occupied state of the solid:

$$I = E_{N-1}^{\mathrm{TOT}} - E_N^{\mathrm{TOT}}, \tag{2.18}$$

where E_{N-1}^{TOT} and E_N^{TOT} is the total ground state energy of the solid with $N-1$ and N electrons present, respectively. In comparison, the electron affinity is defined as the energy required to add an extra electron to the solid:

$$A = E_N^{\mathrm{TOT}} - E_{N+1}^{\mathrm{TOT}}. \tag{2.19}$$

where the term Δ_{XC} takes into account the many-body effects, when an extra electron is added to the system. In first-order approximation, the term Δ_{XC} is given by the energy difference between the exchange-correlation potential $V_{\mathrm{XC}}[n]$ for a system with $N+1$ and N electrons:

$$\Delta_{\mathrm{XC}} = \left(V_{\mathrm{XC}}[n]\big|_{N+1} - V_{\mathrm{XC}}[n]\big|_{N} \right) + \mathcal{O}\left(\frac{1}{N}\right). \tag{2.23}$$

For a solid, the change in the electron density n as a result of the addition of one electron is in the order of $10^{-20}\, n$. Nevertheless, we expect the exchange-correlation potential $V_{\mathrm{XC}}[n]$ related to the 'exact' exchange-correlation function $F_{\mathrm{KS}}[n]$ to be a discontinues function and, thus, Δ_{XC} to be non-zero. However, we do not know the exact exchange-correlation functional F_{KS} and by construction the LDA is a continuous function of the charge density. Therefore, the Kohn-Sham-based DFT in combination with the LDA cannot yield the correct band-gap. Various attempts have been made to improve the exchange-correlation functional to match the exchange-correlation energy of a solid more closely[2]. Nevertheless, the inclusion of the discontinuity remains challenging in the framework of the Kohn-Sham approach.

To retrieve the correct band-gap, DFT has to be formulated in terms of quasi-particles. In practice, the introduction of quasi-particles is often done using the *GW* method [45]. The *GW* method requires computationally very demanding self-consistent calculations and is often impractical for relevant systems [44]. However, approaches like G_0W_0 have been developed that calculated the quasi-particle band-gap in a perturbative approach starting from the solutions of the Kohn-Sham equations. The calculated quasi-particle band-gaps have been shown to be very close in energy to the experimentally determined band-gaps. Moreover, it was demonstrated that, except for the precise band-gap size, the DFT-LDA band structures of valence and conduction band are in good agreement with the quasi-particle band structure. Therefore, the Kohn-Sham approach in combination with the LDA is a valuable tool nevertheless and can be used for the prediction of properties of solids for which the exact band-gap size is of minor importance.

2.3 The $\mathbf{k} \cdot \mathbf{p}$ Theory

The great advantage of DFT is that as an *ab initio* method it does not require any material parameter as an input. The disadvantage is that self-consistent calculations are required, which are computationally expensive and scale with system size. For this reason, alternatives to DFT have been developed, of which the $\mathbf{k} \cdot \mathbf{p}$ theory is one.

The $\mathbf{k} \cdot \mathbf{p}$ method uses perturbation theory to calculate the band structure of selected bands around $\mathbf{k}$-points of high symmetry. In contrast to DFT, it is an empirical method that requires for the knowledge of specific material parameters. We will use $\mathbf{k} \cdot \mathbf{p}$ theory for the investigation of the band-gap bowing of $\mathrm{Ge}_{1-x-y}\mathrm{Si}_x\mathrm{Sn}_y$ alloys in Chap. 3 and also as basis for our self-consistent effective mass calculations concerning the Ge multiple quantum well structures in Chap. 5. In the following, we will discuss the fundamental ideas of $\mathbf{k} \cdot \mathbf{p}$ theory first for bulk semiconductors and afterward semiconductor heterostructures.

[2] An example for an improved exchange-correlation functional is the general gradient approximation (GGA) [47], which does not only dependent on the charge density n but also on its first derivative ∇n. Further improvements of the exchange-correlation functional are possible. Since in our calculations we only use the LDA, we will not elaborate further on this topic. Instead, we refer the interested reader to the work of Perdew *et al.* on the topic of "Jacob's Ladder" [48].

2.3.1 Bulk Semiconductor

When we derived the DFT in Sec. 2.2, we included the entire electronic system into our considerations, including all electron-electron interactions. To derive the $\mathbf{k}\cdot\mathbf{p}$ theory, use the independent-electron approximation[3], where we assume that we can describe the crystal by using the Schröedinger equation of a single electron moving in an effective potential $V(\mathbf{r})$. The potential $V(\mathbf{r})$ includes the effect of the interaction of the electron with the remaining electrons and the nuclei. The non-relativistic independent-electron Schrödinger equation then reads

$$\left[\frac{\mathbf{p}^2}{2m_0}+V(\mathbf{r})\right]\phi(\mathbf{r})=E\,\phi(\mathbf{r}), \tag{2.24}$$

where $\mathbf{p}$ is the momentum operatur, m_0 the free electron mass, and $\phi(\mathbf{r})$ and E are the wavefunction and energy of the independent electron, respectively. Since the effective potential term obeys the same translational invariance as the crystal lattice, solutions to this equation must fulfill Bloch's theorem:

$$\phi_{\mathbf{k}}(\mathbf{r})=e^{i\mathbf{k}\cdot\mathbf{r}}\,u_{\mathbf{k}}(\mathbf{r}), \tag{2.25}$$

where the functions $u_{\mathbf{k}}(\mathbf{r})$ have the same periodicity as the crystal lattice, i. e. they obey the relation

$$u_{\mathbf{k}}(\mathbf{r}+\mathbf{R}_n)=u_{\mathbf{k}}(\mathbf{r}), \tag{2.26}$$

with $\mathbf{R}_n$ any Bravais lattice vector and $\mathbf{k}$ a crystal wavevector. Inserting the Bloch ansatz into Eq. (2.24), we can formulate an eigenvalue equation for the $u_{n\mathbf{k}}$:

$$\left[\frac{p^2}{2m_0}+V(\mathbf{r})+\frac{\hbar^2k^2}{2m_0}+\frac{\hbar}{m_0}\mathbf{k}\cdot\mathbf{p}\right]u_{n\mathbf{k}}(\mathbf{r})=E_n(\mathbf{k})\,u_{n\mathbf{k}}(\mathbf{r}). \tag{2.27}$$

From this point on, different but equivalent derivations of the $\mathbf{k}\cdot\mathbf{p}$ theory are possible [49]. Here, we will derive the $\mathbf{k}\cdot\mathbf{p}$ theory in a perturbative approach. The fundamental idea is that even though we do not in general know the eigenfunctions $u_{n\mathbf{k}}(\mathbf{r})$ for an arbitrary wavevector $\mathbf{k}$, from symmetry considerations as well as experimental measurements we are able to deduce information about the eigenfunctions at high symmetry points $\mathbf{k}_0$. Therefore, we will separate the Hamiltonian above in a Hamiltonian H_0 describing an electron with wavevector $\mathbf{k}_0$ and a perturbation resulting from the difference $\mathbf{k}-\mathbf{k}_0$ of the wavevectors. We find

$$\big(H_0+H_1\big)\,u_{n\mathbf{k}}(\mathbf{r})=\epsilon_n(\mathbf{k})\,u_{n\mathbf{k}}(\mathbf{r}) \tag{2.28}$$

with

$$\begin{aligned} H_0&=\frac{p^2}{2m_0}+V(\mathbf{r}),\\ H_1&=\frac{\hbar}{m_0}(\mathbf{k}-\mathbf{k}_0)\cdot\mathbf{p},\\ \epsilon_n(\mathbf{k})&=E_n(\mathbf{k})-\frac{\hbar^2(\mathbf{k}-\mathbf{k}_0)^2}{2m_0}. \end{aligned} \tag{2.29}$$

In the following, we want to calculate the energy eigenvalues ϵ_n given in Eq. (2.28) perturbatively. To calculate the band structure around the near-gap valleys, it is advantageous to investigate the structure and symmetry of the valence and conduction band.

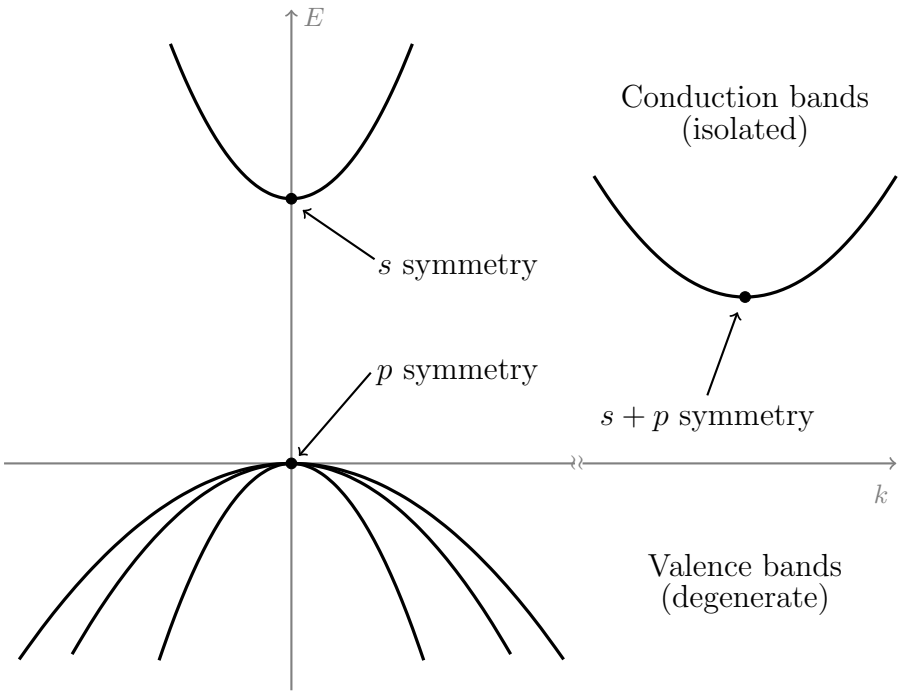

Figure 2.1: *Illustration of the near-band-gap valence and conduction bands in the non-relativistic limit. The valence band maximum is located at the* Γ*-point where three bands are degenerate. The wavefunctions of the three bands at the* Γ*-point feature a symmetry corresponding to the p-orbitals of an single atom. The lowest conduction bands are usually isolated. The wavefunction of the conduction band at the* Γ*-point features a symmetry corresponding to the s-orbitals of a single atom. In contrast, the wavefunctions of conduction minima away from the zone center usually feature a mixed* $s + p$ *symmetry.*

Structure and Symmetry of the Near-Gap Valleys

Figure 2.1 illustrates the band structure around near-gap valleys in the conduction and valence band. The valence band maximum is located at the Γ-point. In the non-relativistic limit, the valence band maximum is three-fold degenerate. As a result of this degeneracy, we have to treat the valence bands using degenerate perturbation theory. In the conduction band, two different valleys are illustrated in Fig. 2.1. At the Γ-point, there is the direct valley. Moreover, we find another minimum at $\mathbf{k} \neq 0$, which represents in the SiGeSn material system either the conduction band minima at the L-point or the Δ-valley. For the conduction band minima, there is a considerable energy separation between the lowest and the next highest band as well as the highest valence band. Therefore, they can be considered as isolated and we can treat them using non-degenerate perturbation theory.

In the later sections, we will see that also symmetry plays an important role in the development of the $\mathbf{k}\cdot\mathbf{p}$ theory. Investigating the symmetry of the bands at the Γ-point, it can be shown that the wavefunctions of the highest valence bands have a symmetry that corresponds to the symmetry of the p-orbits of isolated atoms [50]. In comparison, the wavefunction of the lowest conduction band at the Γ has a symmetry of the s-orbital of an isolated atom. When moving away from the zone center, the wavefunctions at the indirect conduction band valleys feature a mixed $s+p$ symmetry [51].

Using the information about the degeneracy and non-degeneracy of the conduction and valence band as well as the symmetry of the respective wavefunction, we can derive the perturbative expression for the band structure around the band extrema. First, we investigate the isolate conduction bands. Then, we move on to study the degenerate valence bands.

Isolated Bands

For isolated bands, we can develop the so-called effective mass approximation. Following non-degenerate perturbation theory, we find for the lattice-periodic functions in first-order

$$u_{n\mathbf{k}}(\mathbf{r}) = u_{n\mathbf{k}_0}(\mathbf{r}) + \frac{\hbar}{m_0}\sum_{m\neq n}\frac{(\mathbf{k}-\mathbf{k}_0)\cdot\mathbf{p}_{mn}(\mathbf{k}_0)}{E_{n\mathbf{k}_0}-E_{m\mathbf{k}_0}}\,u_{m\mathbf{k_0}}(\mathbf{r}) \tag{2.30}$$

and for the energy $E_{n\mathbf{k}}$ in second-order

$$\begin{aligned} E_{n\mathbf{k}} =& E_n(\mathbf{k}_0) + \frac{\hbar^2(\mathbf{k}-\mathbf{k}_0)^2}{2m_0} + \frac{\hbar}{m_0}(\mathbf{k}-\mathbf{k}_0)\cdot\mathbf{p}_{nn}(\mathbf{k}_0) \\ &+ \frac{\hbar^2}{m_0^2}\sum_{m\neq n}\frac{\left|(\mathbf{k}-\mathbf{k}_0)\cdot\mathbf{p}_{nm}(\mathbf{k}_0)\right|^2}{E_n(\mathbf{k}_0)-E_m(\mathbf{k}_0)}, \end{aligned} \tag{2.31}$$

where $\mathbf{p}_{nm}(\mathbf{k}_0) = \langle u_{m\mathbf{k}_0}|\,\mathbf{p}\,|u_{n\mathbf{k}_0}\rangle$. Since we are usually interested in the band structure around extrema in the near-gap conduction and valence bands, the third term on the r.h.s. of Eq. (2.31) is zero. We can therefore write

$$E_n(\mathbf{k}) = E_n(\mathbf{k}_0) + \frac{\hbar^2}{2}\sum_{ij}(k_{0,i}-k_i)\left(\frac{1}{m^*}\right)_{ij}(k_{0,j}-k_j), \tag{2.32}$$

where we introduced the effective mass tensor

$$\left(\frac{1}{m^*}\right)_{ij} = \frac{1}{m_0}\delta_{ij} + \frac{2}{m_0^2}\sum_{n\neq m}\frac{p^i_{mn}(\mathbf{k}_0)\,p^j_{nm}(\mathbf{k}_0)}{E_n(\mathbf{k}_0)-E_m(\mathbf{k}_0)}. \tag{2.33}$$

[3] This approximation is also sometimes referred to as single-electron approximation.

Let us look at this relation in more detail. For a spherically symmetric dispersion relation, which is commonly assumed for near band-gap states at the Γ-point, the effective mass tensor reduces to a scalar and Eq. (2.32) describes the energy of a free particle with the mass m^*. For conduction band extrema at, e.g. the L- and X-point, the dispersion relation becomes $\mathbf{k}$-dependent and the full tensor has to be considered.

In order to calculate the components of the effective mass tensor, a few simplification can be made. First of all, following the symmetry considerations discussed above, matrix elements $\mathbf{p}_{nm}$ can be ruled out that do not contribute to the effective mass. Furthermore, the sum can usually be reduced to only those states m, which are closest in energy to the band n. For all other bands the denominator $(E_n(\mathbf{k}_0) - E_m(\mathbf{k}_0))$ becomes large, wherefore their contribution to the effective mass can be neglected as well. Nevertheless, the coupling terms $\mathbf{p}_{nm}$ are not given by $\mathbf{k}\cdot\mathbf{p}$ theory but have to be deduced by some other theoretical method. For this reason, rather than attempting to calculate the effective mass, it is often easier to measure the components of the effective mass tensor experimentally by, for example, cyclotron measurements [52, 53].

Degenerate Bands

If relativistic effects are neglected, the three top-most valence bands at the Γ-point are degenerate. The perturbation Hamiltonian H_1 does not lift the degeneracy for $\mathbf{k}_0 = 0$ as can be seen from Eq. (2.29). Therefore, the energy dispersion relation has to be determined in second-order degenerate perturbation theory [54]. The lattice periodic function can then be written as a linear combination of the three degenerate eigenfunctions $|X\rangle$, $|Y\rangle$, and $|Z\rangle$ which correspond in their symmetry properties to the p_x, p_y, and p_z orbitals of an isolated atom:

$$|u_{\mathbf{k}}\rangle = \sum_{m=Z,Y,Z} c_m(\mathbf{k})|m\rangle, \tag{2.34}$$

where $c_m(\mathbf{k}) = \langle m|u_{\mathbf{k}}\rangle$. The coefficients $c_m(\mathbf{k})$ and the energy dispersion can be determined through the matrix equation

$$H_{\mathbf{k}}\mathbf{c}_{\mathbf{k}} = E_{n\mathbf{k}}\mathbf{c}_{\mathbf{k}} \tag{2.35}$$

where $\mathbf{c}_{\mathbf{k}}$ is the vector containing the coefficients $c_m(\mathbf{k})$ and the elements of the 3×3 matrix $H_{\mathbf{k}}$ are defined as

$$H_{\mathbf{k},ij} = \left(E_v + \frac{\hbar^2 k^2}{2m_0}\right)\delta_{ij} + \frac{\hbar^2}{m_0^2}\sum_{\alpha>3}\frac{\mathbf{k}\cdot\mathbf{p}_{i\alpha}\mathbf{k}\cdot\mathbf{p}_{\alpha j}}{E_v - E_\alpha}. \tag{2.36}$$

The index α runs over all those bands other than the three degenerate valence bands. Those bands are often referred to as the remote bands. Using symmetry properties of the degenerate hole states and the momentum operator, as discussed above, the last term in the Hamiltonian $H_{\mathbf{k}}$ can be greatly simplified. We find for the 3×3 matrix

$$H(\mathbf{k}) = \begin{pmatrix} |X\rangle & |Y\rangle & |Z\rangle \\ E_v + Lk_x^2 + M(k_y^2+k_z^2) & Nk_xk_y & Nk_xk_y \\ Nk_yk_x & E_v + Lk_y^2 + M(k_x^2+k_z^2) & Nk_yk_z \\ Nk_zk_x & Nk_zk_y & E_v + Lk_z^2 + M(k_x^2+k_y^2) \end{pmatrix}, \tag{2.37}$$

where the constants L, M, and N are defined as

$$\begin{aligned} L &= \frac{\hbar^2}{2m_0} + \frac{\hbar^2}{m_0^2} \sum_{\alpha>3} \frac{\left|\langle X|p_x|\alpha\rangle\right|^2}{E_v - E_\alpha}, \\ M &= \frac{\hbar^2}{2m_0} + \frac{\hbar^2}{m_0^2} \sum_{\alpha>3} \frac{\left|\langle X|p_y|\alpha\rangle\right|^2}{E_v - E_\alpha}, \\ N &= \frac{\hbar^2}{m_0^2} \sum_{\alpha>3} \frac{\langle X|p_x|\alpha\rangle\langle\alpha|p_y|Y\rangle + \langle X|p_y|\alpha\rangle\langle\alpha|p_x|Y\rangle}{E_v - E_\alpha}, \end{aligned} \tag{2.38}$$

Similarly to the effective masses in the previous section, the three constants L, M, and N are material specific and need to be determined either with another theoretical method or by fitting the expression to experimental band structure data.

Let us investigate once again the effective mass equation for isolated bands and the matrix equation for degenerate band given in Eq. (2.32) and Eq. (2.36), respectively. We notice that either the effective mass tensor m_{ij}^* or the parameters N, M, and L fully determine the band structure around the considered $\mathbf{k}$-point. This comparably small number of material parameters is the great advantage of $\mathbf{k} \cdot \mathbf{p}$ theory over other methods. Particularly, for the case of optoelectronics, where we are primarily interested in a very narrow range of $\mathbf{k}$-vectors around a few near band-edge states. Furthermore, we find that the microscopic structure of the problem is not visible in the equations anymore. This information has been completely absorbed into the material parameters. For this reason, the $\mathbf{k}\cdot\mathbf{p}$ theory is very often also called a continuum method.

Spin-Orbit Coupling

Up to now, we have neglected the influence of the spin-orbit coupling on the dispersion relation. While spin-orbit coupling has only minor influence on the dispersion relation of the conduction bands, it leads to significant contributions to the dispersion relation of the top-most valence band, which is most visible in partial lifting of the degeneracy at the Γ-point. For a complete descriptions of the valence bands, we have to include it into the $\mathbf{k}\cdot\mathbf{p}$ formalism, which we have developed in the previous version.
In a semi-classical picture, spin-orbit coupling can be pictured as the coupling of the magnetic moment created by the rotation of the electrons around the atoms given by the angular momentum $\mathbf{L}$ with the spin $\mathbf{S}$ of the electrons. The spin-orbit coupling, which can be derived from the Dirac equation, can be treated as a perturbation to the wavefunction $\phi_\mathbf{k}$ and is given by [55]

$$H'_{\mathrm{SO}} = \frac{\hbar}{4m_0^2c^2} \left[(\nabla V) \times \mathbf{p}\right] \cdot \sigma, \tag{2.39}$$

where c is the speed of light and the Cartesian components of σ are the Pauli matrices

$$\sigma_x = \begin{pmatrix} 0 & 1 \\ 1 & 0 \end{pmatrix}, \quad \sigma_y = \begin{pmatrix} 0 & -i \\ i & 0 \end{pmatrix}, \quad \sigma_z = \begin{pmatrix} 1 & 0 \\ 0 & -1 \end{pmatrix}. \tag{2.40}$$

The spin-orbit interaction then leads to two additional corrections, which need to be taken into account besides the corrections already included in perturbation term H_1 in Eq. (2.29), given

by:

$$\begin{aligned} H_{\mathrm{SO}} &= \frac{\hbar}{4m_0^2c^2}\left[(\nabla V)\times\mathbf{p}\right]\cdot\sigma + \frac{\hbar^2}{4m_0^2c^2}\left[(\nabla V)\times\mathbf{k}\right]\cdot\sigma \\ &\equiv H_{\mathrm{SO},p} + H_{\mathrm{SO},k}. \end{aligned} \tag{2.41}$$

When comparing the magnitude of the two spin-orbit terms, the first term is of greater importance than the second. In fact, estimates show that the second term influences the value of the eigenenergies only by one percent [56]. For this reason, we follow the standard procedure and only include $H_{\mathrm{SO},p}$ in our further discussion. In order to add the spin-orbit coupling, the basis states have to be extended to now also include the spin. We represent the spin-up or spin-down state of an electron by $|\uparrow\rangle$ and $|\downarrow\rangle$. The number of relevant valence band states therefore increases from three to six, which we write as

$$|X,\uparrow\rangle, |X,\downarrow\rangle, |Y,\uparrow\rangle, |Y,\downarrow\rangle, |Z,\uparrow\rangle, |Z,\downarrow\rangle. \tag{2.42}$$

The angular momentum of the $|X\rangle$, $|Y\rangle$, and $|Z\rangle$ states is one. Therefore, the total angular momentum $\mathbf{J}=\mathbf{L}+\mathbf{S}$ can take the value $j=3/2$ (with four states $j_z=\pm3/2$ and $j_z=\pm1/2$) or $j=1/2$ (with two states $j_z=\pm1/2$). For the movement of electrons in a spherically symmetric potential, the spin-orbit perturbation $H_{\mathrm{SO},p}$ can be rewritten in terms of angular momentum and spin [42, p. 319]:

$$H_{\mathrm{SO},p} = \frac{\hbar}{2m_0^2c^2}\frac{\hbar}{r}\frac{\mathrm{d}V}{\mathrm{d}r}\mathbf{S}\cdot\mathbf{L}. \tag{2.43}$$

where we have used the relation $\mathbf{S}=\hbar/2\,\sigma$ and the assumption that V is spherically symmetric. Furthermore, the quantity $\mathbf{S}\cdot\mathbf{L}$ can be expressed in terms of the eigenvalues j, l, and s of the operators $\mathbf{J}$, $\mathbf{L}$, and $\mathbf{S}$, respectively,

$$\mathbf{S}\cdot\mathbf{L} = \hbar\left[j(j+1)+l(l+1)+s(s+1)\right] = \begin{cases} +1\hbar & \text{for} \quad j=3/2 \\ -2\hbar & \text{for} \quad j=1/2 \end{cases}. \tag{2.44}$$

The states with total angular momentum $j=1/2$ are therefore split from those with angular momentum $j=3/2$. When including the spin-orbit coupling, it is common to transform the original basis states $|X\rangle$, $|Y\rangle$, and $|Z\rangle$ together with the respective spin states into the basis of the total angular momentum. The transformation relations are given by

$$\begin{aligned} |j=\frac{3}{2},j_z=+\frac{3}{2}\rangle &= -\frac{1}{\sqrt{2}}|(X+iY),\uparrow\rangle, \\ |j=\frac{3}{2},j_z=+\frac{1}{2}\rangle &= -\frac{1}{\sqrt{6}}|(X+iY),\downarrow\rangle - 2|Z,\uparrow\rangle, \\ |j=\frac{3}{2},j_z=-\frac{1}{2}\rangle &= \frac{1}{\sqrt{6}}|(X-iY),\uparrow\rangle + 2|Z,\downarrow\rangle, \\ |j=\frac{3}{2},j_z=-\frac{3}{2}\rangle &= \frac{1}{\sqrt{2}}|(X-iY),\downarrow\rangle, \\ |j=\frac{1}{2},j_z=+\frac{1}{2}\rangle &= \frac{1}{\sqrt{3}}(|(X+iY),\downarrow\rangle + |Z,\uparrow\rangle), \\ |j=\frac{1}{2},j_z=-\frac{1}{2}\rangle &= -\frac{1}{\sqrt{3}}(|(X-iY),\uparrow\rangle - |Z,\downarrow\rangle). \end{aligned} \tag{2.45}$$

Analogously to the case without spin-orbit coupling, a matrix equation can be derived that determines the perturbed eigenstates and eigenvalues:

$$H'_{\mathbf{k}}\mathbf{c}_{\mathbf{k}} = E_{n\mathbf{k}}\mathbf{c}_{\mathbf{k}}, \tag{2.46}$$

where $H'_{\mathbf{k}}$ now is a 6×6 matrix given in the basis of the total angular momentum by

$$H'_{\mathbf{k}} = \begin{pmatrix} |\frac{3}{2},\frac{3}{2}\rangle & |\frac{3}{2},\frac{1}{2}\rangle & |\frac{3}{2},-\frac{1}{2}\rangle & |\frac{3}{2},-\frac{3}{2}\rangle & |\frac{1}{2},\frac{1}{2}\rangle & |\frac{1}{2},-\frac{1}{2}\rangle \\ -P-Q & S & -R & 0 & \frac{1}{\sqrt{2}}S & -\sqrt{2}R \\ S^\dagger & -P+Q & 0 & -R & \sqrt{2}Q & -\sqrt{\frac{3}{2}}S \\ -R^\dagger & 0 & -P+Q & -S & -\sqrt{\frac{3}{2}}S^\dagger & -\sqrt{2}Q \\ 0 & -R^\dagger & -S^\dagger & -P-Q & \sqrt{2}R^\dagger & \frac{1}{\sqrt{2}}S^\dagger \\ \frac{1}{\sqrt{2}}S^\dagger & \sqrt{2}Q^\dagger & -\sqrt{\frac{3}{2}}S & \sqrt{2}R & -P-\Delta_0 & 0 \\ -\sqrt{2}R^\dagger & -\sqrt{\frac{3}{2}}S^\dagger & -\sqrt{2}Q^\dagger & \frac{1}{\sqrt{2}}S & 0 & -P-\Delta_0 \end{pmatrix}, \tag{2.47}$$

where P, Q, S, and R are defined as

$$\begin{aligned} P &= \frac{\hbar^2}{2m_0}\gamma_1(k_x^2+k_y^2+k_z^2), \\ Q &= \frac{\hbar^2}{2m_0}\gamma_2(k_x^2+k_y^2-2k_z^2), \\ S &= \frac{\hbar^2}{m_0}\sqrt{3}\gamma_3(k_x-ik_y)k_z, \\ R &= -\frac{\hbar^2}{2m_0}\sqrt{3}(\gamma_2(k_x^2-k_y^2)-2i\gamma_3 k_x k_y), \end{aligned} \tag{2.48}$$

and Δ_0 is the spin-orbit splitting at $\mathbf{k} = 0$ given by $\Delta = 3\langle X,\uparrow|H_{\mathrm{SO},p}|Z,\downarrow\rangle$. The parameters γ_1, γ_2, and γ_3 are the Luttinger parameters. They are related to the earlier defined parameters L, M, and N via [54]

$$\begin{aligned} -\frac{\hbar^2}{2m_0}\gamma_1 &= \frac{1}{3}(L+2M), \\ -\frac{\hbar^2}{2m_0}\gamma_2 &= \frac{1}{6}(L-M), \\ -\frac{\hbar^2}{2m_0}\gamma_3 &= \frac{N}{6}. \end{aligned} \tag{2.49}$$

The components of $\mathbf{c}_{\mathbf{k}}$ correspond, in this order, to the heavy hole (HH) spin-up, light hole (LH) spin-up, LH spin-down, HH spin-down, split-off hole (SO) spin-up, and SO spin-down band. From closer examination of the matrix $H'_{\mathbf{k}}$ given in Eq. (2.47), we see that for $\mathbf{k} = 0$, the upper four bands are degenerate and have the eigenvalue zero while the lowest two bands have eigenvalue $-\Delta_0$. The HH band has in general a smaller dispersion than the LH band, which corresponds to a larger effective mass.

For completeness, we note that other formulations of the $\mathbf{k}\cdot\mathbf{p}$ Hamiltonian exist. In our derivation, we followed the notation of Chuang [57]. However, there are also equivalent formulations by Dresselhaus, Kip, and Kittel [52] as well as Luttinger and Kohn [58]. They differ in the definition of the basis set and the material parameters, but lead to the same

dispersion relation. It is also possible to include more bands than just the three degenerate valence bands. An example is Kane's eight-band Hamiltonian [59, pp. 194-217], where also the coupling to the lowest conduction band at the Γ point is explicitly considered. If even more bands are explicitly taken into account, the range of $\mathbf{k}$-values around $\mathbf{k}_0$ in which the dispersion relation is valid, can be increased. Cardona and Pollak [60] have shown that with 15 bands, the band structure of the entire Brillouin zone can be correctly calculated. This comes at the price of having to diagonalize a larger Hamiltonian and the introduction of additional band structure parameters. For the investigation of optoelectronic properties, we are mainly interested in the energy dispersion in close proximity to band extrema. Therefore, the effective mass formulation and the six-band approach by Luttinger are sufficient.

2.3.2 Heterostructures

The formulation of the $\mathbf{k}\cdot\mathbf{p}$ theory for heterostructures has been controversially discussed since the emergence of the first theoretical studies of semiconductor heterostructures. In heterostructures, the material parameters gain a spatial dependence. Particularly the derivation of the correct ordering of momentum operator and material parameters has been challenging [61–63]. The first person to develop an exact formulation of the $\mathbf{k}\cdot\mathbf{p}$ equations for semiconductor heterostructures was Burt in 1988 using the envelope function method [64–66]. In the following, we outline the derivation of the effective mass approximation for heterostructures using Burt's theory, which we base our description of the $Si_{1-x}Ge_x$/Si multi-quantum-well structure in Chap. 5 upon. It is also possible, to derive a $\mathbf{k}\cdot\mathbf{p}$ matrix description for heterostructures. This, however, is beyond the scope of this work and we refer the interested reader to the work of Foreman, who derived a six-band and eight-band Hamiltonian for zinc-blende crystals [67, 68].

As for bulk material, we start our derivation with the time-independent one-particle Schrödinger equation

$$\left(\frac{\mathbf{p}^2}{2m_0}+V(\mathbf{r})\right)\phi(\mathbf{r})=E\phi(\mathbf{r}) \tag{2.50}$$

where $\mathbf{p}$ is again the momentum operator, m_0 the electron mass, and $V(\mathbf{r})$ the potential. Since we deal with semiconductor heterostructures, we cannot assume the potential to be translation invariant in all spacial dimensions. A key ingredient of the theory developed by Burt is the expansion of $\psi(\mathbf{r})$ in terms of eigenfunctions $U_n(\mathbf{r})$ that are spatially modulated by the so-called envelope functions $F(\mathbf{r})$

$$\phi(\mathbf{r})=\sum_n F_n(\mathbf{r})U_n(\mathbf{r}), \tag{2.51}$$

an approach previously used by Luttinger and Kohn [58] to describe the eigenfunctions of bulk semiconductors encompassing shallow acceptor levels. In their description, the $U_n(\mathbf{r})$ correspond to the lattice-periodic functions at the Γ-point u_{n0} of the bulk crystal. Burt extends their approach to heterostructures by loosening this requirement and solely demanding that the $U_n(\mathbf{r})$ form a complete set of orthonormal functions, referred to as generalized zone-center eigenfunctions in the following. It can be shown that due to this specific choice, the envelope functions and all their derivatives are smooth and continuous everywhere [64].

Inserting ansatz (2.51) into Eq. (2.50), we can derive those equations that govern the behavior of the envelope functions $F_n(\mathbf{r})$. For the kinetic energy term we find

$$-\frac{\hbar^2}{2m_0}\nabla^2\phi(\mathbf{r})=-\frac{\hbar^2}{2m_0}\sum_n\left(F_n''U_n+2F_n'U_n'+F_nU_n''\right). \tag{2.52}$$

As $\{U_n\}$ is a set of orthonormal functions, we can also use these functions to expand the derivatives of U_n, which leads to the expression

$$-\frac{\hbar^2}{2m_0}\nabla\phi = -\sum_n \left(-\frac{\hbar^2}{2m_0}F_n'' - \frac{i\hbar}{m_0}\sum_m p_{nm}F_m' + \sum_m T_{nm}F_m \right), \tag{2.53}$$

with $p_{mn} = \int U_m^* \left(-i\hbar\nabla\right) U_n \,\mathrm{d}\mathbf{r}$ and $T_{mn} = \int U_m^* \left(-\frac{\hbar^2}{2m_0}\nabla^2\right) U_n \,\mathrm{d}\mathbf{r}$. Deriving the potential term in envelope-function form is more challenging. Applying a Fourier transformation to the crystal potential, the envelope functions, and the zone-center functions and rearranging the terms, we find

$$V(\mathbf{r})\phi(\mathbf{r}) = \sum_m \left(\sum_m \int V_{nm}(\mathbf{r},\mathbf{r}')F_m(\mathbf{r}') \right) U_n \tag{2.54}$$

with

$$V_{nm}(\mathbf{r},\mathbf{r}') = \frac{1}{V}\sum_{\mathbf{k},\mathbf{k}'}\sum_{\mathbf{G},\mathbf{G}'} U_{n,\mathbf{G}+\mathbf{G}_1}\tilde{V}_{\mathbf{G}-\mathbf{G}'}(\mathbf{k})U_{m\mathbf{G}'}e^{i(\mathbf{k}_1\cdot\mathbf{r}+\mathbf{k}'\mathbf{r}')}. \tag{2.55}$$

Here, $\tilde{V}_{\mathbf{G}}(\mathbf{k})$ and $U_{m\mathbf{G}}$ are the components of the crystal potential and zone-center eigenfunctions in reciprocal space with reciprocal lattice vector $\mathbf{G}$ and crystal momentum $\mathbf{k}$, respectively, and $\mathbf{G}_1$ is a reciprocal lattice vector defined together with $\mathbf{k}_1$ through the relation $\mathbf{k}+\mathbf{k}' = \mathbf{k}_1 + \mathbf{G}_1$. The total envelope-function equation is then given by combining Eq. (2.53) and Eq. (2.54) and solving for the coefficients of U_n. We find

$$-\frac{\hbar^2}{2m_0}\nabla^2 F_n - \frac{i\hbar}{m_0}\sum_m \mathbf{p}_{nm}\cdot\nabla F_m + \sum_m \int H_{nm}(\mathbf{r},\mathbf{r}')F_m(\mathbf{r}')\mathrm{d}\mathbf{r}' = EF_n, \tag{2.56}$$

where $H_{nm}(\mathbf{r},\mathbf{r}') = T_{nm}\delta(\mathbf{r}-\mathbf{r}') + V_{nm}(\mathbf{r},\mathbf{r}')$. Inspecting Eq. (2.56) more closely, we find that to determine the set of envelope functions requires the evaluation of a nonlocal potential term. This nonlocality is introduced due to fact that both, the envelope functions as well as the crystal potential, are composed of Fourier components that individually lie in the first Brillouin zone, but whose sums lie outside. In order to solve this set of equations, a number of approximations has to be made. The first of those concerns the dropping of the nonlocal parts of $V_{nm}(z,z')$. Burt showed that the potential energy term can be separated into a local and a non-local part $V_{nm}(\mathbf{r})\delta(\mathbf{r}-\mathbf{r}')$ and $V_{nm}^{(\mathrm{nl})}(\mathbf{r},\mathbf{r}')$, respectively, and in addition, that the integral over $\mathbf{r}'$ of the non-local part is approximately zero. The non-local part can therefore be neglected which converts the set of integro-differential equations into a set of purely differential equations given by

$$-\frac{\hbar^2}{2m_0}\nabla^2 F_n - \frac{i\hbar}{m_0}\sum_m p_{nm}\nabla F_m + \sum_m H_{nm}(\mathbf{r})F_m(\mathbf{r}) = EF_n, \tag{2.57}$$

with $H_{nm}(\mathbf{r}) = T_{nm}(\mathbf{r}) + V_{nm}(\mathbf{r})$. Far away from an interface, the $H_{nm}(\mathbf{r})$ approaches the bulk value H_{nm} of the respective material, while in proximity to an interface additional contributions have to be taken into account. $H_{nm}(\mathbf{r})$ can be decomposed into two terms:

$$H_{nm}(\mathbf{r}) = H_{nm}^{(\mathrm{bulk})}(\mathbf{r}) + H_{nm}^{(\mathrm{if})}(\mathbf{r}). \tag{2.58}$$

The term $H_{nm}^{(\mathrm{bulk})}(\mathbf{r})$ can be understood as a step function of the respective bulk values of H_{nm} when crossing an interface, which is softened by Gibbs' oscillations contained in the term $H_{nm}^{(\mathrm{if})}$.

Through Fourier analysis, it can be shown that the components of $H_{nm}^{(\mathrm{if})}$ are only non-zero in proximity to an interface and, most importantly, small in comparison to the bulk contributions, wherefore the term $H_{nm}^{(\mathrm{if})}(\mathbf{r})$ can be dropped.

In order to derive an effective-mass-like equation from the envelope-function equations, we again consider the simplest case of a band whose energy E around an extremum is much closer to the energy of a non-degenerate band edge c than any other band edge. We therefore expect the envelope function $F_c(\mathbf{r})$ belonging to the conduction band-like state $U_c(\mathbf{r})$ to be dominant while all other envelope functions (denoted with the index r) are small. From Eq. (2.57), we find an approximate expression for the envelope functions F_r as a function of the dominant envelope functions in the case of slowly varying envelope functions (slowly varying envelope approximation)

$$F_r \approx \frac{1}{E - H_{rr}} \left(-\frac{i\hbar}{m} \mathbf{p}_{rc} \cdot \nabla F_c + H_{rc} F_c \right). \tag{2.59}$$

Combining Eq. (2.57) and Eq. (2.59), we find an approximate equation for $F_c(\mathbf{r})$

$$\begin{aligned} -\frac{\hbar^2}{2m_0} \nabla \frac{1}{m_c(E,\mathbf{r})} \nabla F_c(\mathbf{r}) - \frac{-i\hbar}{m_0} \mathbf{p}_{cc} \cdot \nabla F_c(\mathbf{r}) + H_{cc}^{(2)}(E,\mathbf{r}) F_c(\mathbf{r}) \\ + \sum_r -\frac{i\hbar}{m_0} \mathbf{p}_{cr} \cdot \nabla \left[\frac{H_{rc}}{E - H_{rr}} \right] F_c(\mathbf{r}) \\ + \sum_r -\frac{i\hbar}{m_0} \frac{\mathbf{p}_{cr} H_{rc} + H_{cr} \mathbf{p}_{rc}}{E - H_{rr}} \cdot \nabla F_c(\mathbf{r}) = E F_c(\mathbf{r}), \end{aligned} \tag{2.60}$$

where we defined $m_c(E,\mathbf{r})$ and $H_{ss}^{(2)}(E,\mathbf{r})$ as

$$\begin{aligned} \frac{1}{m_c(E,\mathbf{r})} &= 1 + \frac{2}{m_0} \sum_r \frac{\mathbf{p}_{cr} \mathbf{p}_{rc}}{E - H_{rr}(\mathbf{r})}, \\ H_{cc}^{(2)}(E,\mathbf{r}) &= H_{cc}(\mathbf{r}) + \sum_r \frac{H_{cr}(\mathbf{r}) H_{rc}(\mathbf{r})}{E - H_{rr}(\mathbf{r})}. \end{aligned} \tag{2.61}$$

Here, the term $m_c(E,\mathbf{r})$ has the meaning of the effective mass as defined earlier for bulk material with the difference that it is now position dependent. We can further simplify Eq. (2.60) by realizing that the second term on the l.h.s. including the expectation value of the momentum operator $\mathbf{p}_{cc}$ is zero, since we are dealing with a local extremum. Furthermore, the fourth and fifth term both include the denominator $E - H_{rr}$. Since we required the band in question to be isolated, this denominator is large and we can neglect both terms and, therefore, arrive at the equation

$$-\frac{\hbar^2}{2m_0} \nabla \cdot \left(\frac{1}{m_c(E,\mathbf{r})} \nabla F_c(\mathbf{r}) \right) + H_{cc}^{(2)}(E,\mathbf{r}) F_c(\mathbf{r}) = E F_c(\mathbf{r}). \tag{2.62}$$

Focusing on the ordering of the momentum operators and the position-dependent effective mass in the first term on the l.h.s., one finds that this corresponds to the ordering that has been proposed prior to Burt by BenDaniel and Duke and is referred to as the BenDaniel Duke Hamiltonian [69]. However, Burt's approach allowed for a rigorous derivation of the operator ordering. Furthermore, investigating the potential term $H_{cc}^{(2)}$ in more detail, we find that this term is dominated by $H_{cc}(\mathbf{r})$ which is the bulk energy expectation value of the zone-center functions U_c for the respective material at position $\mathbf{r}$. These energy values form the potential

background for the charge carriers in band c. Even though Burt calculated the next higher order terms, those are commonly neglected due to their smallness.

Lastly, we need to discuss the boundary conditions of Eq. (2.62) at an interface to fully specify the effective mass second-order differential equation. For the first boundary condition, we require the envelope functions $F_n(\mathbf{r})$ to be continuous everywhere. For the second boundary condition, we cannot require the continuity of the first derivative across an surface. This may seem contradictory as we originally proposed that $F_c(\mathbf{r})$ and its derivatives are smooth and continuous. However, by applying the slowly varying amplitude approximation and only taking into account one band, the smoothness and continuity properties have been weakened. In order to derive the second boundary condition, we integrate Eq. (2.62) over a region of $\pm\varepsilon$ around an interface and then form the limit $\varepsilon \to 0$. Doing this, we find that instead of ∇F_c the expression $1/m_c \nabla F_c$ has to be continuous. Summarizing our findings, we therefore conclude that in order to fulfill the boundary conditions, we require

$$F_c(\mathbf{r}) \qquad \text{and} \qquad \frac{1}{m_c(z,E)} \nabla F_c(\mathbf{r}) \tag{2.63}$$

to be continuous across an interface between two materials. These boundary conditions are also referred to as BenDaniel Duke boundary conditions.

2.4 Other Band Structure Methods

Besides the DFT and $\mathbf{k}\cdot\mathbf{p}$ theory, there are two other very common band structure methods: the empirical pseudopotential method (EPM) and the tight-binding (TB) approach. They will not directly be used in the projects presented here. However, we will reference to them on multiple occasions. Furthermore, an important aspect of this thesis project was to analyze, which band structure methods are most suited to model the different aspects of Si,Ge, and Sn-based heterostructures. Therefore, we want to introduce here the fundamental ideas of both methods, highlight their differences and similarities in comparison to DFT and $\mathbf{k}\cdot\mathbf{p}$ theory, and discuss possible areas of application.

2.4.1 Empirical Pseudopotential Method

Similar to the Kohn-Sham ansatz for DFT, for the EPM it is also assumed that the many-body electron system can be reformulated in terms of an auxiliary system of non-interacting electrons. However, instead of fully deriving the potential term of the auxiliary system as we did for DFT, the potential is inserted as a material parameter. In the following, we will for simplicity restrict our discussion to the non-relativistic version of the EPM. For a fully relativistic version, we refer the reader to the articles by Chelikowsky and Cohen [70] and by Gonzalez *et al.* [71].

We start our derivation of the EPM from the one-electron time-independent Schrödinger equation given by

$$\left[\frac{p^2}{2m_0} + V(\mathbf{r})\right] \phi_{n\mathbf{k}}(\mathbf{r}) = E_n(\mathbf{k})\, \phi_{n\mathbf{k}}(\mathbf{r}) \tag{2.64}$$

Instead of inserting the Bloch ansatz for the wavefunctions $\phi_{n\mathbf{k}}(\mathbf{r})$ as we did for the derivation of the $\mathbf{k}\cdot\mathbf{p}$ theory, we take a closer look at the properties of the electrons in the crystal. We can separate the electrons into two groups: core electrons, which are located close to the nuclei and valence, and conduction electrons, which are mainly located in the interstitial space between the nuclei. For simplicity, we assume that all nuclei are identical and well separated. Then, the

wavefunctions and energies of the core electrons are given by α_j and E_j. The wavefunctions of the valence and conduction electrons have to be orthogonal to the core states. This condition can be satisfied by constructing the wavefunctions $|\phi_{n\mathbf{k}}\rangle$ for valence and conduction electrons as follows

$$|\phi_{n\mathbf{k}}\rangle = |\chi_{n\mathbf{k}}\rangle - \sum_j |\alpha_j\rangle\langle\alpha_j|\chi_{n\mathbf{k}}\rangle, \tag{2.65}$$

where $|\alpha_j\rangle$ is the wavefunction of core electron j inside the crystal. Due to their localization at a specific atom, the wavefunctions of the core electrons do not have a wavevector dependence. Inserting this ansatz into the original one-particle Schrödinger equation, we find

$$H|\chi_{n\mathbf{k}}\rangle - \sum_j \langle\alpha_j|\chi_{n\mathbf{k}}\rangle H|\alpha_j\rangle = E_n(\mathbf{k}) \left[|\chi_{n\mathbf{k}}\rangle - \sum_j |\alpha_j\rangle\langle\alpha_j|\chi_{n\mathbf{k}}\rangle\right], \tag{2.66}$$

where $H = \frac{p^2}{2m_0} + V(\mathbf{r})$. This expression can be rewritten again into a Schrödinger-like equation for the $|\chi_{n\mathbf{k}}\rangle$

$$\left[\frac{p^2}{2m_0} + V(\mathbf{r}) + \sum_j \Big[E_n(\mathbf{k}) - E_j\Big] |\alpha_j\rangle\langle\alpha_j|\right] |\chi_{n\mathbf{k}}\rangle = E_n(\mathbf{k})|\chi_{n\mathbf{k}}\rangle. \tag{2.67}$$

From Eq. (2.67), it is now appropriate to define a new potential term, the pseudopotential,

$$V_{\mathrm{ps}} = V(\mathbf{r}) + \sum_j \Big[E_n(\mathbf{k}) - E_j\Big] |\alpha_j\rangle\langle\alpha_j|. \tag{2.68}$$

As an ansatz for the wavefunctions of both the valence and conduction electrons, a plane-waves expansion can be employed:

$$\chi_{\mathbf{k}}(\mathbf{r}) = \sum_{\mathbf{G}'} c_{\mathbf{k}+\mathbf{G}'}\ \mathrm{e}^{i(\mathbf{k}+\mathbf{G}')\cdot\mathbf{r}}, \tag{2.69}$$

where $\mathbf{G}'$ is a reciprocal lattice vector. Once the pseudopotential is known, the eigenvalue problem in Eq. (2.67) may be solved in a straight-forward manner using standard numerical techniques.

We want to focus a bit more on the pseudopotential term. Due to the periodicity of the lattice, the pseudopotential can be expanded as a Fourier series

$$V_{\mathrm{ps}}(\mathbf{r}) = \sum_{\mathbf{G}} V_{\mathrm{ps}}(\mathbf{G})\ \mathrm{e}^{-i\mathbf{G}\cdot\mathbf{r}}, \tag{2.70}$$

where $\mathbf{G}$ is a reciprocal lattice vector. Now, considering that the core electrons screen the positive charge of the nuclei, it can be shown that the large oscillations around the nuclei present in the potential term $V(\mathbf{r})$ are effectively removed in the pseudopotential $V_{\mathrm{ps}}(\mathbf{r})$. As a consequence, only a small number of Fourier components is required to represent the pseudopotential. As an example, only three parameters are required to model Si, Ge, and Sn in the non-relativistic version of the EPM, which are most commonly determined empirically by fitting the calculated band structure to experimental data. Therefore, even though the EPM is not an *ab initio* method, only very few parameters are required to calculate the entire band structure. Moreover, as no self-consistent cycle is required, the computational complexity of the EPM is smaller than that of the DFT, which makes it an ideal method for band-structure

calculations requiring larger supercells, e. g. in the case of the atomistic modeling of alloys. Using techniques to parallelize the EPM calculations, it could be shown systems with up to 10^6 atoms can be studied [72]. Yet, for these large systems the computational complexity of the problem only allows for the calculation of single eigenvalues, wherefore it is usually not used to calculate the band structure of nanostructures.

2.4.2 Tight-Binding Approach

The central idea of the TB method is almost opposite to that of the EPM. Whereas in the EPM the wavefunctions of valence and conduction electrons are approximated by a plane-waves, in the TB approach those electrons are considered tightly bound to the nuclei and are therefore approximated by a linear combination of atomic orbitals. This thought is in line with the *s*- and *p*-type symmetry properties of near band-gap states discussed within the derivation of $\mathbf{k} \cdot \mathbf{p}$ theory. Again, we simplify our discussion of the TB method by only considering the non-relativistic case. For a discussion of the relativistic equation including spin-orbit splitting, we refer the reader to the work by Vogl *et al.* [73]

Along the line of thought of tightly-bound electrons, the potential term $V(\mathbf{r})$ of the non-relativistic Schrödinger equation can be decomposed into the contributions of the potentials V^{at} of the individual atom

$$H = \frac{p^2}{2m_0} + V(\mathbf{r}), \quad \text{with} \tag{2.71}$$

$$V(\mathbf{r}) = \sum_{n,v} V^{\mathrm{at}}(\mathbf{r} - \mathbf{r}_{nv}). \tag{2.72}$$

Here, the vector $\mathbf{r}_{nv}$ denotes the position of atom v in unit cell n. The vector $\mathbf{r}_{nv}$ can be decomposed into $\mathbf{r}_{nv} = \mathbf{R}_n + \mathbf{b}_v$ where $\mathbf{R}_n$ is the lattice vector to the unit cell n and $\mathbf{b}_v$ is the vector to atom v within the unit cell. For an isolated atom at $\mathbf{r}_{nv}$, the Schrödinger equation reads

$$h_v\, \vartheta_{vm}(\mathbf{r} - \mathbf{r}_{nv}) = \left[\frac{p^2}{2m_0} + V^{\mathrm{at}}(\mathbf{r} - \mathbf{r}_{nv})\right] \theta_{vm}(\mathbf{r} - \mathbf{r}_{nv}) = \tilde{\epsilon}_{vm}\, \theta_{vm}(\mathbf{r} - \mathbf{r}_{nv}), \tag{2.73}$$

where h_v is the Hamilton operator of the isolated atom and θ_{vm} and $\tilde{\epsilon}_{vm}$ are the m-th eigenstate and eigenvalue of this operator which we assume to be known.

For the wavefunction $\phi_{\mathbf{k}}(\mathbf{r})$, which is a solution to the full Hamiltonian of the crystal, we can then make the ansatz

$$\phi_{\mathbf{k}}(\mathbf{r}) = \sum_{v,m} C_{vm}\, \Theta_{vm}(\mathbf{k}, \mathbf{r}), \quad \text{with} \tag{2.74}$$

$$\Theta_{vm}(\mathbf{k}, \mathbf{r}) = \frac{1}{\sqrt{N}} \sum_{n} \mathrm{e}^{i\mathbf{k}\cdot\mathbf{r}_{nv}}\, \vartheta_{vm}(\mathbf{r} - \mathbf{r}_{nv}), \tag{2.75}$$

where N is the number of primitive cells within the lattice. This ansatz corresponds to a superposition of the solutions to the Hamiltonians of the isolated atoms arranged in a manner that fulfills the Bloch condition for periodic potentials. The coefficients C_{vm} can be determined simply by diagonalizing the Hamiltonian matrix $H(\mathbf{k})$ whose elements are given by

$$H_{v'm',vm}(\mathbf{k}) = \langle \Theta_{v'm'}(\mathbf{k}) | H | \Theta_{vm}(\mathbf{k}) \rangle. \tag{2.76}$$

We can divide the Hamiltonian into two parts. The first corresponds to the Hamiltonian of the isolated atom positioned at $\mathbf{b}_{v'}$ inside the unit cell. The second part is a potential term $V'(\mathbf{r})$ that includes the contributions to the potential of all other atoms:

$$H = \frac{p^2}{2m_0} + V^{\mathrm{at}}(\mathbf{r} - \mathbf{b}_{v'}) + V'(\mathbf{r}) \equiv h_{v'} + V'(\mathbf{r}), \tag{2.77}$$

where we defined $h_{v'} = \frac{p^2}{2m_0} + V^{\mathrm{at}}(\mathbf{r} - \mathbf{b}_{v'})$. Taking a closer look again at the individual matrix elements of $H(\mathbf{k})$, we find

$$\begin{aligned} H_{v'm',vm}(\mathbf{k}) &= \epsilon_{v'm'}\, \delta_{vv'}\, \delta_{mm'} \\ &\quad + \sum_n \mathrm{e}^{i\mathbf{k}\cdot(\mathbf{R}_n + \mathbf{b}_v - \mathbf{b}_{v'})} \int \mathrm{d}\mathbf{r}\; \vartheta^*_{v'm'}(\mathbf{r} - \mathbf{b}_{v'})\; V'(\mathbf{r})\; \vartheta_{vm}(\mathbf{r} - \mathbf{R}_n - \mathbf{b}_v), \end{aligned} \tag{2.78}$$

where we introduced the energy ϵ_{vm} to be

$$\epsilon_{vm} = \tilde{\epsilon}_{vm} + \int \mathrm{d}\mathbf{r}\; \vartheta^*_{vm}(\mathbf{r} - \mathbf{b}_v)\; V'(\mathbf{r})\; \vartheta_{vm}(\mathbf{r} - \mathbf{b}_v). \tag{2.79}$$

Eq. (2.78) and Eq. (2.79) illustrate the advantage of the TB approach. The calculation of the eigenfunctions and eigenvalues of the orginal many-body Hamiltonian is reduced to the diagonalization of a Hamiltonian matrix, whose elements are given by integrals over wavefunctions of *isolated* atoms. The task that remains is to reduce the Hamiltonian to a finite size. This can be achieved by two means. One is to restrict the interactions between wavefunctions and potentials to those that are in close spatial proximity to each other, e. g. nearest neighbors or second-nearest neighbors. The other is to limit the set of atomic orbitals that are taken into account. A common choice is to include an s orbital and three p orbitals corresponding to p_x, p_y, and p_z. This is referred to as the sp^3 model [73]. For zinc-blende crystals, Jantu *et al.* showed that a nearest-neighbor interaction together with an extended set of orbitals that also includes five d orbitals and an unoccupied s^* orbital (referred to as the $sp^3d^5s^*$ model) reproduce the band structure correctly up to 6 eV above the valence band edge with sufficient accuracy [74].

In comparison to the $\mathbf{k}\cdot\mathbf{p}$ method, an advantage of the TB approach is that it is possible to calculate the band structure not just around points of high symmetry, but throughout the entire Brillouin zone. The computational complexity of the problem is still small enough to be able to calculate the band structure not only for bulk materials, but also for heterostructures, like quantum wells, wires or dots [75–77].

A disadvantage of the TB method is the relatively large parameter set required. In the semi-empirical version of the tight-binding method, the Hamiltonian elements are not explicitly calculated, but rather used as a fitting parameter to reproduce experimental measurements or theoretical band-structure calculations. For the $sp^3d^5s^*$ model, a total number of 18 parameters is required to describe the bulk band structure of group-IV materials [74]. When alloys are involved, this set is even larger. Particular for group-IV alloys containing Sn, verified band-structure data, which can be used to fit the material parameters, is still largely unavailable. Furthermore, due to the computational complexity of the TB approach (that is still larger than that of the $\mathbf{k}\cdot\mathbf{p}$ method), it is computationally very demanding if one wants to include physical effects that require a self-consistent solution of the problem, e. g. band-bending effects in heterostructures due to excited charge carriers.

3 Chapter 3
SiGeSn Band-Gap Bowing

In this chapter, we study the compositional dependence of the direct band-gap of $Ge_{1-x-y}Si_xSn_y$ ternary alloys. We extract the direct band-gap energy from photoluminescence measurements of two different $Ge_{1-x-y}Si_xSn_y$ samples. Using deformation potential theory, we correct the measured transition energy of the direct band-gap for any effects of strain contained within the sample. Subsequently, we use the corrected values to determine the parameters of an empirical quadratic function relating direct band-gap energy and alloy composition. The results of this chapter have been published previously in [W1].

3.1 Introduction

If we want to use $Ge_{1-x-y}Si_xSn_y$ alloys for optoelectronic applications, we will have to investigate the functional dependence of the direct and indirect band-gap sizes on the composition of the alloy. The knowledge about the compositional dependence of the band-gap is required to be able to build semiconductor devices with specific optical transition energies. Furthermore, by knowing the compositional dependence of the band-gap sizes we can identify the compositional window where the alloy can be expected to be a direct band-gap semiconductor material. The Si_xGe_{1-x} and $Ge_{1-y}Sn_y$ binary alloys have already been investigated intensively in this regard. The functional dependence of the band-gap size on their composition is commonly described in a quadratic interpolation scheme given for the binary alloy Si_xGe_{1-x} by [78]

$$E_{g,i}(x) = E_{g,i}^{\mathrm{Ge}}(1-x) + E_{g,i}^{\mathrm{Si}}x - b_i^{\mathrm{SiGe}}x(1-x), \tag{3.1}$$

where i indicates the specific band-gap, i.e. the band-gaps at the Γ- and L-point or the Δ-valley for group-IV alloys, $E_{g,i}^{\mathrm{Si}}$ and $E_{g,i}^{\mathrm{Ge}}$ are the i-related band-gaps of the elemental semiconductors Si and Ge, respectively, and b_i^{SiGe} is the binary bowing parameter. The bowing parameter can be understood as a second-order correction to the linearly averaged band-gaps of the elemental semiconductors. An analogous scheme can be formulated for the $Ge_{1-y}Sn_y$ binary alloy. For Si_xGe_{1-x} the quadratic correction is comparably small. Studies by D'Costa *et al.* suggest a value of $b_\Gamma^{\mathrm{SiGe}} = 0.21\,\mathrm{eV}$ for the direct band-gap [79]. Weber *et al.* measured a value of $b_\Delta^{\mathrm{SiGe}} = 0.206\,\mathrm{eV}$ and $b_L^{\mathrm{SiGe}} = 0.00\,\mathrm{eV}$ for the Δ-valley and the L-point, respectively [80]. These

values are in good agreement with the values $b_\Delta = 0.11\,\text{eV}$ and $b_L = 0.34\,\text{eV}$ calculated by Moontragoon *et al.* using an mixed-atom EPM approach [81]. For the $Ge_{1-y}Sn_y$ binary alloy, the quadratic correction is larger. For the direct band-gap, values of b_Γ^{GeSn} vary between 1.94 eV and 2.61 eV [37, 79, 82]. For the *L*-related band-gap, Jiang *et al.* measured $b_L^{\text{GeSn}} = 1.03\,\text{eV}$ [82]. The measured bowing parameter for the direct band-gap is in agreement with the *ab initio* calculations by Yin *et al.*, which revealed a bowing parameter of 2.87 eV for $y < 0.25$ for the direct band-gap. Yin *et al.* also show that the larger bowing parameter of the $Ge_{1-y}Sn_y$ alloy in comparison to Si_xGe_{1-x} alloy is a result of structural disorder within the alloy due to the large difference in the lattice constants between Ge and Sn [83].

Whereas the experimental and theoretical results for the Si_xGe_{1-x} and $Ge_{1-y}Sn_y$ binary alloys are in good agreement with each other, results for the compositional-dependence of the band-gap of the $Ge_{1-x-y}Si_xSn_y$ ternary alloy are still controversially discussed. Gallagher *et al.* studied the compositional dependence of the direct band-gap of $Ge_{1-x-y}Si_xSn_y$ investigating samples with either low Sn ($0 < y < 0.04$) and high Si ($0.05 < x < 0.20$) concentrations or high Sn ($0.04 < y < 0.10$) and low Si concentrations ($0 < x < 0.05$) [84]. They found for Si and Sn concentrations with $x + y < 0.5$ that the size of the direct band-gap can be described as a linear function of the compositions x and y. For larger concentrations, on the other hand, D'Costa *et al.* found that the band-gap size $E_{g,i}(x, y)$ is a quadratic function of the composition and proposed a quadratic interpolation scheme similar to Eq. (3.1) for the binary alloys [85]:

$$\begin{aligned} E_{g,i}(x,y) =& E_{g,i}^{\text{Ge}}(1-x-y) + E_{g,i}^{\text{Si}}x + E_{g,i}^{\text{Sn}}y \\ &- b_i^{\text{SiGe}}x(1-x-y) - b_i^{\text{GeSn}}(1-x-y)y \\ &- b_i^{\text{SiSn}}xy, \end{aligned} \tag{3.2}$$

where b_i^{SiGe}, b_i^{GeSn}, b_i^{SiSn} are the bowing parameters for band-gap i of the binary alloys SiGe, GeSn, and SiSn. While the SiGe and GeSn bowing parameters are known with sufficient accuracy, the experimental determination of the bowing parameter b_i^{SiSn} is more challenging. Owing to the large lattice mismatch between Si and Sn, the growth of high quality SiSn alloys is hindered [86]. To date, no systematic experimental study on the bowing parameter of the SiSn binary alloy has been reported. For this reason, D'Costa *et al.* deduced its value from optical measurements of the direct band-gap of ternary $Ge_{1-x-y}Si_xSn_y$ alloys lattice-matched to Ge and found a value of $b_\Gamma^{\text{SiSn}} = 13.2\,\text{eV}$. The same interpolation equation has also been used by Lin *et al.* that found $b_\Gamma^{\text{SiSn}} = -21\,\text{eV}$ for $Ge_{1-x-y}Si_xSn_y$ alloys with a lattice constant different from Ge [87]. Moreover, also theoretical calculations are in disagreement with each other. Moontragoon *et al.* [21] used the EPM together with the known parametrization of bulk Si, Ge, and Sn and calculated a SiSn bowing parameter of $b_\Gamma^{\text{SiSn}} = 3.92\,\text{eV}$. In contrast, Sant *et al.* [88] used custom pseudopotentials that reproduced the experimentally measured GeSn band-gap bowing behavior and calculated $b_\Gamma^{\text{SiSn}} = -5.95\,\text{eV}$.

The large variations of the SiSn bowing parameter in theory and experiment also leads to large variations of the band-gap energy when Eq. (3.2) is used, which makes a reliable prediction of the band-gap size of $Ge_{1-x-y}Si_xSn_y$ alloys impossible at the moment. For this reason, we also investigated the compositional dependence of the direct band-gap of $Ge_{1-x-y}Si_xSn_y$ alloys. Specifically, we studied $Ge_{1-x-y}Si_xSn_y$ alloys grown on Ge virtual substrates with high Si and Sn concentrations. Performing photoluminescence (PL) measurements to extract the direct band-gap size, we attempt to determine the SiSn bowing parameter using Eq. (3.2). In contrast to earlier studies, we apply a strain correction of the measured band-gap values in order to obtain the band-gap size of the relaxed alloy. To include a strain correction, we

also perform measurements to determine the compositional-dependence of the $Ge_{1-x-y}Si_xSn_y$ lattice constant.

The outline of this chapter is as follows. In Sec. 3.2, we introduce the theoretical foundations of the strain correction. We perform the strain correction in the framework of $\mathbf{k}\cdot\mathbf{p}$ theory. In Sec. 3.3, we introduce the theoretical foundations required to understand the PL measurements of bulk semiconductors. In Sec. 3.4, we introduce the investigated samples as well as the measurement setups used for this study. In Sec. 3.5, we discuss the measurement results and our theoretical analysis. We conclude our findings in Sec. 3.5 with a summary and outlook.

3.2 Strained Semiconductors

If two semiconductor materials with different lattice constants are grown on top of each other, mechanical stress will be introduced into the crystal. This has strong implications on both the growth process and the band structure of the strained material. In the following, we will first give a short description on the growth modes found in group-IV heteroepitaxy. This will be followed by the derivation of the relation between stress and strain and, lastly, a discussion of the effects of strain on the band structure.

As strain related effects are important for both semiconductor electronics and optoelectronics, a variety of literature is available on the topic [89, 90]. Here, we will mainly follow the reasoning of Sun *et al.* [54].

3.2.1 Growth Modes

Performing hetero-epitaxial growth of a $Ge_{1-x-y}Si_xSn_y$ alloys on a thick substrate, two growth phases can be observed[1]. In the first phase, called Frank-van-der-Merwe growth, the adatoms form homogeneous layers on top of the substrate referred to as *wetting layer* [92]. This growth mode continues until the stress related energy reaches a threshold. If the material deposition continues, 3D islands start to form as a mechanism of strain relaxation, a growth mode referred to as Stranski-Krastanov growth [93]. The thickness of the wetting layer depends on the lattice mismatch between substrate and epilayer as well as the growth conditions. If the mismatch is not too large, as is the case for the here investigated samples, the epilayer thickness can reach tens of nanometers. The formation of the wetting layer during Frank-van-der-Merwe growth is only possible, because the epilayer assumes the in-plane lattice constant of the substrate, while the out-of-plane lattice constant will be either expanded or stretched. Since the epilayer nevertheless retains a crystalline form, this growth mode is also referred to *pseudomorphic growth*. We can distinguish between two cases. If the lattice constant of the substrate a_S is smaller than the lattice constant of the epilayer a_E, the epilayer will be tensile strained (see Fig. 3.1). While the in-plane lattice constant is stretched to fit the lattice constant of the substrate, the out-of-plane lattice constant is elongated in order to reduce the overall stress. On the other hand, if $a_E > a_S$, the situation is reverse. The in-plane lattice constant of the epilayer is compressively strained while the out-of-plane lattice constant is elongated.

In the following, we review the relationship between stress and strain in more detail in order to understand the relationship between the in-plane and the out-of-plane lattice constants. Afterward, we introduce deformation potential theory as an addition to $\mathbf{k}\cdot\mathbf{p}$ theory developed in

[1] For certain $Ge_{1-x-y}Si_xSn_y$ material compositions and growth conditions, surface segregation of Sn can be observed [91]. Here, we do not consider these cases and only focus on crystalline samples.

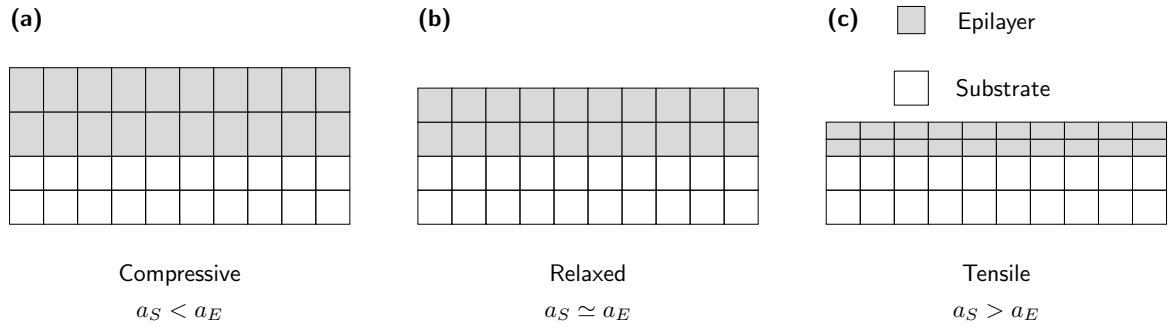

Figure 3.1: *Schematic of an epilayer (gray) with lattice constant a_E grown on a thick substrate (white) with lattice constant a_S. Depicted are (a) a compressively strained, (b) a relaxed, and (c) tensile strained epilayer. For a compressively strained epilayer, the out-of-plane lattice constant increases. For a tensile strained epilayer, the out-of-plane lattice constant decreases.*

Chap. 2 to include the effects of strain on the band structure of the epilayer. For all derivations, we assume a defect free crystal structure.

3.2.2 Strain and Stress

In the introduction to the growth modes of group-IV semiconductors, we have already used the terms stress and strain without providing a full definition. *Strain* describes the deformation of the crystal as a result a external forces, while *stress* is defined as the force in response to deformations. If a crystal is deformed, the atoms of a crystal are displaced from their usual position within the crystal. We may describe the positions of the atoms within the unstrained lattice using the basis vectors $\hat{\mathbf{x}}$, $\hat{\mathbf{y}}$, and $\hat{\mathbf{z}}$, which we, for simplicity, assume to be unit vectors. Under a small uniform deformation of the crystal, these unit vector will change their length and direction. The basis vectors $\hat{\mathbf{x}}'$, $\hat{\mathbf{y}}'$, and $\hat{\mathbf{z}}'$ of the deformed lattice can be written in terms of the unstrained unit vectors as

$$\begin{aligned}\hat{\mathbf{x}}' &= (1+\tilde{\varepsilon}_{xx})\hat{\mathbf{x}} + \tilde{\varepsilon}_{xy}\hat{\mathbf{y}} + \tilde{\varepsilon}_{xz}\hat{\mathbf{z}},\\ \hat{\mathbf{y}}' &= \tilde{\varepsilon}_{yx}\hat{\mathbf{x}} + (1+\tilde{\varepsilon}_{yy})\hat{\mathbf{y}} + \tilde{\varepsilon}_{yz}\hat{\mathbf{z}},\\ \hat{\mathbf{z}}' &= \tilde{\varepsilon}_{zx}\hat{\mathbf{x}} + \tilde{\varepsilon}_{zy}\hat{\mathbf{y}} + (1+\tilde{\varepsilon}_{zz})\hat{\mathbf{z}},\end{aligned} \tag{3.3}$$

where the coefficients $\tilde{\varepsilon}_{ij}$ define the deformation of the crystal. For a general position vector $\mathbf{r} = x\hat{\mathbf{x}} + y\hat{\mathbf{y}} + z\hat{\mathbf{z}}$, which is displaced to position $\mathbf{r}' = x\hat{\mathbf{x}}' + y\hat{\mathbf{y}}' + z\hat{\mathbf{z}}'$ under a uniform deformation, we can define the displacement $\mathbf{u}$:

$$\begin{aligned}\mathbf{u} = \mathbf{r}' - \mathbf{r} &= x(\hat{\mathbf{x}}' - \hat{\mathbf{x}}) + y(\hat{\mathbf{y}}' - \hat{\mathbf{y}}) + z(\hat{\mathbf{z}}' - \hat{\mathbf{z}})\\ &= (x\tilde{\varepsilon}_{xx} + y\tilde{\varepsilon}_{yx} + z\tilde{\varepsilon}_{zx})\hat{\mathbf{x}}\\ &+ (x\tilde{\varepsilon}_{xy} + y\tilde{\varepsilon}_{yy} + z\tilde{\varepsilon}_{zy})\hat{\mathbf{y}}\\ &+ (x\tilde{\varepsilon}_{xz} + y\tilde{\varepsilon}_{yz} + z\tilde{\varepsilon}_{zz})\hat{\mathbf{z}}.\end{aligned} \tag{3.4}$$

For a non-uniform deformation, the displacement $\mathbf{u}$ turns into a position-dependent vector field $\mathbf{u}(\mathbf{r})$. The deformations $\tilde{\varepsilon}_{ij}$ are related to the displacement field $\mathbf{u}(\mathbf{r})$ through

$$\begin{aligned}\tilde{\varepsilon}_{xx} &= \frac{\partial u_x}{\partial x}, \quad \tilde{\varepsilon}_{yx} = \frac{\partial u_x}{\partial y}, \quad \tilde{\varepsilon}_{zx} = \frac{\partial u_x}{\partial z},\\ \tilde{\varepsilon}_{xy} &= \frac{\partial u_y}{\partial x}, \quad \tilde{\varepsilon}_{yy} = \frac{\partial u_y}{\partial z}, \quad \tilde{\varepsilon}_{zy} = \frac{\partial u_y}{\partial z},\\ \tilde{\varepsilon}_{xz} &= \frac{\partial u_z}{\partial x}, \quad \tilde{\varepsilon}_{yz} = \frac{\partial u_z}{\partial y}, \quad \tilde{\varepsilon}_{zz} = \frac{\partial u_z}{\partial z},\end{aligned} \tag{3.5}$$

or more generally $\tilde{\varepsilon}_{ij} = \frac{\partial u_j}{\partial x_i}$. These terms can be understood as first-order coefficients of a Taylor series of $\mathbf{u}(\mathbf{r})$ around $\mathbf{r}$. Rather than working with the deformations $\tilde{\varepsilon}_{ij}$, one usually works with the strain tensor ε_{ij} which is given, in the limit of small deformations, by[2]

$$\varepsilon_{ij} = \frac{1}{2}(\tilde{\varepsilon}_{ij} + \tilde{\varepsilon}_{ji}). \tag{3.6}$$

The diagonal elements ε_{ii} of the strain tensor define the relative change in length along the direction $\hat{\mathbf{x}}_i$, whereas the off-diagonal elements ε_{ij} with $i \neq j$ define the shear strain due to angular distortions. By construction, the strain tensor is symmetric. Thus, only six out of the nine components are required to fully define the strain tensor[3].

If a crystal is deformed, the atoms inside the lattice react with a force in response to the strain. This force is given by the stress tensor τ_{ij}. The component τ_{ij} of the stress tensor is defined as the force exerted per unit area in the direction $\hat{\mathbf{x}}_j$ on a plane whose outward normal vector lies along the direction $\hat{\mathbf{x}}_i$. The stress tensor is also defined to be symmetric in order to separate out a torque of the crystal. The strain tensor ε_{ij} and the stress tensor τ_{ij} are related to each other by a generalized Hooke's law

$$\tau_{ij} = \sum_{l,m} C_{ijlm}\varepsilon_{lm}, \tag{3.7}$$

where C_{ijlm} are components of a fourth-rank tensor called elastic stiffness tensor. As the stress and strain tensor are both symmetric, this relationship can be simplified by redefining ε_{ij} and τ_{ij} to the six-component vectors

$$\varepsilon = (\varepsilon_{xx}, \varepsilon_{yy}, \varepsilon_{zz}, \varepsilon_{xy}, \varepsilon_{xz}, \varepsilon_{yz})^T \tag{3.8}$$

and

$$\tau = (\tau_{xx}, \tau_{yy}, \tau_{zz}, \tau_{xy}, \tau_{xz}, \tau_{yz})^T, \tag{3.9}$$

which reduces the elastic stiffness tensor C_{ijlm} to the second-rank tensor c_{ij} with 6×6 components

$$\tau_i = \sum_j c_{ij}\varepsilon_j. \tag{3.10}$$

Using symmetry relations, it can be shown that the complexity of the elastic stiffness tensor τ_{ij} can be reduced greatly. For cubic crystals, the elastic stiffness tensor τ_{ij} is composed of only three independent components and has the form

$$\underline{\underline{c}} = \begin{pmatrix} c_{11} & c_{12} & c_{12} & 0 & 0 & 0 \\ c_{12} & c_{11} & c_{12} & 0 & 0 & 0 \\ c_{12} & c_{12} & c_{11} & 0 & 0 & 0 \\ 0 & 0 & 0 & c_{44} & 0 & 0 \\ 0 & 0 & 0 & 0 & c_{44} & 0 \\ 0 & 0 & 0 & 0 & 0 & c_{44} \end{pmatrix}. \tag{3.11}$$

In analogy, we can define the reverse relationship between stress and strain as

$$\varepsilon_i = \sum_j s_{ij}\tau_j, \tag{3.12}$$

[2] In an engineering context, the strain tensor is often defined as e_{ij} rather than ε_{ij}. The tensors ε_{ij} and e_{ij} are related to each other by $e_{ii} = \varepsilon_{ii}$ and $e_{ij} = 2\varepsilon_{ij}$ for $i \neq j$. In the following, we strictly use ε_{ij}.

[3] The strain tensor is defined to be symmetric to remove rotations of the entire body that do not contribute to the deformation.

where s_{ij} is the so-called compliance tensor. The compliance tensor is subject to the same symmetry principles as the stiffness matrix and assumes the form

$$\underline{\underline{s}} = \begin{pmatrix} s_{11} & s_{12} & s_{12} & 0 & 0 & 0 \\ s_{12} & s_{11} & s_{12} & 0 & 0 & 0 \\ s_{12} & s_{12} & s_{11} & 0 & 0 & 0 \\ 0 & 0 & 0 & s_{44} & 0 & 0 \\ 0 & 0 & 0 & 0 & s_{44} & 0 \\ 0 & 0 & 0 & 0 & 0 & s_{44} \end{pmatrix}, \tag{3.13}$$

where the components s_{11}, s_{12}, and s_{44} are defined as

$$\begin{aligned} s_{11} &= \frac{c_{11} + c_{12}}{(c_{11} - c_{12})(c_{11} + 2c_{12})}, \\ s_{12} &= -\frac{c_{12}}{(c_{11} - c_{12})(c_{11} + 2c_{12})}, \\ s_{44} &= \frac{1}{c_{44}}. \end{aligned} \tag{3.14}$$

Pseudomorphic Strain

Equation 3.10 and Eq. (3.12) are valid for cubic crystal under an arbitrary external pressure. We now want to look at the special case of a pseudomorphically strained thin film with lattice constant a_L grown on a substrate with lattice constant a_S along the (001) direction. For the case of pseudomorphic growth, the lattice constants of the epilayer parallel to the interface will adopt the lattice constant of the substrate. Using Eq. (3.3), the parallel strain components are therefore given by

$$\varepsilon_{xx} = \varepsilon_{yy} = \frac{a_S - a_L}{a_L} \equiv \varepsilon_{\parallel}. \tag{3.15}$$

There are no restrictions on the lattice constant along the growth direction. In order to calculate the strain state perpendicular to the interface, we can use the strain-stress relation as defined in Eq. (3.12). With $\tau_{xx} = \tau_{yy}$ set to an arbitrary constant and all other components of τ_{ij} set to zero, we find

$$\varepsilon_{zz} = -2\frac{c_{12}}{c_{11}}\varepsilon_{\parallel} \equiv \varepsilon_{\perp}. \tag{3.16}$$

The total strain tensor in the case of pseudomorphic growth along the [001] direction is therefore given by

$$\underline{\underline{\varepsilon}} = \begin{pmatrix} \varepsilon_{\parallel} & 0 & 0 \\ 0 & \varepsilon_{\parallel} & 0 \\ 0 & 0 & \varepsilon_{\perp} \end{pmatrix}. \tag{3.17}$$

Using Eq. (3.15) and Eq. (3.16), the equilibrium lattice constant a_L can be calculated once the lattice constant parallel $a_{\parallel}$ and perpendicular $a_{\perp}$ to the interface are known:

$$a_L = \frac{a_{\perp} + 2\frac{c_{12}}{c_{11}}a_{\parallel}}{1 + 2\frac{c_{12}}{c_{11}}}. \tag{3.18}$$

This equation becomes very practical in combination with x-ray diffraction (XRD) measurements of a crystal.

Equation 3.17 describes the strain tensor in a pseudomorphically strained crystal within the regime of linear elasticity. Depending on the size of the components $\varepsilon_{\parallel}$ and $\varepsilon_{\perp}$, the band structure of the crystal will be affected by this strain. In the next section, we discuss how to calculate the strain-related change in the band structure within the framework of deformation potential theory.

3.2.3 Deformation Potential Theory

In the PL measurements that we discuss in Sec. 3.5.3, the luminescence is a result of the radiative recombination of electrons and holes located in close proximity to points of high symmetry in the Brillouin zone. Therefore, $\mathbf{k} \cdot \mathbf{p}$ theory and effective mass approximation are the natural choices for the analysis of these measurements. In Sec. 2.3 of Chap. 2 we already developed the $\mathbf{k} \cdot \mathbf{p}$ formalism and derived the effective mass approximation. What we want to do now, is to extend the theory to incorporate the effects of strain on the band structure. At first sight, this appears to be an ideal case for the application of perturbation theory as we have assumed the distortions of the lattice to be small. However, one has to be careful when formulating the problem. Even though the distortions are small, they change the periodicity of the crystal. This means that for certain positions $\mathbf{r}$, the change in the potential will be of the order of the unperturbed potential itself. This problem can be addressed for the $\mathbf{k} \cdot \mathbf{p}$ method in the framework of the deformation potential theory, which was original developed by Pikus and Bir [94] and then further elaborated by others [95, 96].

The central idea behind deformation potential theory is to formulate the entire problem in the vector space of the deformed lattice first and then transform it back into the original vector space. Consequently, we will start our derivation of the deformation potential theory with the one-particle Hamiltonian H' of the deformed crystal in the coordinate system of the deformed coordinate lattice given by

$$H' = \frac{\mathbf{p}'^2}{2m_0} + V(\mathbf{r}'), \tag{3.19}$$

where m_0 is the electron mass, $\mathbf{p}'$ is the momentum operator of the electron, and $V(\mathbf{r}')$ describes the full crystal potential of the deformed lattice. Note that we have neglected any relativistic effects for the moment.

To transform the Hamiltonian H' into the coordinate system of the original lattice, we need a number of relationships. The transformation of the space coordinates between the deformed and the original coordinate system in the regime of small deformations is given for each vector component r_i' according to Eq. (3.3) by

$$r_i' = r_i + \sum_j \varepsilon_{ij}\, r_j \quad \text{and conversely} \quad r_i = r_i' - \sum_j \varepsilon_{ij}\, r_j'. \tag{3.20}$$

In analogy, the component-wise transformation relation for the crystal wavevectors k_i' can be defined as

$$k_i' = k_i - \sum_j \varepsilon_{ij}\, k_j \quad \text{and} \quad k_i = k_i' + \sum_j \varepsilon_{ij}\, k_j'. \tag{3.21}$$

Furthermore, the transformation relation for the derivatives is given by

$$\frac{\partial}{\partial r_i'} = \sum_j \frac{\partial r_j}{\partial r_i'} \frac{\partial}{\partial r_j} = \frac{\partial}{\partial r_i} + \sum_j \epsilon_{ij} \frac{\partial}{\partial r_j}. \tag{3.22}$$

Thus, for the components of the momentum operator p_i' we can write

$$p_i' = p_i - \sum_j \varepsilon_{ij}\, p_j \quad \text{and} \quad p'^2 = p^2 - 2\sum_{ij} p_i p_j \varepsilon_{ij}. \tag{3.23}$$

We also need to transform the potential $V(\mathbf{r}')$ back into the original coordinate system with the additional constraint that the transformed potential should satisfy the periodicity of the original crystal potential. We do this by defining

$$V(\mathbf{r}') = V[(\mathbb{1} + \underline{\underline{\varepsilon}})\,\mathbf{r}] = V_0(\mathbf{r}) + \sum_{ij} V_{ij}\varepsilon_{ij} \tag{3.24}$$

where

$$V_{ij} = \lim_{\varepsilon\to 0} \frac{V[(\mathbb{1} + \underline{\underline{\varepsilon}})\,\mathbf{r}] - V_0(\mathbf{r})}{\varepsilon_{ij}} = \frac{\partial V}{\partial \varepsilon_{ij}}. \tag{3.25}$$

Here, $V_0(\mathbf{r})$ is the original crystal potential with no deformations. The terms V_{ij} are a measure of how strong the potential changes as a function of the strain. It can be seen that the change in the potential scales linearly with strain. Therefore, the requirements for the application of perturbation theory are fulfilled. Using Eq. (3.23) and Eq. (3.24), we can transform the Hamilton H' into the original coordinate system:

$$H' = \frac{\mathbf{p}'^2}{2m_0} + V(\mathbf{r}') = \frac{p^2}{2m_0} + V_0(\mathbf{r}) + \sum_{ij}\left(-\frac{1}{m_0}p_i p_j + V_{ij}\right)\varepsilon_{ij}. \tag{3.26}$$

Finally, we also need to transform the Bloch functions $\phi_{n\mathbf{k}'}(\mathbf{r}')$ that solve the Hamiltonian H' back into the original coordinate system:

$$\phi_{n\mathbf{k}'}(\mathbf{r}') = \mathrm{e}^{i\mathbf{k}'\cdot\mathbf{r}'} u_{n\mathbf{k}'}(\mathbf{r}') = \mathrm{e}^{i\mathbf{k}\cdot\mathbf{r}}\; u'_{n\mathbf{k}}(\mathbf{r}), \tag{3.27}$$

where $u'_{n\mathbf{k}}(\mathbf{r})$ represent the zone-center functions of the deformed crystal as a function of the space coordinate of the original coordinate system. Using ansatz (3.27) to solve Eq. (3.26), a $\mathbf{k}\cdot\mathbf{p}$ Hamiltonian can be derived for the strained system. For the case of an expansion around $\mathbf{k}_0 = 0$, we find

$$\left[H_0 + \frac{\hbar}{m_0}\mathbf{k}\cdot\mathbf{p} + H_\epsilon + H_{\epsilon k}\right] u'_{n\mathbf{k}} = \left[E_n(\mathbf{k}) - \frac{\hbar^2 k^2}{2m_0}\right] u'_{n\mathbf{k}} \tag{3.28}$$

with

$$\begin{aligned} H_0 &= \frac{p^2}{2m_0} + V_0(\mathbf{r}), \\ H_\varepsilon &= \sum_{ij}\left(-\frac{1}{m_0}p_i p_j + V_{ij}\right)\varepsilon_{ij}, \\ H_{\varepsilon\mathbf{k}} &= -\frac{2\hbar}{m_0}\sum_{ij}\varepsilon_{ij} k_i p_j. \end{aligned} \tag{3.29}$$

We can use the same perturbation method as for the unstrained case and expand the lattice periodic functions $u'_{n\mathbf{k}}(\mathbf{r})$ in the basis functions of the Hamiltonian H_0. We will do this in the following for the conduction and valence bands separately.

Conduction Bands

In analogy to the case of a relaxed semiconductor treated in Sec. 2.3.1 of Chap. 2, we want to derive the energy dispersion $E_n(\mathbf{k})$ of the conduction bands in an effective mass formulation. For the band edge energy $E_n(\mathbf{k} = 0)$, only the operator H_ε is relevant. Due to symmetry considerations, we have to differentiate between the different conduction band valleys. At the Γ-point, the unperturbed eigenfunction of lowest conduction band have the symmetry of the atomic s-orbitals (see Sec. 2.3.1 for details). We identify the unperturbed wavefunction by $|S\rangle$. As a result of the s-symmetry, it can be shown that all terms of H_ε including V_{ij} and p_{ij} with $i \neq j$ vanish, leaving only the contributions related to ε_{ii}:

$$\begin{aligned}\langle S|H_\varepsilon|S\rangle &= \langle S|\sum_{i,j}\left(-\frac{1}{m_0}p_i p_j + V_{ij}\right)\varepsilon_{ij}|S\rangle \\ &= \langle S|\sum_{i}\left(-\frac{1}{m_0}p_i p_i + V_{ii}\right)\varepsilon_{ii}|S\rangle \\ &\equiv a_c(\varepsilon_{xx}+\varepsilon_{yy}+\varepsilon_{zz}),\end{aligned} \tag{3.30}$$

where we introduced the deformation potential a_c defined as[4]

$$a_c = \langle S|\sum_{i} -\frac{1}{m_0}p_i p_i + V_{ii}|S\rangle. \tag{3.31}$$

Thus, only the diagonal components ε_{ii} of the strain tensor ε_{ij} determine the absolute shift of the conduction band. As a result, the shift in energy of E_c^Γ in first order perturbation theory is purely a result of the change in volume of the unit cell, referred to as hydrostatic strain[5]. Due to symmetry, it can be shown that $\langle S|H_{\varepsilon\mathbf{k}}|S\rangle$ vanishes for all values of $\mathbf{k}$. Nevertheless, the strain also effects the dispersion relation, i.e., the components of the effective mass tensor $(1/m^*)_{ij}$. This is a result of the fact that besides the lowest conduction bands also all other band edge energies $E_n(\mathbf{k} = 0)$ are shifted by the strain as well. As the higher band edge energies are required for the calculation of the effective mass tensor (see Eq. (2.33) of Chap. 2), the effective mass tensor is affected itself. The strain-related change of the effective mass cannot be modeled within the framework of the effective mass approximation. Yet, as this effect is expected to change the value of the components of the effective mass tensor $(1/m')_{ij}$ by less than 10%, it is usually neglected [97]. Thus, the dispersion relation for the conduction Γ-valley in the effective mass approximation is given by

$$E_\mathrm{c}^\Gamma(\mathbf{k}) = E_\mathrm{c}^\Gamma(0) + \frac{\hbar^2}{2}\sum_{ij} k_i \left(\frac{1}{m^*}\right)_{ij} k_j + a_c(\varepsilon_{xx}+\varepsilon_{yy}+\varepsilon_{zz}). \tag{3.32}$$

For the conduction bands at the L and Δ-point, the situation is more complicated. First of all, the conduction bands away from the Γ-point are made up of s- and p-type states. Therefore, symmetry arguments used for the zone-center do not apply anymore and the dispersion relation $E_n(\mathbf{k})$ is now also effected by the off-diagonal components of the strain tensor ε_{ij}, which are related to shear strain. Therefore, the introduction of a second deformation potential is

[4] The symbols for the hydrostatic deformation potential and the lattice constant can be confused easily. Nevertheless, we make use of this notation as it is the common notation in the literature. In the following, we clarify the meaning of the symbol at each occurrence.

[5] To first order in the components ε_{ij}, the hydrostatic strain is only related to the diagonal elements of the strain tensor: $\Delta V/V = \mathrm{Tr}[\underline{\varepsilon}] = \varepsilon_{xx}+\varepsilon_{yy}+\varepsilon_{zz}$, where $\Delta V/V$ is the relative volume change.

required. Furthermore, the conduction band valley away from the zone center are degenerate. Depending on the geometric properties of the deformations, those valleys may be effected differently which leads to a splitting of the bands and a partial removal of the degeneracy. Both of these effects can be modeled using the deformation potentials Ξ_d^ζ and Ξ_u^ζ introduced by Herring and Vogt [98]. The energy shift $\Delta E_{\mathrm{c,hydro}}^\zeta$ of valley $\zeta = L, X$ due to hydrostatic strain is given by

$$\Delta E_{\mathrm{c,hydro}}^\zeta = (\Xi_d^\zeta + \frac{1}{3}\Xi_u^\zeta)(\varepsilon_{xx} + \varepsilon_{yy} + \varepsilon_{zz}). \tag{3.33}$$

The quantity $(\Xi_d^\zeta + 1/3\Xi_u^\zeta)$ can be understood as the hydrostatic deformation potential for the indirect conduction band valleys. In addition, a direction-dependent splitting term has to be taken into account. We find for uniform uniaxial stress along the [111] direction that the degeneracy of the Δ-valley remains unchanged due to its position within the Brillouin zone. In contrast, the degeneracy of the conduction band minima at the L-point is partially lifted. The splitting $\Delta E_{\mathrm{c,shear}}^{\mathrm{L}}$ relative to the average conduction band energy takes the form

$$\Delta E_{\mathrm{c,shear}}^{\mathrm{L}} = +\frac{2}{3}\Xi_u^{\mathrm{L}}\varepsilon_{xy} \tag{3.34}$$

for valley along the [111] direction and

$$\Delta E_{\mathrm{c,shear}}^{\mathrm{L}} = -\frac{1}{3}\Xi_u^{\mathrm{L}}\varepsilon_{xy} \tag{3.35}$$

for valleys along the $[\bar{1}11]$, $[1\bar{1}1]$, and $[11\bar{1}]$ directions.

On the other hand, for pseudomorphic growth along the [001] direction, the six-fold degenerate Δ-valleys split into the two-fold degenerate Δ_2 valleys (k-vector parallel to the stress direction) and the four-fold degenerate Δ_4 valleys (k-vector perpendicular to the stress direction). The energy splitting $\Delta E_\Delta^{\mathrm{c,hydro}}$ relative to the average conduction band energy is given by

$$\Delta E_{\mathrm{c,hydro}}^{\Delta} = +\frac{2}{3}\Xi_u^{\Delta}(\varepsilon_{zz} - \varepsilon_{xx}) \tag{3.36}$$

for the valleys along the [001] and [100] directions and

$$\Delta E_{\mathrm{c,hydro}}^{\Delta} = -\frac{1}{3}\Xi_u^{\Delta}(\varepsilon_{zz} - \varepsilon_{xx}) \tag{3.37}$$

for the valleys along the [100], $[\bar{1}00]$, [010] and $[0\bar{1}0]$ directions. In contrast, the valley degeneracy for the L-valley remains unchanged in this case. The conduction band deformation potentials are crystal specific and are tabulated for all elemental group-IV semiconductors [22].

Valence Bands

To calculate the effects of strain on the valence bands, we need to evaluate the strain-related terms of the $\mathbf{k} \cdot \mathbf{p}$ Hamiltonian. As in the case for a relaxed crystal discussed in Sec. 2.3.1, we will apply second-order degenerate perturbation theory and formulate a matrix eigenvalue equation in terms of the states $|X\rangle$, $|Y\rangle$, and $|Z\rangle$. Subsequently, we need to transform this matrix into the basis of the total angular momentum to also include the spin-orbit coupling, which contributes non-neglectable to the valence band energies.

Similar to the case of the conduction bands, the expectation value of the operator $H_{\varepsilon k}$ for the states $|X\rangle$, $|Y\rangle$, and $|Z\rangle$ vanishes due to symmetry considerations. For the diagonal

matrix elements of H_ε, we find that due to symmetry only those terms with ε_{ii} for $i = x, y, z$ contribute:

$$\begin{aligned}\langle X|H_\varepsilon|X\rangle =& \sum_{i,j}\langle X|\left(-\frac{1}{m_0}p_ip_j + V_{ij}\right)\varepsilon_{ij}|X\rangle \\ =& \quad \langle X|\left(-\frac{1}{m_0}p_xp_x + V_{xx}\right)|X\rangle\varepsilon_{xx} \\ &+ \langle X|\left(-\frac{1}{m_0}p_yp_y + V_{yy}\right)|X\rangle\varepsilon_{yy} \\ &+ \langle X|\left(-\frac{1}{m_0}p_zp_z + V_{zz}\right)|X\rangle\varepsilon_{zz} \\ =& \quad l\varepsilon_{xx} + m(\varepsilon_{yy} + \varepsilon_{zz}).\end{aligned} \tag{3.38}$$

For the off-diagonal matrix elements, it can be shown that only one addend is non-vanishing:

$$\begin{aligned}\langle X|H_\varepsilon|Y\rangle =& \sum_{ij}\langle X|\left(-\frac{1}{m_0}p_ip_j + V_{ij}\right)\varepsilon_{ij}|Y\rangle \\ =& \langle X|\left(-\frac{1}{m_0}p_xp_y + V_{xy}\right)|Y\rangle \\ =& n\varepsilon_{xy}.\end{aligned} \tag{3.39}$$

For symmetry reasons, all other matrix elements follow accordingly. The factors l, m, and n are the valence band deformation potentials. They are crystal specific and, similar to the conduction band deformation potentials, tabulated for common crystals [22]. Including the spin-orbit coupling and transforming the matrix into the basis of the total angular momentum as we did before for the unstrained case (see Eq. (2.45) in Chap. 2 for the details of the transformation), we find the 6×6 matrix

$$H'_{\mathbf{k}} = \begin{pmatrix} |\frac{3}{2},\frac{3}{2}\rangle & |\frac{3}{2},\frac{1}{2}\rangle & |\frac{3}{2},-\frac{1}{2}\rangle & |\frac{3}{2},-\frac{3}{2}\rangle & |\frac{1}{2},\frac{1}{2}\rangle & |\frac{1}{2},-\frac{1}{2}\rangle \\ -P-Q & S & -R & 0 & \frac{1}{\sqrt{2}}S & -\sqrt{2}R \\ S^\dagger & -P+Q & 0 & -R & \sqrt{2}Q & -\sqrt{\frac{3}{2}}S \\ -R^\dagger & 0 & -P+Q & -S & -\sqrt{\frac{3}{2}}S^\dagger & -\sqrt{2}Q \\ 0 & -R^\dagger & -S^\dagger & -P-Q & \sqrt{2}R^\dagger & \frac{1}{\sqrt{2}}S^\dagger \\ \frac{1}{\sqrt{2}}S^\dagger & \sqrt{2}Q^\dagger & -\sqrt{\frac{3}{2}}S & \sqrt{2}R & -P-\Delta_0 & 0 \\ -\sqrt{2}R^\dagger & -\sqrt{\frac{3}{2}}S^\dagger & -\sqrt{2}Q^\dagger & \frac{1}{\sqrt{2}}S & 0 & -P-\Delta_0 \end{pmatrix}, \tag{3.40}$$

where P, Q, S, and R are now defined as

$$\begin{aligned} P &= P_k + P_\varepsilon, \\ Q &= Q_k + Q_\varepsilon, \\ S &= S_k + S_\varepsilon, \\ R &= R_k + R_\varepsilon. \end{aligned} \tag{3.41}$$

The terms P_k, Q_k, S_k, and R_k are defined identically to the case of a relaxed crystal:

$$\begin{aligned} P_k &= \frac{\hbar^2}{2m_0}\gamma_1(k_x^2+k_y^2+k_z^2)+P_\varepsilon, \\ Q_k &= \frac{\hbar^2}{2m_0}\gamma_2(k_x^2+k_y^2-2k_z^2), \\ S_k &= \frac{\hbar^2}{m_0}\sqrt{3}\gamma_3(k_x-ik_y)k_z, \\ R_k &= -\frac{\hbar^2}{2m_0}\sqrt{3}(\gamma_2(k_x^2-k_y^2)-2i\gamma_3k_xk_y). \end{aligned} \tag{3.42}$$

The terms P_ε, Q_ε, S_ε, and R_ε are related to the effects of strain arising from the operator H_ε:

$$\begin{aligned} P_\epsilon &= a_v(\epsilon_{xx}+\epsilon_{yy}+\epsilon_{zz}), \\ Q_\epsilon &= -\frac{b}{2}(\epsilon_{xx}+\epsilon_{yy}-2\epsilon_{zz}), \\ S_\epsilon &= -d(\epsilon_{xz}-i\epsilon_{yz}), \\ R_\epsilon &= \frac{\sqrt{3}}{2}b(\epsilon_{xx}-\epsilon_{yy})-id\epsilon_{xy}. \end{aligned} \tag{3.43}$$

Here, a_v, b, and d are the Pikus-Bir deformation potentials. They are related to l, m, and n by [6]

$$\begin{aligned} a_v &= -\frac{2}{3}(l+2m), \\ b &= \frac{2}{3}(l-m), \\ d &= \frac{n}{\sqrt{3}}. \end{aligned} \tag{3.44}$$

From inspecting Eq. (3.43), we see that the deformation potential a_v determines an absolute shift of the bands due to hydrostatic strain whereas the deformation potential b leads to a splitting of the HH and LH bands. In contrast, deformation potential d is related to shear strain only.

For a general strain, the matrix elements P_ε, Q_ε, S_ε, and R_ε lead to a coupling of the bands even for the case of $k = 0$. An analytical calculation of the eigenvalues is challenging. For the case of biaxial strain, the situation is simpler and can be treated analytically. For the band edge energies of the HH, LH, and SO band, one finds:

$$\begin{aligned} E_{HH}(k=0) &= -P_\varepsilon - Q_\varepsilon, \\ E_{LH}(k=0) &= -P_\varepsilon + \frac{1}{2}\left(Q_\varepsilon - \Delta + \sqrt{9Q_\varepsilon^2+2\Delta Q_\varepsilon+\Delta^2}\right), \\ E_{SO}(k=0) &= -P_\varepsilon + \frac{1}{2}\left(Q_\varepsilon - \Delta - \sqrt{9Q_\varepsilon^2+2\Delta Q_\varepsilon+\Delta^2}\right). \end{aligned} \tag{3.45}$$

From Eqs. (3.45), it can be seen that the degeneracy of the HH and LH band at the Γ-point is lifted as a result of the uniaxial strain.

[6] In the literature, the sign of a_v is sometimes defined in the opposite way. Which definition was used can be determined by remembering that tensile hydrostatic strain shifts the valence bands upwards.

3.3 Theory of Bulk Photoluminescence

In the study presented here, we attempt to extract the band-gap size of $Ge_{1-x-y}Si_xSn_y$ alloys from PL spectra. In the investigation of electronic structures, PL is a very powerful tool since it is a non-destructive measurement method and luminescence from direct and indirect band-gaps can be observed [99, 100]. Nevertheless, this strength can also be a drawback as PL measurements will require a great deal of interpretation, if the band structure is not known *a priori* and direct and indirect band-gaps are lying close in energy. To facilitate this interpretation, we discuss the origin of the PL in greater detail in the following.

To measure PL, electron-hole pairs are created by optical excitation. The photon energy of the excitation radiation is usually larger than the direct band-gap of the investigated semiconductor. Therefore, electrons and holes are initially created in states within the upper range of the conduction and valence bands. Due to the strong electron-phonon coupling in semiconductors, electrons (and holes equivalently) first get scattered towards lower energy states (see Fig. 3.2). This scattering happens between states of the same band (intraband scattering) or, for indirect semiconductors, also to the energetically lower indirect conduction band (interband scattering). The occupation numbers of the direct and indirect valley depend on the energy difference between the valleys and the rates of the excitation, relaxation, and recombination processes. For the electrons in both the direct and indirect valleys, a recombination with holes at the top of the valence band can proceed radiatively or non-radiatively. For the radiative processes, we have to distinguish between a direct and an indirect spontaneous recombination. The electrons situated at the Γ-point have the same crystal wavevector as the holes. They can therefore recombine directly by emitting a photon that carries the excess energy. The electrons, which have been scattered to the indirect valley, have a different crystal wavevector than the holes. Therefore, a radiative recombination is only possible in combination with an elastic or inelastic scattering process. Depending on the scattering process, the energy of the emitted phonon may not be equivalent to the energy difference of the electronic levels involved in the recombination process.

From the direct and the indirect valley, also non-radiative recombination is possible. In bulk semiconductors, there are two dominant mechanisms: Shockley-Reed-Hall (SRH) and Auger recombination [101]. SRH recombination describes the recombination of electrons and holes via localized energy levels within the forbidden band-gap region caused by dislocations and impurities within the crystal and at the surface. In case of an indirect recombination, the localized states absorb the difference in momentum between electron and hole state. Auger recombination, on the other hand, describes the recombination of an electron-hole pair during which a third carrier is excited to a higher energetic state. It is the dominant recombination channel when high excitation densities are used and the investigated semiconductor is of high purity [102]. The excited charge carrier then relaxes to the lowest (highest) conduction (valence) band by transferring excess energy and momentum to phonons.

In the following, we will investigate in more detail the radiative recombination channel that lead to the PL signal. In our elaborations, we will limit ourselves to the simplest case of band-to-band recombination. In principle, direct and indirect radiative transitions can also occur through donor and acceptor levels or between electrons and holes belonging to an exciton. These special cases lead to a modification of the energy of the emitted photon [90]. However, as we will see later the experimental PL spectra are broadened, which does not allow to distinguish these features.

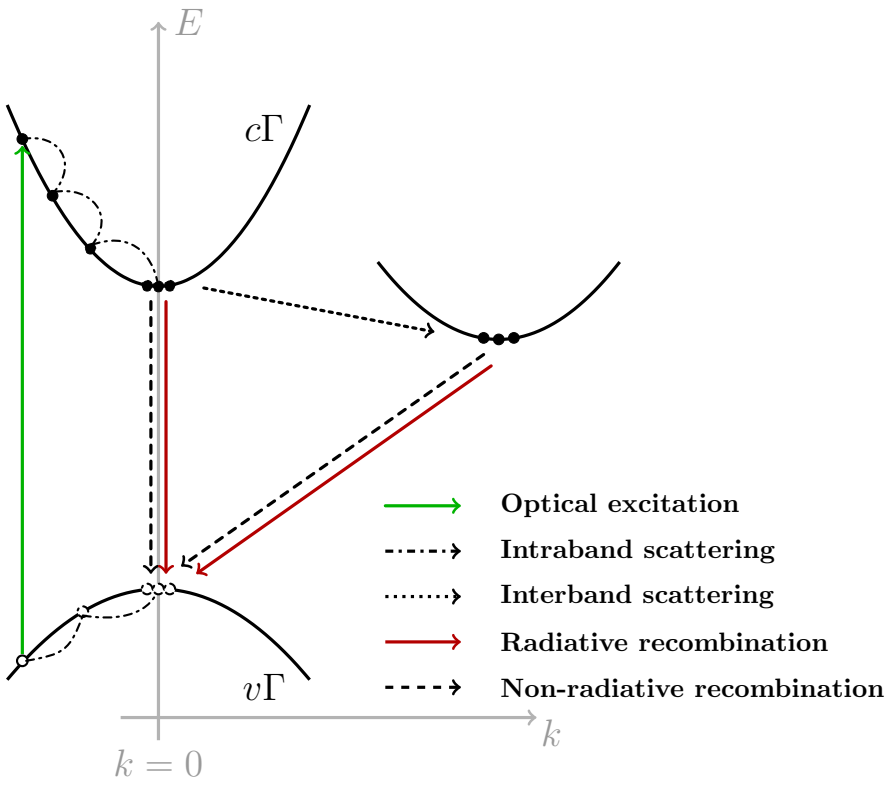

Figure 3.2: *Illustration of the processes involved in creation of PL in an indirect semiconductor. After the creation of an electron-hole pair due to optical excitation, the (electron) hole gets scattered to the bottom (top) of the band at the* Γ*-point. Electrons can also scatter to the lower indirect conduction band. From the direct valley and the indirect valley radiative and non-radiative recombination with the hole states in the valence band is possible.*

3.3.1 Spontaneous Direct Radiative Recombination Rate

We start our discussion of the spontaneous direct radiative recombination by deriving the interaction Hamiltonian between electronic states and an electromagnetic field. For a single particle system described by the Hamiltonian $H_0 = p^2/2m_0 + V(r)$, an electric field can be included into the system via minimal coupling, i.e., by the replacement $\mathbf{p} \to \mathbf{p} + e\mathbf{A}$, where $e > 0$ is the elementary charge and $\mathbf{A}$ is the vector potential of the electromagnetic field [103]. The total Hamiltonian is then given by

$$H = H_0 + \frac{e}{2m_0}(\mathbf{p}\cdot\mathbf{A} + \mathbf{A}\cdot\mathbf{p}) + \frac{e^2\mathbf{A}^2}{2m_0}. \tag{3.46}$$

In the Coulomb gauge ($\nabla\cdot\mathbf{A} = 0$), $\mathbf{p}$ and $\mathbf{A}$ commutate and, therefore, the term in parentheses is equal to $2\,\mathbf{A}\cdot\mathbf{p}$. Furthermore, for the field strengths considered here, the last term $e^2A^2/2m_0$ can be neglected in comparison to the terms linear in A. The vector potential of a plane-wave of frequency ω and polarization $\hat{\mathbf{e}}$ in second quantization is given by

$$\mathbf{A}(\omega) = \sqrt{\frac{\hbar}{2\omega\epsilon V}}(a_{\hat{\mathbf{e}}}\,\mathrm{e}^{i(\mathbf{k}_\lambda\cdot\mathbf{r}-\omega t)} + a^\dagger_{\hat{\mathbf{e}}}\,\mathrm{e}^{-i(\mathbf{k}_\lambda\cdot\mathbf{r}-\omega t)})\hat{\mathbf{e}}, \tag{3.47}$$

where $a_{\hat{\mathbf{e}}}$ and $a^\dagger_{\hat{\mathbf{e}}}$ are the annihilation and creator operator of a photon with polarization $\hat{\mathbf{e}}$, respectively, $\mathbf{k}_\lambda$ is the photon momentum, $\epsilon = \epsilon_r\epsilon_0$ is the permittivity of the environment[7], and V is the volume of the system. Therefore, we find for the interaction Hamiltonian between electronic states and electromagnetic field

$$H^{\text{e.m.}}_{\text{int}} = \frac{e}{m_0}\sqrt{\frac{\hbar}{2\omega\epsilon V}}(a_{\hat{\mathbf{e}}}\,\mathrm{e}^{i(\mathbf{k}_\lambda\cdot\mathbf{r}-\omega t)} + a^\dagger_{\hat{\mathbf{e}}}\,\mathrm{e}^{-i(\mathbf{k}_\lambda\cdot\mathbf{r}-\omega t)})\hat{\mathbf{e}}\cdot\mathbf{p}. \tag{3.48}$$

In a spontaneous direct radiative transition, an electron initially occupies a state with wavevector $\mathbf{k}$ in the lowest conduction band around the Γ-point and recombines with a hole with wavevector $\mathbf{k}'$ also situated in proximity to the Γ-point. During the process of recombination a photon of energy $\hbar\omega$ is emitted. We can therefore define the initial state $|i\rangle$ and final state $|f_\omega\rangle$ as follows

$$\begin{aligned} |i\rangle &= |\phi^\Gamma_c(\mathbf{k})\rangle|0\rangle, \\ |f_\omega\rangle &= |\phi^\Gamma_v(\mathbf{k}')\rangle|0\cdots 1_\omega\cdots 0\rangle, \end{aligned} \tag{3.49}$$

where both states are a product state of the electronic state and the photonic state of the system. In the single-particle picture, we can write the electronic state in the Bloch form as

$$\langle\mathbf{r}|\phi^\alpha_n(\mathbf{k})\rangle = \frac{1}{\sqrt{V}}\mathrm{e}^{i\mathbf{k}\cdot\mathbf{r}}u^\alpha_n(\mathbf{r}), \tag{3.50}$$

where V is the volume of the sample and $u^\alpha_n(\mathbf{r})$ is the lattice-periodic function of band n located at the valley α in the Brillouin zone. Furthermore, the energies of the electronic part of the initial and final state $|i\rangle$ and $|f_\omega\rangle$ are given by $E^\Gamma_c(\mathbf{k})$ and $E^\Gamma_v(\mathbf{k}')$, respectively. Thus, the matrix

[7] Here, we assumed that permittivity of the semiconductor is a real constant. The negligence of the complex part is justified by the thickness of the investigated sample that does not lead to self-absorption. The negligence of the frequency dependence is justified by the limited spectral range of the PL emission.

element $\langle f_\omega | H_{\text{int}}^{\text{e.m.}} | i \rangle$ is given by

$$\begin{aligned} \langle f_\omega | H_{\text{int}}^{\text{e.m.}} | i \rangle &= \frac{e}{m_0} \sqrt{\frac{\hbar}{2\omega\epsilon V}} \langle 0 \cdots 1_\omega \cdots 0 | a_{\hat{\mathbf{e}}}^\dagger | 0 \rangle \mathrm{e}^{i\omega t} \, \delta_{\mathbf{k},\mathbf{k}'} \, \mathbf{p}_{cv}^\Gamma \cdot \hat{\mathbf{e}} \\ &= \frac{e}{m_0} \sqrt{\frac{\hbar}{2V\omega\epsilon}} \mathrm{e}^{i\omega t} \, \delta_{\mathbf{k},\mathbf{k}'} \, \mathbf{p}_{cv}^\Gamma \cdot \hat{\mathbf{e}}, \end{aligned} \tag{3.51}$$

where we used the definition

$$\mathbf{p}_{cv}^\Gamma = \int_\Omega \mathrm{d}\mathbf{r} \, u_c^\Gamma(\mathbf{r}) \, \mathbf{p} \, u_v^\Gamma(\mathbf{r}) \tag{3.52}$$

and also made use of the fact that the lattice periodic functions of the conduction and valence band at the Γ-point are orthogonal to each other and that the photon wavevector $\mathbf{k}_\lambda$ is much smaller than the electron and hole wavevectors $\mathbf{k}$ and $\mathbf{k}'$ and, therefore, can be neglected. Consequently, optical transitions can only happen between initial and final states $|i\rangle$ and $|f_\omega\rangle$ with identical crystal momenta, which results into the Kronecker delta $\delta_{\mathbf{k},\mathbf{k}'}$ in Eq. (3.51). Using Fermi's Golden rule [104], we can calculate the transition probability per unit of time between $|i\rangle$ and $|f_\omega\rangle$

$$\begin{aligned} P_{i \to f_\omega} &= \frac{2\pi}{\hbar} \left| \langle f_\omega | H_{\text{em}} | i \rangle \right|^2 \delta(E_f' - E_i') \\ &= \frac{2\pi}{\hbar} \left(\frac{e}{m_0} \right)^2 \frac{\hbar}{2\omega\epsilon V} \left| \hat{\mathbf{e}} \cdot \mathbf{p}_{cv}^\Gamma \right|^2 \delta(E_c^\Gamma(\mathbf{k}) - E_v^\Gamma(\mathbf{k}) - \hbar\omega), \end{aligned} \tag{3.53}$$

where the energies E_i' and E_f' describe the total energy, i.e. electronic and photonic part, of the initial and final state. The spontaneous direct radiative recombination rate per unit volume for photon emissions in a frequency range $\mathrm{d}(\hbar\omega)$ is then given by summing $P_{i \to f_\omega}$ over all possible electronic initial and final states and field polarizations weighted by the Fermi-Dirac distributions $f_{\text{e}}(E_c^\Gamma(\mathbf{k}))$ and $f_{\text{h}}(E_v^\Gamma(\mathbf{k}))$ for electrons and holes and the optical density of states $G_\Omega(\hbar\omega)$ per unit volume [8]

$$R_{\text{sp}}(\hbar\omega)\mathrm{d}(\hbar\omega) = \frac{2}{V} \sum_{c,v} \sum_{\mathbf{k}} \sum_{\hat{\mathbf{e}}} P_{i \to f_\omega} f_{\text{e}}(E_c^\Gamma(\mathbf{k})) f_{\text{h}}(E_v^\Gamma(\mathbf{k})) G_\Omega(\hbar\omega) V \mathrm{d}(\hbar\omega), \tag{3.55}$$

where the factor 2 accounts for the spin-degeneracy of electron and hole states. We can simplify Eq. (3.55) by explicitly calculating the sum over all possible emission directions and photon polarizations

$$\sum_{\hat{\mathbf{e}}} \left| \hat{\mathbf{e}} \cdot \mathbf{p}_{cv}^\Gamma \right|^2 = \sum_{i=1,2} \int_\Omega \mathrm{d}\Omega \left| \hat{\mathbf{e}}_i \cdot \mathbf{p}_{cv}^\Gamma \right|^2 \tag{3.56}$$

We choose our coordinate system in such a way that $\mathbf{p}_{cv}^\Gamma$ is pointing into the direction of the z-axis. Furthermore, we choose the polarization vector $\hat{\mathbf{e}}_1$ to be parallel to the vector $\mathbf{p}_{cv}^\Gamma \times \mathbf{k}_\lambda$ and $\hat{\mathbf{e}}_2$ to be parallel to $\mathbf{k}_\lambda \times \hat{\mathbf{e}}_1$. With this choice, we find $|\hat{\mathbf{e}}_1 \cdot \mathbf{p}_{cv}^\Gamma|^2 = 0$, while

[8] Here, we define the optical density of states as the total number of photonic modes per unit volume contained in the energy interval $\mathrm{d}(\hbar\omega)$ and the solid angle $\mathrm{d}\Omega$ for a given polarization. It can be obtained by calculating the number of modes per unit volume contained within a small cube $\mathrm{d}k_{\lambda,x}\mathrm{d}k_{\lambda,y}\mathrm{d}k_{\lambda,z} = \mathrm{d}^3\mathbf{k}_\lambda$ in phase space

$$\frac{\mathrm{d}^3\mathbf{k}_\lambda}{(2\pi)^3} = \frac{k_\lambda^2}{(2\pi)^3}\mathrm{d}k_\lambda\mathrm{d}\Omega = \frac{n^3(\hbar\omega)^2}{(2\pi\hbar c)^3}\mathrm{d}\Omega\mathrm{d}(\hbar\omega) \equiv G_\Omega(\hbar\omega)\mathrm{d}\Omega\mathrm{d}(\hbar\omega), \tag{3.54}$$

where we used the dispersion relation for a photon of wavevector $\mathbf{k}_\lambda$ in a medium with a refractive index n given by $k_\lambda = n\omega/c$.

$|\hat{\mathbf{e}}_2 \cdot \mathbf{p}_{cv}^{\Gamma}|^2 = \sin^2\vartheta |\mathbf{p}_{cv}^{\Gamma}|^2$, where ϑ is the azimuthal angle in spherical coordinates. Then the integral from Eq. (3.56) becomes

$$2\pi \int_0^{\pi} \sin\vartheta \mathrm{d}\vartheta \, \sin^2\vartheta \, |\mathbf{p}_{cv}^{\Gamma}|^2 = \frac{8\pi}{3} |\mathbf{p}_{cv}^{\Gamma}|^2. \tag{3.57}$$

Thus, we can rewrite the direct spontaneous radiative recombination rate given in Eq. (3.55) as

$$\begin{aligned} R_{\mathrm{sp}}(\hbar\omega) = \frac{1}{V} \sum_{c,v} \sum_{\mathbf{k}} \frac{2\pi}{\hbar} \frac{8\pi}{3} \left(\frac{e}{m_0}\right)^2 \frac{\hbar}{2\omega\epsilon V} |\mathbf{p}_{cv}^{\Gamma}|^2 G_{\Omega}(\hbar\omega) f_{\mathrm{e}}(E_c^{\Gamma}(\mathbf{k})) f_{\mathrm{h}}^{\Gamma}(E_v(\mathbf{k})) \\ \times \delta(E_c(\mathbf{k}) - E_v(\mathbf{k}) - \hbar\omega) \end{aligned} \tag{3.58}$$

Since we are mainly interested in those states with wavevector $\mathbf{k}$ in close proximity to the Γ-point, we can use the effective mass approximation. Hence, for the conduction band number c and the valence band number v at the Γ-point, the dispersion relation is given by

$$\begin{aligned} E_c^{\Gamma}(\mathbf{k}) &= E_c^{\Gamma} + \frac{\hbar^2 k^2}{2m_c^*}, \\ E_v^{\Gamma}(\mathbf{k}) &= E_v^{\Gamma} - \frac{\hbar^2 k^2}{2m_v^*}, \end{aligned} \tag{3.59}$$

where m_c^* and m_v^* are the effective masses of the respective bands and the energies E_c^{Γ} and E_v^{Γ} are the band-edge energies. Note that instead of a tensor, we used only a scalar effective mass, which is a reasonable simplification for bands around the Γ-point. If the quasi-Fermi levels F_{e} and F_{h} for electrons and holes are more than $4k_{\mathrm{B}}T$ away from all considered conduction and valence band edges, where k_{B} is the Boltzmann constant and T the lattice temperature, we can approximate the Fermi-Dirac statistics by the Maxwell-Boltzmann statistics. The spontaneous direct radiative recombination rate is then given by

$$\begin{aligned} R_{\mathrm{sp}}(\hbar\omega) = \sum_{c,v} \frac{ne^2 |\mathbf{p}_{cv}^{\Gamma}|^2 \hbar\omega}{6\pi^3 m_0^2 c^3 \hbar^2 \epsilon_0} \left(\frac{2m_{cv}^*}{\hbar}\right)^{3/2} \sqrt{\hbar\omega - E_{cv}} \exp\left(-\frac{\hbar\omega - E_{cv}}{k_{\mathrm{B}}T}\right) \\ \times \Theta(\hbar\omega - E_{cv}^{\Gamma}) \exp\left(-\frac{E_{cv}^{\Gamma} - F_{eh}}{k_{\mathrm{B}}T}\right) \end{aligned} \tag{3.60}$$

where $\Theta(x)$ is the Heaviside function[9], $1/m_{cv}^* = 1/m_c^* + 1/m_v^*$ the inverse reduced mass, $E_{cv}^{\Gamma} = E_c^{\Gamma} - E_v^{\Gamma}$ the difference between conduction and valence band edge, and $F_{\mathrm{eh}} = F_{\mathrm{e}} - F_{\mathrm{h}}$ the difference between the quasi-Fermi levels for electrons and holes.

From Eq. (3.60), we see that the PL spectrum is the superposition of the PL of each conduction and valence band pair. The luminescence peak of each such pair shows a characteristic square-root behavior above the energy E_{cv}^{Γ} and decreases exponentially for large energies. The contribution of each conduction and valence band pair to the total recombination rate R_{sp} is determined by the size of the reduced mass m_{cv}^*, the matrix element $|\mathbf{p}_{cv}^{\Gamma}|^2$ as well as the difference between E_{cv} and F_{eh}.

[9]Here, we define the Heaviside function $\Theta(x)$ in the following way:

$$\Theta(x) = \begin{cases} 0, & \text{for} \quad x < 0 \\ 1, & \text{for} \quad x \geq 0 \end{cases}. \tag{3.61}$$

3.3.2 Spontaneous Indirect Radiative Transition Rate

For indirect transitions of group-IV semiconductor alloys, the initial electronic states are either located at the L-point or the Δ-valley (in the following abbreviated by ζ). As for direct transitions, the electronic final states are located in the valence bands around the Γ-point. As we have seen through the derivation of the direct transition matrix element, a recombination of electrons and holes is only possible, if initial and final states have the same crystal momenta. Thus, for the indirect recombination, we have to take into account elastic and inelastic scattering mechanisms that provide the missing momentum. We will start with the elastic scattering processes, which are facilitated by the electron-phonon scattering. For elastic scattering processes, the initial and final states are given by

$$|i\rangle = |\phi_c^{\zeta}(\mathbf{k})\rangle|0\rangle|\cdots n_{\mathrm{ph}}(\mathbf{q})\cdots\rangle, \tag{3.62}$$

$$|f^{\mathrm{abs}}\rangle = |\phi_v^{\Gamma}(\mathbf{k}')\rangle|0\cdots 1_{\omega}\cdots 0\rangle|\cdots (n_{\mathrm{ph}}(\mathbf{q})-1)\cdots\rangle, \tag{3.63}$$

$$|f^{\mathrm{em}}\rangle = |\phi_v^{\Gamma}(\mathbf{k}')\rangle|0\cdots 1_{\omega}\cdots 0\rangle|\cdots (n_{\mathrm{ph}}(\mathbf{q})+1)\cdots\rangle, \tag{3.64}$$

where the first two kets of the product state represent the electronic and the photonic state, which we have already introduced for the direct transition. The last ket in the product state represents the phononic state of the system where $n_{\mathrm{ph}}(\mathbf{q})$ indicates the number of phonons with wavevector $\mathbf{q}$. Similarly, we also have to include the electron-phonon interaction into the interaction Hamiltonian, which reads for the phonon-assisted indirect radiative recombination:

$$H_{\mathrm{int}} = H_{\mathrm{int}}^{\mathrm{e.m.}} + H_{\mathrm{int}}^{\mathrm{ph}}, \tag{3.65}$$

where the term $H_{\mathrm{int}}^{\mathrm{e.m.}}$ describes the interaction between electronic system and electromagnetic field and the term $H_{\mathrm{int}}^{\mathrm{ph}}$ the interaction between electronic system and lattice vibrations.

In principle, phonon-assisted recombination can proceed along two pathways. In a type-I indirect recombination process, the electron will first emit or absorb a phonon and then recombine radiatively with a hole in the valence band. In contrast, in a type-II indirect recombination process, first a photon is emitted and then the electron is scattered to the Γ-point. The latter process is suppressed as the difference between the total energy of the intermediate and final state is much large than for the former. Thus, we can define the intermediate states for either phonon absorption $|m^{\mathrm{em}}\rangle$ or phonon emission $|m^{\mathrm{abs}}\rangle$ by

$$|m^{\mathrm{em}}\rangle = |\phi_c^{\Gamma}(\mathbf{k}'')\rangle|0\rangle|\cdots (n_{\mathrm{ph}}(\mathbf{q})-1)\cdots\rangle, \tag{3.66}$$

$$|m^{\mathrm{abs}}\rangle = |\phi_c^{\Gamma}(\mathbf{k}'')\rangle|0\rangle|\cdots (n_{\mathrm{ph}}(\mathbf{q})+1)\cdots\rangle. \tag{3.67}$$

To calculate the spectrally-resolved emission rate of photons resulting from indirect band-to-band recombination, we make use of Fermi's Golden Rule for second-order transitions [104]

$$P_{i\to f} = \frac{2\pi}{\hbar}\left|\sum_m \frac{\langle i|H_{\mathrm{int}}|m\rangle\langle m|H_{\mathrm{int}}|f\rangle}{E'_m - E'_f}\right|^2 \delta(E'_i - E'_f), \tag{3.68}$$

where the states $|i\rangle$, $|m\rangle$, and $|f\rangle$ describe the initial, intermediate, and final states. The energies E'_i, E'_m, and E'_f denote the total energy of the respective states including the contributions from the electronic system, the electromagnetic field, and the phonons. When summing over the intermediate states, in principle, we have to include all conduction bands at the Γ-point. However, due to the energy separation between these bands and the denominator in Eq. (3.68),

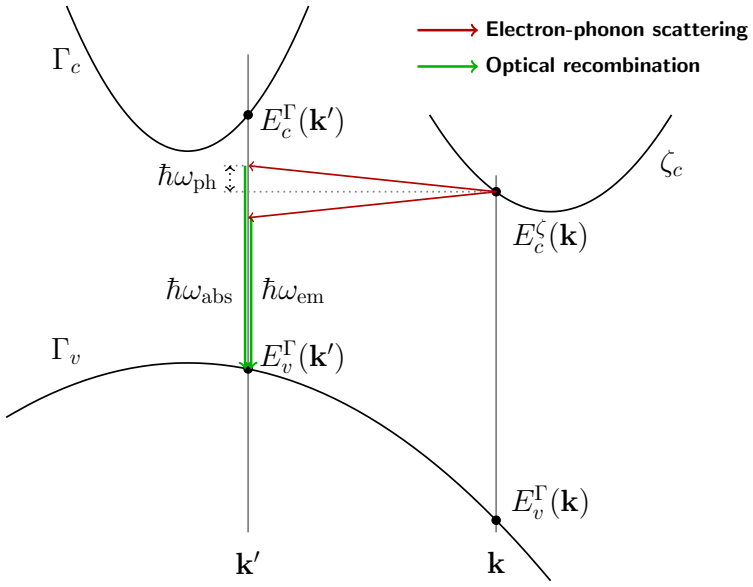

Figure 3.3: *Illustration of the indirect phonon-assisted radiative transition. In group-IV semiconductors, the lowest conduction band (here indicted by ζ) is either located at the L-point or the Δ-valley. In an indirect phonon-assisted recombination, first a phonon of energy $\hbar\omega_{\mathrm{ph}}$ is either absorbed or emitted which leads to a scattering of the electron to an intermediate state at the Γ-point. Afterward, the electron recombines radiatively with a hole by emitting a photon of energy $\hbar\omega_{\mathrm{abs}}$ or $\hbar\omega_{\mathrm{em}}$ depending on the preceding electron-phonon interaction.*

only the lowest conduction band contributes significantly to the transition probability. For this reason, we limit the sum in Eq. (3.68) to only the lowest conduction band.

The electron-phonon interaction Hamiltonian $H_{\mathrm{int}}^{\mathrm{ph}}$ in second quantization has the following form[10]

$$H_{\mathrm{int}}^{\mathrm{ph}} = \sum_{\mathbf{q},\mathbf{k}} D_{\mathbf{q}} (b_{\mathbf{q}} + b_{-\mathbf{q}}^\dagger) c_{\mathbf{k}+\mathbf{q}}^\dagger c_{\mathbf{k}}, \tag{3.69}$$

where $b_{\mathbf{q}}$ and $b_{-\mathbf{q}}^\dagger$ are the bosonic annihilation and creation operators of a phonon while $c_{\mathbf{k}}$ and $c_{\mathbf{k}+\mathbf{q}}^\dagger$ are the fermionic annihilation and creation operators of an electron [105]. In practice, the cumulative effect of phonons belonging to one phonon branch is often modeled by a single dispersionless phonon of energy $\hbar\omega_{\mathrm{ph}}$. The factor $D_{\mathbf{q}}$ can then be written as [106]

$$D_{\mathbf{q}} = D_{\mathrm{eff}} \sqrt{\frac{\hbar^2}{2\rho_{\mathrm{M}} V \hbar\omega_{\mathrm{ph}}}}. \tag{3.70}$$

where D_{eff} is an effective deformation potential, ρ_{M} is the mass density of the sample, and V is the volume of the sample. The squared matrix element for the electron-phonon interaction is then given by

$$\left| \langle i | H_{\mathrm{int}}^{\mathrm{ph}} | m^{\mathrm{em/abs}} \rangle \right|^2 = D_{\mathrm{eff}}^2 \frac{\hbar^2}{2\rho_{\mathrm{M}} V \hbar\omega_{\mathrm{ph}}} \delta_{\mathbf{k}'',\mathbf{k}\mp\mathbf{q}} \times (n_{\mathrm{ph}} + \frac{1}{2} \pm \frac{1}{2}), \tag{3.71}$$

[10] In the definition of the electron-phonon interaction Hamiltonian $H_{\mathrm{int}}^{\mathrm{ph}}$, we presumed for simplicity that only one phonon branch participates in the indirect recombination. If more than one phonon branch is involved, the contributions have to be added.

where the upper (lower) sign corresponds to the emission (absorption) of a phonon. The absolute value squared of the expectation value of the electromagnetic interaction between intermediate state and final state is given in analogy to the calculations for the direct transition in Sec. 3.3.1 by

$$\left|\langle m^{\mathrm{em/abs}}|H_{\mathrm{int}}^{\mathrm{e.m.}}|f^{\mathrm{em/abs}}\rangle\right|^2 = \left(\frac{e}{m_0}\right)^2 \frac{\hbar}{2V\omega\epsilon_0\epsilon}\delta_{\mathbf{k}',\mathbf{k}''}\left|\mathbf{p}_{cv}^{\Gamma}\cdot\hat{\mathbf{e}}\right|^2. \tag{3.72}$$

The rate of spontaneous emission of photons in the energy interval $\mathrm{d}(\hbar\omega)$ per unit volume V via phonon-assisted recombination can then be calculated by summing over all electronic and phononic degrees of freedom and polarization modes $\hat{\mathbf{e}}$ related to the emitted photons

$$R_{\mathrm{sp}}^{\mathrm{ind}}(\hbar\omega)d(\hbar\omega) = \frac{1}{V}\sum_{i,f}\sum_{\hat{\mathbf{e}}} P_{i\to f} f_c(\mathbf{k}) f_v(\mathbf{k}') G(\hbar\omega) V \mathrm{d}(\hbar\bar{\omega}). \tag{3.73}$$

In analogy to the derivation of the direct transition rate of Sec. 3.3.1, we compute the sum over the photon states. Furthermore, if we assume that only the lowest indirect conduction band is populated, we can replace the sum over the initial and final states by the sum

$$\sum_{i,f} \to 2N_\zeta \sum_{\mathrm{abs,em}} \sum_{v} \sum_{\mathbf{k}\,,\mathbf{k}'}, \tag{3.74}$$

where the factor 2 takes into account the spin-degeneracy and N_ζ is the number of degenerate valleys for the initial state, a quantity that we did not have to consider for the direct transition. We obtain for the indirect spontaneous radiative recombination rate

$$\begin{aligned} R_{\mathrm{sp}}^{\mathrm{ind}}(\hbar\omega) = C_{\mathrm{ind}} \sum_{\mathrm{abs,em}} (n_{\mathrm{ph}} + \frac{1}{2} \pm \frac{1}{2}) \sum_{v} \left|\mathbf{p}_{vc}^{\Gamma}\right|^2 \frac{1}{V^2} \sum_{\mathbf{k},\mathbf{k}'} f_e(E(\mathbf{k})) f_h(E(\mathbf{k}')) \\ \times\hbar\omega \frac{\delta\left(E(\mathbf{k}) - E(\mathbf{k}') \mp \hbar\omega_{\mathrm{ph}} - \hbar\omega\right)}{\left(E_i(\mathbf{k}_i) - E_m(\mathbf{k}_f) \mp \hbar\omega_{\mathrm{ph}}\right)^2}, \end{aligned} \tag{3.75}$$

where C_{ind} is defined as

$$C_{\mathrm{ind}} = N_\zeta \frac{|D_{\mathrm{eff}}|^2 e^2 n}{3\pi\epsilon_0 c^3 \rho_{\mathrm{M}} m_0^2 \hbar\omega_{\mathrm{ph}}}. \tag{3.76}$$

The upper (lower) sign in Eq. (3.75) corresponds to the phonon emission (absorption). The number of phonons n_{ph} is given by the Bose-Einstein distribution

$$n_{\mathrm{ph}} = \frac{1}{\mathrm{e}^{\frac{\hbar\omega_{\mathrm{ph}}}{k_{\mathrm{B}}T}} - 1}. \tag{3.77}$$

From the rate equation given in Eq. (3.75), we can conclude that the indirect transition is generally weaker than the direct transition due to the proportionality of the recombination rate to the number of phonons in the system. Furthermore, we expect two luminescence peaks per phonon branch (phonon replica) located at an energy $\hbar\omega_{\mathrm{ph}}$ below and $\hbar\omega_{\mathrm{ph}}$ above the indirect band-gap energy, corresponding to the phonon emission and absorption process. The phonon energies of Si and Ge are in the order of $k_{\mathrm{B}}T$ at room-temperature or larger [107]. Thus, we expect the phonon emission process to be the dominating process.

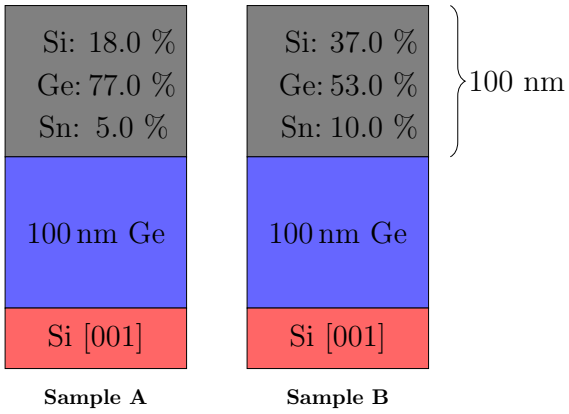

Figure 3.4: *Layer structure of samples. The bottom layer is the Si substrate (red), followed by a* 100 nm*-thick Ge virtual substrate (blue), and the* 100 nm*-thick* $Ge_{1-x-y}Si_xSn_y$ *sample layer (gray).*

Besides the elastic scattering processes, the required momentum for an indirect transition can also be provided via inelastic scattering processes. In bulk semiconductors, inelastic scattering processes are based on impurity scattering or alloy scattering. We will not discuss these processes in detail. We only note that the luminescence due to the inelastic scattering process is associated to a zero-phonon line that has a peak at an energy corresponding to approx. the indirect band-gap and, therefore, lies in the middle between phonon emission and phonon absorption luminescence [89, 108].

3.4 Sample Preparation and Experimental Details

The growth and characterization of the samples were performed in a collective effort by the group of Prof. Jörg Schulze at the University of Stuttgart, the Materials Research Department of the Leibniz-Institut für innovative Mikroelectronik (IHP), and the Institute of Semiconductor Nanoelectronics (Peter Grünberg Insitute) at the Forschungszentrum Jülich.

The $Ge_{1-x-y}Si_xSn_y$ layers were deposited by means of solid-source molecular beam epitaxy on 4" Si (001) substrates. Fluxes of the Sn and Ge effusion cells as well as of the Si electron beam evaporator were calibrated separately and adjusted to obtain a total growth rate of 1 Å/s. The sample growth started with 50 nm of Si (buffer layer) at 600 °C to improve the 4" Si(001) substrate quality after the in-situ epi-cleaning process. A 100 nm-thick layer of Ge was then deposited at a substrate temperature of 330 °C followed by an annealing step at 810 °C to form a virtual substrate (VS) for subsequent epitaxial growth of high-quality relaxed $Ge_{1-x-y}Si_xSn_y$ layers. On this VS, a 100 nm-thick $Ge_{1-x-y}Si_xSn_y$ layer was grown at a substrate temperature of 160 °C. We will discuss two samples in the following: one with a (Si, Sn) nominal composition of (19at.%, 5at.%), in the following referred to as Sample A, and one with nominal composition of (42at.%,10at.%), in the following referred to as Sample B (see Fig. 3.4). In both cases, the nominal concentration were chosen such that the $Ge_{1-x-y}Si_xSn_y$ alloys are lattice-matched to the Ge-VS.

The experimental methods available for the characterization of the sample were Rutherford backscattering spectrometry (RBS), XRD, and microphotoluminescence (μPL). The RBS measurements were performed employing 1.4 MeV He+ ions from a Tandetron accelerator at a back scattering angle of 170° in both random and crystal channeling mode. Fitting of the

random spectra was performed using the RUMP simulation software [109], which yields stochiometric information within an error of less than 0.5 %.

The XRD measurements were performed with a SmartLab diffractometer from Rigaku using CuK_α radiation. For the reciprocal space map (RSM), a high-resolution setup in line-focus geometry was used with a channel-cut Ge (400 x 2) beam collimator and a Ge (220 x 2) analyzer crystal.

The μPL measurements were carried out using a custom-designed Horiba setup featuring a 50× optical microscope (numerical aperture A=0.65), a high resolution spectrometer optimized for infrared measurements (Horiba iHR320), an extended-InGaAs detector (0.6 eV-1.1 eV detection range), and a Si CCD detector (1.1 eV-2.3 eV). The excitation laser wavelength was 532 nm. All spectra were collected at room-temperature as well as at normal incidence in backscattering geometry. A white-body lamp was used to determine the optical response of the setup used for the calibration of the spectra.

3.5 Experimental Results and Theoretical Analysis

In the following, we will describe the results of the experimental characterization of the samples and the theoretical analysis that is based on those results. We will start with the structural characterization consisting of the composition and strain analysis and then move on to the optical characterization and the calculation of the band-gap bowing.

3.5.1 Material Composition

The investigation of the material composition was performed using RBS. In RBS, a beam of high kinetic energy particles are focused onto the sample. From the energy distribution of the backscattered particles, information about the samples material composition and layer structure can be inferred. For the sample discussed here, RBS measurements were performed at three distinct positions: at the center of the wafer, at the edge, and at an intermediate position. At each position, two RBS measurements were performed. First, the sample were oriented in a random direction with respect to the velocity of the high kinetic energy particles. In a second measurement, referred to as channeling, the velocity of the particles was aligned along a high symmetry direction of the crystal. Representative RBS plots for Sample A and Sample B are shown in Fig. 3.5. The observed peaks correspond to the backscattering of particles at the different layers of the sample. The peak at the highest energy corresponds to the backscattering at the surface. The minimum channeling yield, defined as the ratio between channeling and random spectra directly behind the surface peak, was measured to have the rather low value of 6 % (12 %) for Sample A (Sample B) indicating a high atom-substitutionality in the epilayer. Simulating the random RBS measurement, the material composition were determined. The measured compositions show a gradient of roughly 1 % from the center of the wafer to the edge due to the asymmetric position of the material sources (see Table 3.1).

When comparing the averaged measured material composition with the nominal values target in the growth process (see Tab. 3.1), we find for Sample A a deviation of at most 2 %. The Sn concentration with 5.8 % is slightly larger than the target concentration of 5 %. For Sample B, we find that the average Sn concentration of 9.2 % is slightly below the targeted value of 10 %. Moreover, for the Si and Ge concentration, we find a deviation of roughly 4 % in comparison to the nominal values with a higher silicon concentration than the targeted one. Thus, we expect larger strain in Sample B in comparison to Sample A.

Table 3.1: *Material concentrations according to RBS measurements performed at the middle of the wafer, the edge and an intermediate position. Also displayed is the average value of all positions compared to the nominal concentrations (given in parentheses). Reproduced from T. Wendav* et al., *"Compositional dependence of the band-gap of $Ge_{1-x-y}Si_xSn_y$ alloys", Appl. Phys. Lett.* ***108,*** *242104 (2016), with the permission of AIP Publishing.*

Sample A	%Si	%Ge	%Sn
middle	18.5	76.0	5.5
intermittent	19.3	75.0	5.7
edge	19.5	74.3	6.2
mean	19.1 (18)	75.1 (77)	5.8 (5)
Sample B	%Si	%Ge	%Sn
middle	41.8	49.5	8.7
intermittent	41.8	49.2	9.0
edge	42.2	48.0	9.8
mean	41.9 (37)	48.9 (53)	9.2 (10)

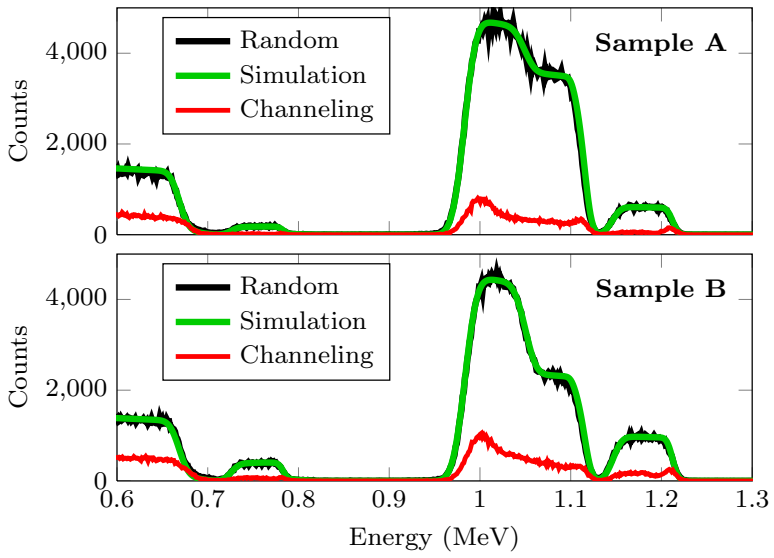

Figure 3.5: *Representative plot of the RBS data (black), simulation (green) and channeling (red) recorded at the center of the wafer for sample A (top) and sample B (bottom). The observed peaks can be attributed to the backscattering at different layers within the samples. A simulation was performed to retrieve the material composition of the sample. The channeling measurement indicates a high atom-substitutionality in the epilayer. Reproduced from T. Wendav* et al., *"Compositional dependence of the band-gap of $Ge_{1-x-y}Si_xSn_y$ alloys", Appl. Phys. Lett.* ***108,*** *242104 (2016), with the permission of AIP Publishing.*

3.5.2 Lattice Constants and Strain

The lattice constants were determined using XRD. Based on the diffraction pattern of the sample, one can extract information about the crystal lattice of the sample. Figure 3.6 shows the RSM of our samples around the (224) Bragg reflection of Ge and $Ge_{1-x-y}Si_xSn_y$. In each RSM two peaks can be identified, which correspond to the SiGeSn and the Ge Bragg reflection, respectively. As the crystal structure of the Ge VS is identical for both samples, the Ge peak position is the same in both RSM. For the $Ge_{1-x-y}Si_xSn_y$ reflections, we find that the value of the reciprocal space vector q_x is identical to that of the Ge reflection for both samples, while the value of reciprocal space vector q_z is different. From the identical q_x values we can infer that all layers have the same in-plane lattice constant and are therefore pseudomorphically grown on each other. The difference in the q_z value indicates a different strain state of the $Ge_{1-x-y}Si_xSn_y$ epilayers in Sample A and Sample B. Using standard equations [110], we can calculate the in-plane lattice constant $a_\parallel$ from the the value of q_x and the perpendicular lattice constant $a_\perp$ from q_z for both samples. These values are given in Tab. 3.2 together with the unstrained lattice constant a_{EXP} calculated according to Eq. (3.18). We find that the $Ge_{1-x-y}Si_xSn_y$ layers of both samples are tensile strained with a biaxial strain of $\epsilon_\parallel = 0.09\%$ ($\epsilon_\parallel = 0.56\%$) for Sample A (Sample B). The different strain states of the samples support our compositional analysis where we found that the measured composition of Sample A is closer to the nominal composition targeted by the growth process than the composition of Sample B.

We compare the unstrained lattice constant a_{EXP} with that which can be obtained by Vegard's law [111] and by the nonlinear relationship proposed by Aella *et al.* [112]. According to Vegard's law, the lattice constant a_{VEG} of an alloy can be calculated by linearly averaging the lattice constants of the constituent materials according to their concentrations:

$$a_{\mathrm{VEG}}(x,y) = a_{\mathrm{Si}}x + a_{\mathrm{Sn}}y + a_{\mathrm{Ge}}(1-x-y), \tag{3.78}$$

where a_{Si}, a_{Ge}, and a_{Sn} are the lattice constants of the elemental semiconductors Si, Ge, and Sn, respectively. In contrast, Aella *et al.* proposed a nonlinear relationship, similar to the bowing equation for the band-gap, to estimate the lattice constant of the $Ge_{1-x-y}Si_xSn_y$ alloys, which has subsequently been used in other studies [81, 113]. Aella *et al.* argue that the compositional dependence of the lattice constant a_{SiGe} and a_{GeSn} of the Si_xGe_{1-x} and $Ge_{1-y}Sn_y$ binary alloy behave like

$$\begin{aligned} a_{\mathrm{SiGe}}(x) &= a_{\mathrm{Si}}x + a_{\mathrm{Ge}}(1-x) + \theta_{\mathrm{SiGe}}x(1-x), \\ a_{\mathrm{GeSn}}(y) &= a_{\mathrm{Ge}}y + a_{\mathrm{Sn}}(1-y) + \theta_{\mathrm{GeSn}}y(1-y), \end{aligned} \tag{3.79}$$

where $\theta_{\mathrm{SiGe}} = -0.026\,\text{Å}$ [114] and $\theta_{\mathrm{GeSn}} = 0.166\,\text{Å}$ [115] have been measured experimentally. Therefore, the lattice constant of the $Ge_{1-x-y}Si_xSn_y$ alloy can be estimated by combining both equations:

$$\begin{aligned} a_{\mathrm{EMP}}(x,y) = a_{\mathrm{Ge}} + (a_{\mathrm{Si}} - a_{\mathrm{Ge}})x + \theta_{\mathrm{SiGe}}x(1-x) \\ + (a_{\mathrm{Sn}} - a_{\mathrm{Ge}})y + \theta_{\mathrm{SnGe}}y(1-y). \end{aligned} \tag{3.80}$$

Using the averaged compositions obtained via RBS measurements, we can calculate the expected lattice constants according to Vegard's law and according to the empirical relation by Aella *et al.* and compare it to the lattice constant obtained by our XRD measurements (see Tab. 3.2). Even though the relative difference for both approaches is less than 1%, we find that the prediction made with Vegard's law lies closer to the experimentally determined values. Moreover, the predictions made following the empirical relationship of Ref. [112] lie outside

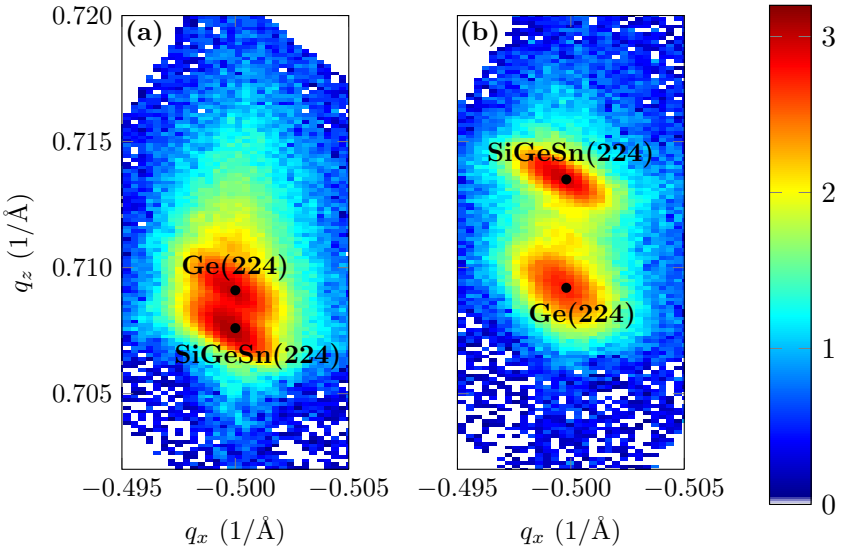

Figure 3.6: *RSM of the middle of the wafer for (a) Sample A and (b) Sample B. The colorbar indicates the intensity of the reflected light on a logarithmic scale in arbitrary units. The identical reciprocal space vector q_x for Ge VS and epilayer indicates a pseudomorphic growth. The difference in the reciprocal space vector q_z identifies a difference in lattice constant between the Ge VS and the epilayer. Reproduced from T. Wendav* et al., *"Compositional dependence of the band-gap of $Ge_{1-x-y}Si_xSn_y$ alloys", Appl. Phys. Lett.* ***108,*** *242104 (2016), with the permission of AIP Publishing.*

the interval of uncertainty of the XRD measurements (0.006Å) for both samples. We therefore conclude that, at least for the compositions investigated here, the nonlinear behavior of the lattice constant of the Si_xGe_{1-x} and $Ge_{1-y}Sn_y$ binary alloys compensate each other and the linear average according to Vegard's law forms a better description of the lattice constant of the ternary alloy than the empirical relation proposed by Aella *et al.*[11]

3.5.3 Photoluminescence and Band-Gap Bowing

The band-gap of the $Ge_{1-x-y}Si_xSn_y$ ternary alloys was determined using μPL spectroscopy. μPL measurements were performed at eleven equidistant positions along the radius of the waver from the center to the edge. In all the measurements, we have predominantly observed a strong peak around 0.90 eV for both Sample A and Sample B with a shoulder towards lower energies (see Fig. 3.7 for representative spectra). We attribute the stronger peak to the direct transition and the low energy shoulder to the indirect gap transition [116]. Optical recombination processes are more efficient for direct band-gap transitions and can be expected to lead to a higher PL signal intensity. Furthermore, we can expect the contribution of the indirect transition to the PL signal to be small because of the lack of self-absorption in our thin GeSiSn layers [100]. The signal of the indirect transition is too weak to be quantitatively analyzed. Therefore, we will only concentrate on the stronger direct transition. To extract the peak energy, we fitted the peak with a Gaussian (data shown in Fig. 3.8). Due to local variations in concentration that cannot be captured by RBS but affects our μPL measurements, we see variations in spectral

[11] The material parameters used for this analysis are given in App. B.

Table 3.2: *Parallel and perpendicular lattice constants as measured by XRD and, based on this, unstrained lattice constant a_{EXP}. Comparison to lattice constant a_{VEG} calculated according to Vegard's law, and lattice constant a_{EMP} calculated according to Ref. [112]. Values in parentheses indicate the deviation from the experimental value in percent. Reproduced from T. Wendav* et al., *"Compositional dependence of the band-gap of $Ge_{1-x-y}Si_xSn_y$ alloys", Appl. Phys. Lett.* ***108,*** *242104 (2016), with the permission of AIP Publishing.*

Sample	$a_{\parallel}$ (Å)	$a_{\perp}$ (Å)	a_{EXP} (Å)	a_{VEG} (Å)	a_{EMP} (Å)
A	5.663	5.653	5.658	5.663 (-0.09)	5.668 (-0.18)
B	5.665	5.640	5.631	5.640 (-0.15)	5.647 (-0.28)

shape and peak positions with the broadening of the direct transition peak most likely due to concentration variations within the μPL sampling volume. Note that we did not observe any μPL-related features in the photon energy region above 1.1 eV.

As a first step to calculate the bowing parameter of the SiSn binary alloy, we corrected the band-gap of the samples for the tensile strain. The hydrostatic strain component of the biaxial tensile strain shifts the conduction band at the Γ-point upwards in energy. In addition, the tensile strain leads to a splitting of the heavy hole and light hole band by shifting the light hole band upward in energy and the heavy hole band downward. The PL energy of the direct transition therefore corresponds to the energy difference of the lowest conduction band and the light hole band at the Γ-point. Using Eq. (3.45) and (3.32), we can estimate the shifts in energy due to strain and correct the measured PL luminescence for the case of a relaxed crystal. For the material parameters required in Eq. (3.2), we used the values given in Tab. B.1 of App. B for the elemental semiconductors Si, Ge, and Sn. In accordance with the literature [28, 29] and our findings on the lattice constant, all material parameters were linearly averaged to match the measured compositions of the samples. The material composition for each PL data point was calculated by linear interpolation of the RBS data based on the data in Tab. 3.1. For Sample A (Sample B), strain leads, on average, to a decrease of the band-gap by 4 meV (82 meV), see Fig. 3.8.

From the strain corrected band-gap energies the SiSn bowing parameter was calculated according to Eq. (3.2). For the band-gaps of the constituent materials Si, Ge, and Sn as well as the SiGe bowing parameter, we followed D'Costa *et al.* and used the values 4.1 eV, 0.8 eV, −0.41 eV, and 0.21 eV, respectively [79, 117]. For the GeSn bowing parameters, several values can be found in the literature varying between 1.94 eV and 2.61 eV [37, 79]. Here, we use the value of 2.46 eV [82]. However, as will become clear in the following, the bowing behavior of the GeSiSn band-gap is dominated by the SiSn bowing parameter and, therefore, variations of the GeSn bowing parameter have only a minor effect. The SiSn bowing parameter is shown in Fig. 3.9. We perform a two-way analysis calculating the mean value of the bowing parameter for Sample A and Sample B separately as well as across all samples. For Sample A and Sample B, we obtain a value of (29 ± 5) eV and (24 ± 4) eV, respectively, while the mean value across all samples is (24 ± 2) eV. Within the experimental uncertainties, we do not see a concentration dependence of the bowing parameter for our samples. Therefore, we use the value of (24 ± 2) eV for our further discussion.

If we do not include the correction for the strain effects, we calculate the mean bowing constant to be (26 ± 2) eV. The change in the bowing parameter due to the strain correction corresponds to a decrease of roughly 8 %, which is in the order of the experimental uncertainty.

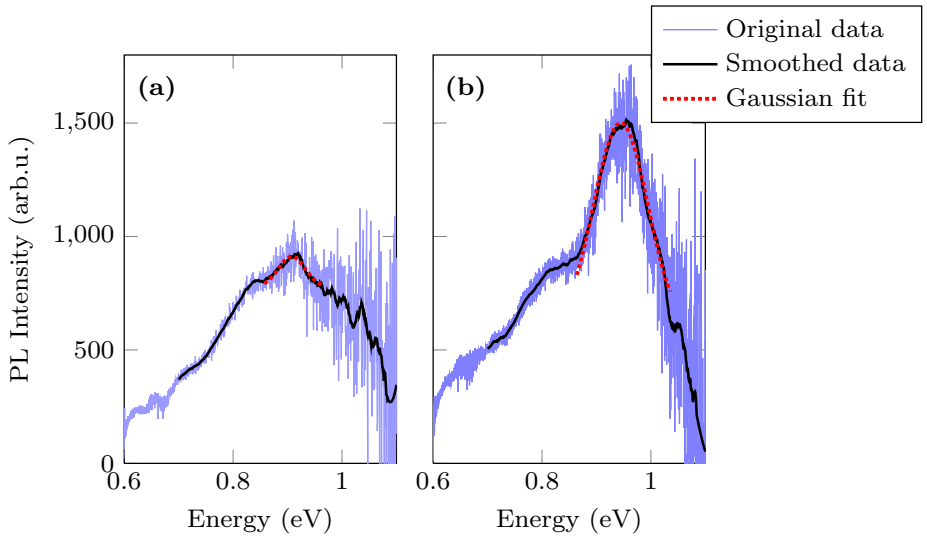

Figure 3.7: *Examplary PL spectra of (a) Sample A and (b) Sample B. Displayed are original data (blue), smoothed data (black), and Gaussian fit (red dashed). A strong peak at* 0.9 eV *is observed and a smaller shoulder towards lower energies. We attribute these peaks to the direct and the indirect recombination, respectively. Reproduced from T. Wendav* et al., *"Compositional dependence of the band-gap of* $Ge_{1-x-y}Si_xSn_y$ *alloys", Appl. Phys. Lett.* ***108,*** *242104 (2016), with the permission of AIP Publishing.*

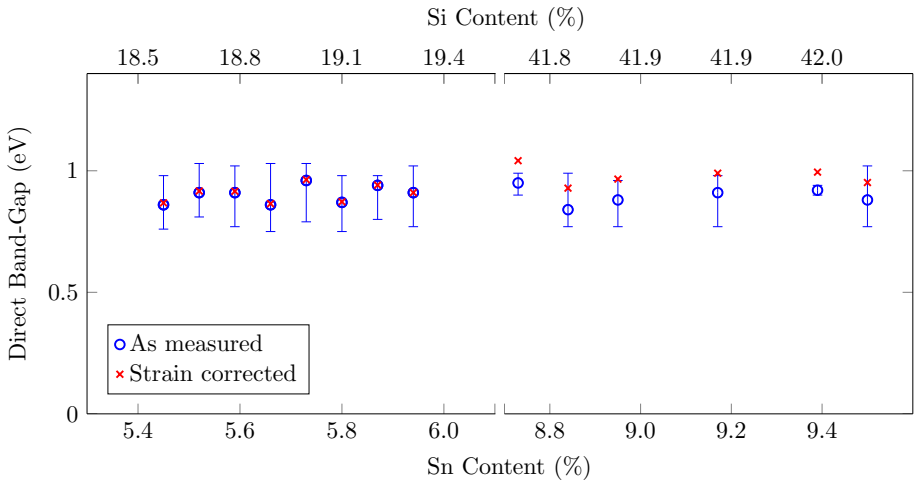

Figure 3.8: *Direct band-gap as measured by μPL and strain corrected value. The data clustered around low (high) Sn content correspond to Sample A (Sample B). Error bars are equivalent for as measured and strain corrected samples. The strain correction only affects Sample B, where it leads to an increase of the band-gap size. The increase is in the order of magnitude of the experimental uncertainties. Reproduced from T. Wendav* et al., *"Compositional dependence of the band-gap of* $Ge_{1-x-y}Si_xSn_y$ *alloys", Appl. Phys. Lett.* ***108,*** *242104 (2016), with the permission of AIP Publishing.*

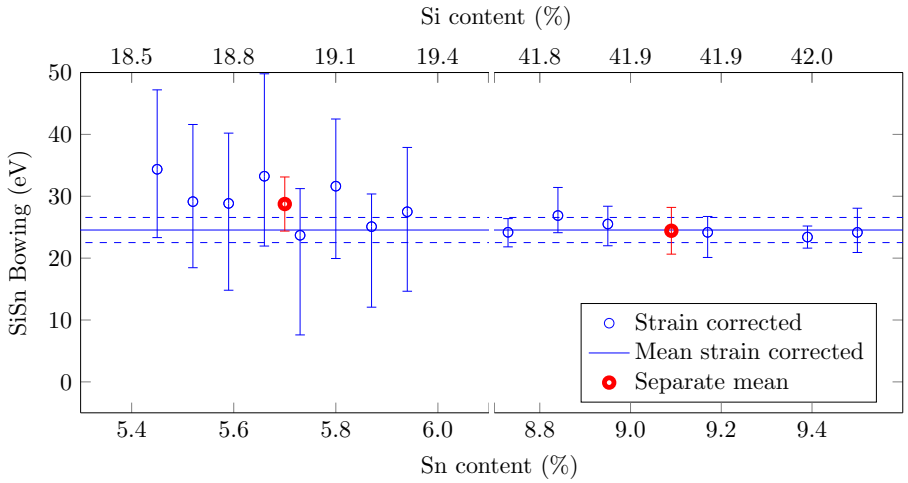

Figure 3.9: *SiSn bowing parameter calculated after strain correction (blue circles). The data clustered around low (high) Sn content correspond to Sample A (Sample B). Also shown are the average SiSn bowing parameter over Sample A/Sample B only (red circles) and the average SiSn bowing parameter calculated over all values (blue line) with error bars (dashed blue line).*

Also, the change in the bowing constant is mainly a result of the strain correction of the measured band-gaps of Sample B.

In Fig. 3.10(a) we compare our predictions of the composition dependence of the direct band-gap for Ge lattice-matched $Ge_{1-x-y}Si_xSn_y$ alloys with the experimental studies of D'Costa *et al.* and Gallagher *et al.* [84, 117]. Gallagher *et al.* experimentally investigated two classes of partially relaxed $Ge_{1-x-y}Si_xSn_y$ alloys samples. One class included samples with a high Sn concentration ($y < 0.10$), but low Si concentration ($x < 0.05$). The other class included samples with a higher Si concentration ($x < 0.18$), but a lower Sn concentration ($y < 0.04$). They investigated the compositional dependence of the direct band-gap and found a linear relationship. D'Costa *et al.* investigated Ge-lattice matched $Ge_{1-x-y}Si_xSn_y$ alloys with Si concentrations of $x < 0.40$ and Sn concentration of $y < 0.10$. Analyzing the direct band-gap they also used the nonlinear relationship given in Eq. (3.2) to describe the compositional dependence.

A significant difference between our study and that of D'Costa *et al.* is that D'Costa *et al.* predict the direct band-gap of $Ge_{1-x-y}Si_xSn_y$ alloys always to be larger than that of pure Ge while, using the result of our experiments, in contrast, we predict a smaller band-gap for $Ge_{1-x-y}Si_xSn_y$ alloys with a Sn concentration above approx. 12 %. This has significant implications when comparing the size of the direct band-gap to that of the indirect band-gap, as we will see later. Focusing on the predictions made by Gallagher *et al.*, we find that both our parametrization of the bowing equation as well as that used by D'Costa *et al.* overestimate the band-gap for small Sn concentrations where our prediction is closer in value due to the larger bowing parameter.

It is also interesting to examine the size of the direct band-gap in contrast to that of the indirect band-gaps of $Ge_{1-x-y}Si_xSn_y$. As experimentally we only had access to the direct band-gap, we compare our predictions to those made by Sant *et al.* [88] using empirical pseudopotentials (see Fig. 3.10(b)). In their study, Sant *et al.* calibrated the pseudopotentials of Si, Ge, and Sn in order to match the band-gap bowing behavior of the $Ge_{1-y}Sn_y$ alloy at

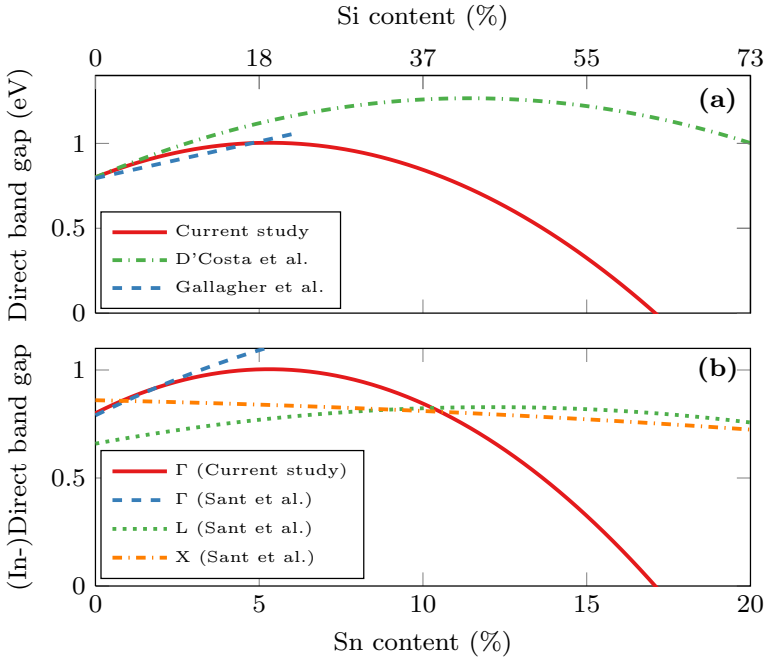

Figure 3.10: *(a) Prediction of the size of the direct band-gap according to our study (red), D'Costa et al. (green), and Gallagher et al. (blue dashed). (b) Comparison of the concentration dependence of the direct band-gap Γ with X and L indirect band-gaps as computed by Sant et al. Both figures assume a Ge lattice-matched $Ge_{1-x-y}Si_xSn_y$ alloy. In comparison to the study of D'Costa et al., our study predicts Ge lattice-matched $Ge_{1-x-y}Si_xSn_y$ alloys to become direct semiconductor with a Sn concentration $y > 11\,\%$. Reproduced from T. Wendav* et al., *"Compositional dependence of the band-gap of $Ge_{1-x-y}Si_xSn_y$ alloys", Appl. Phys. Lett.* ***108,*** *242104 (2016), with the permission of AIP Publishing.*

room-temperature. We find that for Sn concentrations larger than approx. 11 %, the size of the direct band-gap as predicted by our investigation is smaller than the indirect band-gaps at the X- and L-point as predicted by Sant *et al.* The lattice-matched $Ge_{1-x-y}Si_xSn_y$ alloy therefore undergoes a transition from indirect to direct band-gap semiconductor. This is in contrast to the predictions of D'Costa *et al.* where $Ge_{1-x-y}Si_xSn_y$ lattice matched to Ge always is an indirect semiconductor.

We want to note here, however, that the predictions concerning the direct band-gap of Sant *et al.* imply the opposite sign for the SiSn bowing parameter in comparison to ours.

3.6 Summary and Outlook

In conclusion, we investigated the band-gap of two $Ge_{1-x-y}Si_xSn_y$ alloys with a (Si,Sn) nominal composition of (19 at. %, 5 at. %) and (42 at. %, 10 at. %), respectively, which are closely lattice-matched to Ge. With the help of PL measurements, we extracted the direct transition energy of the samples. Using XRD as well as RBS measurements, we corrected the measured optical transition energy for the effects of residual strain caused by the lattice mismatch between epilayer and substrate. Using a semi-empirical bowing equation based on the band-gaps of the

elemental semiconductors and the binary bowing terms, we calculated a SiSn bowing parameter of $(24 \pm 2)\,\mathrm{eV}$.

Comparing the predictions for the direct band-gap of Ge lattice-matched $Ge_{1-x-y}Si_xSn_y$ alloys made by three experimental studies, including ours, we found considerable disagreement between them. In particular, we found that when combining our parametrization of the bowing equation and the results of the theoretical study of Sant *et al.* [88], we expect the $Ge_{1-x-y}Si_xSn_y$ alloys lattice matched to Ge to become direct semiconductors when the Sn concentration exceeds 12 %. This is in conflict with the investigation performed by D'Costa *et al.* [117] that predict $Ge_{1-x-y}Si_xSn_y$ alloys, which are lattice-matched to Ge, to be indirect semiconductors independent of the composition.

We can only speculate about the cause of this discrepancy. One possible explanation for this, as already put forward by Beeler *et al.* [118], is that the bowing parameter b_Γ^{SiSn} is either composition-dependent or that higher order terms have to be included in Eq. (3.2) in order to predict the direct band-gap of $Ge_{1-x-y}Si_xSn_y$ over a broad range of compositions.

In order to resolve the discrepancies, further experiments on $Ge_{1-x-y}Si_xSn_y$ samples that span a greater range of material concentrations have to be performed. One of the key questions to answer is whether Ge lattice-matched $Ge_{1-x-y}Si_xSn_y$ will indeed turn into a direct band-gap semiconductor for large Sn concentrations.

Furthermore, it would be helpful to investigate in more detail spatial fluctuations in the composition of the sample. The XRD and RBS only provide spatially averaged information on strain and composition, while the μPL measurements record the luminescence emitted from a, in comparison, relatively small volume. If, for example, there is a gradient in the Sn concentration along the growth direction due to the segregation of Sn, it will affect the PL signal, while XRD and RBS measurements remain largely unaffected. For a greater spatial resolution, nano-XRD microscopy as well as energy-dispersive XRD could be used [W3, 119].

Besides experimental efforts, there is also a need for more detailed theoretical calculations. The advantage of theoretical calculations is that composition and strain can be precisely controlled. However, the two most recent studies by Moontragoon *et al.* and Sant *et al.* using the EPM show a large discrepancy in the prediction of the SiSn bowing parameter for the direct band-gap [21, 88]. While Moontragoon *et al.* used the bulk Si, Ge, and Sn pseudopotentials and calculated a SiSn bowing parameter of 3.92 eV for the band-gap at the Γ-point, Sant *et al.* used custom pseudopotentials that reproduced the experimentally measured GeSn band-gap bowing behavior and calculated $-5.95\,\mathrm{eV}$. Recognizing the importance of the choice of pseudopotentials parameters, new approaches to verify the choice of pseudopotentials are required to increase the predictive power of the EPM. Also *ab initio* calculations of the compositional-dependence of the band-gaps of the ternary alloy would be interesting. However, due to the large supercells required for the calculations they are computationally demanding. Therefore, the feasibility of these calculations has to be investigated.

Chapter 4

4 Band Alignment between Si, Ge, and Sn

In this chapter, we investigate the band alignment of Si, Ge, and Sn relative to each other. To do so, we perform interface calculations for Si and Ge as well as Ge and Sn using density functional theory. We focus on the alignment of the valence bands. For the exchange correlation functional, we use the local density approximation (LDA) since the LDA reproduces the valence band structure of semiconductors well and is also computationally efficient. In contrast to our initial assumption that the main challenge in this calculation is the incorporation of higher order strain effects due to the large lattice mismatch between the elemental semiconductors, we find that the band alignment calculations are severely influenced by the underestimation of the semiconductor band-gaps typical for the LDA. While for the SiGe heterojunction this problem is partly compensated by a band-gap opening due to strain and confinement effects, the GeSn heterojunction becomes metallic with a false type-III band alignment. The resulting charge separation at the interface leads to a strong electric field, which in turn influences the band alignment. Therefore, we conclude that exchange-correlation functionals beyond the LDA are required to calculate the band alignment between Ge and Sn.

4.1 Introduction

An important input parameter for both $\mathbf{k}\cdot\mathbf{p}$ and effective mass calculations of heterostructures is the band alignment between the different semiconductor materials that make up the structure. These parameters determine the potential landscape that electrons and holes move in and therefore influence the optical transitions. Whereas the band alignment between Si and Ge has already been studied intensively, both theoretically (see Refs. [120–122]) and experimentally (see Refs. [123–126]), the band alignment between Si and Ge and Sn has not. So far, measurements of the band alignment between the valence band maximum (VBM) of Ge and $Si_{1-x-y}Ge_xSn_y$ have only been performed by a single group for three specific compositions [27]. One of the reasons for this lack of experimental data is that the measurement of the band alignment is challenging. It requires high purity samples. Trap states and contaminations at the interface change the electronic structure and, therefore, influence the band alignment [127]. In addition, due to the

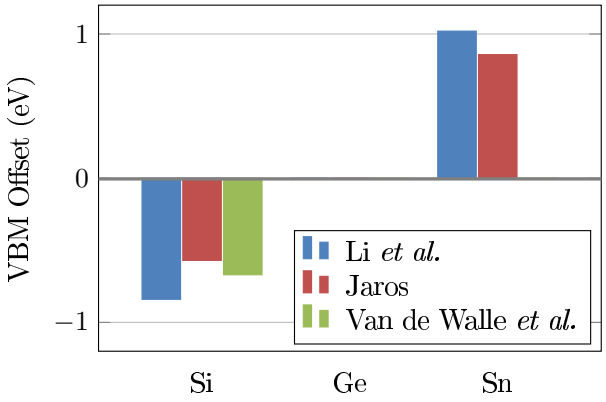

Figure 4.1: *Natural band offsets for the Si and Sn VBM relative to Ge according to Jaros [128], Li et al. [129], and Van de Walle et al. [120].*

large lattice mismatch between Si, Ge, and Sn, band offset measurements usually involve binary or ternary alloys of the three materials. This, however, requires high accuracy in the growth process for the alloy to match the targeted composition and also for the composition to be spatially homogeneous. Furthermore, also strain affects the band alignment at a heterojunction. In order to extract the band alignment between semiconductors without the effects of strain, the semiconductors at the heterojunction have to be lattice-matched. Yet, this limits the compositions for which the band alignment can be measured. As a consequence, theoretical studies of the band alignment of semiconductors are important. While on the one hand side, they can be used to validate experimental measurements, on the other hand side, they also allow for a detailed investigation of the effects of strain, interface orientation, and interface quality on the band alignment.

Yet, the results of the theoretical investigations for the band alignment between Si, Ge, and Sn are controversially discussed as well. So far, only two theoretical studies have been performed which took very different approaches: the author of Ref. [128] used a simple analytical model to calculate the band alignments between Si, Ge, and Sn based on bulk properties of the elementary semiconductors, while the authors of Ref. [129] performed DFT-LDA calculations for, among others, the SiGe and GeSn interfaces[1]. Their predictions for the absolute energy of the VBM of the three unstrained semiconductors with respect to Ge is given in Fig. 4.1. We find that both studies predict the VBM of Si to be lower and the VBM of Sn to be higher than that of Ge. However, the actual values deviate from each other. Li finds the VBM of Si to be roughly 300 meV lower and the VBM of Sn to be roughly 200 meV higher in energy in comparison to the results of Jaros. This difference is considerable when compared with the fundamental band-gap of Ge (670 meV at room temperature). It is not clear which of the values is in better agreement with the physical reality. We can compare the results for the already investigated band offset between Si and Ge with an earlier DFT calculation by Van de Walle *et al.* [120], which is in agreement with the results of experimental investigations [125]. We find that Jaros result lies approx. 100 meV below that of the Van de Walle *et al.*. This might be a result of the approximations used in Jaros's simplified model. However, also the calculations of Li are roughly 200 meV larger than the result of Van de Walle *et al.*.

The reason for the discrepancy between the band alignment calculated by Van de Walle *et al.* and Li might be a result of the strain correction that Li applied to his calculations. Li

[1] In the following, we refer to the two publication only by their first authors, which are Jaros and Li, respectively.

determines the band offset of the group-IV elemental semiconductors by investigating the band structure of interfaces between various combinations of group-IV elemental semiconductors. As a result of the difference lattice constants of the group-IV semiconductors, the band structure of the interface is affected by strain. Li uses a procedure to correct for the effects of strain up to first order for each interface calculation. Using a least-square fitting algorithm applied to the results of the individual interface calculations he determines the absolute band alignment between all group-IV semiconductors. Due to the large lattice mismatch between Ge and Sn of 16 %, it is possible that a strain correction to first order might not be sufficient. Through the least-square fitting procedure, the insufficiently strain-corrected band offset between Ge and Sn might have also influenced the band alignment between Si and Ge and caused the discrepancy to the result of Van de Walle *et al.*. To investigate the strain correction related to the Ge and Sn band offset, we repeat the DFT-LDA calculation of the band offsets between the three semiconductors attempting to extend the studies of Li to now also include corrections of nonlinear strain effects.

This chapter is structured as follows: In Sec. 4.2, we explain the theoretical foundations of band alignment calculations. We briefly explain the method used by Jaros and then turn our attention to DFT-based band alignment calculations. Furthermore, we introduce the `exciting` code, which is an all-electron Kohn-Sham-based DFT implementation, that we use for our investigations. In Sec. 4.3, we present bulk band structure calculations of Si, Ge, and Sn as performed with DFT, which serve as the basis for our interface calculations. In Sec. 4.4, we discuss the results of our interface calculations without explicitly considering effects of strain. In Sec. 4.5, we then focus on the effects of strain on the interface calculations. We conclude this chapter with a summary and outlook in Sec. 4.6.

4.2 Theory of Heterojunction Band Alignments

4.2.1 Defining the Problem

We start our discussion by defining the band alignment problem between two semiconductors A and B with two different band-gaps of size $E_{\mathrm{g}}^{\mathrm{A}}$ and $E_{\mathrm{g}}^{\mathrm{B}}$, respectively, in a more rigorous fashion. Bringing these semiconductors together will introduce a discontinuity in the VBM and the conduction band maximum (CBM) at the interface. This situation is schematically depicted in Fig. 4.2(a). Therefore, the band alignment between these two semiconductors is fully solved by either determining the magnitude of the valence band offset (VBO), indicated by ΔE_{v}, or the magnitude of the conduction band offset (CBO), indicated by ΔE_{c}. Since strain affects the size of the band-gaps, the values of ΔE_{c} and ΔE_{v} are also affected by the strain condition of the semiconductors [130, 131]. In order to separate the effects of strain from the band alignment problem, the *natural* band offset is defined as the band offset between two semiconductors in their specific equilibrium crystal structure.

Depending on the band alignment between the two semiconductors and the size of their band-gaps, three different alignment types can be identified (see Fig. 4.2(b)). In a type-I alignment (straddling gap), the VBM and the CBM are both found on the same side of the interface. In contrast, in a type-II alignment (staggering gap), the VBM and the CBM lie on different side of the interface. This leads to profound differences also in the optical properties. While excited electrons and holes are effectively captured within a single layer in quantum well (QW) structures with a type-I alignment, a type-II alignment will lead to their spatial separation and therefore make a recombination less likely. In addition, the separation of charge carriers leads to the build-up of an electric field and consequently to a shift of energy levels.

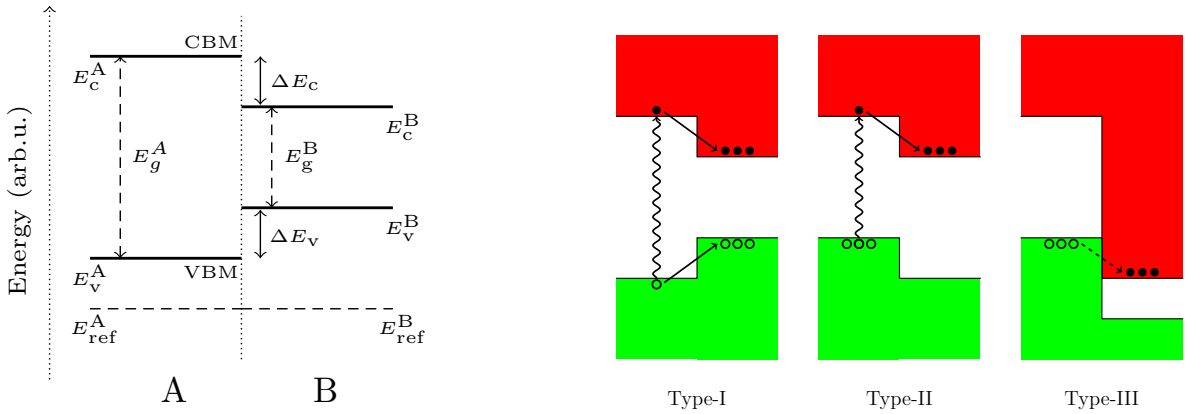

(a) Definition **(b)** Alignment Types

Figure 4.2: *(a) Schematic of the band structure lineup problem between semiconductors A and B. (b) Illustration of the band alignment types following Ref. [90].*

Nevertheless, in both type-I and type-II the energy of the VBM is always below that of the CBM. This is different in a type-III alignment (broken gap), where the CBM on one side of the junction is below that of the VBM on the other side of the junction. This leads to the flow of electrons from the topmost valence-band states to the lower conduction-band states with the result of the build-up of a strong electric field even in the absence of an external excitation of charge carriers.

The band offset between two semiconductors is determined by the rearrangement of charges at the interface, which leads to the so called interface dipole and, in turn, to a discontinuity of the average electrostatic potential on either side of the heterojunction. The theoretical methods that have been developed to predict the band alignment between semiconductors can be divided into two categories. The first category includes all those techniques that attempt to calculate the full solutions to the Schrödinger equation of an interface structure. In principle, we know the full Hamilton operator at an interface and, as a result, can calculate its full electronic structure. In the past, computational resources were often not sufficient to investigate the electronic band structure of an interface in its entirety. Thus, approximation techniques were developed like the linear response theory [132] and the self-consistent tight-binding approach [133]. Today, the available computational resources are often sufficient to investigate the interface structures using DFT [134–136]. The advantage of all these methods is that they capture the effects of individual properties of the materials making up the interface. Yet, for each material combination at an interface, a separate calculation is required.

The second category contains all those methods that attempt to solve the band alignment problem by constructing simplified models of the electron dynamics at the interface. These models attempt to capture the relevant physical effects that influence the band alignment, but do not require a full electronic structure calculation of the interface itself. The assumption of all those models is that it is possible to associate a reference level with each semiconductor, which introduces an absolute energy scale. At an interface between any two semiconductors, the bands are aligned by simply aligning the reference levels (see Fig. 4.2(a)), which enables a trivial calculation of the valence and conduction band offsets. It is assumed that the reference level is a property of the bulk material. This implies that the band offsets resulting from these models are linear, transitive, and independent of interface orientation. Experimental and theoretical investigations have shown that those simple models are most successful for the description of

non-polar isovalent interfaces, like those found between group-IV elements [137]. However, these methods are often based on simplified models and do not take all mechanisms into account that contribute to the band alignment and therefore can only provide an approximate value for the band alignment. The oldest heterojunction theory is Anderson's electron-affinity rule, which uses the electron affinity[2] as the common reference level [138]. The disadvantage of Anderson's model is that the electron affinity is not a bulk property but strongly depends on the surface structure of the semiconductor. Therefore a number of other models where proposed. Examples of model approaches are the theory by Frensley and Kroemer [139], the charge neutrality level by Tersoff [140], model solid theory [141], and also Jaros' simple analytic model. It is beyond the scope of this work to describe all models in detail. Here, we only focus on the simple analytical model by Jaros and self-consistent first-principle calculations. For a broader overview of band alignment techniques, we refer the reader to the review by Tersoff [142, p. 3ff] as well as the review by Franciosi and Van de Walle [137].

Jaros' Simple Analytical Model

Jaros' derivation starts from the definition of the static dielectric constant of semiconductors. It can be shown that the dielectric constant in first-order perturbation theory expanded in a plane-wave basis $|\mathbf{k}+\mathbf{G}\rangle$ for a static perturbation $\mathrm{e}^{i\mathbf{q}\cdot\mathbf{r}}$ is given by [143]

$$\epsilon(\mathbf{q}) = 1 + \frac{4\pi e^2}{q^2} \sum_{\mathbf{k},\mathbf{G}} \frac{\left|\langle \mathbf{k}|\mathrm{e}^{i\mathbf{q}\cdot\mathbf{r}}|\mathbf{k}+\mathbf{q}+\mathbf{G}\rangle\right|^2 \left[f(\mathbf{k}) - f(\mathbf{k}+\mathbf{q}+\mathbf{G})\right]}{E(\mathbf{k}+\mathbf{q}+\mathbf{G}) - E(\mathbf{k})}, \tag{4.1}$$

where $\mathbf{q}$ is the wavevector of the perturbation, $\mathbf{k}$ is the reduced wavevector, $\mathbf{G}$ the reciprocal lattice vector, and $f(\mathbf{k})$ the occupation number of the state $|\mathbf{k}\rangle$. Considering the case $\mathbf{q} \to 0$, it can be shown that Eq. (4.1) reduces to the much simpler expression [143]

$$\epsilon \approx 1 + \left(\frac{\hbar\omega_\mathrm{p}}{E_\mathrm{g}}\right)^2, \tag{4.2}$$

where ω_p is the plasma frequency given by

$$\omega_\mathrm{p} = \sqrt{\frac{4\pi n e^2}{m_e}}. \tag{4.3}$$

Here, n is the electron density which is given, e. g. , in a zinc-blende lattice by $32/a^3$ where a is the lattice constant. Given the values for the lattice constant and the dielectric constant of a semiconductor (which have been tabulated for many semiconductors for example in Ref. [22]), it is possible to calculate the band-gap E_g. This band-gap is not equal to the fundamental band-gap of the semiconductor, but rather the energy difference between the lowest conduction and the highest valence band of the same $\mathbf{k}$-value averaged over the entire Brillouin zone. Using the nearly-free electron model as a simplified model to understand our semiconductors, this energy gap can also be interpreted as the energy gap found at the edge of the Jones zone [144]. Jaros' key idea to align the energy levels of two semiconductors at an interface is to equate their Fermi energies. In the nearly-free electron model, the Fermi energy lies exactly in

[2] The electron affinity for solids is defined as the energy difference between the vacuum level and the conduction band minimum of the semiconductor.

the middle of the band-gap. The discontinuity of the bands at a heterojunction formed by two semiconductors A and B is, in a first approximation, given by

$$\delta E = [E_{\mathrm{g}}(\mathrm{A}) - E_{\mathrm{g}}(\mathrm{B})]/2. \tag{4.4}$$

Jaros' argues further that the nearly-free electron model better describes the valence than the conduction band. From full band structure calculations, it is known that the lowest conduction band is usually a rapidly varying function of the reduced wavevector. However, this is not reflected in the density of states and therefore large deviation from the average band-gap are expected. Thus, valid predictions of the conduction band offset using Eq. (4.4) are unlikely. In contrast, the highest valence band is usually quite flat. For this reason, Jaros limits his model to make prediction on the valence band discontinuity only:

$$\Delta E_{\mathrm{v}} = [E_{\mathrm{g}}(\mathrm{A}) - E_{\mathrm{g}}(\mathrm{B})]/2. \tag{4.5}$$

This approach is limited by the variation in valence band width between different crystals. This is particularly true for crystals of different ionicity as crystals with a large ionicity usually show a smaller valence band width than a crystal with small ionicity. Therefore, when comparing crystals of different ionicity, the valence band discontinuity is systematically underestimated. This effect is however compensated for crystals of comparable ionicity.

Furthermore, Jaros' method does not take into account differences in the lattice constant. For this reason, the method is only able to calculate the natural VBO. The discussion of the band structure does also not include the effects of spin-orbit splitting, but rather calculates the difference in energy between the barycenter of the HH, LH, and SO band. In order to take into account the spin-orbit interaction on the VBO, it has to be added afterwards for each crystal.

Self-Consistent First-Principles Calculations

Valence Band Offset Calculations Naively, one could think that by knowing the electronic structure of the individual bulk semiconductors and then comparing the calculated energy eigenvalues of either the lowest conduction band or highest valence band states it is possible to determine the CBO ΔE_{c} and the VBO ΔE_{v}. However, due to the long-range nature of the Coulomb force, the average potential in an infinite system is illdefined. Therefore, the band structure calculations of the individual solids cannot provide sufficient information on the band alignment [145].

Thus, a full calculation of the interface is necessary to calculate the band alignment between two semiconductors in a fully self-consistent first-principle approach. Due to the periodic boundary conditions required by many solid-state DFT implementation, this is usually realized by performing a supercell calculation of a single unit cell of a superlattice that consists of alternating slabs of the two semiconductors under investigation. Yet, it is not sufficient to just compare the relative energies of the VBM or the CBM on both sides of the slab to calculate the band offset. The difficulty here is that in order to reduce the computational complexity of the problem, it is best to reduce the slab thickness to a minimum. If the slab thickness is of the order of a few atomic layers, the VBM and CBM will be shifted due to the confinement energy of the charge carriers. As this shift depends on particular aspects of the band structure, it is in general different for both semiconductors. This difficulty can be circumvented by performing two types of calculations (see also Fig. 4.3):

(i) Performing bulk band structure calculations for semiconductor A and B, the energy difference $E_{\mathrm{v,ref}}$ between the VBM and a chosen reference level can be calculated.

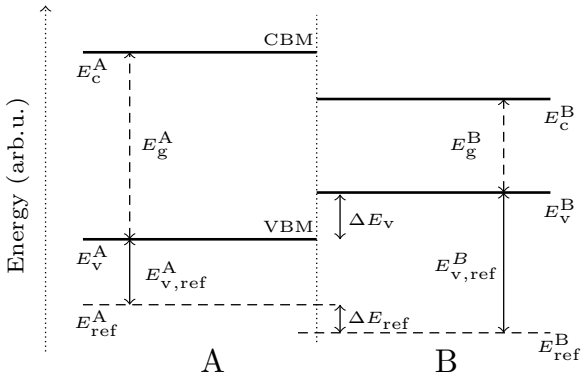

Figure 4.3: *Illustration of the calculation of VBO and CBO between two semiconductors A and B using DFT. The energies E_v indicate the absolute energy of the VBM of each semiconductor. The VBO ΔE_v can be calculated in two steps. In two individual bulk calculations, the energy difference $E_{v,1s}$ between the energy of the VBM E_v and the 1s core energy E_{1s} can be calculated for semiconductors A and B. Using a supercell calculation containing an interface of semiconductor A and B, the energy difference ΔE_{1s} between the energy of the 1s core states on each side of the interface can be calculated. The CBO can be calculated using the calculated VBO ΔE_v and externally provided band-gap energies E_g for each semiconductor. The values of the VBO ΔE_v and the CBO ΔE_c will be equal to the natural VBO and natural CBO, if the lattice constants of semiconductor A and B are identical. Otherwise a strain correction of the values has to be performed.*

(ii) From a band structure calculation of an interface comprising a slab of semiconductor A and B the difference of the reference energy ΔE_{ref} of both semiconductors can be calculated.

Combining the information from both bulk and interface calculation, the VBO between semiconductor A and B is fully determined as

$$\begin{aligned}\Delta E_{\mathrm{v}} &= (E_{\mathrm{v}}^{\mathrm{B}} - E_{\mathrm{ref}}^{\mathrm{B}}) - (E_{\mathrm{v}}^{\mathrm{A}} - E_{\mathrm{ref}}^{\mathrm{A}}) + (E_{\mathrm{ref}}^{\mathrm{B}} - E_{\mathrm{ref}}^{\mathrm{A}}) \\ &\equiv \Delta E_{\mathrm{v,ref}}^{\mathrm{B}} - \Delta E_{\mathrm{v,ref}}^{\mathrm{A}} + \Delta E_{\mathrm{ref}}.\end{aligned} \tag{4.6}$$

The reference level $E_{1\mathrm{s}}^{\mathrm{A/B}}$ has to fulfill two criteria. It must provide an absolute scale for the energy eigenvalues and converge rapidly with slab size. For DFT implementations based on pseudopotentials, this reference level is commonly chosen to be the average electrostatic potential [121, 146]. For all-electron DFT implementations the average electrostatic potential is numerically difficult to calculate due to the singularities around the nuclei. Instead, the 1s core state of the center atom of each slab is commonly used as the reference level [129]. Both the average electrostatic potential and the 1s core state are much less affected by the confinement of the charge carriers in a supercell calculation than the VBM or the CBM energies. As `exciting` is an all-electron DFT implementation, we will use the 1s core state energy as the reference level in our calculations ($E_{\mathrm{ref}} \equiv E_{1\mathrm{s}}$).

In our derivations, we have only considered the calculation of the VBO using DFT. The calculation of the CBO using Kohn-Sham-based DFT proves to be challenging due to the underestimation of band-gap of many semiconductors (see the discussion in Sec. 2.2.4). While the underestimation of the band-gap has significant influence on the calculation of the CBO, it was found that the VBO is often still correct since the valence bands are calculated correctly by the Kohn-Sham-based DFT. For this reason, we only focused on the calculation of the VBO in the following. The CBO is commonly calculated on basis of the VBO with the values of the experimentally measured band-gaps [142, p. 14].

Strain Correction If the lattice constants of semiconductors A and B are approximately equal, the calculated VBO ΔE_{v} will be identical to the natural VBO. If the lattice constants are different, then bulk and supercell calculations described above will be performed at a common lattice constant. This common lattice constant is usually chosen to be the average lattice constant of both semiconductors in order to minimize the maximum strain present in the semiconductors involved in the interface calculation. Rather then the *natural* VBO ΔE_{v}, one obtains the strained VBO $\Delta \overline{E}_{\mathrm{v}}$ from the calculation described above. In order to calculate the natural VBO ΔE_{v}, the effects of strain have to be separate out from the strained VBO $\Delta \overline{E}_{\mathrm{v}}$. This can be done by using absolute deformation potential (ADP). The ADP of the VBM of a semiconductor is defined as the absolute shift of the energy E_{v} of the VBM as a function of relative change in volume of the unit cell:

$$a_{\mathrm{v}} = \frac{\partial E_{\mathrm{v}}}{\partial \ln V}, \tag{4.7}$$

where V is the volume of the unit cell [147]. Using this information, we can calculate the natural VBO by correcting the strained VBO $\Delta \overline{E}_{\mathrm{v}}$ of semiconductors A and B using

$$\Delta E_{\mathrm{v}} = \Delta \overline{E}_{\mathrm{v}} + a_{\mathrm{v}}(\mathrm{A})(\Delta V/V)_{\mathrm{A}} + a_{\mathrm{v}}(\mathrm{B})(\Delta V/V)_{\mathrm{B}}, \tag{4.8}$$

where $a_{\mathrm{v}}(\mathrm{A})$ and $a_{\mathrm{v}}(\mathrm{B})$ are the ADP of the VBM for semiconductor A and B, respectively, and $(\Delta V/V)_{\mathrm{A}}$ and $(\Delta V/V)_{\mathrm{B}}$ is the relative volume change between the equilibrium structure of semiconductors A and B and the average crystal structure used for the interface calculation, respectively.

As for the calculation of the VBO, the difficulty in calculating the ADP of the VBM is that an absolute energy scale is required in order to calculate the absolute shift of the VBM with strain. It was shown that this difficulty can be circumvented by calculating the ADP of a semiconductor in a two step procedure [148]:

(i) Using a bulk band structure calculations, we can calculate the change of the energy difference $E_{\mathrm{v,ref}}$ as a function of relative change in volume of the unit cell. From this, we can determine the deformation potential (DP) of $E_{\mathrm{v,ref}}$ defined as

$$d_{\mathrm{v,ref}} = \frac{\partial E_{\mathrm{v,ref}}}{\partial \ln V}. \tag{4.9}$$

This property is referred to solely as DP, since its calculation does not require an absolute energy scale.

(ii) Through a supercell calculation consisting of alternating slabs of tensile and compressively strained material of the same semiconductor, the absolute shift in energy due to strain of the reference energy E_{ref} can be calculated and with this the ADP a_{ref} of the reference energy

$$a_{\mathrm{ref}} = \frac{\partial E_{\mathrm{ref}}}{\partial \ln V}. \tag{4.10}$$

Taking the results of bulk and supercell calculation together, we can calculate the ADP of the VBM according to:

$$a_{\mathrm{v}} = d_{\mathrm{v,ref}} + a_{\mathrm{ref}}. \tag{4.11}$$

One challenge remains for the calculation of the ADP of the reference level using the supercell approach. Constructing the supercell, we can only stretch or decrease the lattice constant in one direction. Therefore, the calculated ADP of the reference level will only correspond to one specific direction (uniaxial ADP). In order to calculate the unidirectional ADP, uniaxial ADPs for different strain directions need to be calculated and then averaged. The authors of Ref. [149] showed that the uniaxial ADPs $a_{\mathrm{v}}(\hat{r})$ for strain direction $\hat{r}$ can be expanded in terms of lattice harmonics K_ν, which are symmetry-adapted linear combinations of spherical harmonic functions

$$a_{\mathrm{v}}(\hat{r}) = c_0 + \sum_{\nu} c_\nu \, K_\nu(\hat{r}), \tag{4.12}$$

where c_ν are the expansion coefficients of the harmonic functions and c_0 is the direction-independent constant. Using the orthonormal relations of the lattice harmonics, it can be shown that the angular averaged value a_{v} is simply given by c_0. Moreover, for an expansion of the lattice harmonics up to order $l_{\max} = 4$, the angular averaged ADP is given by the weighted average of the uniaxial ADPs of the [100] and [110] strain directions [131]:

$$a_{\mathrm{v}} = c_0 = (4a_{\mathrm{v}}^{[110]} + a_{\mathrm{v}}^{[100]})/5. \tag{4.13}$$

4.2.2 Computational Aspects of DFT: the `exciting` Code

The band-offset calculations presented in this thesis were performed using the DFT method as implemented in the code `exciting`. Before we present the results of our band-structure calculations, we want to take a closer look at `exciting`. In particular, we want to introduce the basis set that is used in the `exciting` code and the related numerical parameters. Furthermore, we take a closer look at the smearing function, which plays an important role in convergence studies.

Basis Set

A common way of classifying DFT implementations is by the basis set in which the electronic wave functions are expanded. Three fundamental classes can be identified: localized orbitals, plane waves, and augmented functions [39]. In implementations based on localized orbitals, the electronic wave function is expanded in functions, e. g. , Gaussians which are centered around the atoms. In the plane-wave approach, in contrast, the valence electrons are represented in a plane-wave basis while the electrons occupying the deeper-lying levels are combined with the nuclei in a so-called pseudopotential term.

The `exciting` code which has been used for the band-structure calculations presented in this thesis, on the other hand, uses augmented plane waves (APW), which falls into the category of augmented functions. The central idea behind APWs is that the space is divided into two regions: The muffin-tin (MT) region around the nuclei and the interstitial (I) region between the nuclei. Different basis functions are used to expand the Kohn-Sham orbitals in the two regions. For a Kohn-Sham orbital of band index i and wavevector $\mathbf{k}$, we can write according to the APW method [150, 151]:

$$\varphi_{i,\mathbf{k}}(\mathbf{r}) = \sum_{\mathbf{G}} c_{i,\mathbf{G}}(\mathbf{k})\, \chi^{\mathrm{APW}}_{\mathbf{k}+\mathbf{G}}(\mathbf{r}), \tag{4.14}$$

where $\{\mathbf{G}\}$ are the reciprocal lattice vectors and $c_{i,\mathbf{G}}$ are the expansion coefficients for the basis function $\chi^{\mathrm{APW}}_{\mathbf{k}+\mathbf{G}}$. The basis functions themselves are given by

$$\chi^{\mathrm{APW}}_{\mathbf{k}+\mathbf{G}}(\mathbf{r}) = \begin{cases} \sum_{lm} A^{\mathbf{k}+\mathbf{G}}_{lm\alpha}\, u_{l\alpha}(r_\alpha)\, Y_{lm}(\hat{\mathbf{r}}_\alpha) & \text{for} \quad r_\alpha \leq R_{\mathrm{MT}} \\ \frac{1}{\sqrt{\Omega}} \mathrm{e}^{i(\mathbf{k}+\mathbf{G})\cdot\mathbf{r}}, & \text{for} \quad \mathbf{r}\,\epsilon\,\mathrm{I}, \end{cases} \tag{4.15}$$

where R_{MT} is the radius of the MT region. Each plane wave in the I region is augmented with an expansion in spherical harmonics $Y_{lm}(\hat{\mathbf{r}}_\alpha)$ and radial functions $u_{l\alpha}(\mathbf{r}_\alpha)$ in the MT region around the nuclei at position $\mathbf{R}_\alpha$ where $\mathbf{r}_\alpha = \mathbf{r} - \mathbf{R}_\alpha$. Within the MT region, the Kohn-Sham potential as introduced in Section 2.2.2 is in good approximation spherically symmetric. The radial function $u_{l\alpha}(\mathbf{r})$ must therefore satisfy the radial Schrödinger equation

$$\left\{ -\frac{\hbar^2}{2m_e}\frac{\mathrm{d}^2}{\mathrm{d}r^2} + \frac{\hbar^2}{2m_e}\frac{l(l+1)}{r^2} + V_0(r) - \epsilon_{i\mathbf{k}} \right\} r\, u_{l\alpha}(r) = 0 \tag{4.16}$$

where the $V_0(r)$ is spherical average of the Kohn-Sham potential $V_{KS}(\mathbf{r})$. After the calculation of $u_{l\alpha}(r)$, the expansion coefficients $A^{\mathbf{k}+\mathbf{G}}_{lm\alpha}$ can be fully obtained using the matching condition of the plane wave and the spherical harmonics at the interface between the I and the MT region. With this, a generalized eigenvalue problem for every $\mathbf{k}$-value can be formulated

$$H^{\mathbf{k}}\, C^{\mathbf{k}} = \epsilon_{\mathbf{k}}\, S^{\mathbf{k}}\, C^{\mathbf{k}}, \tag{4.17}$$

where $C^{\mathbf{k}}$ is the vector of the coefficients defined in Eq. 4.14 and the matrices $H^{\mathbf{k}}$ and $S^{\mathbf{k}}$ are given as

$$\begin{aligned} H^{\mathbf{k}}_{\mathbf{G}\mathbf{G}'} &= \langle \chi^{\mathrm{APW}}_{\mathbf{k}+\mathbf{G}} | -\frac{\hbar^2}{2m_e}\nabla^2 + V_{\mathrm{KS}}(\mathbf{r}) | \chi^{\mathrm{APW}}_{\mathbf{k}+\mathbf{G}'} \rangle, \\ S^{\mathbf{k}}_{\mathbf{G}\mathbf{G}'} &= \langle \chi^{\mathrm{APW}}_{\mathbf{k}+\mathbf{G}} | \chi^{\mathrm{APW}}_{\mathbf{k}+\mathbf{G}'} \rangle. \end{aligned} \tag{4.18}$$

In order to make the problem numerically tractable, the matrix dimensions have to be limited by defining a plane wave cutoff value $|\mathbf{k}+\mathbf{G}| < G_{\max}$. As the muffin-tin radius determines the size of the interstitial region and therefore also influences the number of plane waves required to reach a chosen level of accuracy, it is sensible to define the cutoff using the dimensionless parameter $m_{\mathrm{RG}} = R_{\mathrm{MT}}\, G_{\max}$. Furthermore, the band structure calculation is only calculated for a limited number of $\mathbf{k}$-vectors by defining a $\mathbf{k}$-point grid ($n_{\mathbf{k}} \times n_{\mathbf{k}} \times n_{\mathbf{k}}$) that spans the first Brillouin zone.

At first sight, Eq. (4.18) looks like an ordinary eigenvalue problem that can be solved using standard numerical techniques. However, closer examination of the defining equation for the radial function given in Eq. (4.16) reveals that in order to calculate the radial function, the energy eigenvalues of the generalized eigenvalue equation have to be known. Therefore, the matrices $H^{\mathbf{k}}$ and $S^{\mathbf{k}}$ are energy dependent which leads to a nonlinear eigenvalue problem that is not trivially solvable.

One approach to make Eq. (4.18) linear is to replace the energy eigenvalues $\epsilon_{i\mathbf{k}}$ by a fixed value $\epsilon_{l\alpha}$ for each momentum l of atom α. It can be shown that the difference between the actual energy eigenvalue ϵ and the chosen value $\epsilon_{l\alpha}$ results in an error of the order of $\mathcal{O}(\epsilon_{\alpha l} - \epsilon)$ for the wave functions and band energies and $\mathcal{O}(\epsilon_{\alpha l} - \epsilon)^2$ for the total energies. As a result, the energy parameter $\epsilon_{l\alpha}$ have to almost coincide with the energy ϵ for a reasonably accurate result. However, this does not allow for separate energies values for states with the same l but different principle quantum numbers. Instead of making the approximation $u_{l\alpha}(r_\alpha, \epsilon) \approx u_{l\alpha}(r_\alpha, \epsilon_{l\alpha})$, one can improve on the accuracy by using a Taylor expansion

$$u_{l\alpha}(r_\alpha, \epsilon) \approx u_{l\alpha}(r_\alpha, \epsilon_{l\alpha}) + (\epsilon_{l\alpha} - \epsilon)\, \dot{u}_{l\alpha}(r_\alpha, \epsilon_{l\alpha}). \tag{4.19}$$

where $\dot{u}_{l\alpha}(r_\alpha, \epsilon_{l\alpha}) = \partial u_{l\alpha}(r_\alpha, \epsilon_{l\alpha})/\partial\epsilon$. The energy-dependence in the second term of Eq. (4.19) is not desired, however the Taylor expansion tells us that a more accurate solution of the Kohn-Sham equation can be found by including the energy derivative $\dot{u}_{l\alpha}(\mathbf{r})$ into the search space. This leads to the definition of the linear augmented plane waves (LAPW):

$$\chi^{\mathrm{LAPW}}_{\mathbf{k}+\mathbf{G}}(\mathbf{r}) = \sum_{lm} \left[A^{\mathbf{k}+\mathbf{G}}_{lm\alpha}\; u_{l\alpha}(\mathbf{r}_\alpha, \epsilon_{l\alpha}) + B^{\mathbf{k}+\mathbf{G}}_{lm\alpha}\; \dot{u}_{l\alpha}(\mathbf{r}_\alpha, \epsilon_{l\alpha}) \right] Y_{lm}(\mathbf{r}_\alpha) \tag{4.20}$$

The coefficients $A^{\mathbf{k}+\mathbf{G}}_{lm\alpha}$ and $B^{\mathbf{k}+\mathbf{G}}_{lm\alpha}$ are, similar to the the APW definition, determined through the matching condition of $\chi^{\mathrm{LAPW}}_{\mathbf{k}+\mathbf{G}}(\mathbf{r})$ at the boundary between MT and I region. Although this definition of $A^{\mathbf{k}+\mathbf{G}}_{lm\alpha}$ and $B^{\mathbf{k}+\mathbf{G}}_{lm\alpha}$ does not establish a clear relationship between Eq. (4.19) and Eq. (4.20), it can be shown [150] that the error on the band and total energy behaves as $\mathcal{O}(\epsilon_{l\alpha} - \epsilon)^2$ and $\mathcal{O}(\epsilon_{l\alpha} - \epsilon)^4$, respectively.

Even though the LAPW method shows an improvement over the APW method with fixed energy values, the constraints on the coefficients $A^{\mathbf{k}+\mathbf{G}}_{lm\alpha}$ and $B^{\mathbf{k}+\mathbf{G}}_{lm\alpha}$ reduces the linear space in which solutions can be searched for. An alternative approach to linearize the APW was introduced in [152]. The authors proposed to add local orbitals (lo) to the APW with

frozen energy in order to increase the flexibility of the function space which are defined as

$$\phi_\mu = \begin{cases} \delta_{\alpha\alpha_\mu}\delta_{ll_\mu}\delta_{mm_\mu}\left[a_\mu\, u_{l\alpha}(\mathbf{r}_\alpha,\epsilon_{l\alpha}) + b_\mu\, \dot{u}_{l\alpha}(\mathbf{r}_\alpha,\epsilon_{l\alpha})\right], & r_\alpha \leq R_{\mathrm{MT}} \\ 0, & \mathbf{r}\epsilon\ \mathrm{I}. \end{cases} \tag{4.21}$$

These functions are required to be non-zero only inside the MT region. It can be shown that the total wave function represented in the APW+lo basis within the MT region of atom α is then given as

$$\phi_{i\mathbf{k}} = \sum_{lm}\left[c_{lm}^{i\mathbf{k}}\, u_{l\alpha}(\mathbf{r}_\alpha,\epsilon_{l\alpha}) + d_{lm\alpha}^{i\mathbf{k}}\, \dot{u}_{l\alpha}(\mathbf{r}_\alpha,\epsilon_{l\alpha})\right] Y_{lm}(\mathbf{r}_\alpha). \tag{4.22}$$

This expression looks similar to the LAPW expression. However, due to the additional requirement of the smoothness at the boundary, the LAPW basis is less flexible compared to the APW+lo basis. This has proven to be particularly useful when describing semicore states, which are located in the MT and I region.

The `exciting` code supports an even wider range of basis sets belonging to the family of LAPW methods than described above. In this work, we restrict ourselves to the APW, APW(+lo), and LAPW(+lo) basis sets. The combination in which they are used as well as the frozen energy parameters are defined for every crystal in form of an XML file. In App. A, we included the XML files for Si, Ge, and Sn that were used for the calculations presented within this thesis.

Methfessel-Paxton Smearing Function

The materials that we want to investigate are semiconductors. However, as we have already pointed out in Chap. 2, the band-gaps of semiconductors are often underestimated due to the shortcomings of LDA. As we will discuss shortly, this is also true for Ge and Sn. As a result, the band structure of those materials resembles those of semi-metals or metals with partially occupied bands. The calculation of many band structure related properties, like the total energy, require an integration of a given function over the Brillouin zone. For metals, due to the partial occupation of bands and the steplike behavior of the Fermi-Dirac distribution at zero temperature, the integrand is discontinuous and therefore requires a very fine mesh of **k**-points inside the Brillouin zone. In order to remove the discontinuity, it is desirable to smear out the occupation of states around the Fermi surface. This can be achieved by using the Fermi-Dirac distribution with temperatures larger than zero. However, using the Fermi-Dirac distribution as a smearing function introduces an error in the integration as is depicted schematically in Fig. 4.4(a). A more sophisticated choice is the smearing function proposed by Methfessel and Paxton [153]. The derivative of the step-function is the δ-function. Methfessel and Paxton derived an approximated $D_N(x)$ to the δ-function based on Hermite polynomials $H_n(x)$ up to order N. Integrating the approximated δ-function accordingly, an approximation S_N to the step-function can be found, which is given by

$$\begin{aligned} S_0(x) &= \frac{1}{2}\left[1 - \mathrm{erf}(x)\right], \\ S_N(x) &= S_0(x) + \sum_{n=1}^{N} A_n\, H_{2n-1}(x)\, \mathrm{e}^{-x^2}, \end{aligned} \tag{4.23}$$

where the factors A_n are defined as $A_n = (-1)^n/(4^n n!\sqrt{\pi})$. It can be shown that replacing the step-function with S_N does not lead to significant errors if the function that one wants to

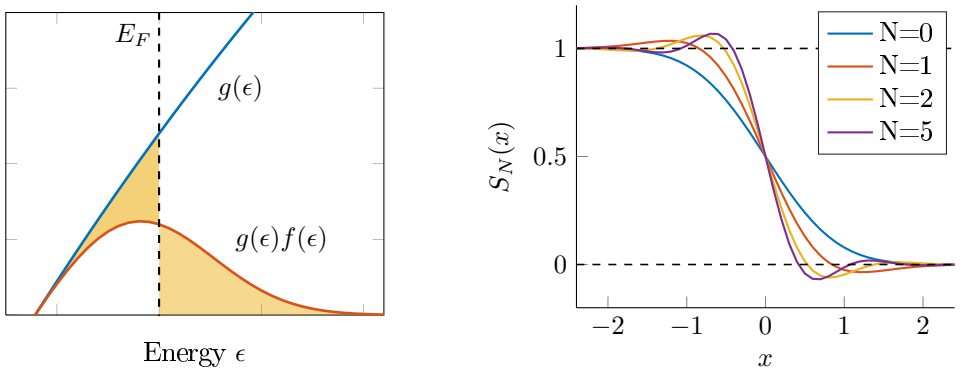

(a) Integration Error **(b)** Methfessel-Paxton Function

Figure 4.4: *(a) Depiction of the integration error: Function $g(\epsilon)$ and its production with the Fermi-function $f(\epsilon)$ at a temperature $T > 0$ shown for different energies around the Fermi energy E_F. The yellow area below and above the Fermi energy E_F are not equal in size. (b) Methfessel-Paxton function S_N for different orders N. The zeroth order is equivalent to a Fermi function for temperatures $T > 0$. Higher order Methfessel-Paxton functions can produce occupation numbers, which are larger than one or negative.*

integrate can be represented as a polynomial of degree $2N$ or less in the range where $S_N(x) - S(x)$ is appreciably non-zero. Note, that the zeroth order corresponds to a simple Fermi-Dirac-like smearing. The width of the smearing can be influenced by introducing a scaling factor ϵ_s such that $x = \epsilon/\epsilon_s$. In general, it can be said that the higher the density of **k**-point grid, the smaller is the required ϵ_s parameter.

A peculiarity of the Methfessel-Paxton approach is that occupation numbers larger than one as well as negative occupation numbers can be introduced, which result in an unphysical description of the system (see Fig. 4.4(b)).

For all calculation presented in this work, we use the Methfessel-Paxton approach of order $N = 2$. The smearing is always given in units of the Hartree energy (hartree).

4.3 Bulk Semiconductors

The initial step in the calculation of the band alignment is the calculation of the bulk band structure of the pure semiconductors Si, Ge, and Sn. We will perform this in two steps. First, we conduct convergence studies in order to determine the values for the numerical parameters of the APW method that generate reliable results. Then, using the determined values for the numerical parameters, we calculate the bulk material properties that are important for the band alignment and discuss them in detail.

4.3.1 Convergence Studies

The quantity we are most interested in for the calculation of the band alignment is the energy difference $E_{v,1s}$ between the VBM and the 1s core state for each semiconductor. Convergence studies of this quantity were performed with respect to the basis set parameter m_{RG}, the number of **k**-points per dimension $n_{\mathbf{k}}$, and the smearing width ϵ_s. For the plane wave cut-off

value $G_{\max}$, we used the value 12.0 that has been used for previous studies.

We first analyzed the convergence behavior varying the basis set parameter m_{RG} and the number of **k**-points per dimension $n_{\mathbf{k}}$ in the interval [5.0,9.0] and [4,20], respectively, while keeping the smearing parameter ϵ_{s} at a constant value of $0.001\,E_{\mathrm{h}}$. The results of this calculation are shown in Figs. 4.5(a), 4.6(a), and 4.7(a) for Si, Ge, and Sn, respectively. We expect the computation performed with the highest values for m_{RG} and $n_{\mathbf{k}}$ to be most accurate. For this reason, we define the convergence error E_{conv} to be the difference between $E_{\mathrm{v,1s}}$ calculated with each parameter combination and the most accurate calculation performed with $(m_{\mathrm{RG}}, n_{\mathbf{k}}) = (9.0, 20)$. From the figures, it can be seen that to achieve an accuracy in the order of 1 meV, m_{RG} has to be set to 9.0 while $n_{\mathbf{k}}$ has to be at least 10. Furthermore, we see a qualitative difference in the convergence behavior between Si, on the one hand side, and Ge and Sn, on the other hand side. While Si shows convergence in the order of 10 meV even for values of m_{RG} below 9.0, the convergence error E_{conv} for Ge and Sn will still be in the order of 1 eV if m_{RG} is below 9.0. We will come back to this point when discussing the band structure of Si, Ge, and Sn.

In a second convergence study, the number of **k**-points per dimension $n_{\mathbf{k}}$ and smearing parameter ϵ_{s} were varied in the interval [4,20] and [$0.001\,E_{\mathrm{h}}$,$0.100\,E_{\mathrm{h}}$] while basis set parameter m_{RG} was set constant to a value of 9.0. The results for Si, Ge, and Sn are shown in Fig. 4.5(b), 4.6(b), and 4.7(b), respectively. For this combination of parameters, we expect the computation performed with the highest number of **k**-points $n_{\mathbf{k}}$ and the smallest smearing parameter ϵ_{s} to be most accurate. Therefore, we define the convergence error E_{conv} to correspond to the energy difference relative to the calculation performed with $(n_{\mathbf{k}}, \epsilon_{\mathrm{s}}) = (20, 0.001\,E_{\mathrm{h}})$. The results of this calculation are shown in Figs. 4.5(b), 4.6(b), and 4.7(b) for Si, Ge, and Sn, respectively. We find that for $n_{\mathbf{k}}$ set to 10 and ϵ_{s} set to $0.001\,E_{\mathrm{h}}$, the convergence error E_{conv} is in the order of 1 meV. In addition, we again find a qualitative difference in the convergence behavior between Si, on the one hand side, and Ge and Sn, on the other hand side. While the convergence error E_{conv} is identical for ϵ_{s} set to $0.001\,E_{\mathrm{h}}$ and $0.010\,E_{\mathrm{h}}$ for Si, the values of $E_{\mathrm{v,ref}}$ calculated with ϵ_{s} set to $0.010\,E_{\mathrm{h}}$ and $0.001\,E_{\mathrm{h}}$ differ for small number of **k**-points $n_{\mathbf{k}}$ for Ge and Sn. Again, we will later see that this difference in convergence behavior between Si, Ge and Sn is directly related to the band structure of the semiconductors. Furthermore, we want to point out that the convergence error E_{conv} for $\epsilon_{\mathrm{s}} = 0.100\,E_{\mathrm{h}}$ remains at a value of roughly -20 meV independent of the number of **k**-points.

Besides the convergence behavior of the energy difference $E_{\mathrm{v,1s}}$ between VBM and 1s core level, the convergence behavior of the fundamental band-gaps E_{g} was analyzed as well in order to estimate the convergence error on the remaining part of the band structure. We find that the convergence behavior of the fundamental band-gap E_{g} follows that of the difference $E_{\mathrm{v,1s}}$ between VBM and 1s core state for each semiconductor. For this reason, we limit our discuss to the results for Si only (see in Figs. 4.5(c) and 4.5(d)). In Fig. 4.5(c), as before, the basis set parameter m_{RG} and number of **k**-points per dimension $n_{\mathbf{k}}$ are varied in the interval [5.0,9.0] and [4,20], respectively, while keeping fixed at $\epsilon_{\mathrm{s}} = 0.001\,E_{\mathrm{h}}$. We define the convergence error E_{conv} as the difference in band-gap energy E_{g} with respect to the most accurate calculation performed with $(m_{\mathrm{RG}}, n_{\mathbf{k}}, \epsilon_{\mathrm{s}}) = (9.0, 20, 0.001\,E_{\mathrm{h}})$. We find that for an accuracy on the order of 1 meV or below, the basis set parameter m_{RG} must be set to a value of at least 8.0 and the number of **k**-points per dimension $n_{\mathbf{k}}$ to larger than 8. In Fig. 4.5(d), the same convergence study is performed now with the basis parameter m_{RG} set to 9.0 and the number of **k**-points per dimension $n_{\mathbf{k}}$ and the smearing width ϵ_{s} varied in the interval [4,20] and [$0.001\,E_{\mathrm{h}}$,$0.100\,E_{\mathrm{h}}$], respectively. We find that for $n_{\mathbf{k}}$ set to 10 and ϵ_{s} set to $0.001\,E_{\mathrm{h}}$, the convergence error E_{conv} is in the order of 1 meV. Moreover, for ϵ_{s} set to $0.100\,E_{\mathrm{h}}$, the convergence error E_{conv} is

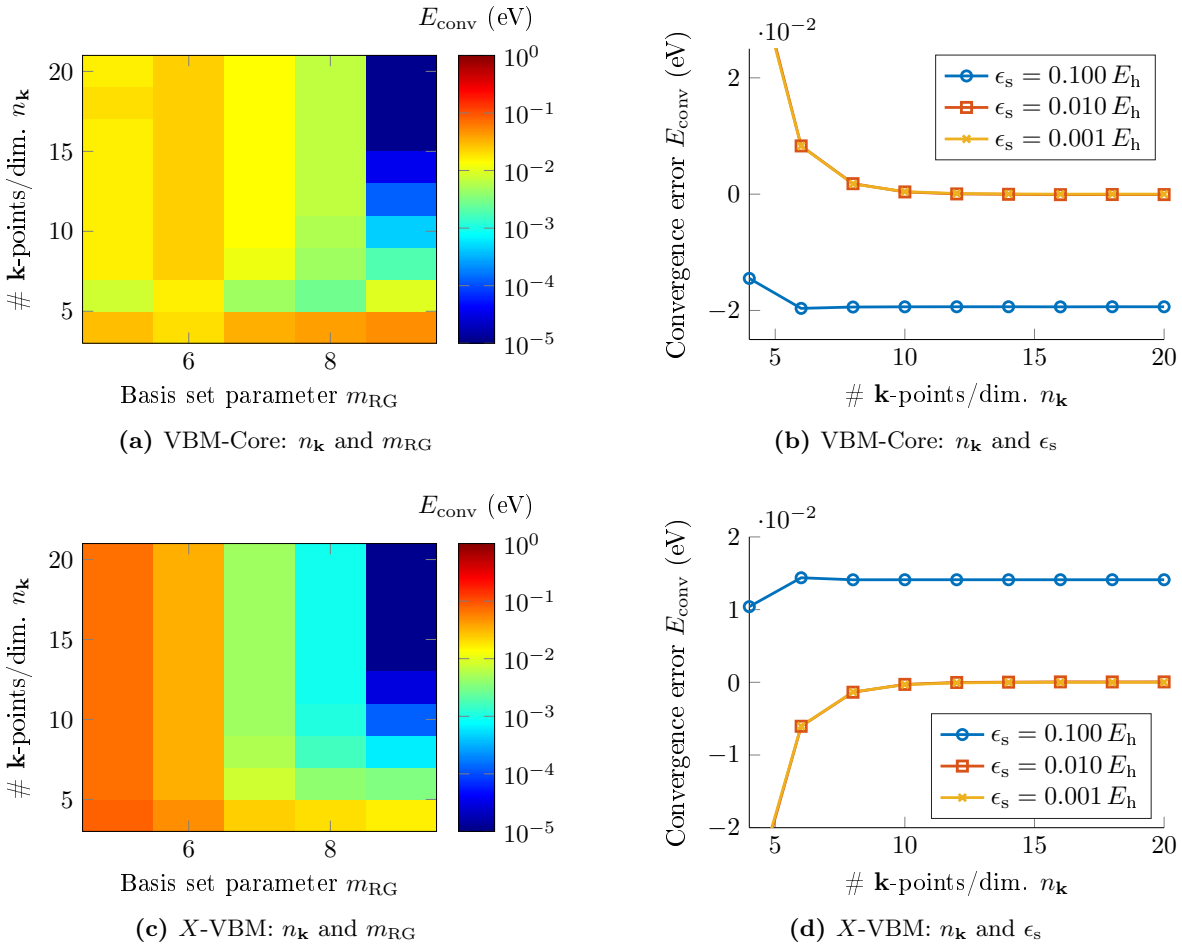

(a) VBM-Core: $n_{\mathbf{k}}$ and m_{RG}

(b) VBM-Core: $n_{\mathbf{k}}$ and ϵ_{s}

(c) X-VBM: $n_{\mathbf{k}}$ and m_{RG}

(d) X-VBM: $n_{\mathbf{k}}$ and ϵ_{s}

Figure 4.5: *Convergence study for the the energy difference between VBM and 1s core state at the* Γ*-point for Si as a function of (a) the number of* **k***-points per dimension* $n_{\mathbf{k}}$ *and basis-set parameter* m_{RG} *with* $\epsilon_{\text{s}} = 0.001\,E_{\text{h}}$ *and (b) the number of* **k***-points per dimension* $n_{\mathbf{k}}$ *and the smearing parameter* ϵ_{s} *with* $m_{\text{RG}} = 9.0$*. The convergence error* E_{conv} *is calculated with respect to the energy calculated with* $(m_{\text{RG}}, n_{\mathbf{k}}, \epsilon_{\text{s}}) = (9, 20, 0.001\,E_{\text{h}})$*. Analogous graphs (c) and (d) for the* X*-related band-gap.*

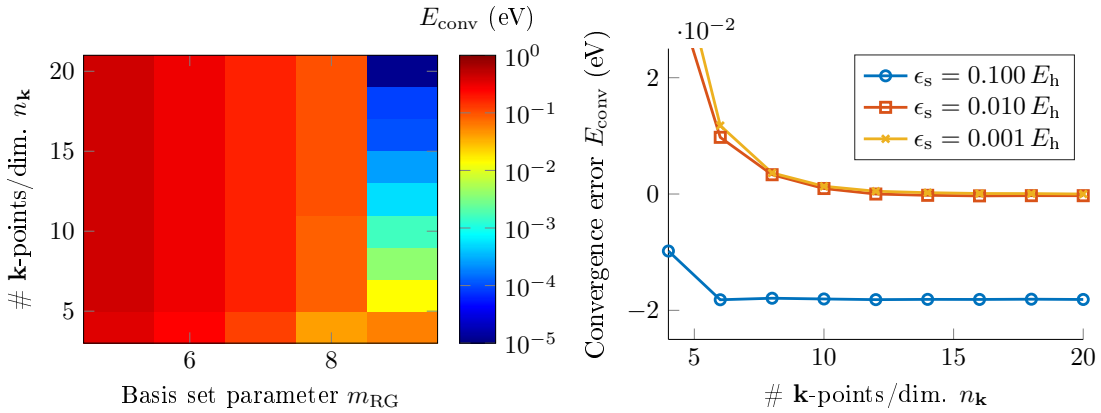

(a) VBM-Core: $n_{\mathbf{k}}$ and m_{RG} **(b)** VBM-Core: $n_{\mathbf{k}}$ and ϵ_{s}

Figure 4.6: *Convergence study for energy difference between VBM and 1s core state at the Γ-point for Ge as a function of (a) the number of* **k***-points per dimension* $n_{\mathbf{k}}$ *and the basis set parameter* m_{RG} *with* $\epsilon_{\mathrm{s}} = 0.001\,E_{\mathrm{h}}$ *and (b) the number of* **k***-points per dimension* $n_{\mathbf{k}}$ *and the smearing parameter* ϵ_{s} *with* $m_{\mathrm{RG}} = 9.0$*. The convergence error* E_{conv} *is calculated with respect to the energy calculated with the* $(m_{\mathrm{RG}}, n_{\mathbf{k}}, \epsilon_{\mathrm{s}}) = (9, 20, 0.001\,E_{\mathrm{h}})$*.*

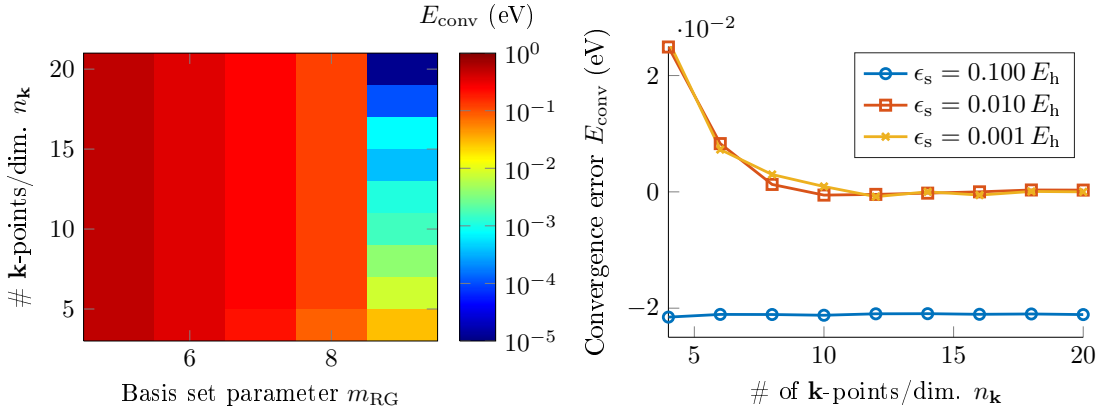

(a) VBM-Core: `ngridk` and `rgkmax` **(b)** VBM-Core: `ngridk` and `swidth`

Figure 4.7: *Convergence study for energy difference between VBM and 1s core state at the Γ-point for Sn as a function of (a)* $n_{\mathbf{k}}$ *and* m_{RG} *parameters with* $\epsilon_{\mathrm{s}} = 0.001\,E_{\mathrm{h}}$ *and (b)* $n_{\mathbf{k}}$ *and* ϵ_{s} *with* $m_{\mathrm{RG}} = 9.0$*. The convergence error* E_{conv} *is calculated with respect to the energy calculated with the* $(m_{\mathrm{RG}}, n_{\mathbf{k}}, \epsilon_{\mathrm{s}}) = (9, 20, 0.001)$*.*

independent of the **k**-point density for large values of $n_{\mathbf{k}}$ and remains constant at a value of roughly 15 meV.

Concluding our investigations of the convergence behavior, we find that using the parameters $(m_{\mathrm{RG}}, n_{\mathbf{k}}, \epsilon_{\mathrm{s}}) = (9, 10, 0.001\, E_{\mathrm{h}})$ the energy differences between different bands of the band structure are converged to roughly 1 meV or better for all semiconductors. Furthermore, we find that using the smearing parameter that is too large, i. e. , larger than $0.010\, E_{\mathrm{h}}$, leads to a shift of the energy bands.

4.3.2 Bulk properties

In the following, we investigate the bulk band structure of the semiconductors Si, Ge, and Sn in more detail. In particular, we are interested in the size of their fundamental band-gaps. This will be of particular importance for the interpretation of the interface calculations later. Furthermore, we investigate the lattice constants of the materials using the volume optimization functionality of `exciting`. These are required for the investigation of the effects of strain on the VBO that we will perform later. For all calculations, we will use the parameters $(m_{\mathrm{RG}}, n_{\mathbf{k}}, \epsilon_{\mathrm{s}}) = (9, 10, 0.001\, E_{\mathrm{h}})$.

In Figs. 4.8(a), 4.8(b), and 4.8(c), the bulk band structure of Si, Ge, and Sn are shown, respectively. First of all, we want to point out that for these calculations as well as all following calculations spin-orbit coupling was neglected in order to achieve lower computation times. As a result, the heavy hole (HH), light hole (LH), and split-off hole (SO) are degenerate. While this does not have a strong effect for the band structure of Si, for which the spin-orbit splitting is fairly small ($\Delta_{\mathrm{SO}} = 44$ meV), it is noticeable for Ge where the spin-orbit splitting is on the order of 300 meV. Similarly, for Sn the conduction band lying below the VBM is degenerate with the HH and therefore the negative band-gap is not visible. Nevertheless, this is expected to have no influence on the calculation of the VBO [154]. As is common practice, we will introduce the effects of spin-orbit coupling as a post-processing step to our band-structure calculations by shifting the VBM by 1/3 of the experimentally measured spin-orbit splitting Δ_{SO} to higher energies.

Furthermore, in all band structures we can observe the drawback of the Kohn-Sham approach to DFT in combination with the LDA: The underestimation of the fundamental band-gaps of semiconductors. For silicon, we find a value of 0.46 eV for the fundamental band-gap which stands in stark contrast to the experimentally reported value of 1.17 eV for the case of low temperatures [22]. The situation is even more drastic for the case of Ge and Sn. For Ge, the difference between the lowest conduction band at the L-point and the VBM, the fundamental band-gap, is reported to be 0.74 eV in the low temperature regime [22]. The LDA calculation, however, achieves a zero-band-gap at the Γ-point. Furthermore, the lowest conduction band at the L-point is higher than the CBM at the Γ-point, indicating not only an underestimation of the band-gap size but also an incorrect band ordering. For Sn, the LDA calculation predicts a zero-band-gap at the Γ-point in agreement with experimental observation [22]. However, the lowest conduction band at the L-point is predicted to lie below the VBM, turning Sn into a metal. This is why we observe a difference in the convergence behavior of Ge and Sn with respect to Si in Sec. 4.3.1. Due to the metallic character of Ge and Sn, choosing an intermediate value for the smearing parameter ϵ_{s} leads to a faster convergence of the relative band structure energies with respect to the number of **k**-points per dimensions $n_{\mathbf{k}}$ than choosing a small value for ϵ_{s}. Moreover, a larger basis set parameter m_{RG} is required in order to describe the band structure of these semiconductors.

Even though using the Kohn-Sham-based DFT in combination with LDA leads to under-

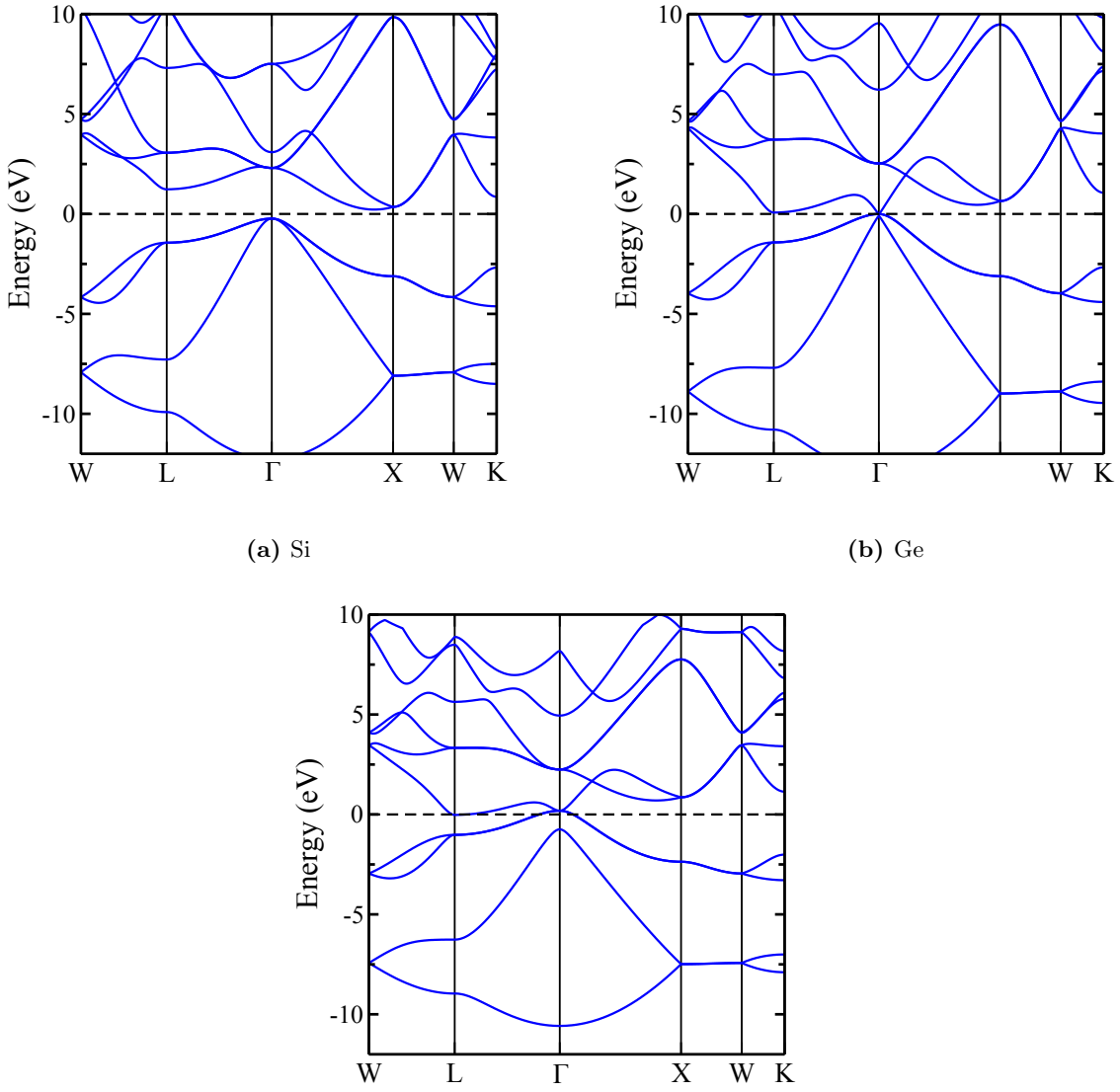

(a) Si

(b) Ge

(c) Sn

Figure 4.8: *Bulk band structure of Si, Ge, and Sn as calculated by the* `exciting` *code using LDA. The dashed line indicates the Fermi energy. Spin-orbit coupling has been neglected for computational efficiency. The fundamental band-gaps are underestimated for Si, Ge, and Sn. While Si remains a semiconductor in the LDA calculations, Ge turns into a semimetal and Sn into a metal.*

Table 4.1: *Lattice parameter for Si, Ge, and Sn as calculated with* `exciting`*. Given in parentheses are the experimentally measured lattice constants [22]. The relative difference between calculated and measured lattice constants is less than 1 %.*

	Si	Ge	Sn
Lattice Constant (Å)	5.409 (5.431)	5.639 (5.659)	6.487 (6.489)

estimated band-gaps and an incorrect band ordering of the conduction bands, it is still assumed that the band alignment is correct if the alignment of the VBM is calculated. Therefore, we continue with our calculation of the band alignment focusing on the alignment of the VBM only.

In Tab. 4.1, the lattice constants as calculated with `exciting` are shown together with those measured experimentally. The lattice constant of Sn as calculated by DFT is just 0.002 Å smaller than the experimentally determined value. This discrepancy is larger for Si and Ge. For those, our DFT calculations underestimate the lattice constant by roughly 0.02 Å. Nevertheless, this results only in a relative error of less than 1 %. Therefore, the relative differences between the lattice constants of the three materials are approximately those observed in experiment, which is important for the interface and strain calculations presented in the following. For those, we will use the lattice constants as calculated by DFT.

4.4 Interface Calculations

In order to calculate the band alignment between Si, Ge, and Sn, we perform a supercell calculation of the interface between Si and Ge as well as a supercell calculation of the interface between Ge and Sn. This combination of materials reduces the amount of strain experienced by the different semiconductors on both sides of the interface. Assuming transitivity for the band alignment of the three materials, which is commonly observed in nonpolar isovalent heterojunctions [142], these two calculations fully determine the band alignment of all three semiconductors.

Earlier studies suggest that the band alignment for nonpolar isovalent heterojunctions also do only depend weakly on the interface orientations. For the case of SiGe, the authors of Ref. [120] found a difference in the band alignment between the (001) and (111) interface orientation of 40 meV. In order to reduce the computational complexity of the problem, we limit ourselves to the calculation of the (001) interface. In general, also the structural relaxation of the atoms close to the interface affects the VBO. As this is also found to be of marginal influence for the SiGe interface, we neglect this effect and perform all our calculations on an ideal diamond lattice.

In constructing the supercell, we follow Li [129] and set up the interface calculation for two semiconductors A and B with a supercell containing the unit cell of a $(\mathrm{A})_n(\mathrm{B})_n$ superlattice, where n describes the number of atomic layers in each slab. If the lattice constants of the two elements A and B differ from each other, as it is the case for combinations between Si, Ge, and Sn, we compress the crystal with the larger lattice constant and expand the crystal with the smaller lattice constant in order to form a crystal with a lattice constant equal to the arithmetic average of both elements (see Fig. 4.9).

We start our discussion of the interface calculation with an examination of the convergence behavior as a function of the number of atomic layers per slab n and the smearing parameter ϵ_s. Then we discuss electronic properties of the interface, and at the end attempt to calculate the band alignment between the VBM of the elementary semiconductors. Results for the SiGe and GeSn interfaces will be presented side-by-side. As stated above, the SiGe interface has already been well researched. Therefore, it will serve as a reference point for the calculation of the GeSn interface.

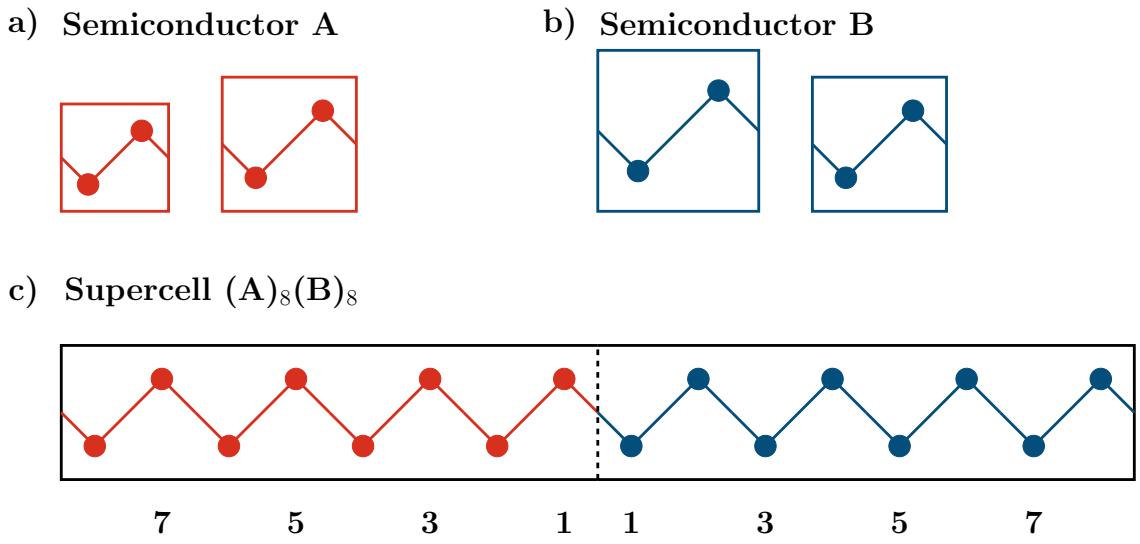

Figure 4.9: *Illustration of a supercell construction. (a) and (b) show the unitcell of two semiconductors A and B with two atoms each. The semiconductors feature different lattice constants. The first step in constructing a supercell is to expand, respectively, shrink the unitcell of the semiconductors to match the average lattice constant of both. Then, the supercell containing a slab of semiconductor A and semiconductor B is constructed by concatenating a selected number of unitcells. Shown here is a* $(A)_8(B)_8$ *supercell with* $n = 8$ *atomic layers per slab. When referring to particular layers within the supercell, we use the numbering scheme displayed below the supercell. Periodic boundary conditions are applied to both unitcell and supercell calculation. The supercell corresponds to the unitcell of a superlattice.*

4.4.1 Convergence: Number of Atomic Layers and Smearing

The quantity of interest in our calculations is the energy difference ΔE_{1s} between the 1s core state energies of the innermost atoms inside the slab on each side of the interface. In order to verify that the value we are calculating is bulklike, i. e. that it does not significantly change when we increase the thickness of the slabs inside the supercell, we performed convergence studies. For this, the difference in the 1s core states was calculated for slab sizes n ranging from 4 to 20 atomic layers. Furthermore, we investigated how the broadening of the smoothing function affects the offset between the core states by varying the smearing parameter ϵ_s from $0.001\,E_h$ to $0.100\,E_h$. The results of these calculations are shown for both the SiGe and GeSn interface in Fig. 4.10. Here, the convergence error E_{conv} is defined as the difference between the value of ΔE_{1s} calculated with n atomic layers per slab and $n+4$ atomic layers. We would like to reach a convergence error on the order of 1 meV which is indicated by the dashed line.

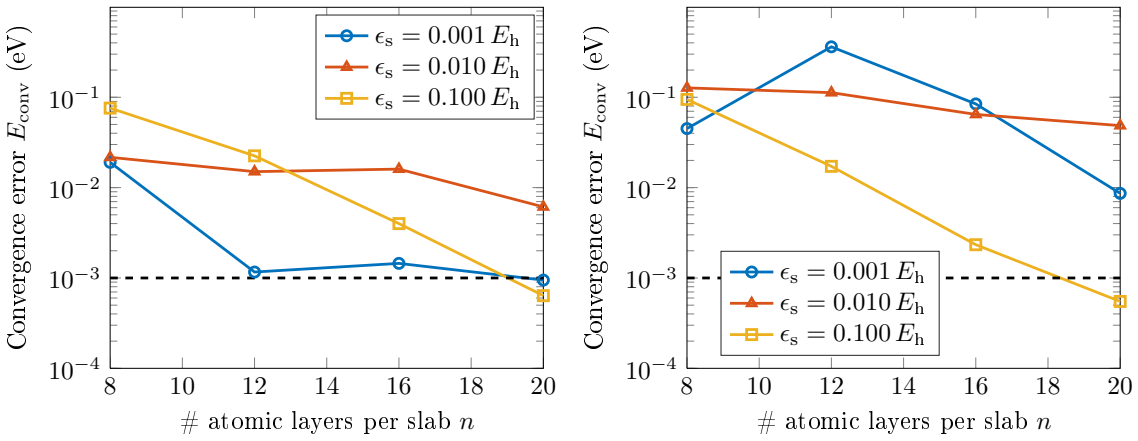

(a) SiGe **(b)** GeSn

Figure 4.10: *Convergence error E_{conv} of the energy difference between the 1s core state energies ΔE_{1s} on each side of the interface as a function of the number of atomic layers per slab n for (a) the SiGe interface and (b) the GeSn interface. The convergence error E_{conv} is defined as the difference between the value of ΔE_{1s} calculated with n atomic layers per slab and $n+4$ atomic layers. Lines are guides to the eye only. The target convergence error is indicated by the dashed line.*

We find the convergence behavior as a function of slab thickness and broadening of the smoothing function to be quite complex. However, comparing the results for the SiGe and the GeSn interface, we find two similarities:

- Setting $\epsilon_s = 0.100\,E_h$ (yellow squares), the convergence error shows an exponential decrease with slab thickness with a value in the order of 3 meV for a slab thickness of 16 atomic layers and below 1 meV for 20 atomic layers.

- For $\epsilon_s = 0.010\,E_h$ (red triangles), the convergence error is almost constant, i. e. independent of slab thickness, with a value between 10 meV and 100 meV.

However, a fundamental difference can also be observed:

- Setting $\epsilon_s = 0.001\,E_h$ (blue circles), we find that the convergence error decreases from approximately 10 meV to 1 meV for the SiGe interface when the slab thickness is increased from 8 to 12 atomic layers and then stays around the latter value even for larger slab sizes. For the GeSn interface, the convergence error first increases from 50 meV to above 100 meV when going from 8 to 12 atomic layers. Increasing the slab size even further reduces the convergence error. However, even for a slab thickness of 20 atomic layers, it is still around 10 meV.

Thus, we find that the SiGe and GeSn interface calculations behave similar in terms of convergence when the smearing parameter is large. If the broadening is chosen to be small, the converge error of the SiGe interface decreases very quickly, while the GeSn calculations do not reach our convergence target even for the largest slab thickness used. These difference can be understood, when discussing the electronic interface properties as done in the next section.

Electronic Interface Properties

The results presented here were calculated with $n = 16$ atomic layers per slab and $\epsilon_s = 0.001\,E_h$ for the SiGe interface and $\epsilon_s = 0.100\,E_h$ for the GeSn interface resulting in a convergence error in the order of a few meV for the alignment of the core states.

In Fig. 4.11, the layer-projected density of states (PDOS) is shown for the SiGe interface for the atomic layers {1, 3, 5, 7, 9} of the Si and Ge slab[3]. We see that for layer 1, which is closest to the interface, the PDOS inside the Si and Ge slab are almost identical. Moving further into the middle of the slabs, the PDOS become more bulklike developing characteristic features like the peak at 3 eV for Si. Comparing the PDOS of layers 7 and 9 inside one slab, we find that they are almost identical, which indicates that the electronic properties within the middle of each slab are indeed bulklike.

Investigating layer 1 more closely, we find a band-gap of approximately 270 eV on both the Si and the Ge side without any indications for mid-gap states. This is in agreement with our expectation as the bonds formed between Si and Ge atoms closest to the interface are isovalent, i. e. no dangling bonds are present. Inspecting the PDOS of the central layers, we find a band-gap of approximately 440 eV (540 eV) for the Si (Ge) slab. Comparing this to their respective bulk values of 0.47 eV (0.00 eV), we find that the band-gap inside the Si slab is slightly decreased while the band-gap inside the Ge slab is increased. This is a result of the strain present within both the Si and Ge layer. While the lattice constant inside the Si slab is larger than its equilibrium value, which leads to a smaller band-gap, the lattice constant in the Ge slab is smaller, which leads to a larger band-gap. In addition, we find that the valence band is slightly higher inside the Ge slab, while the conduction band is lower inside the Si slab. This leads to a confinement of electrons (holes) inside the Si (Ge) slab, which partially compensates the decrease of the band-gap inside the Si slab, while it aggravates the increase of the band-gap inside the Ge slab.

The picture is different for the GeSn interface (see Fig. 4.12). Again, we see that for the layers closest to the interface, the PDOS is almost identical for the Ge and the Sn slab, while the PDOS becomes more bulklike towards the middle of the slab. Investigating the band-gap in the central atomic layer of each slab, we find a band-gap of approximately 50 eV inside the Sn slab, whereas no band-gap is present in the center of the Ge slab. This is again the results of strain inside the slabs. Due to the compressive strain inside the Sn slab, the band-gap is now larger than for the case of the bulk crystal at its equilibrium lattice constant. The Ge slab, in

[3] See Fig. 4.9 for a definition of the numbering scheme of the atomic layers inside the supercell.

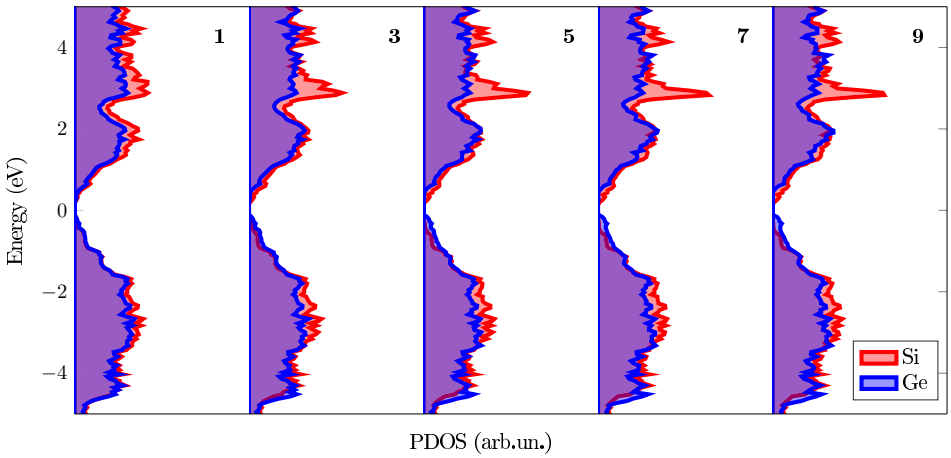

Figure 4.11: *PDOS for selected layers inside the Si (red) and Ge (blue) slab of the SiGe supercell. The numbering of the layers follows Fig. 4.9, i. e. layer number 1 corresponds to the layer closest to the interface while layer 9 is situated in the middle of the slab. A band-gap can be identified for both the Si and the Ge layers.*

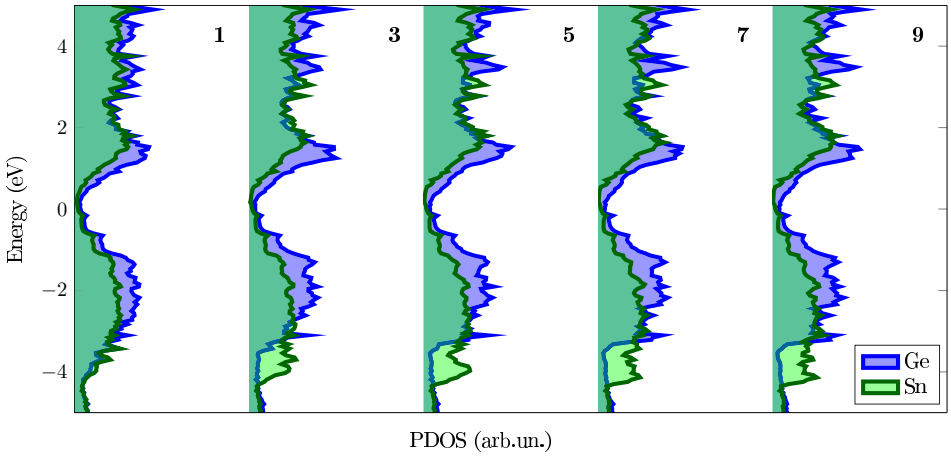

Figure 4.12: *PDOS for selected layers inside the Ge (blue) and Sn (green) slab of the GeSn supercell. The numbering of the layers follows Fig. 4.9, i. e. layer number 1 corresponds to the layer closest to the interface while layer 9 is situated in the middle of the slab. While a band-gap can be identified for the Sn layers, the PDOS of the Ge layers indicates no band-gap.*

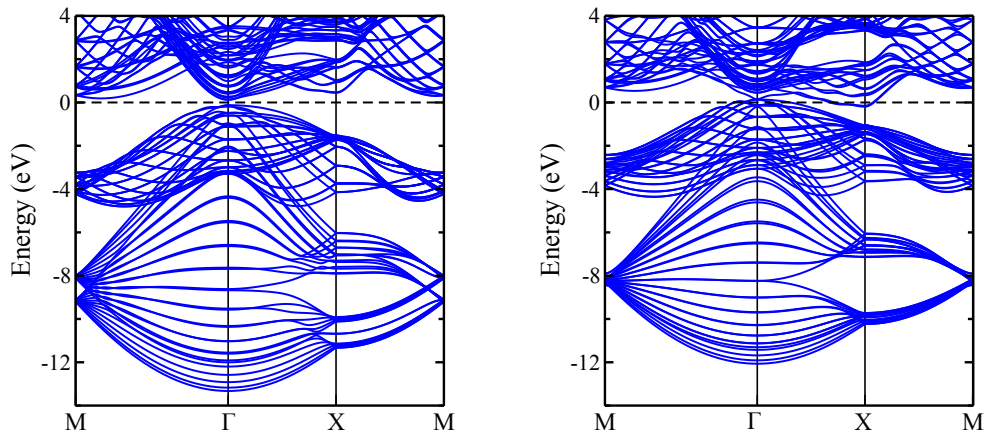

(a) SiGe **(b)** GeSn

Figure 4.13: *2D band structure of (a) the SiGe interface and (b) the GeSn interface. The Fermi energy is indicated by the dashed line. While for the SiGe interface a band-gap is clearly visible, for the GeSn interface the conduction and valence bands overlap.*

comparison, is tensile strained. While we find a zero band-gap for the Ge bulk calculations, conduction and valence bands now overlap due to the tensile strain. In addition, we find that the VBM of Sn appears to be energetically higher than the region where the PDOS of Ge becomes minimal and we expect valence and conduction bands to overlap.

To further investigate the differences in the electronic structures of the SiGe and GeSn interface, we compare their 2D band structure (see Fig. 4.13). From a general perspective, we see that both the SiGe and GeSn 2D band structure ($k_z \equiv 0$) show a higher density of bands compared to the band structures of the bulk Si, Ge, and Sn, which is due to the confinement of charge carriers within the structure and the resulting quantized energy levels. A clear difference between the SiGe and GeSn band structure can be seen around the Fermi energy (dashed line). For the SiGe interface, the lowest conduction and the highest valence bands are separated by a band-gap. Another interesting observation is that the lowest conduction and the highest valence band are both located at the Γ-point which makes the SiGe interface a direct semiconductor - a fact that has been reported earlier for superlattices made of strained Si and the Ge slabs [155–157]. For the GeSn interface, we find that the highest valence band is located at the Γ-point, while the lowest conduction band is situated around the X-point. Most importantly, there is no forbidden energy region separating the bands. The CBM lies below the VBM, which lowers the Fermi energy to a position inside the valence band. We can therefore conclude that the GeSn interface is metallic.

As a consequence, we expect these electrons that would, in the case of a bulk calculation, occupy the topmost valence band states inside the Sn slab now to flow over to the lower lying conduction-band states into the Ge slab. The resulting redistribution of charges causes a strong electric field over the entire structure, which could in principle be the cause for the observed convergence behavior for small values of the smearing parameter ϵ_s.

To understand the charge redistribution and the relation with the smearing parameter ϵ_s in detail, we compare the charges inside the MT sphere for each atom inside the interface

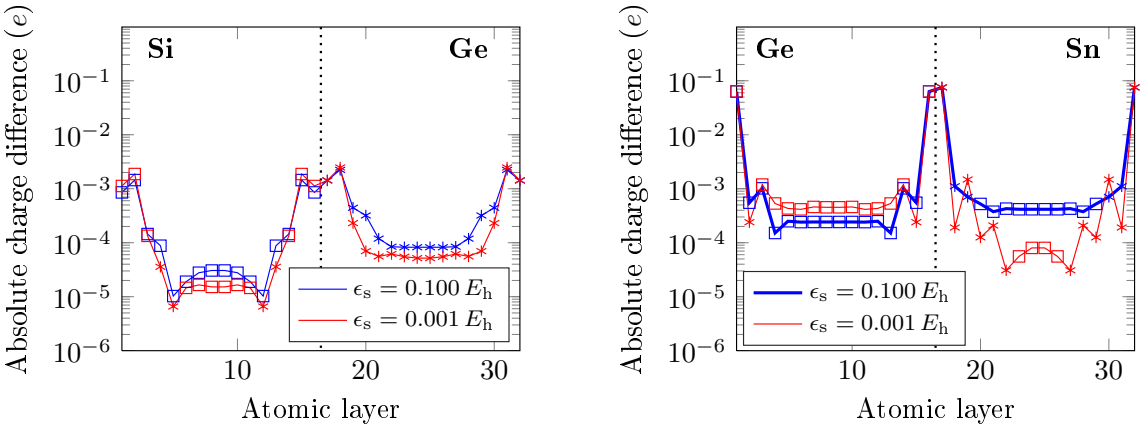

(a) SiGe **(b)** GeSn

Figure 4.14: *Absolute difference in the number of electrons inside the muffin-tin radius for each atom of the (a) SiGe and (b) GeSn interface calculation compared to their respective bulk values for different values of smearing parameter ϵ_s. A square indicates a surplus of electrons, while missing electrons are indicated by a star. Lines are guides to the eye. The position of the interface is indicated by the dotted line.*

supercell with its corresponding bulk value (see in Fig. 4.14)[4]. We start our discussion of the charge difference for the case of $\epsilon_s = 0.001\,E_h$. For the SiGe interface, we find:

- The largest absolute difference in charge can be found around the atoms situated closest to the interface. On the Si side we find a surplus of electrons of the order of 10^{-3} (indicated by squares), while roughly the same amount of charges are missing around the Ge atoms (indicated by stars). We relate this strong redistribution of charges around the interface to the interface dipole, which is the cause for the offset between the VBM in both materials at the interface.

- The charge difference in the middle of the slab is in the order of 10^{-5} for both the Si and Ge slab. While there is an oscillation between missing and surplus electrons inside the Si slab, electrons are mostly missing on the Ge slab.

In contrast, for the GeSn interface, we can make the following observations:

- Similar to the case of the SiGe interface, we find the largest absolute difference in charge around the interface. However, for the GeSn interface this difference is two order of magnitude larger (10^{-1}). Furthermore, the charge surplus is now on the side of the Ge slab, while we find a charge deficit on the side of Sn.

[4] In principle, it is more conclusive to investigate differences in the total charge density on either side of the interface with respect to the bulk case. However, this is difficult for an all-electron code as the charge density exhibits δ-like distributions around the atomic cores, which lead to large numeric errors when calculating charge differences. For this reason, we limit ourselves to the analysis of the charge difference in the MT sphere, which can be calculated more exactly. This also has the advantage that we do not have to determine the precise position of the interface. Nevertheless, the charge density in the MT region can only be taken as an indication for the total electron distribution

- In the center of the Ge slab, the charge difference is now an order of magnitude larger, which is caused mainly by a charge surplus. Inside the Sn slab, we find a more complex charge rearrangement. While on average 10^{-4} charges are missing in the size layers closest to the interface, there is a charge surplus on the order of 10^{-5} for the four innermost layers inside the Sn slab.

Summarizing these observations, we find a much stronger charge redistribution within the GeSn supercell than we observe for the SiGe supercell for both the layers around the interface as well as those around the center of each slab. In particular, we find that there is a strong charge surplus in the Ge layer of the GeSn supercell, which supports our hypothesis that electrons flow from the Sn slab into the Ge slab.

The remaining question to understand is why the convergence behavior improves if larger values of the smearing parameter ϵ_s are used. In Fig. 4.14, for $\epsilon_\mathrm{s} = 0.100\,E_\mathrm{h}$, we observe:

- For the SiGe interface, the calculated charge difference remains on the same order of magnitude as for the case of a smaller smearing parameter ϵ_s. Nevertheless, we observe for the Si slab that the oscillations of the charge difference that were noticeable in the region between interface and slab center have vanished. We mainly observe surplus charges in the center of the slab. For the center of the Ge slab, we observe that the charge difference is slightly more evenly distributed.

- The same behavior is visible for the GeSn supercell. The charge difference appears to be more evenly spread out over the central region of each slab. Furthermore, the surplus charge inside the Ge slab is lowered.

Summing up these findings, we conclude that using a larger smearing parameter ϵ_s leads to a more equal distribution of surplus and deficit charges within the center region of each slab. This is inline with the idea that by using a large smearing parameter ϵ_s, electrons are excited into conduction band states, which are more delocalized. Particularly for the GeSn supercell, we see that the charge surplus in the center of the Ge slab is reduced. This is likely a result of the artificial excitation of conduction band states within the Ge slab, which are then blocked for electrons coming from the top of the valence band of the Sn slab. In consequence, the convergence of the GeSn interface calculations with a large smoothing parameter is not achieved as a result of the smoothing of integral kernels as discussed in Sec. 4.3.1, but due to the change of the physical system. This is in line with the observation that with the parameter combination $(n_\mathbf{k}, \epsilon_\mathrm{s}) = (10, 0.001\,E_\mathrm{h})$ the band structures of bulk Si, Ge, and Sn are fully converged. The question that needs to be answered is, if using of a large smearing parameter leads indeed to the correct result of the VBO. We investigate this for the SiGe interface in the next section.

4.4.2 Valence Band Offset for the SiGe Interface

We calculated the VBO for the SiGe interface as a function of the smearing parameter ϵ_s. The results of these calculations are shown in Fig. 4.15a. We find that for values of the smearing parameter ϵ_s below the band-gap of the interface structure (dashed line), the VBO is lies around 0.62 eV. If the value of the smearing parameter ϵ_s is increased beyond that value, we first observe a decrease of the VBO to a value of 0.30 eV and, for values of the smearing parameter ϵ_s above $0.080\,E_\mathrm{h}$, oscillations of the VBO around the value of 0.40 eV with an amplitude of 0.10 eV. For values of the smearing parameter ϵ_s that are below the band-gap our calculated value lies close to the value proposed by Van de Walle *et al.* [120]. From the dependence of the VBO on the smearing parameter, we can conclude that using a high value for the smearing parameter ϵ_s

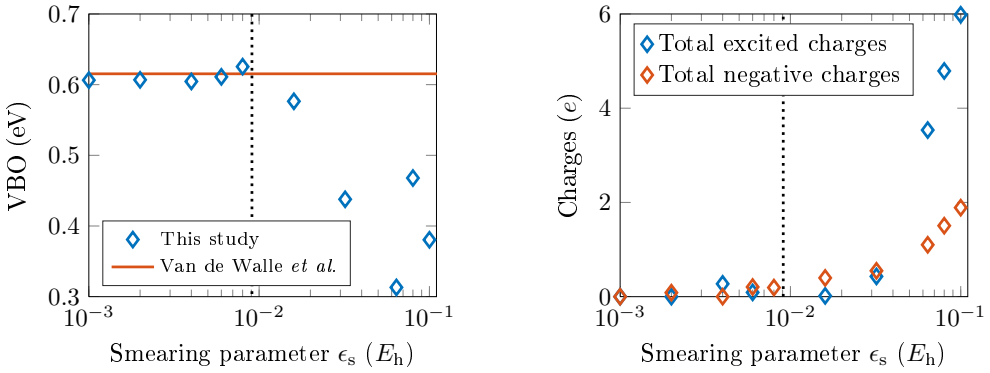

(a) VBM Offset **(b)** Occupation Numbers

Figure 4.15: *(a) VBO for the SiGe system as a function of the smearing parameter ϵ_s. The red line indicates the VBO as calculated in Ref. [120] (b) Number of negative and excited charges at the Γ-point introduced in the system due to the Methfessel-Paxton smearing as a function of the the smearing parameter ϵ_s for the SiGe supercell. The dashed line indicates the band-gap of the SiGe supercell. Once the smearing parameter is larger than the band-gap of the SiGe supercell, the calculated VBO is unphysical as a result of the excited and negative charges in the system.*

may help to achieve convergence with respect to the slab thickness. However, it also affects the value of the VBO severely. It is not totally clear yet how the smearing parameter affects the value of the VBO severely if the smearing parameter is larger than the band-gap. By choosing a smearing parameter that is larger than the band-gap, electrons are excited into the conduction band. In Fig. 4.15(b), the number of charges at the Γ-point occupying excited states is shown. It can be seen that this number is fairly small below 0.5 electrons for values of ϵ_s below $0.010\,E_h$. For larger values of the smearing parameter ϵ_s, this number strongly increases up to a value of 6 electrons for the largest value of ϵ_s investigated. Thus, by choosing a large smearing parameter, we are not calculating the VBO of the ground state of the SiGe interface, but rather the VBO of some excited state. In addition, by selecting a large smearing parameter, the Methfessel-Paxton smearing function introduces negative occupation numbers into the electronic structure of the interface, which also influence the physical properties of the system. The total negative charge found in the interface calculation for the Γ-point as a function of the smearing parameter ϵ_s is shown in Fig. 4.15(b). We find that for values of ϵ_s below the band-gap, the negative charges is at most $0.20\,e$, while for higher values of the smearing parameter a sharp increase of the negative charges up to a value of $2\,e$ can be seen.

From the SiGe VBO as a function of the smearing parameter ϵ_s, we conclude that if the value of ϵ_s is chosen too high, i. e. above the value of the band-gap for the SiGe superlattice, the VBM offset is not calculated correctly. For the GeSn system, convergence with respect to the slab thickness can only be achieved with the smearing parameter ϵ_s set to 0.100. For this value, however, the physical properties of the system are significantly affected by the smearing. Thus, using the current numerical setup, we cannot calculate the band alignment for the GeSn structure. Since Li also used DFT-LDA-based approach for his calculations, these might have been affected by the underestimation of the Ge band-gap in a similar manner.

As a consequence of the underestimation of the Ge band-gap, we cannot calculate the

GeSn VBO. Therefore, we also cannot answer the question if the discrepancy between the VBO as calculated by Jaros and Li is a result of higher-order strain effects. Nevertheless, it is interesting to investigate if, in principle, higher-order strain effects play a role in the calculation of the natural VBO. In the next section, we attempt a first estimate of the higher-order strain effects by separately investigating the absolute shift of the VBM as a function of strain for the elemental semiconductors Si, Ge, and Sn.

4.5 Nonlinear Effects of Strain

When we investigated the SiGe and GeSn band offsets, we performed all band structure calculations on a diamond lattice with an average lattice constant of the respective elemental semiconductors. To determine the natural VBO, the calculated VBO has to be corrected according to Eq. (4.8) using the ADP of the VBM for each semiconductor. When calculating the ADP of the VBM, Li approximated the derivative of the absolute energy E_v of the VBM with respect to a volume deformation by a finite difference [129]:

$$a_\mathrm{v} = \frac{\partial E_\mathrm{v}}{\partial \ln V} \approx \frac{E_\mathrm{v}(+\Delta V/V) - E_\mathrm{v}(-\Delta V/V)}{2\Delta V/V}, \tag{4.24}$$

where the volume deformation corresponds to a tensile, respectively, compressive strain of the lattice constant by $\varepsilon = \pm 0.01$. This definition as well as the strain correction given in Eq. (4.8), is based on the assumption that the ADP of the VBM, a_v, is independent of the applied volume deformation. While this might be a valid approximation for the band alignment calculations between Si and Ge where the lattice constant is strained by $\varepsilon = 0.021$, we suspect nonlinear effects to be relevant for for the band alignment calculations between Ge and Sn where the strain is in the order of $\varepsilon = \pm 0.08$ [158, 159].

Since we have already shown in Sec. 4.4.2 that our current numerical approach does not allow us to calculate the VBO for the GeSn interface, our goal is not to perform a full strain correction of the previously calculated VBOs. We rather want to investigate how strong the nonlinear effects of strain are. For this, we focus on calculations involving volume expansions only. We perform bulk and supercell calculations where we apply volume expansion of up to 10 %. We then define the *effective* DP of the VBM for a relative volume deformation $\Delta V/V$ as

$$\bar{d}_\mathrm{v}(\Delta V/V) = \frac{\Delta E_{\mathrm{v,1s}}(\Delta V/V) - \Delta E_{\mathrm{v,1s}}(0)}{\Delta V/V} \tag{4.25}$$

and analogously the *effective* ADP for the 1s core state energy for orientations α:

$$\bar{a}^\alpha_\mathrm{1s}(\Delta V/V) = \frac{E_\mathrm{1s}(\Delta V/V) - E_\mathrm{1s}(0)}{\Delta V/V}, \tag{4.26}$$

where $\Delta E_{\mathrm{v,1s}}(0)$ is the energy difference of the VBM and the 1s core state and $E_\mathrm{1s}(0)$ the absolute energy of the 1s core state at the equilibrium lattice constant, respectively. In case nonlinear effects of strain can be neglected, these effective properties will be approximately constant. However, if nonlinear effects need to be taken into account, the values of the effective properties will depend on the magnitude of the volume deformation.

To calculate the ADP of the VBM we need to perform an angular average of $\bar{a}^\alpha_\mathrm{1s}$ over the directions $\alpha = \{[100], [110]\}$ as described in Eq. (4.13). However, previous studies have shown that the investigation of the uniaxial strain along the [110] requires an internal lattice relaxation [148]. As we are only performing a qualitative study at the moment, we reduce

the computational complexity of the problem by limiting ourselves to strain along the [100] direction only. In analogy to Eq. (4.11), we define the *effective* uniaxial ADP $\bar{a}_{\mathrm{v}}^{[100]}$ of the VBM as

$$\bar{a}_{\mathrm{v}}^{[100]}(\Delta V/V) = \bar{a}_{\mathrm{1s}}^{[100]}(\Delta V/V) + \bar{d}_{\mathrm{v,1s}}(\Delta V/V). \tag{4.27}$$

Note that in this definition, $\bar{a}_{\mathrm{v}}^{[100]}$ only includes effects of hydrostatic strain. Effects of shear strain, e. g. band splittings, are excluded.

4.5.1 Convergence Behavior

Before we can analyze the effective uniaxial ADPs $\bar{a}_{\mathrm{1s}}^{[100]}$ of the 1s core state, we need to verify their convergence. For a tensile strain of $\varepsilon = 0.01$ along the [100] direction, we check the convergence behavior of the energy difference ΔE_{1s} between the 1s core states in the relaxed and tensile strained slab as a function of the number of atomic layers n and the smearing parameter ϵ_{s}. We define the convergence error E_{conv} as the change in energy when increasing the slab thickness from n to $n+4$ atomic layers. The convergence error E_{conv} for Ge and Sn are shown in Fig. 4.16(a) and (b), respectively. For a value of $\epsilon_{\mathrm{s}} = 0.001\,E_{\mathrm{h}}$, the convergence error does not decrease with system size. On the other hand, when using a value of 0.100 for the smearing parameter ϵ_{s}, we obtain calculations for a slab size of $n = 16$ with a convergence error on the order or below $10^{-3}\,\mathrm{eV}$. The convergence behavior appears to be related to the underestimation of the band-gap of Ge and Sn as in the case of the GeSn heterostructure (see Sec. 4.4.1). As we have argued in the previous section, no quantitative information can be extracted from calculations, which make use of a large smearing parameter ϵ_{s}.

The convergence behavior is different for Si (see Fig. 4.16(c)), where we find for $\epsilon_{\mathrm{s}} = 0.001\,E_{\mathrm{h}}$, the energy difference between the 1s core states converges quickly for the [001]. For a slab thickness of $n = 12$, the convergence error is on the order of 10^{-3}. Therefore, we limit our strain investigation in the following to Si only. Even though this does not provide a full analysis of strain effects in the Si, Ge, and Sn material system, it can still provide information if nonlinear effects of strain are relevant for the calculation of the VBO.

4.5.2 Special Case: Si

The results for the effective DP $\bar{d}_{\mathrm{v,1s}}$ of the energy difference between VBM and 1s core state and the effective ADP $\bar{a}_{\mathrm{1s}}^{[100]}$ of the 1s core state of Si are shown in Figs. 4.17(a) and 4.17(b), respectively. For the effective DP $\bar{d}_{\mathrm{v,1s}}$, we find a positive value, meaning that for an expansion of the crystal, the VBM moves upward in energy with respect to the 1s core state. It is noticeable that the effective DP is not constant, but decreases from a value of 2.22 eV for a relative volume change of 1% to 2.10 eV for a relative volume change of 10%. For the effective ADP $\bar{a}_{\mathrm{1s}}^{[100]}$ of the 1s core states, in contrast, we find a negative value. Moreover, for an increasing volume deformations, it becomes smaller in terms of its absolute value.

Adding the effective DP $\bar{d}_{\mathrm{v,1s}}$ and the uniaxial effective ADP $\bar{a}_{\mathrm{1s}}^{[100]}$ according to Eq. (4.27), we calculate the uniaxial effective ADP $\bar{a}_{\mathrm{v}}^{[100]}$ of the VBM for strain along the [100] direction (see Fig. 4.16c). If the value of $\bar{a}_{\mathrm{v}}^{[100]}$ is constant over the entire spectrum of relative volume deformations, the effect of strain on the absolute energy of the VBM would be purely linear. However, we find that the value of the uniaxial effective ADP $\bar{a}_{\mathrm{v}}^{[100]}$ decreases with increasing volume deformations. This is an indication that nonlinear effects might be important.

Before we analyze further the nonlinear effects, we want to validate our calculations. For this, we compare the ADP of the VBM for a relative expansion of 1 % with the results of

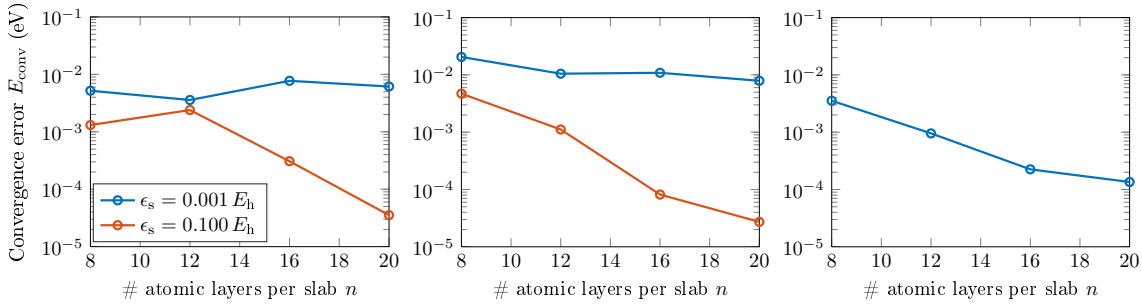

(a) Ge [001] **(b)** Sn [001] **(c)** Si [001]

Figure 4.16: *Convergence behavior of the energy difference between the 1s core state energies in a superlattice of alternating relaxed and tensile strained slabs for (a) Ge, (b) Sn, and (c) Si. The convergence error E_{conv} is defined as the difference of $E_{1\mathrm{s}}$ when calculated with a slab thickness of n atomic layers and $n+4$ atomic layers. A tensile strain of $\varepsilon = 0.01$ was applied along the [100] direction. Lines are guides to the eye only. While for Si the convergence error decreases with slab size for a smearing of $\epsilon_{\mathrm{s}} = 0.001\,E_{\mathrm{h}}$, a smearing of $\epsilon_{\mathrm{s}} = 0.100\,E_{\mathrm{h}}$ is required for the convergence error of Ge and Sn to decrease.*

previous studies that calculated this value for small deformations (see Tab. 4.2). We find that the results of the studies are all within the same order of magnitude as our results. A majority of workers has calculated the ADP of the VBM for the [100] direction to be 1.5 eV, while the result of Van de Walle *et al.* with 1.3 eV and ours with 1.17eV are slightly below that. The results of Li *et al.* are the most recent and were obtained using the largest number of layers in the supercell calculations. For this reason, their value is very likely the most accurate. The discrepancy between our value and the value of Li *et al.* might be caused by our setup of the superlattice calculation where we limit our calculation to tensile strain only. Furthermore, we did not perform a relaxation of the atoms around the interface between relaxed and strained slab, which can cause small changes in the valence band offset [160]. Nevertheless, we conclude that our calculations are good enough for an estimate of the nonlinear effects of strain.

To determine if the nonlinear effects of the strain on the absolute energy of the VBM

Table 4.2: *Uniaxial ADP a_{v}^{001} of the VBM in the limit of small relative volume changes (1 %) along the [100] direction. Comparison of the result of this work to previous studies. The VBM ADP of this work is approx. 20 % smaller than the results of previous studies. The discrepancy might be a result of the missing interface relaxation and the limitation to tensile strain.*

	$a_{\mathrm{v}}^{[100]}$ (eV)
This work	1.17
Li *et al.* [149]	1.50
Van de Walle *et al.* [148]	1.3
Resta *et al.* [161]	1.5
Franceschetti *et al.* [130]	1.5

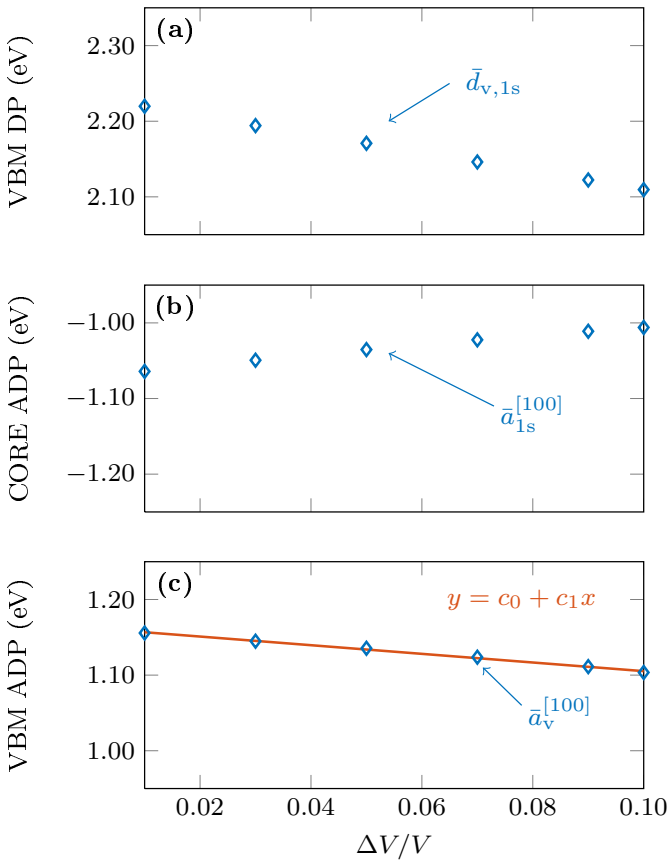

Figure 4.17: *(a) DP of the energy difference between VBM and 1s core state, (b) ADP of the 1s core state , and (c) the ADP of the VBM for tensile strain along the [100] direction as a function of relative volume change $\Delta V/V$. The VBM DP, the core ADP, and the VBM ADP show a functional dependency on the relative volume change.*

Table 4.3: *Comparison of strain related absolute shifts of the VBM of Si estimated based on the [100] effective ADP $\bar{a}_{\mathrm{v}}^{[100]}$ of the VBM with an ADP that has a constant, linear, and quadratic functional dependence on the relative volume change. Numbers in parentheses are the difference to constant model in eV. The values of $\Delta V/V$ correspond to the hydrostatic strain experienced by Si in a SiGe and in a SiSn supercell calculation, respectively.*

$\Delta V/V$	VBM Strain Shift (eV)			Remark
	constant	linear	quadratic	
6.4 %	0.07	0.07 (-0.00)	0.07 (-0.00)	SiGe
30.3 %	0.38	0.32 (-0.06)	0.29 (-0.09)	SiSn

are important, we fit the dependence of the uniaxial effective ADP $\bar{a}_{\mathrm{v}}^{[100]}$ with a first-order polynomial. Using this polynomial, we calculate the absolute shift in energy of the VBM of Si due to hydrostatic strain along [001] and compare it to the result obtained by assuming a constant effective ADP of the VBM which is that for a volume deformation of 1 % (see Tab. 4.3). We focus in the following on the shift for two relative volume changes: 6.4 % and 30.3 %, which is the volume deformation experienced by Si in a SiGe and SiSn superlattice calculation, respectively. We find that for the smaller relative volume change, the strain causes an absolute shift of the VBM in the order of 70 meV. No difference between the constant and linear model of the effective ADP of the VBM can be observed. This is different for the larger relative volume change of 30.3 %, where we observe an energy shift of 0.38 eV for the constant effective ADP while we only find a shift of 0.29 eV for the linear effective ADP. This results in a difference of 60 meV. Since the numerical accuracy of our calculations is in the order of a few meV, a 60 meV is significant. Furthermore, the discrepancy between constant and linear approach accounts for approx. 10 % of the natural VBO between Si and Ge.

Instead of a linear approximation of the effective ADP of the VBM, we can also use a quadratic expression and calculate the shift of the VBM (see also Tab. 4.3). We find that for the 6.4 % volume change, we find a no difference between the models, while for the 30.3 % volume change the difference in the energy shift of the VBM increases to 90 meV.

Therefore, we can conclude that for relative volume deformations involved in the SiGe interface, nonlinear strain effects are negligible. For relative volume deformations involved in the SiSn and similarly in the GeSn interface, nonlinear strain effects lead to a difference of at least 60 meV in the absolute energy of the VBM of Si. For a complete strain correction of the VBM offset between materials, we also have to investigate the the energy shift of Ge and Sn. Depending on the functional dependence of the ADP of the VBM on compressive strain for those materials, the nonlinear effects might compensate each other or even increase. This has to be investigated in more detail in a DFT setup that correctly reproduces the band-gaps of Ge and Sn. We discuss this in more detail in the next section.

4.6 Summary and Outlook

The goal of our calculation was to investigate the deviations of the natural VBO for Si, Ge, and Sn as calculated by Jaros [128] using an analytical model and Li *et al.* [129] employing DFT calculations. Our initial hypothesis was that nonlinear strain effects that have not been properly

taken into account by Li *et al.* are the reason for the difference in the results. However, in our investigation we found that the band-alignment calculations between Si, Ge, and Sn using Kohn-Sham-based DFT are severely influenced by the underestimation of the semiconductor band-gaps. While for the SiGe heterojunction this problem is partly compensated by a band-gap opening due to strain and confinement effects, the GeSn heterojunction becomes metallic. This leads to a false type-III band alignment for the GeSn interface that causes a charge separation and subsequently a strong electric field even far away from the interface, which manifests itself in a slow convergence of the band offset with system size. While a large smearing parameter can improve the convergence behavior of the calculations, it also affects the value of the band offset leading to a wrong result. Therefore, we have to conclude that the band offset calculations for Si, Ge, and Sn performed by Jaros are the best estimate available at the moment.

The underestimation of the band-gap also lead to convergence issues during the investigation of nonlinear strain-dependent energy shift of the VBM. In particular, the homojunction calculations between relaxed and strained Ge and Sn semiconductors have not converged. For this reason, our studies have solely focused on the ADP of the VBM for Si, we were able to qualitatively show that for hydrostatic strain encountered in heterojunctions involving Sn, nonlinear strain effects effect the absolute energy of the VBM by at least 60 meV.

From these observations, several new research questions emerge. In order to perform band-offset calculations for the Si, Ge, and Sn material system using DFT, the band-gaps of the materials need to be corrected. One possibility is to correct the band-gaps by employing the *GW* method in a perturbation approach. However, when we use the *GW* method perturbatively for our interface calculations, the band structure calculated with *GW* are based on the Kohn-Sham eigenstates. Yet, the Kohn-Sham eigenstates are severely influenced by the charge separation as a consequence of the underestimated band-gap of Ge. Therefore, perturbation theory cannot be used.

More suitable for our case is the usage of empirical exchange-correlation functionals. One possibility are the hybrid exchange-correlation functionals (HFs). HFs linearly combine the nonlocal Hartree-Fock exchange term with the local DFT exchange-correlation energy [162]. Even though, there is no physical motivation for the linear combination of the nonlocal Hartree-Fock exchange term with the local DFT exchange-correlation energy, the band structure calculated with HFs show improved properties. Originally developed in the context of molecular modeling, where the HF showed improvements of the predicted atomic ionization energies, ionization potentials, and proton affinities, HFs also improved the predictions of properties of solids. Most remarkable is the opening of the direct and indirect band-gaps for semiconductors in comparison to calculations using purely LDA or GGA [163]. However, HFs are computationally demanding. Interface computations with HFs have only been performed in the framework of a pseudopotential-based DFT solver. An alternative option to HFs is the LDA-1/2 functional, which employs the standard LDA together with half-occupation [164]. Like the HF, the LDA-1/2 functional cannot be derived exactly. Nevertheless, investigations have shown that the LDA-1/2 functional increases the band-gap energy of solds [165, 166]. As there is no free parameter available to tune the band-gap size as it exists for the HF, one would first have to investigate whether the increase for Ge and Sn is sufficiently large to remove the false type-III alignment.

Beyond the use of a more appropriate exchange-correlation functional, future studies also need to include investigations of the influence of structural relaxation on the band offset. Moreover, it would also be very interesting to investigate the band offset not only between the elementary semiconductors, but also between alloys [167]. This would model more closely the experimental reality where Sn can only be grown on Si or Ge as part of an alloy of these

materials. As band structure calculations of alloys require large unit cells and also multiple calculations for the different atomic configurations of the alloy [168], it has to be verified that the computational requirements can be met, which depends highly on the functional used.

For the investigation of the nonlinear strain effects, approaches that open up the band-gap of Ge and Sn also need to be applied. Furthermore, a quantitative study including larger volume deformations needs to be performed. We have observed a strain dependence of the ADPs up to a volume deformation of 10 % and then extrapolated to values up to 30 % using first and second order polynomials which lead to different results. Large volume deformations need to be investigated to determine the polynomial order for the description of the ADPs beyond 10 %. Furthermore, investigations on the nonlinear dependence of the ADPs on compressive strain are required as well as a full angular average.

Chapter 5

5 Effective Mass Model for SiGe Heterostructures

In this chapter, we investigate the photoluminescence (PL) emission from a Ge multiple quantum well (multiple-QW) structure. Our investigation of the PL emission is primarily focused on the spontaneous phonon-assisted radiative recombination. To investigate the PL emission theoretically, we developed a strategy based on a self-consistent multivalley effective mass model in combination with second-order perturbation theory. Based on this, we are able to study PL spectra as a function of excitation density and temperature. Comparing experimental data with our simulation results, we gain a deeper understanding of the underlying physical processes. The results of this chapter have been published in Ref. [W2].

5.1 Introduction

In the previous two chapters, our investigations were focused on gaining a better understanding of basic material properties of the SiGeSn material system. In this chapter, we turn our attention towards the investigation of heterostructures and their interaction with light. To model these heterostructures, we use the effective mass approximation. The effective mass approximation requires a set of material parameters that is smaller than that of the TB method. Nevertheless, as we have seen in the previous two chapters, a lot of these material parameters are still unknown for the SiGeSn material system. For this reason, we limit our first attempt to model the light-matter interaction in heterostructure to those heterostructures composed of SiGe only.

Focusing on their potential use as light sources, nanostructures based on the SiGe system have already been extensively researched [169–172]. While no efficient light source could yet be developed based on the SiGe material sytem, other applications were proposed. Kuo *et al.* successfully demonstrated the use of strained Ge QWs sandwiched between Ge-rich barrier layers and embedded in a diode structure for light modulation based on the quantum-confined Stark effect [18, 173]. Furthermore, there is ongoing interest in designing SiGe QW structures for intraband transitions for applications not only in QW infrared photodetectors [174–177], but also in quantum cascade laser structures [178].

One of the main challenges in utilizing SiGe-based QW structures for optical device applications is the thermal quenching of their luminescence. In most experiments on SiGe/Si QWs, PL spectra can only be observed at temperatures below a few tens of degrees Kelvin [179, 180]. The thermal PL quenching is mainly related to nonradiative recombination centers [179] that can originate, e.g., from structural defects such as dislocations. Higher growth temperatures have been shown to reduce thermal quenching [179, 181]; however, they also lead to Si and Ge interdiffusion and thus to the broadening of heterointerfaces [182]. Although room temperature PL has been reported in Ge QWs sandwiched between $Si_{1-x}Ge_x$ barriers [183], those structures have the disadvantage of requiring a relatively thick SiGe virtual substrate to accommodate the large lattice mismatch between the Si substrate and the QW structures.

Here, we investigate the room temperature PL emission of a specific multiple quantum well (multiple-QW) sample. The QW sample was grown by repeatedly depositing 5.5 monolayers (ML) of Ge and overgrowing them with Si at low growth temperatures directly on Si, without using a virtual substrate technology. It features ultrathin wells with a Ge concentration exceeding 60 %. Experimental investigation of the PL emission show that the PL of the multiple-QW sample is not significantly quenched at room-temperatures. However, the physical mechanisms responsible for the reduced thermal quenching are not clear. To interpret the PL spectra, we developed a strategy to simulate the PL emission of the sample based on a coupled Schrödinger-Poisson description in the effective mass approximation. Even though the PL emission of various SiGe/Si QW structures have been extensively investigated experimentally, theoretical calculations of the PL spectrum based on an effective mass approach have not been reported in the literature. In studies comparing measured PL spectra with theoretical calculations, the PL transition energies are commonly computed by taking into account the topmost valence and bottommost conduction states only [184, 185]. This can be helpful in cases of low optical excitation and temperature. However, for higher temperatures and stronger excitations, the PL shape strongly depends on the filling of the bands due to the optically excited excess carrier density and on the temperature-dependent quasi-Fermi distributions of the excited charge carriers, which leads to the population of higher energy subband states, as well as to relevant band bending effects. In our analysis, we describe the features from indirect recombination between quantum confined states relying on second-order perturbation theory, which, to our knowledge, has not been reported elsewhere in the literature.

The presentation of the results of our investigation is organized as follows. In Sec. 5.2, we describe the sample and give an overview of the measurement results. In Sec. 5.3, we describe our effective mass model. In Sec. 5.4, we introduce the theory of heterostructure PL. In Sec. 5.5, we apply our model to the Ge multiple-QW sample and compare the results of our simulation with the experimental findings. We conclude our analysis in Sec. 5.6 by discussing the physical consequences of our findings and give an outlook on future work.

5.2 Experimental Details

To be able to develop a theoretical model of the PL emission from our sample, we need to understand the structure of the Ge multiple-QW sample and the conditions under which the measurements were performed. First, we describe the preparation of the sample and the measurement setups used for its characterization. Then, we give an overview of the structural investigations of the sample. Finally, we describe the PL measurements.

The experimental work presented here was performed collaboratively by the group of Prof. Jörg Schulze at the University of Stuttgart, the Materials Research Department of the

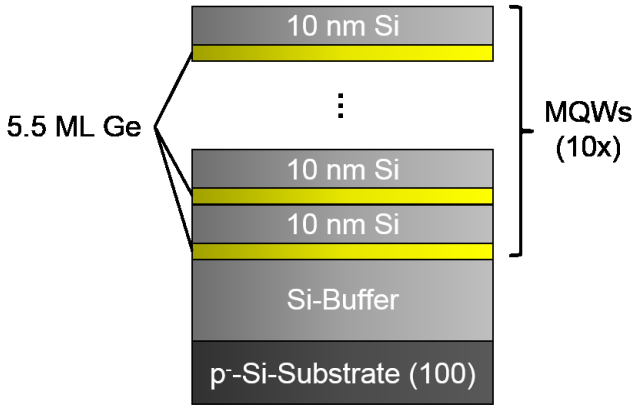

Figure 5.1: *Schematic of the Ge multiple-QW stack sequence. Using solid source molecular beam epitaxy, a* 100−nm*-thick buffer layer was grown on a Si (100) substrate. On top, a 10-period sequence was deposited of which each period consists of* 5.5 monolayers *(ML) of Ge and* 10 nm *of Si. Reproduced from T. Wendav* et al., *"Photoluminescence from ultrathin Ge-rich multiple quantum wells observed up to room temperature: Experiments and modeling", Phys. Rev. B* ***94,*** *245304 (24 2016).* ©*2016 by the American Physical Society.*

Leibniz-Institut für innovative Mikroelectronik (IHP), the New Materials Group at the University of Vigo (Spain), and the group of Prof. Peter Weger at the Brandenburg University of Technology.

5.2.1 Sample Preparation and Measurement Setups

The nominally intrinsic Ge multiple-QW sample was fabricated by solid source molecular beam epitaxy on a Si (100) substrate[1]. After thermal desorption of the native oxide, a 100−nm-thick Si buffer layer was grown at 600 °C. A 10 period sequence in which each individual period consists of 5.5 monolayers (ML) of Ge and 10 nm of Si (see Fig. 5.1) was grown at a constant growth temperature of 350 °C. The Ge layers were grown at a rate of $0.087\,\text{Å}\,\text{s}^{-1}$ while for the Si spacer layers a growth rate of $1\,\text{Å}\,\text{s}^{-1}$ was used. Transmission electron microscopy (TEM) measurements were obtained using a JEOL JEM-2010F microscope. Raman scattering experiments were performed at room temperature in a back scattering geometry on an alpha300 R confocal Raman microscope (WITec), using a diode-pumped solid state laser with a wavelength of 532 nm as excitation source. The spot size of the excitation on the sample was approximately $1.4\,\mu\text{m}^2$ with a power of approximately 4 mW measured close to the external sample surface. XRD measurements were carried out with a SmartLab diffractometer from Rigaku using CuK_α radiation. Lastly, μPL measurements were carried out for lattice temperatures varying between 80 K and 300 K using a custom-designed Horiba setup featuring a 50× optical microscope (numerical aperture A = 0.65), a high resolution spectrometer optimized for infrared measurements (Horiba iHR320) and an extended-InGaAs detector (0.6 eV-1.1 eV detection range). A 532 nm-laser with an output power between 10 mW and 500 mW was focused onto the sample surface with an excitation power density ranging in between $3.2 \times 10^4\,\text{Wcm}^{-2}$ and $160 \times 10^4\,\text{Wcm}^{-2}$.

[1] In principle, an intrinsic semiconductor sample is free of any impurities that could act as electron acceptors or donors. Due to contaminations the growth of such a pure semiconductor is not possible. Therefore, one uses the term nominally intrinsic to indicate the existence of an unintentional background doping. For our sample, this is an unintentional p-type doping of the order of $1 \times 10^{16}\,\text{cm}^{-3}$.

All spectra were collected at normal incidence in backscattering geometry and a white-body lamp was used to determine the optical response of the setup used for the calibration.

5.2.2 Structural Analysis

As a consequence of the 4.2 % lattice mismatch between Ge and Si, pure Ge grown on a Si substrate experiences compressive strain. In equilibrium conditions, this strain is released via the spontaneous formation of Ge dots, on top of a coherent Ge wetting layer, following the so-called Stranski-Krastanow growth mode. The critical thickness of the wetting layer at which dot formation occurs is a function of growth temperature and can exceed several ML [186]. As can be observed in the bright field transmission electron spectroscopy (BF-TEM) and in the high resolution transmission electron spectroscopy (HR-TEM) images (Fig. 5.2a and Fig. 5.2b, respectively), because of the low growth temperature chosen here, the Ge layer thickness is below the critical thickness necessary for island formation, and the resulting sample contains SiGe QWs rather than dots. The sample is crystalline and no threading dislocations are visible. Using the HR-TEM image, we estimate the thickness of the Ge-rich regions to be in the 1.1 nm–1.4 nm range, which indicates an intermixing of Si and Ge in the well regions [187].

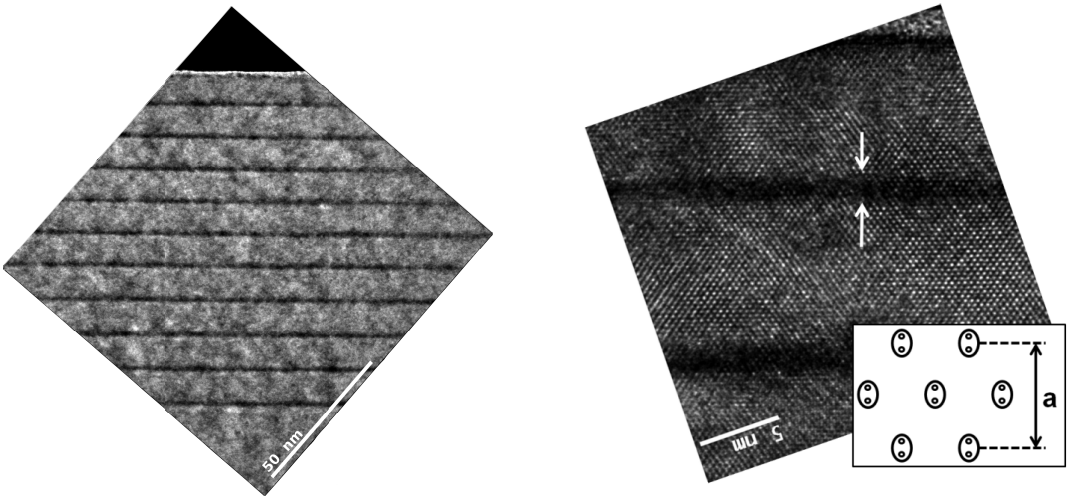

(a) BF-TEM **(b)** HR-TEM

Figure 5.2: *(a) Bright field transmission electron microscopy image (BF-TEM) showing the layer sequence of the Ge multiple-QW sample. Even though the interfaces between the layers are rough, island formation cannot be observed. Moreover, the sample is crystalline without any threading dislocations. (b) High resolution transmission electron microscopy image (HR-TEM) showing an excerpt of three Ge quantum well regions. The size of the quantum wells can be estimated by counting the TEM reflections. The inset shows a schematic of the individual atomic layers in the (110) plane. One lattice constant contains four atomic layers, but two atomic layers are so close to each other that they are seen as a single elliptical reflection in the TEM image. Reproduced from T. Wendav* et al., *"Photoluminescence from ultrathin Ge-rich multiple quantum wells observed up to room temperature: Experiments and modeling", Phys. Rev. B* ***94,*** *245304 (24 2016).* ©*2016 by the American Physical Society.*

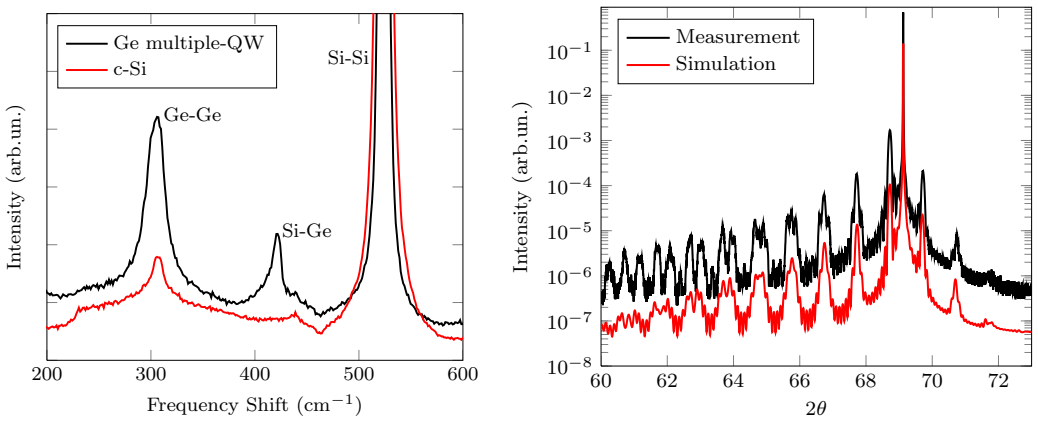

(a) Raman Spectra **(b)** XRD ω-2θ-Scan

Figure 5.3: *(a) Comparison of the Raman spectra from c-Si (red) and the Ge multiple-QW sample (black) normalized to the Si-Si vibrational mode. Clearly visible are the Ge-Ge and Si-Ge vibrational modes in the Ge multiple-QW sample. (b) XRD ω-2θ scan along the (004) direction of the Ge multiple-QW sample (black). The large number of higher order superlattice peaks indicates good homogeneity of the QWs within the sample. The XRD data was fitted with a multiple square well model (red) from which the thickness and Ge concentration of each layer was obtained. Reproduced from T. Wendav* et al., *"Photoluminescence from ultrathin Ge-rich multiple quantum wells observed up to room temperature: Experiments and modeling", Phys. Rev. B* ***94,*** *245304 (24 2016).* ©*2016 by the American Physical Society.*

To obtain more information on the composition and lattice strain of the QWs, Raman and XRD analysis was used. Using Raman spectroscopy, the wavenumber of the optical phonon modes of the semiconductor can be measured. The frequencies of the phonon modes is influenced by both the composition and the strain state of the structure. In Fig. 5.3(a), Raman data of the sample together with that of a bulk Si (001) reference are shown. For both samples, a strong peak can be observed at approximately $520\,\mathrm{cm}^{-1}$ corresponding to the Si-Si vibrational mode. For the Ge multiple-QW sample, we find two additional modes at approximately $300\,\mathrm{cm}^{-1}$ and $420\,\mathrm{cm}^{-1}$, which cannot be found in the Si spectrum. These correspond to the Ge-Ge and Si-Ge vibrational modes. To isolate the Raman signal of the multiple-QW from that of the Si substrate, the Si spectrum I_{Si} is subtracted from the sample spectrum I_S, i.e. $I_S - FI_{\mathrm{Si}}$, where F is a scaling factor obtained by taking the ratios of the Si-Si vibrational mode at $520\,\mathrm{cm}^{-1}$ [188, 189]. From the resulting multiple-QW spectrum, the frequencies $\omega_{\mathrm{Ge-Ge}} = 303.95\,\mathrm{cm}^{-1}$ and $\omega_{\mathrm{Si-Ge}} = 421.27\,\mathrm{cm}^{-1}$ for the Ge-Ge and Ge-Si modes can be obtained, respectively. Based on these values, the Ge concentration x and the biaxial strain ϵ_{xx} in the well region can be estimated using the empirical relations [189]

$$\begin{aligned}\omega_{\mathrm{Si-Ge}} &= 400 + 29x - 95x^2 + 213x^3 - 170x^4 + b_{\mathrm{Si-Ge}}\epsilon_{xx},\\ \omega_{\mathrm{Ge-Ge}} &= 283 + 5x + 12x^2 + b_{\mathrm{Ge-Ge}}\epsilon_{xx},\end{aligned} \tag{5.1}$$

where both frequencies are given in cm^{-1}. For the strain-shift coefficients $b_{\mathrm{Ge-Ge}}$ and $b_{\mathrm{Si-Ge}}$,

the empirical relations given in Ref. [190] were used:

$$\begin{aligned} b_{\mathrm{Si-Ge}} &= -190(x-1)^4 - 555, \\ b_{\mathrm{Ge-Ge}} &= -190(x-1)^4 - 460. \end{aligned} \tag{5.2}$$

An average Ge concentration of $x = (0.68 \pm 0.01)$ within the QW layer and a compressive strain of approximately $\epsilon_{xx} = -2.64\,\%$ was determined. The main errors in this analysis originate from the uncertainties associated with the strain-shift coefficients, but also from the fact that Ge content as well as strain could be inhomogeneously distributed within the QWs.

Further insights in the multiple-QW structure were obtained by XRD measurements. In Fig. 5.3(b), the results of an ω-2θ-scan along the (004) direction together with diffraction simulation results are shown. An ω-2θ-scan probes the thickness and composition of the different layers in the structure. Each peak in Fig. 5.3(b) is a result of constructive interference of x-ray waves diffracted at different interfaces in the structure. The large number of higher order superlattice peaks indicates good homogeneity of the QWs within the sample. XRD simulations were used to extract thickness and composition of the different layers from the ω-2θ-scan. For the simulation, sharp interfaces between well and barrier regions were assumed. Good agreement between experiment and simulation was obtained for an average Ge content $x_{\mathrm{av}} = (0.69 \pm 0.08)$ and an average well thickness of $w_{\mathrm{av}} = (1.2 \pm 0.2)\,\mathrm{nm}$. Assuming pseudomorphic growth as well as neglecting material diffusion (i.e. assuming a box profile of the Ge content within the well) this analysis yields a total number 4.9 ML of Ge deposited, which is close to the nominal value of 5.5 ML used in the growth process.

The results of the TEM, Raman, and XRD measurements concerning the geometry and composition of the sample are in good agreement with each other. Based on these findings, we will later construct our effective mass model. Next, we give an overview over the optical properties of the sample.

5.2.3 Optical properties

The optical properties of the sample have been investigated by μPL at different pump power densities and sample temperatures. In the following, we will present an overview of those measurements and discuss some general features of the recorded PL spectra that will give us a first impression of which physical processes are relevant for the modeling of the PL spectra. First, we discuss the excitation density dependent measurements and afterward the temperature-dependent measurements.

The excitation-density-dependent measurements were conducted at a constant lattice temperature of $T = 80\,\mathrm{K}$ with excitation densities varying between $3.2 \times 10^4\,\mathrm{W\,cm^{-2}}$ and $160 \times 10^4\,\mathrm{W\,cm^{-2}}$. In Fig. 5.4(a), the recorded PL spectra are shown. The PL intensity increases by a factor of 20 when the excitation density increases from $3.2 \times 10^4\,\mathrm{W\,cm^{-2}}$ to $160 \times 10^4\,\mathrm{W\,cm^{-2}}$ and blueshifts from 740 meV to 830 meV. A fitting procedure of the PL spectra with different numbers of Gaussian peaks shows that the signal can best be described by a convolution of two Gaussian peaks (shown in the inset of Fig. 5.4(b)). Furthermore, as shown in Fig. 5.4(b), the deconvolution analysis reveals that the energy separation between the two peaks is approximately 51 meV over the entire pump-power range. In quantum confined structures consisting of Ge-rich regions surrounded by regions of pure Si, it is commonly observed that the holes are localized within the Ge-rich region around the Γ-point while the electrons are localized mainly within the Si region in the Δ-valleys [177, 191, 192]. Therefore, it is reasonable to attribute the lower energy feature to an indirect band-to-band recombination assisted by spontaneous emission of phonons with appropriate momentum, while the higher

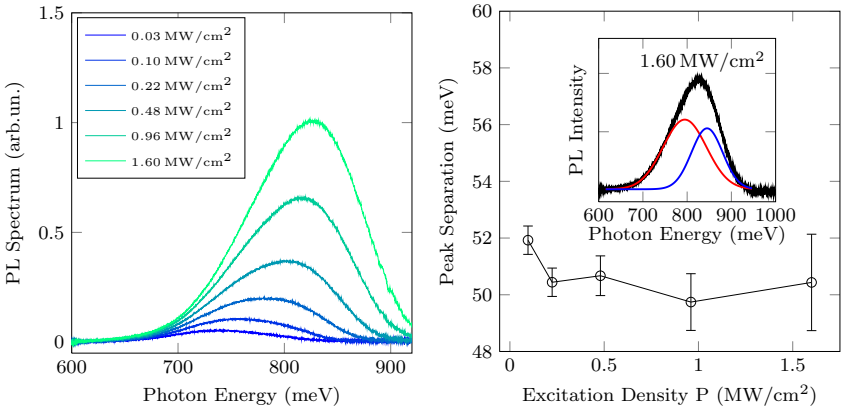

(a) PL Spectra **(b)** Deconvolution

Figure 5.4: *(a) Experimentally observed PL spectra at* $T = 80\,\mathrm{K}$ *for different excitation densities. With higher excitation density, the PL emission blueshifts and the integrated PL emission increases. (b) Energy separation between phonon-assisted and NP peak as a function of the excitation density* P*. The energy separation is in the order of* $51\,\mathrm{meV}$*. The inset shows a deconvolution of a PL spectrum with two Gaussian peaks, which were identify as the phonon-assisted (red) and NP feature (blue). Points are connected for clarity. Reproduced from T. Wendav* et al.*, "Photoluminescence from ultrathin Ge-rich multiple quantum wells observed up to room temperature: Experiments and modeling", Phys. Rev. B* ***94,*** *245304 (24 2016).* ©*2016 by the American Physical Society.*

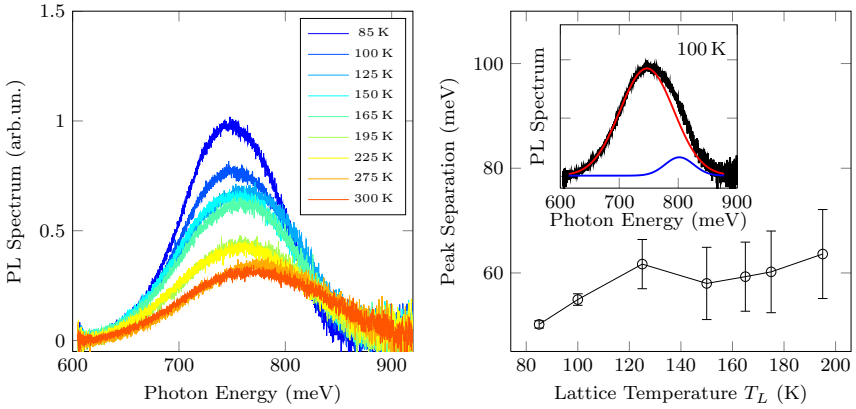

Figure 5.5: *(a) Experimental PL spectra recorded at* $9.6 \times 10^4\,\mathrm{Wcm^{-2}}$ *excitation power for different lattice temperatures. Increasing the temperature leads to a reduction of the integrated PL signal and a blueshift of the PL peak. (b) Energy separation between phonon-assisted and NP feature as a function of the lattice temperature* T*. The energy separation increases for larger temperatures. The inset shows a deconvolution of a PL spectrum with two Gaussian peaks, which we identify as the phonon-assisted (red) and NP feature (blue). Points are connected for clarity. Reproduced from T. Wendav* et al.*, "Photoluminescence from ultrathin Ge-rich multiple quantum wells observed up to room temperature: Experiments and modeling", Phys. Rev. B* ***94,*** *245304 (24 2016). ©2016 by the American Physical Society.*

energy must be related to the presence of an elastic scattering channel (no-phonon (NP) recombination) which provides the missing momentum for the same indirect transition. Consequently, the energy separation between the peaks is the phonon energy required for the phonon-assisted recombination. The phonon energy is very close to the transverse optical phonon energy of bulk Si (58.8 meV) at the X-point [80]. However, also the Si-Ge vibrational mode has a comparable energy (50 meV) [80]. Since our spectral resolution does not allow to resolve the two phonon channels, we cannot determine which of these processes contributes to the phonon-assisted recombination mechanism.

In a second investigation, the PL emission was studied at a constant excitation density of $9.6 \times 10^4\,\mathrm{W\,cm^{-2}}$, while varying the lattice temperature T in the 80−300 K range (see Fig. 5.5(a)). With increasing temperature, the spectra become broader and the PL peak energy blueshifts by approximately 30 meV. Note, the PL intensity is not significantly quenched up to room-temperature, the total integrated intensity being reduced by a factor of three when the lattice temperature T is increased from 80 K to 300 K. Regarding the spectral blueshift, we notice that this behavior seems to be in conflict with the temperature-driven shrinking of both the Si and Ge band gaps. Both the origin of the reduced thermal quenching and the blueshift of the PL spectra are unclear. In analogy to the excitation-dependent measurements, the phonon-assisted and NP features were resolved by Gaussian deconvolution. Due to thermal broadening effects, this kind of analysis was successful only for temperatures $T < 200\,\mathrm{K}$. For spectra recorded within this range, the energy separation increases from 51 meV to roughly 60 meV when the lattice temperature is increased from 80 K to 200 K (see Fig. 5.5(b)).

Summarizing the results of the PL measurements, we find that the PL peak blueshifts and the PL intensity increases when the excitation density is increased. When the temperature is increased, the PL peak also blueshift while the PL intensity decreases, but is not significantly quenched. For both measurement series, we find that the PL signal can be deconvoluted with two Gaussians that we attribute to the phonon-assisted and NP recombination. Consequently, we identify two goals for our theoretical investigation. First, our calculations should verify that the primary recombination mechanisms for our sample are indeed due to phonon-assisted and NP processes. Secondly, our theory should give us a greater insight into the excitation-density and temperature dependence of the PL emission. In the next section, we take the first step toward the modeling of the PL spectra and develop the self-consistent effective mass model that will serve as the basis for the calculation of the PL spectra.

5.3 Self-Consistent Effective Mass Model

As a first step in calculating the PL spectra of the Ge multiple-QW structure, we calculate the eigenstates of the system in the framework of a self-consistent multivalley effective mass approach. Before we explain the details of our approach, we start with an overview of our model.

In our self-consistent multivalley effective mass model, we include for the conduction band the Γ-point, L-point, and the Δ-valley, which are the lowest valleys in the conduction band of the SiGe material system. In the valence band, we include the HH, LH, and SO band. As will become clear in Sec. 5.5.1 when we analyze the band structure of the Ge multiple-QW sample, the holes are trapped in the Ge-rich well region while the electrons are localized in the Si barrier layer. As a consequence of the spatial separation of the charges, an electric field is created around the interface regions, which leads to the bending of the valence and conduction bands. The strength of the electric field depends on the number of excited charge carriers present in the system. Thus, to find the eigenvalues and eigenstates of the system, we have to include the electrostatic potential due to the charge separation into the effective mass Schrödinger equation. We do this in a self-consistent matter, which is illustrated in Fig. 5.6. Initially, the potential term $V(z)$ in the effective mass Schrödinger equation only includes the potential due to the band profile $V^{\alpha,l}$ for each band (α, l), where l marks the band index within the conduction or valence band which are indicated by $\alpha = \{\mathrm{c}, \mathrm{v}\}$. The Schrödinger equation is solved for each band separately. The eigenfunction and eigenenergies are then used to calculate the quasi-Fermi levels of the conduction and valence bands for a given excess carrier density n_{exc} and lattice temperature T. Next, the electrostatic potential V_σ is calculated based on the quasi-Fermi levels and resulting distribution of electrons and holes within the structure. The electrostatic potential is thereafter added to the potential profile of the bands to form the new potential term for the Schrödinger equation. The new potential term affects the distribution of charge carriers, which is taken into account in the next iteration. The self-consistent loop ends when the difference between the electrostatic potential calculated in two consecutive iterations is smaller than a predefined threshold (usually the numerical accuracy).

To continue with a more detailed description, we present our effective mass approach in two parts. First, we discuss the calculation of the eigenstates and eigenenergies in a multivalley effective mass model without the effect of the electric field. Secondly, we show how the multivalley effective mass model can be coupled to the Poisson equation to include the effects of the electric field due to the separation of electrons and holes. Lastly, we discuss selected details of the numerical implementation of our model.

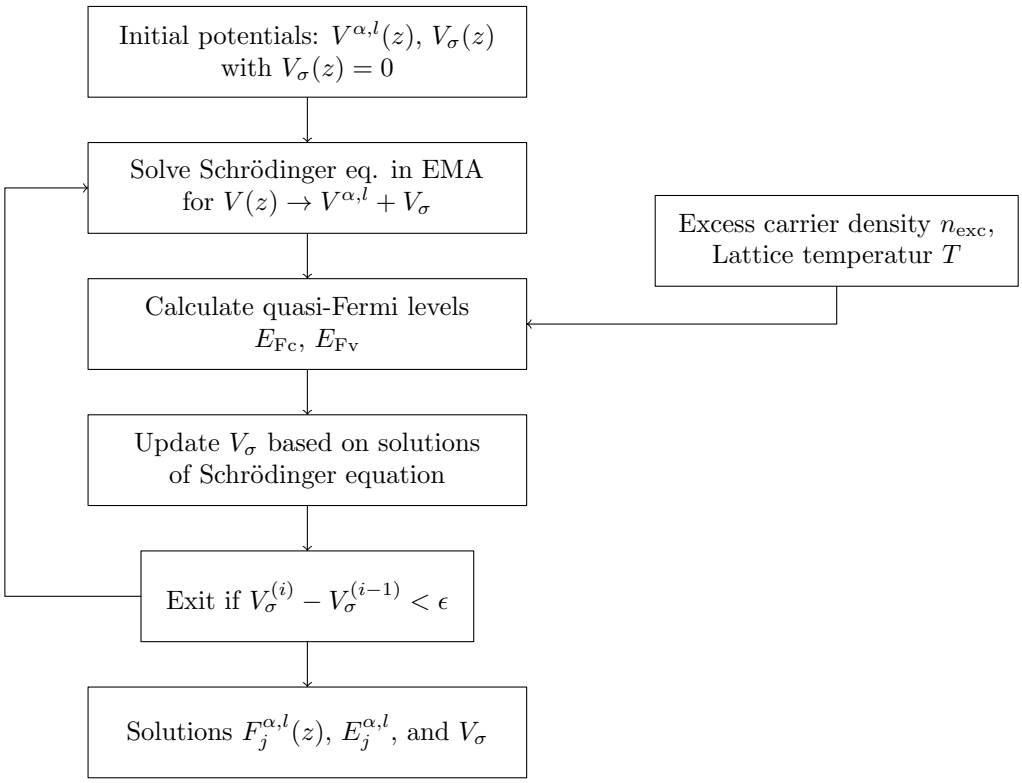

Figure 5.6: *Schematic of the self-consistent loop used to solve the coupled Poisson-Schrödinger equation. Initially, the electrostatic potential $V_\sigma(z)$ is set to zero. Initially, the potential term $V(z)$ of the Schrödinger equation only includes the layer specific band-edge energies $V^{\alpha,l}$ for each band (α, l) included in the model. The effective mass Schrödinger equation is solved for each band separately. Using an externally provided excess carrier density n_{exc} and lattice temperature T, the electron and hole quasi-Fermi energies E_{Fc} and E_{Fv} are calculated. Based on this, the electrostatic potential term $V_\sigma(z)$ is calculated. If the change in the electrostatic potential $V_\sigma(z)$ between two consecutive iterations is smaller than a predefined parameter ϵ, the calculation stops. Otherwise the calculation is repeated for the updated potential term $V(z)$.*

5.3.1 Multivalley Effective Mass Model

The Schrödinger equation in the effective mass approximation for charge carriers in the multiple-QW structure is given according to Eq. (2.62) by

$$\left[-\frac{\hbar^2}{2}\nabla\begin{pmatrix}1/m_x^{\alpha,l}(z) & 0 & 0\\ 0 & 1/m_y^{\alpha,l}(z) & 0\\ 0 & 0 & 1/m_z^{\alpha,l}(z)\end{pmatrix}\nabla + V^{\alpha,l}(z)\right]\phi_j^{\alpha,l}(\boldsymbol{\rho},z,\mathbf{k}_\parallel) = E_j^{\alpha,l}(\mathbf{k}_\parallel)\;\phi_j^{\alpha,l}(\boldsymbol{\rho},z,\mathbf{k}_\parallel), \tag{5.3}$$

where the growth direction of the QW structure is along the z-direction and we introduced appropriately cylindrical coordinates $(\boldsymbol{\rho},z)$. This equation is valid for all excited charge carriers in the different near-gap valleys, which we distinguish by the index (α,l), where α takes the value of c for a conduction and v for a valence band and l identifies the near-gap valley l in each band. The term $V^{\alpha,l}$ represents the potential term of each valley. Furthermore, we introduce the functions $1/m_x^{\alpha,l}(z)$, $1/m_y^{\alpha,l}(z)$, and $1/m_z^{\alpha,l}(z)$, which are the components of the inverse effective mass tensor along the respective directions. Both, the components of the inverse effective mass tensor and the potential term $V^{\alpha,l}$ are z-dependent. Also, $\phi_j^{\alpha,l}$ and $E_j^{\alpha,l}$ are the j-th eigenfunction and energy eigenvalue of band (α,l), respectively. Due to the layer structure along the z-direction, the z-component of the wavevector $\mathbf{k}$ is not a valid quantum number anymore. Instead, we introduce the wavevector $\mathbf{k}_\parallel$ that lies within the xy-plane, where the semiconductor remains periodic. Note that in Eq. (5.3), we require the effective mass tensor to be fully diagonal.

According to Sec. 2.3.2, we can make the following Ansatz for the eigenfunction $\phi_j^{\alpha,l}$

$$\phi_j^{\alpha,l}(\boldsymbol{\rho},z,\mathbf{k}_\parallel) = \frac{1}{\sqrt{A}}\mathrm{e}^{i\mathbf{k}_\parallel\cdot\boldsymbol{\rho}}\,F_j^{\alpha,l}(z)\;u^{\alpha,l}(\boldsymbol{\rho},z), \tag{5.4}$$

where A is the cross section of the multiple-QW structure, $F_j^{\alpha,l}$ is the envelope function, and $u^{\alpha,l}$ the zone center function for valley (α,l). Using this Ansatz in Eq. (5.3), we find for the envelope functions $F_j^{\alpha,l}$ of band (α,l) the eigenvalue equation

$$\left[-\frac{\hbar}{2}\frac{\mathrm{d}}{\mathrm{d}z}\frac{1}{m_\perp^{\alpha,l}(z)}\frac{\mathrm{d}}{\mathrm{d}z} + V^{\alpha,l}(z)\right]F_j^{\alpha,l}(z) = E_j^{\alpha,l}\;F_j^{\alpha,l}(z). \tag{5.5}$$

Here, $E_j^{\alpha,l}$ is related to the total energy of the charge carrier by

$$E_j^{\alpha,l}(\mathbf{k}_\parallel) = E_j^{\alpha,l} + \frac{\hbar^2 k_\parallel^2}{2m_{\parallel,j}^{\alpha,l}}, \tag{5.6}$$

where $m_{\parallel,j}^{\alpha,l}$ is the average effective mass of subband j of band (α,l) parallel to the interface and defined as [193]

$$\frac{1}{m_{\parallel,j}^{\alpha,l}} = \int_{-\infty}^{\infty}\mathrm{d}z\frac{|F_j^{\alpha,l}(z)|^2}{m_{\mathrm{2D}}^{\alpha,l}(z)}. \tag{5.7}$$

Here, $m_{\mathrm{2D}}^{\alpha,l}(z)$ is the position-dependent 2D density of states mass, which is given by [53]

$$m_{\mathrm{2D}}^{\alpha,l}(z) = \sqrt{m_x^{\alpha,l}(z) m_y^{\alpha,l}(z)}. \tag{5.8}$$

The components $m_x^{\alpha,l}(z)$, $m_y^{\alpha,l}(z)$, and $m_z^{\alpha,l}(z)$ of the effective mass tensor as well as the potential term $V^{\alpha,l}(z)$ are parameters that need to be provided externally. In the following, we describe how we obtain these parameters from the material parameters of Si and Ge.

Band Edge Energies

In the effective mass Schrödinger equation, the term $V^{\alpha,l}(z)$ describes the potential that a charge carrier in band (α, l) experiences and corresponds to the band edge energy of band (α, l) in each layer of the QW structure. The band edge energy throughout the structure can be derived by combining information about the sizes of the direct and indirect band-gaps for each layer with information about the alignment of the band-gaps between layers.

For Si and Ge, the band-gaps at the Γ-point, L-point, and Δ-valley are known [22]. To calculate the band-gaps of $\mathrm{Si}_{1-x}\mathrm{Ge}_x$ alloys, we linearly average the band-gaps for the Γ- and L-point and use the bowing equations given in Ref. [80] for the Δ-valley. At an interface between elemental Si and Ge, the authors of Ref. [121] calculated the band offset between the barycenter of the HH, LH, and SO bands for $\mathrm{Si}_{1-x}\mathrm{Ge}_x$ alloys grown on Si, which we use to determine the alignment of bands at the interface between layers.

Furthermore, we consider the effects of strain on the band-gap energies. Due to the difference of the lattice constants for the various $\mathrm{Si}_{1-x}\mathrm{Ge}_x$ alloys, individual layers in the multiple-QW structure can be strained. To take into account the shift of the band edge energies due to strain, we use the equations derived in Sec. 3 of Chap. 3. For the valence band edge energies, the shift of the band edge energy as a function of strain is given by

$$\Delta E_\varepsilon^{\mathrm{HH}} = -P_\varepsilon - Q_\varepsilon, \tag{5.9}$$

$$\Delta E_\varepsilon^{\mathrm{LH}} = -P_\varepsilon + \frac{1}{2}\left(Q_\varepsilon - \Delta + \sqrt{9Q_\varepsilon^2 + 2\Delta Q_\varepsilon + \Delta^2}\right), \tag{5.10}$$

$$\Delta E_\varepsilon^{\mathrm{SO}} = -P_\varepsilon + \frac{1}{2}\left(Q_\varepsilon - \Delta - \sqrt{9Q_\varepsilon^2 + 2\Delta Q_\varepsilon + \Delta^2}\right), \tag{5.11}$$

where $P_\varepsilon = a_v(\varepsilon_{xx} + \varepsilon_{yy} + \varepsilon_{zz})$ and $Q_\varepsilon = -\frac{b}{2}(\varepsilon_{xx} + \varepsilon_{yy} - 2\varepsilon_{zz})$ and ε_{ij} are the components of the strain tensor tensor $\underline{\underline{\varepsilon}}$. The shift of the conduction band edge energies is given by

$$\Delta E_\varepsilon^{\Gamma} = a_c^{\Gamma}\,\mathrm{Tr}(\varepsilon), \tag{5.12}$$

$$\Delta E_\varepsilon^{\mathrm{L}} = a_c^{\mathrm{L}}\,\mathrm{Tr}(\varepsilon), \tag{5.13}$$

$$\Delta E_\varepsilon^{\Delta_4} = a_c^{\Delta}\,\mathrm{Tr}(\varepsilon) - \frac{1}{3}(\varepsilon_{zz} - \varepsilon_{xx}), \tag{5.14}$$

$$\Delta E_\varepsilon^{\Delta_2} = a_c^{\Delta}\,\mathrm{Tr}(\varepsilon) + \frac{2}{3}(\varepsilon_{zz} - \varepsilon_{xx}). \tag{5.15}$$

For the description of $\mathrm{Si}_{1-x}\mathrm{Ge}_x$ alloys, we average the material parameters a_{v}, b, a_{c}^{Γ}, $a_{\mathrm{c}}^{\mathrm{L}}$, and a_{c}^{Δ} linearly according to the composition.

Finally, for calculating the variation of the band gap size with temperature, we use the empirical equation by Varshni given by [194]

$$E_g^{\alpha,l}(T) = E_g^{\alpha,l}(0) - \frac{\alpha' T^2}{T + \beta'}, \tag{5.16}$$

where $E_g^{\alpha,l}(0)$ is the band-gap of band (α, l) at zero-temperature and α' and β' are two fitting parameters. For the band-gap at the L-point of Si and the Δ-valley of Ge, no data on the temperature dependence is available. We therefore use the parametrization of the other material, respectively.

Effective Masses

To derive the effective masses for each layer in our multiple-QW structure, we differentiate between valence and conduction bands. For the valence bands, it can be shown that the effective masses of HH, LH, and SO can be derived analytically from the six-band $\mathbf{k} \cdot \mathbf{p}$ Hamiltonian given in Eq. (3.40) as a function of the Luttinger parameters $\{\gamma_1, \gamma_2, \gamma_3\}$ [195]:

$$\frac{m_z^{\mathrm{HH}}}{m_0} = \frac{1}{\gamma_1 - 2\gamma_2} \qquad \frac{m_{x,y}^{\mathrm{HH}}}{m_0} = \frac{1}{\gamma_1 + \gamma_2}, \tag{5.17}$$

$$\frac{m_z^{\mathrm{LH}}}{m_0} = \frac{1}{\gamma_1 + 2f_+\gamma_2} \qquad \frac{m_{x,y}^{\mathrm{LH}}}{m_0} = \frac{1}{\gamma_1 - f_+\gamma_2}, \tag{5.18}$$

$$\frac{m_z^{\mathrm{SO}}}{m_0} = \frac{1}{\gamma_1 - 2f_-\gamma_2} \qquad \frac{m_{x,y}^{\mathrm{SO}}}{m_0} = \frac{1}{\gamma_1 - f_-\gamma_2}, \tag{5.19}$$

where $f_\pm$ is defined as

$$f_\pm = \frac{2x\left[1 + \frac{2}{3}\left(x - 1 \pm \sqrt{1 + 2x + 9x^2}\right)\right] + 6x^2}{\frac{3}{4}\left(x - 1 \pm \sqrt{1 + 2x + 9x^2}\right)^2 + x - 1 \pm \sqrt{1 + 2x + 9x^2} - 3x^2} \tag{5.20}$$

with

$$x = \frac{-\frac{b}{2}(\varepsilon_{xx} + \varepsilon_{yy} - 2\varepsilon_{zz})}{\Delta_{\mathrm{SO}}}, \tag{5.21}$$

where ε_{ij} are the components of the strain tensor and Δ_{SO} corresponds to the spin-orbit splitting. The effect of pseudomorphic strain on the effective masses of LH and SO is accounted for by the factor $f_\pm$. The HH is to first order unaffected by strain. To calculate the effective masses of $Si_{1-x}Ge_x$ alloys, we use the compositional dependence of the Luttinger parameters $\{\gamma_1, \gamma_2, \gamma_3\}$ for $Si_{1-x}Ge_x$ alloys given in Ref. [32].

For the effective masses of the Δ-valley and the L-point, we use the values derived numerically with an EPM approach for pseudomorphic (100)-strained $Si_{1-x}Ge_x$ alloys grown on an unstrained $Si_{1-y}Ge_y$ substrate [32]. For the effective mass at the Γ-point, we use the effective mass of relaxed Ge for all alloy compositions and strain states for lack of data [196].

In our treatment of the effective masses, we have to consider that the inverse effective mass tensor is always given in the principle axis system of the valley, for which the inverse effective mass tensor is diagonal. The principle axis system does not necessarily correspond to the Cartesian coordinates used in Eq. (5.3). This is only the case for the conduction and valence bands at the Γ-point. For the Δ-valleys, the principle axes are parallel to the Cartesian coordinate axes, which requires a trivial transformation of the inverse effective mass tensor. The situation is more complicated for the valleys located at the L-point. A nontrivial coordinate transformation is required to obtain the inverse effective mass tensor in the coordinate system of the effective mass Schrödinger equation. This coordinate transformation leads to an inverse

effective mass tensor that also includes off-diagonal elements. For the L-valley located at position $\mathbf{k} = \frac{\pi}{a}(1,1,1)$ in the Brillouin zone, the transformed effective mass tensor reads [197]:

$$\left(\frac{1}{m^*}\right)_{ij} = \begin{pmatrix} \frac{2m_\mathrm{l}+m_\mathrm{t}}{2m_\mathrm{l}m_\mathrm{t}} & \frac{m_\mathrm{t}-m_\mathrm{l}}{3m_\mathrm{l}m_\mathrm{t}} & \frac{m_\mathrm{t}-m_\mathrm{l}}{3m_\mathrm{l}m_\mathrm{t}} \\ \frac{m_\mathrm{t}-m_\mathrm{l}}{3m_\mathrm{l}m_\mathrm{t}} & \frac{2m_\mathrm{l}+m_\mathrm{t}}{2m_\mathrm{l}m_\mathrm{t}} & \frac{m_\mathrm{t}-m_\mathrm{l}}{3m_\mathrm{l}m_\mathrm{t}} \\ \frac{m_\mathrm{t}-m_\mathrm{l}}{3m_\mathrm{l}m_\mathrm{t}} & \frac{m_\mathrm{t}-m_L}{3m_\mathrm{l}m_\mathrm{t}} & \frac{2m_\mathrm{l}+m_\mathrm{t}}{2m_\mathrm{l}m_\mathrm{t}} \end{pmatrix}, \tag{5.22}$$

where m_l and m_t are the longitudinal and transverse effective masses of the original diagonal effective mass tensor in the principle axis system, respectively. Using the generalized kinetic energy operator T given by

$$T = \frac{1}{2}\sum_{i,j} p_i\, w_{ij}\, p_j, \tag{5.23}$$

where the p_i are the components of the momentum operator $\mathbf{p}$ and $w_{ij} \equiv (1/m^*_{ij})$ is equivalent to the inverse effective mass tensor, we find that the motion of the electron in the x, y, and z directions are coupled. As a result, we cannot solve the Schrödinger equation independently for the in-plane and out-of-plane motion as intended in Eq. (5.5). To decouple the motion again, we apply the procedure described in Ref. [198] to diagonalize the inverse effective mass tensor of the L-valley. As before, we express the solution of the Schrödinger equation for a QW structure in envelope function notation:

$$\phi(x,y,z) = \xi(z)\mathrm{e}^{ik_1x+k_2y}, \tag{5.24}$$

where we neglected the lattice-periodic function $u(\boldsymbol{\rho}, z)$ and dropped the band index (α, l) for simplicity. Furthermore, k_1 and k_2 are the components of the crystal wavevector $\mathbf{k}_\parallel$. Inserting this Ansatz into the Schrödinger equation with the generalized kinetic energy operator as given in Eq. (5.23), we find a new differential equation for $\xi(z)$:

$$-\frac{1}{2}w_{33}\hbar^2\frac{\mathrm{d}^2\xi}{\mathrm{d}z^2} - \hbar^2(w_{13}k_1 + w_{23}k_2)\frac{\mathrm{d}\xi}{\mathrm{d}z} - (V(z)+E')\xi(z) = 0, \tag{5.25}$$

where the energy term E' is related to the total energy $E(k_1,k_2)$ of the charge carriers with momentum $\mathbf{k}_\parallel = (k_1,k_2)$ by

$$E = E' + \frac{1}{2}\hbar^2(w_{11}k_1^2 + 2w_{12}k_1k_2 + w_{22}k_2^2). \tag{5.26}$$

The second term in Eq. (5.25) still includes a coupling of the components k_1 and k_2 of the in-plane crystal momentum and a first-order derivative in the z-direction. To remove the coupling, we perform a second transformation given by

$$\xi(z) = \zeta(z)\mathrm{e}^{-iz(w_{12}k_1+w_{23}k_2)/w_{33}}, \tag{5.27}$$

which transforms the eigenvalue equation into

$$-\frac{\hbar^2}{2}\frac{\mathrm{d}\zeta}{\mathrm{d}z}\frac{1}{m_z^*}\frac{\mathrm{d}\zeta}{\mathrm{d}z} + V(z)\zeta(z) = E''\zeta(z), \tag{5.28}$$

where we used $m_z^* = w_{33}^{-1}$. This equation is equivalent to Eq. (5.5) except for the total energy term, which is now given by

$$E(k_1,k_2) = E'' + \frac{1}{2}\hbar^2\left[\left(w_{11}-\frac{w_{13}^2}{w_{33}}\right)k_1^2 + 2\left(w_{12}-\frac{w_{13}w_{23}}{w_{33}}\right)k_1k_2 + \left(w_{22}-\frac{w_{23}^2}{w_{33}}\right)k_2^2\right]. \tag{5.29}$$

The shape of Eq. (5.28) is equivalent to Eq. (5.5). Thus, we can still use Eq. (5.5) for all conduction and valence band valleys. We only have to redefine the 2D density of states mass $m_{2D}^{\mathrm{c,L}}$ for the L-valley previously given in Eq. (5.8) to

$$m_{2D}^{\mathrm{cL}}(z) = \left[\left(w_{11} - \frac{w_{13}^2}{w_{33}} \right) \left(w_{22} - \frac{w_{23}^2}{w_{33}} \right) - \left(w_{12} - \frac{w_{13} w_{23}}{w_{33}} \right)^2 \right]^{-1/2}, \tag{5.30}$$

where the z-dependence of the 2D density of states mass is contained within the z-dependence of the inverse effective mass tensor w_{ij}.

With this equation, we fully defined our multivalley effective mass model and the appropriate effective masses and potential profiles, which serve as input parameters. What we left out so far is the contribution of the electric field to the potential term $V^{\alpha,l}(z)$, which is caused by the spatial separation of charges within the structure. The effect of the electric field can be included into our calculations using the Schrödinger-Poisson coupling.

5.3.2 Poisson-Schrödinger Coupling

In SiGe heterostructures, electrons are typically confined within the Si-rich layers, whereas holes are confined to the Ge-rich regions due to the type-II band alignment. This separation of charge leads to the creation of an electric field, which introduces a band bending. The relationship between the electric field $\mathbf{E}$ and the charge density ϱ is given according to Gauss' law by [199]

$$\nabla \mathbf{E} = \frac{\varrho}{\epsilon_r \epsilon_0}, \tag{5.31}$$

where ϵ_r is the relative permittivity and ϵ_0 the permittivity of the vacuum. Furthermore, the electrostatic potential V_ϱ is related to the electric field by the differential equation

$$\mathbf{E} = -\nabla V_\varrho. \tag{5.32}$$

Substituting the electric field in Eq. (5.31) with the expression in Eq. (5.32), we obtain the Poisson equation

$$\nabla^2 V_\varrho = -\frac{\varrho}{\epsilon_r \epsilon_0}. \tag{5.33}$$

The electrostatic potential needs to be added to the potential term $V^{\alpha,l}(z)$ in the Schrödinger equation to include the band bending effects caused by the electric field. Instead of solving the Poisson equation, we follow a different approach when calculating the potential numerically. For a 1-dimensional structure consisting of infinite small layers of thickness δz with a surface charge density σ, each layer produces an electric field $\mathbf{E}$ perpendicular to it of size

$$\mathbf{E} = \frac{\sigma}{2\epsilon_r \epsilon_0} \hat{\mathbf{e}}_z. \tag{5.34}$$

The total electric field can then be calculated by summing over all layers of the structure

$$\mathbf{E}(z) = \sum_{z'=-\infty}^{\infty} \frac{\sigma(z')}{2\epsilon_r(z')\epsilon_0} \mathrm{sign}(z - z') \hat{\mathbf{e}}_z, \tag{5.35}$$

where the sign-function ensures that the sign of the electric field of each infinitely small layer is included correctly depending on its position z' relative to position z. Here, we limit our

investigation to intrinsic semiconductors and neglect any background doping. The charge density $\sigma(z)$ of a single layer is given by the sum over the occupied electron and hole states at position z

$$\sigma(z) = -e \sum_{\alpha=\mathrm{c,v}} \sum_{l} \sum_{j} n_j^{\alpha,l} \, |\phi_j^{\alpha,l}(z)|^2 \, \delta z, \tag{5.36}$$

where $n_j^{\alpha,l}$ represents the surface density of excited charge carriers in subband j of band (α, l). The surface density of excited charge carriers is given by the integral over the product of the 2D density of states $\rho_{\mathrm{2D}}^{\alpha,l}$ and the Fermi-function for $f_\alpha(E, E_{F\alpha})$ with the quasi-Fermi level $E_{F\alpha}$ for holes respectively electrons

$$n_j^{\alpha,l} = D^{\alpha,l} \int_{E_j^{\alpha,l}}^{\infty} \rho_j^{\alpha,l}(E) f_\alpha(E, E_{F\alpha}) \mathrm{d}E, \tag{5.37}$$

where $D^{\alpha,l}$ is the number of degenerate valleys of the band. The density of states for QW structures in the effective mass approximation is just a constant and given for each band (α, l) by

$$\rho_j^{\alpha,l}(E) = \frac{m_{\parallel,j}^{\alpha,l}}{\pi\hbar^2}, \tag{5.38}$$

The Fermi-function for conduction and valence band reads

$$\begin{aligned} f_\mathrm{c}(E, E_\mathrm{Fc}) &= \frac{1}{\mathrm{e}^{(E-E_\mathrm{Fc})/k_\mathrm{B}T} + 1}, \\ f_\mathrm{v}(E, E_\mathrm{Fv}) &= \frac{1}{\mathrm{e}^{(E_\mathrm{Fv}-E)/k_\mathrm{B}T} + 1}, \end{aligned} \tag{5.39}$$

where k_B is the Boltzmann constant and T the lattice temperature. Combining Eq. (5.37), Eq. (5.38), and Eq. (5.39), we find for the surface density of electrons within a conduction subband

$$n_j^{\mathrm{c},l} = D^{\mathrm{c},l} \int_{E_j^{\mathrm{c},l}}^{\infty} \frac{m_{\parallel,j}^{\mathrm{c},l}}{\pi\hbar^2} \frac{1}{\mathrm{e}^{(E-E_\mathrm{Fc})/k_\mathrm{B}T} + 1} \mathrm{d}E = D^{\mathrm{c},l} \frac{m_j^{\mathrm{c},l} k_\mathrm{B} T}{\pi\hbar^2} \ln\left(\mathrm{e}^{(E_\mathrm{Fc}-E)/k_\mathrm{B}T} + 1\right). \tag{5.40}$$

For the surface density of holes within a valence subband, we find

$$n_j^{\mathrm{v},l} = -D^{\mathrm{v},l} \frac{m_{\parallel,j}^{\mathrm{v},l} k_\mathrm{B} T}{\pi\hbar^2} \ln\left(\mathrm{e}^{(E-E_\mathrm{Fv})/k_\mathrm{B}T} + 1\right). \tag{5.41}$$

Here, we chose the opposite sign in comparison to the conduction band expression to take into account that occupied valence bands contribute with positive charge in Eq. (5.36). The quasi-Fermi level for conduction and valence band itself is determined by the relationship

$$n_\mathrm{exc} = \sum_{l} \sum_{j} n_j^{\mathrm{c},l} = \sum_{l} \sum_{j} n_j^{\mathrm{v},l}, \tag{5.42}$$

where n_exc is the surface density of excited electron-hole pairs which needs to be provided as an input parameter. Combining Eq. (5.35) with Eq. (5.36) and Eq. (5.42), the electric field inside the structure can be calculated. Instead of using the differential approach of Eq. (5.32) to calculate the electrostatic potential from the electric field, we can formulate an integral relationship between both

$$V_\sigma(z) = -\int_{-\infty}^{z} \mathrm{d}z \, |\mathbf{E}(z)|. \tag{5.43}$$

By adding the potential term $V_\sigma(z)$ in Eq. (5.43) to the potential term $V^{\alpha,l}$ given in Eq. (5.5) for each band (α, l), the effective mass Schrödinger equation can be solved self-consistently following the schematic in Fig. 5.6.

Lastly, we want to briefly describe how the effective mass Schrödinger equation can be solved numerically.

5.3.3 Numerical Realization

In order to solve the effective mass envelope function equation given in Eq. (5.5) numerically, we use the finite difference method. We discretize our 1D QW structure by uniformly distributing N nodes over the space of interest. The position of each node is given by $z_i = i\,\delta z$, where δz is the distance between two neighboring nodes. We approximate the first derivative of a function $f(z)$ at node i by the finite difference

$$\left.\frac{\mathrm{d}f}{\mathrm{d}z}\right|_{z_i} \approx \frac{f(z_{i-1}) - f(z_{i+1})}{2\delta z}. \tag{5.44}$$

Generalizing this equation to the second derivative, we can approximate the effective mass envelope function by:

$$\begin{aligned} -\frac{\hbar^2}{(\delta z)^2}\left(\frac{1}{m_{i-1/2}}\right)\phi_{i-1} \\ + \left[\frac{\hbar^2}{(\delta z)^2}\left(\frac{1}{m_{i-1/2}} + \frac{1}{m_{i+1/2}}\right) + V_i\right]\phi_i, \\ - \frac{\hbar^2}{(\delta z)^2}\left(\frac{1}{m_{i+1/2}}\right)\phi_{i+1} = E\phi_i \end{aligned} \tag{5.45}$$

where for simplicity we dropped the band index (α, l) for the potential term $V^{\alpha,l}$ and the effective mass term $m^{\alpha,l}$ and used the convention $V_i = V(z_i)$, $\phi_i = \phi(z_i)$, $m_{i-1/2} = (m(z_i) + m(z_{i-1}))/2$, and $m_{i+1/2} = (m(z_i) + m(z_{i+1}))/2$. This equation may be rewritten into a matrix eigenvalue equation given by

$$\sum_j^N A_{ij}\phi_j = E\phi_i, \tag{5.46}$$

where the matrix elements A_{ij} are defined as

$$A_{ij} = \begin{cases} -\frac{\hbar^2}{(\delta z)^2}\left(\frac{1}{m_{i-1/2}}\right) & \text{if} j = i-1, \\ \frac{\hbar^2}{(\delta z)^2}\left(\frac{1}{m_{i-1/2}} + \frac{1}{m_{i+1/2}}\right) + V_i & \text{if} j = i, \\ -\frac{\hbar^2}{(\delta z)^2}\left(\frac{1}{m_{i+1/2}}\right) & \text{if} j = i+1, \\ 0 & \text{otherwise.} \end{cases} \tag{5.47}$$

The matrix A_{ij} is symmetric. Moreover, the matrix elements A_{ij} are nonzero only on the diagonal, sub- and superdiagonal. The matrix A_{ij} is appropriately modified for the applied boundary conditions, which one can select to be either periodic or Dirichlet. Therefore, our

approach can be used to investigate both superlattices and single QW structures. The matrix eigenvalue equation can be solved using standard eigenvalue solvers. In our implementation, we use the QR algorithm as implemented in `LAPACK`, which makes use of the tridiagonal structure of the matrix A_{ij}.

Using the self-consistent effective mass model described above, we are now able to calculate the eigenenergies and eigenstates of our multiple-QW structure. To calculate the PL spectra of the structure, we have to understand how we can obtain the PL spectrum from the eigenstates. Thus, we now turn our attention to the theory of heterostructure PL.

5.4 Theory of Heterostructure Photoluminescence

The theory of heterostructure PL can be developed in analogy to the theory of bulk PL, which we treated in Sec. 3.5.3 of Chap. 3. Again, we can divide the PL spectrum into peaks that stem from direct and peaks that stem from indirect radiative recombination mechanisms. From the investigation of the experimental PL measurements, we suspect that the observed emission is due to indirect recombination processes. This will be confirmed in the investigation of the band structure of the Ge multiple-QW in Sec. 5.5.1, where we will find that the lowest conduction band states are the confined states related to the Δ-valleys while the confined states of the Γ-band are roughly 2 eV higher. As a result, the observed PL is primarily a result of the indirect recombination involving either phonons (phonon-assisted recombination) or elastic scattering centers like crystal defects, alloy disorder, or interfaces roughness (NP recombination). Therefore, we focus our theoretical description of the PL emission to the indirect recombination processes. First, we describe the phonon-assisted processes and, afterward, move on to the NP processes. A description of the direct recombination mechanisms can be found in Ref. [90].

5.4.1 Phonon-Assisted Spontaneous Radiative Recombination

As discussed in detail in Sec. 3.5.3, we can limit the our derivation of the phonon-assisted recombination processes to type I processes during which the electronic system interacts with a phonon before the emission of a photon (see Fig. 5.7). To calculate the spectrally-resolved emission rate of photons resulting from indirect band-to-band recombination, we again apply Fermi's Golden Rule for second-order transitions:

$$P_{i\to f} = \frac{2\pi}{\hbar}\left|\sum_m \frac{\langle f|H_{\text{int}}|m\rangle\langle m|H_{\text{int}}|i\rangle}{E'_m - E'_i}\right|^2 \delta(E'_i - E'_f), \tag{5.48}$$

where the states $|i\rangle$, $|m\rangle$, and $|f\rangle$ describe the initial, intermediate, and final state. The energies E'_i, E'_m, and E'_f denote the total energy of the respective states including the contributions from the electronic system, the electromagnetic field, and the phonon field. As for bulk material, the term H_{int} is the interaction Hamiltonian and can be split into the interaction of the electronic system with the electromagnetic field $H_{\text{int}}^{\text{e.m.}}$ and the interaction of the electronic system and the lattice vibrations $H_{\text{int}}^{\text{ph}}$:

$$H_{\text{int}} = H_{\text{int}}^{\text{e.m.}} + H_{\text{int}}^{\text{ph}}. \tag{5.49}$$

For our Ge multiple-QW structure, the initial states are the populated subbands of the strain-split Δ-valley Δ_2 and Δ_4 valleys (indicated in the following by cΔ). The electronic final states are the populated subbands of the HH, LH, and SO bands (indicated by vΓ). Similar to

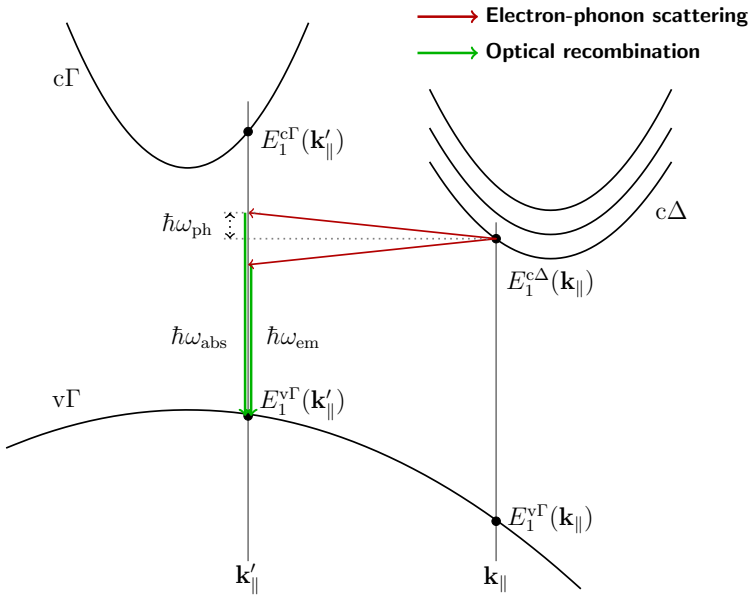

Figure 5.7: *Schematic of the phonon-assisted recombination in the Ge multiple-QW sample. Shown is the indirect recombination of an electron at the lowest subband of the* cΔ *valley with a hole in the* vΓ *valley. Due to the large energetic separation between valence and conduction subbands at the* Γ*-point, only the lowest subband for the* cΓ *and* vΓ *band are shown.*

bulk semiconductors, the initial and final states are given by product states consisting of the electronic, the photonic, and phononic state of the system:

$$|i\rangle = |\phi_a^{c\Delta}(\mathbf{k}_\parallel)\rangle|0\rangle|\cdots n_{ph}(\mathbf{q})\cdots\rangle, \tag{5.50}$$

$$|f^{abs}\rangle = |\phi_b^{v\Gamma}(\mathbf{k}'_\parallel)\rangle|0\cdots 1_\omega\cdots 0\rangle|\cdots (n_{ph}(\mathbf{q})-1)\cdots\rangle, \tag{5.51}$$

$$|f^{em}\rangle = |\phi_b^{v\Gamma}(\mathbf{k}'_\parallel)\rangle|0\cdots 1_\omega\cdots 0\rangle|\cdots (n_{ph}(\mathbf{q})+1)\cdots\rangle, \tag{5.52}$$

where $\mathbf{k}_\parallel$ describes the in-plane momentum of the charge carriers, b and c are the subband indices of the initial and final electronic state, respectively, and $n_{ph}(\mathbf{q})$ is the number of phonon with wave vector $\mathbf{q} \equiv (\mathbf{q}_\parallel, q_z)$ present in the system. Moreover, the full wave function of the electronic part of the system is given in cylindrical coordinates $\mathbf{r} = (\boldsymbol{\rho}, z)$ by

$$\langle \mathbf{r}|\phi_a^{\alpha,l}(\mathbf{k}_\parallel)\rangle = \frac{1}{\sqrt{A}} e^{i\mathbf{k}_\parallel\cdot\boldsymbol{\rho}} F_a^{\alpha,l}(z)\, u^{\alpha,l}(\boldsymbol{\rho}, z). \tag{5.53}$$

Here, $F_a^{\alpha,l}(z)$ is the envelope function of subband a of band (α, l), $u^{\alpha,l}(\boldsymbol{\rho}, z)$ is the lattice-periodic function, and A is the area of cross section perpendicular to the growth direction. The intermediate states for phonon emission and absorption are given by

$$|m^{em}\rangle = |\phi_1^{c\Gamma}(\mathbf{k}''_\parallel)\rangle|0\rangle|\cdots (n_{ph}(\mathbf{q})+1)\cdots\rangle, \tag{5.54}$$

$$|m^{abs}\rangle = |\phi_1^{c\Gamma}(\mathbf{k}''_\parallel)\rangle|0\rangle|\cdots (n_{ph}(\mathbf{q})-1)\cdots\rangle, \tag{5.55}$$

respectively. Here, we have already made use of the fact that due to the strong confinement of the electrons, there is a strong energy separation of the conduction subbands at the Γ-point.

Therefore, we can limit the sum over the intermediate states in Eq. (5.48) to the lowest subband only. The contribution of higher subbands is suppressed as a result of the large energy difference $E'_m - E'_f$ in the denominator of Eq. (5.48).

The phonon-electron interaction Hamiltonian for confined electronic states has the following form [200]:

$$H_{\text{int}}^{\text{ph}} = \sum_{\mathbf{q}_\parallel, q_z} \sum_{n,m} \sum_{\mathbf{k}_\parallel} D_{\mathbf{q}_\parallel, q_z} M^{j,j'}_{\alpha,\alpha',l,l'}(q_z)(b_{\mathbf{q}} + b^\dagger_{-\mathbf{q}}) c^\dagger_{\alpha,l,j,\mathbf{k}_\parallel+\mathbf{q}_\parallel} c_{\alpha',l',j',\mathbf{k}_\parallel}, \tag{5.56}$$

where $b_{\mathbf{q}}$ and $b^\dagger_{-\mathbf{q}}$ are the bosonic annihilation and creation operators for a phonon with momentum $\pm\mathbf{q}$ while $c_{\alpha,l,j,\mathbf{k}_\parallel}$ is the fermionic annihilation operator of an electron in subband j of band (α, l) with in-plane momentum $\mathbf{k}_\parallel$ and $c^\dagger_{\alpha,l,j,\mathbf{k}_\parallel}$ is the respective annihilation operator [105]. The matrix $M^{j,j'}_{\alpha,\alpha',l,l'}(q_z)$ determines the strength of the transition from subband j of band (α, l) to subband j' of band (α', l') as a function of q_z and is a result of the symmetry breaking along the z-direction.

Since we cannot resolve the different phonon branches experimentally, we follow for simplicity Refs. [106, 201] and approximate the electron-phonon interaction considering only an effective bulklike dispersionless phonon. We set the phonon energy equal to the measured energy separation between the NP and phonon-assisted spectral features ($\hbar\omega_{\text{ph}} = 51\,\text{meV}$). Consequently, we can assume for $D_{\mathbf{q}_\parallel, q_z}$

$$D_{\mathbf{q}_\parallel, q_z} = D_{\text{eff}} \sqrt{\frac{\hbar^2}{2\rho_{\text{M}} V \hbar\omega_{\text{ph}}}}, \tag{5.57}$$

where ρ_{M} is the mass density of the crystal, V is the volume, and D_{eff} is an effective deformation potential. Thus, the squared matrix element for the electron-phonon interaction is given by

$$\left|\langle i|H_{\text{int}}^{\text{ph}}|m^{\text{em/abs}}\rangle\right|^2 = D_{\text{eff}}^2 \frac{\hbar^2}{2\rho_{\text{M}} V \hbar\omega_{\text{ph}}} \delta_{\mathbf{k}''_\parallel, \mathbf{k}_\parallel \mp \mathbf{q}_\parallel} \times (n_{\text{ph}} + \frac{1}{2} \pm \frac{1}{2}) \times \left|M_{i,m}(q_z)\right|^2, \tag{5.58}$$

where $M_{i,m}(q_z)$ corresponds to the term $M^{j,j'}_{\alpha,\alpha',l,l'}(q_z)$ in Eq. (5.56). Considering cΔ and cΓ for the initial and intermediate states, $M_{i,f}(q_z)$ can be written as

$$M_{i,m}(q_z) \equiv M_a^{\text{c}\Delta}(q_z) = \int_{-L_{\text{w}}/2}^{+L_{\text{w}}/2} \left(F_a^{\text{c}\Delta}(z)\right)^* e^{iq_z z} F_1^{\text{c}\Gamma}(z)\,\text{d}z, \tag{5.59}$$

where L_{w} is the combined length of a single well and barrier region.

Identical to bulk material, the electromagnetic interaction Hamiltonian $H_{\text{int}}^{\text{e.m.}}$ can be written as

$$H_{\text{int}}^{\text{e.m.}} = \frac{e}{m_0} \sqrt{\frac{\hbar}{2\omega\epsilon V}} (a_{\hat{\mathbf{e}}}\, \text{e}^{i(\mathbf{k}_{\lambda\parallel}\cdot\boldsymbol{\rho} + \mathbf{k}_{\lambda\perp} z - \omega t)} + a^\dagger_{\hat{\mathbf{e}}}\, \text{e}^{-i(\mathbf{k}_{\lambda\parallel}\cdot\boldsymbol{\rho} + k_{\lambda\perp} z - \omega t)}) \hat{\mathbf{e}} \cdot \mathbf{p}, \tag{5.60}$$

where $a_{\hat{\mathbf{e}}}$ and $a^\dagger_{\hat{\mathbf{e}}}$ are the annihilation and creator operator of a photon with polarization $\hat{\mathbf{e}}$, respectively, $\mathbf{k}_\lambda = (\mathbf{k}_{\lambda\parallel}, k_{\lambda\perp})$ is the photon momentum, $\epsilon = \epsilon_r \epsilon_0$ is the permittivity of the environment[2], and V is the volume of the system. The absolute value squared of the expectation

[2] Due to the thickness of the sample, self-absorption of the PL can be neglected. Moreover, the spectral range of the PL emission is limited to a small frequency range. Therefore, we approximate the permittivity to be real and constant for all frequencies.

value of the electromagnetic interaction between intermediate state and final state is then given by

$$\left|\langle m^{\mathrm{em/abs}}|H_{\mathrm{int}}^{\mathrm{e.m.}}|f^{\mathrm{em/abs}}\rangle\right|^2 = \left(\frac{e}{m_0}\right)^2 \frac{\hbar}{2V\omega\epsilon_0\epsilon}\delta_{\mathbf{k}_\parallel'',\mathbf{k}_\parallel'} \times \left|\mathbf{p}_{\mathrm{v}\Gamma,\mathrm{c}\Gamma}\cdot\hat{\mathbf{e}}\right|^2 \times \left|I_b^{\mathrm{v}\Gamma}\right|^2, \tag{5.61}$$

where we defined $\mathbf{p}_{\mathrm{v}\Gamma,\mathrm{c}\Gamma}$ and $I_b^{\mathrm{v}\Gamma}$ as

$$\mathbf{p}_{\mathrm{v}\Gamma,\mathrm{c}\Gamma} = \int_\Omega u_{\mathrm{v}\Gamma}(\boldsymbol{\rho},z)\,\mathbf{p}\,u_{\mathrm{c}\Gamma}(\boldsymbol{\rho},z)\,\mathrm{d}\boldsymbol{\rho}\,\mathrm{d}z, \tag{5.62}$$

$$I_b^{\mathrm{v}\Gamma} = \int_{-L_\mathrm{w}/2}^{+L_\mathrm{w}/2} F_{\mathrm{c}\Gamma}^1(z)^* F_{\mathrm{v}\Gamma}^b(z)\mathrm{d}z. \tag{5.63}$$

$$\tag{5.64}$$

Note that we have neglected the in-plane photon momentum $\mathbf{k}_{\lambda,\parallel}$ as the photon wavevector is much smaller than the carrier wavevectors. Along the same line of argumentation, we assumed the product $k_{\lambda\perp}z$ to be constant and close to zero in the expression for $I_b^{\mathrm{v}\Gamma}$ and assume $\mathrm{e}^{ik_{\lambda\perp}z} \approx 1$. Similar to the matrix $M_{\alpha,\alpha',l,l'}^{j,j'}(q_z)$ in Eq. (5.56), the integral $I_{\mathrm{v}\Gamma}^b$ is a result of the symmetry breaking along the z-direction.

The spectrally-resolved rate of spontaneous emission of photons via phonon-assisted recombinations can then be calculated by summing over all electronic and phononic degrees of freedom and polarization modes related to photons emitted normally to the sample surface. Considering the Fermi functions $f_\mathrm{c}(E_i(\mathbf{k}_{\parallel,i}))$ and $f_\mathrm{v}(E_f(\mathbf{k}_{\parallel,f})$ for electrons and holes, we obtain in analogy to Eq. (3.73) in Chap. 3

$$R_{\mathrm{sp}}^{\mathrm{ind}}(\hbar\omega)d(\hbar\omega) = \frac{1}{V}\sum_{\hat{\mathbf{e}}}\sum_{i,f} P_{i\to f} f_\mathrm{c}(E_i(\mathbf{k}_{\parallel,i}))f_\mathrm{v}(\mathbf{k}_{\parallel,f}))VG_\Omega(\hbar\omega)\mathrm{d}(\hbar\omega), \tag{5.65}$$

where $G_\Omega(\hbar\omega)$ is the density of states per unit volume of the electromagnetic field. Replacing the sum over initial, intermediate, and final states with the appropriate formalism for our QW structure

$$\sum_{i,f} \to \sum_{\mathrm{em,abs}}\sum_{c\Delta,v\Gamma}\sum_{a,b}\sum_{\mathbf{k}_\parallel,\mathbf{k}_\parallel',\mathbf{k}_\parallel''}\sum_{\mathbf{q}_\parallel}\sum_{q_z}, \tag{5.66}$$

we find for the spectrally-resolved rate of spontaneous emission the expression

$$\begin{aligned} R_{\mathrm{sp}}^{\mathrm{ind}}(\hbar\omega) = C_{\mathrm{ind}} \sum_{\mathrm{em,abs}}\sum_{\mathrm{c}\Delta,\mathrm{v}\Gamma}\sum_{a,b}\sum_{\mathbf{k}_\parallel}\sum_{\hat{\mathbf{e}}} N_{\mathrm{c}\Delta}\left|I_b^{\mathrm{v}\Gamma}\right|^2\left|\mathbf{p}_{\mathrm{v}\Gamma,\mathrm{c}\Gamma}\cdot\hat{\mathbf{e}}\right|^2 \\ \times \sum_{\mathbf{q}_\parallel}(n_{\mathrm{ph}}+\frac{1}{2}\pm\frac{1}{2})\left|\sum_{q_z} M_a^{\mathrm{c}\Delta}(q_z)\right|^2 \\ \times (\hbar\omega) f_\mathrm{c}\left(E_a^{\mathrm{c}\Delta}(\mathbf{k}_\parallel)\right) f_\mathrm{v}\left(E_b^{\mathrm{v}\Gamma}(\mathbf{k}_\parallel \mp \mathbf{q}_\parallel)\right) \\ \times \frac{\delta\left(E_a^{\mathrm{c}\Delta}(\mathbf{k}_\parallel) - E_b^{\mathrm{v}\Gamma}(\mathbf{k}_\parallel \mp \mathbf{q}_\parallel) \mp \hbar\omega_{\mathrm{ph}} - \hbar\omega\right)}{\left(E_a^{\mathrm{c}\Delta}(\mathbf{k}_\parallel) - E_1^{\mathrm{c}\Gamma}(\mathbf{k}_\parallel \mp \mathbf{q}_\parallel) \mp \hbar\omega_{\mathrm{ph}}\right)^2}, \end{aligned} \tag{5.67}$$

where $N_{\mathrm{c}\Delta}$ accounts for the degeneracy of the cΔ-valleys and the constant C_{ind} is defined as

$$C_{\mathrm{ind}} = 2D_{\mathrm{eff}}^2\frac{2\pi}{\hbar}\frac{\hbar}{2\epsilon V}\frac{\hbar}{2\rho_\mathrm{M}V\hbar\omega_{\mathrm{ph}}}\left(\frac{e}{m_0}\right)^2\frac{n^3\hbar}{(2\pi\hbar c)^3}. \tag{5.68}$$

Equation 5.67 gives a full description for the calculation of the spontaneous phonon-assisted radiative recombination rate for each photon energy $\hbar\omega$. For the numerical evaluation of Eq. (5.67), we require information on the energies $E_a^{\mathrm{c}\Delta}(\mathbf{k}_\parallel)$, $E_b^{\mathrm{v}\Gamma}(\mathbf{k}_\parallel)$, and $E_1^{\mathrm{c}\Gamma}(\mathbf{k}_\parallel)$, on the polarization dependent-dipole matrix elements $\mathbf{p}_{\mathrm{v}\Gamma,\mathrm{c}\Gamma}$ at the Γ-point, the number of phonons n_{ph}, and the constant C_{ind}. While we obtain the energies $E_a^{\mathrm{c}\Delta}(\mathbf{k}_\parallel)$, $E_b^{\mathrm{v}\Gamma}(\mathbf{k}_\parallel)$, and $E_1^{\mathrm{c}\Gamma}(\mathbf{k}_\parallel)$ from our self-consistent multivalley effective mass model, the polarization dependent-dipole matrix elements $\mathbf{p}_{\mathrm{v}\Gamma,\mathrm{c}\Gamma}$ need to be provided externally. We calculate them by means of a $sp^3d^5s^*$ first-neighbor TB code [197, 202]. The number of phonons n_{ph}, we calculate using Bose-Einstein-statistics.

The constant C_{ind} is not required for our calculation since we will not be interested in absolute recombination rates. The reason for this will become clear in the next section, where we turn our attention to the NP spontaneous radiative recombination rate.

5.4.2 No-Phonon Spontaneous Radiative Recombination

The scattering of electrons to the Γ-point cannot only be facilitated by phonons (elastic scattering), but also by structural imperfects that act as scattering centers (inelastic scattering). As a result of the ultrathin well region in our sample, the dominate inelastic scattering channel is due to interface roughness [203, 204].

Interface roughness scattering is caused by the variations of the thickness of the layers and the subsequent variations of the potential in the xy-plane. The autocorrelation function $S(\boldsymbol{\rho})$ of the in-plane thickness fluctuations $\Delta_z(\boldsymbol{\rho})$ is usually assumed to be normally distributed [205]

$$S(\boldsymbol{\rho}) = \langle \Delta_z(\boldsymbol{\rho})\Delta_z(\boldsymbol{\rho}')\rangle = \Delta^2 \mathrm{e}^{-\frac{|\boldsymbol{\rho}-\boldsymbol{\rho}'|^2}{\Lambda^2}}, \tag{5.69}$$

where Δ is the mean height of the roughness profile and Λ correlation length. The in-plane thickness fluctuation $\Delta_z(\boldsymbol{\rho})$ leads to perturbations of the potential term $V^{\alpha,l}(z)$ in Eq. (5.5) [206]. These perturbations can act as inelastic scattering centers and provide the missing momentum for electrons in the Γ-valley to be scattered to the Γ-point where they can recombine radiatively with holes in the valence band. The scattering rates related to the interface roughness is commonly calculated based on second-order perturbation theory using Fermi's Golden Rule [206]. There are two challenges when we try to apply this approach to our system. One challenge is that in order to calculate the scattering rate, the mean height Δ of the roughness profile and the correlation length Λ need to be known, but were not measured for our sample. The second challenge is that due to the small width of the Ge region, the perturbations of the well thickness are on the same order of magnitude as the well thickness itself. For this reason, the perturbation theory is not valid for our multiple-QW structure. Thus, we decided not to include the absolute rate of the no-phonon processes into our model.

Nevertheless, we can still extract information about the NP feature in the PL spectrum. Using the Bose-Einstein statistics, it can be shown that the phonon-assisted recombination rate is dominated by phonon emission over the entire investigated temperature range due to the large effective phonon energy used in our model. Consequently, we can attain the peak energy of the NP line by blueshifting the phonon-assisted spectrum by the effective phonon energy.

In conclusion, using the theoretical approach described above, we are able to calculate the phonon-assisted feature of the PL spectrum and the peak energy of the NP feature. The electron and hole states required for these calculations are provided by our self-constistent multivalley effective mass model. With this theoretical framework, we now return to the experimental data and try to analyze the measured PL spectra in greater detail.

5.5 Modeling of the Ge Multiple-QW Photoluminescence

To find the origin of the excitation-density and temperature-dependent behavior of the PL spectra discussed in Sec. 5.2.3, we apply our theoretical model to the Ge multiple-QW sample. First, we investigate the excitation-density-dependent measurements, which we use to calibrate and test our model. Afterward, we study the temperature-dependent measurements.

5.5.1 Excitation Density Dependent Measurements

Investigating the excitation dependent PL spectra serves two purposes. When we introduced our effective mass model in Sec. 5.3.1, we defined the material parameters describing the SiGe material system. What we have not determined so far are the geometrical dimensions of the Ge-rich region and its material composition. Also, we have not yet specified the excess carrier density n_{exc}, which serves as an input parameter for the self-consistent solution of the coupled Schrödinger-Poisson equations. In the following section, we first determine these parameters. Afterward, we validate our parameter selection by comparing theoretical and measured PL spectra.

Charge Density, Material Composition, and Geometry

The excess carrier density n_{exc} of excited electron-hole pairs within the system is an input parameter for the self-consistent Poisson-Schrödinger calculations. One approach to calculate the excess carrier density n_{exc} is by formulating and solving the rate equation for the charge density of the electrons n and holes p in the structure. Assuming a homogeneous distribution of charges over the entire structure and neglecting any spatial fluctuations of the absorption and recombination rate, the rate equation of the charge density of the electrons can be written in case of a continues excitation (steady state) and for an intrinsic semiconductor as

$$\frac{\mathrm{d}n_{\mathrm{exc}}}{\mathrm{d}t} = G - R_{\mathrm{nr}}(n_{\mathrm{exc}}) - R_{\mathrm{rad}}(n_{\mathrm{exc}}) = 0, \tag{5.70}$$

with absorption rate G, non-radiative and radiative recombination rates R_{nr} and R_{rad}. The radiative recombination rate consists of the sum of the rates of the phonon-assisted processes and the NP processes. The non-radiative rates are determined by trap-assisted recombination (Shockley-Reed-Hall recombination, SRH) and Auger recombination [57]. In general, the non-radiative recombination processes are dominating in semiconductor heterostructures. Therefore, we can make the approximation

$$\frac{\mathrm{d}n_{\mathrm{exc}}}{\mathrm{d}t} \approx G - R_{\mathrm{nr}}(n_{\mathrm{exc}}) = 0. \tag{5.71}$$

Due to the small width of the quantum wells, the excitation radiation is mainly absorbed in the silicon barrier regions. As silicon has been thoroughly investigated in the past decades, absorption data can readily be found in the literature [207]. Finding a valid approximation for the recombination rates is more challenging. Even though the functional forms for the recombination mechanisms are known [57, 208], the proportionality constants determining their relative intensities are highly sample dependent. A determination of the excess carrier density n_{exc} using the rate equation is therefore not possible.

Instead of solving the rate equation, an empirical relationship for the excess carrier density n_{exc} as a function of excitation density P can be formulated based on the integrated PL luminescence measured for the phonon-assisted recombination. In Fig. 5.8, the integrated PL

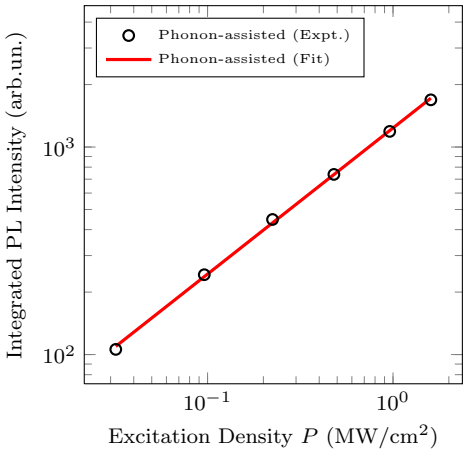

Figure 5.8: *Measured integrated PL intensity of phonon-assisted peak (black circles) as a function of the excitation density P shown on a double-logarithmic scale. The integrated PL intensity follows a power law. A fit (red) was used to extract the scaling exponent. Reproduced from T. Wendav* et al., *"Photoluminescence from ultrathin Ge-rich multiple quantum wells observed up to room temperature: Experiments and modeling", Phys. Rev. B* ***94,*** *245304 (24 2016).* *©2016 by the American Physical Society.*

luminescence $I_{\text{int}}^{\text{ph}}$ of the phonon-assisted line is shown as a function of excitation density P on a double logarithmic scale. It can be observed that the phonon-assisted line follows a power law given by

$$I_{\text{int}}^{\text{ph}} = A\,P^b, \tag{5.72}$$

where A is a proportionality constant and b the scaling exponent. Furthermore, we know that the integrated PL luminescence is proportional to n_{exc}^2. Thus, we can derive a relationship between excitation density and excess carrier density given by

$$n_{\text{exc}} = C\,P^{b/2}, \tag{5.73}$$

where C is a proportionality constant. The proportionality constant C and the scaling exponent b can both be determined from fits to the experimental data. The scaling exponent can be extracted directly from fitting the integrated PL luminescence $I_{\text{int}}^{\text{ph}}$. Fitting a power law to the phonon-assisted line in Fig. 5.8, we find a scaling exponent of (0.70 ± 0.01).[3] For the determination of the proportionality constant, we use the experimentally obtained phonon-assisted PL spectrum. We set the proportionality constant to a value for which the blueshift of the PL spectra shown in Fig. 5.4(a) can be reproduced.

Regarding the material composition, we use a square profile with constant material compositions inside and outside the well. For the barrier regions, we use pure Si while for the well region we use $\text{Si}_{1-x}\text{Ge}_x$ with $x = 0.68$, which corresponds closely to the average Ge concentration measured by Raman spectroscopy. We note that the assumption of a square well is only

[3] The value of the scaling exponent is close to 2/3, which indicates that the recombination dynamics is dominated by the Auger recombination. The Auger recombination scales for intrinsic semiconductors with n_{exc}^3 [57]. If the Auger recombination is the dominant recombination channel, then it follows from Eq. (5.71) that $G \propto n_{\text{exc}}^3$ and as G scales linearly with the excitation density $P \propto n_{\text{exc}}^3$. The integrated PL intensity scales with $I_{\text{int}} \propto n_{\text{exc}}^2$. Thus, we can conclude $I_{\text{int}} \propto n_{\text{exc}}^{2/3}$.

an approximation of the Ge distribution within the sample, which is likely to be influenced by segregation effects. However, determining the position-dependent Ge distribution within the QWs would necessitate an experimental technique with sub-nm resolution.

Concerning the thickness of the well, we notice that the transition energies of our ultrathin Ge multiple-QWs are quite sensitive to small variations of the well thickness, due to the strong confinement of the holes in the valence band. Consequently, in our simulations we tuned, starting from the HR-TEM and XRD measurements, the QW thickness of the adopted square profile in order to improve the agreement between theoretical and experimental PL peak energies. We find that an effective QW thickness of 1.6 nm, which is only slightly larger than the XRD estimates of (1.2 ± 0.2) nm, places our theoretical results within 20 meV of the experimentally determined values. In principle, this difference can be reduced by optimizing the well thickness even further. However, as we are mainly interested in the relative shifts of the peak energy as a function of the excitation density and lattice temperature, we are satisfied with this result. To justify the introduction of the effective square well thickness, we notice that different material parameters, such as band offsets and confinement masses, whose precise values are unknown, influence the calculated transition energies. For example, increasing the HH mass along the confinement direction by 10 % results in an increase of the transition energy by about 10 meV. An effective QW thickness for the adopted multiple-QW square profile can then be regarded as a way to consider the uncertainties associated to the material parameters for Si, Ge, and $Si_{1-x}Ge_x$ alloys.

The value of the optimized fitting used in the following together with the experimental values, if available, are summarized for convenience in Tab. 5.1.

Due to limited computational resources, all calculations introduced in the following are performed for a single-QW with periodic boundary conditions. The application of periodic boundary conditions is justified by the fact that the investigated structure consists of 10 QW layers for which the PL intensity coming from the outer two wells can be neglected over the cumulative PL intensity coming from the inner wells.

Table 5.1: *Summary of the values used for the excess carrier density, the QW width, and the QW composition. Comparison to the measured values.*

Parameter	Theory	Experiment
Scaling exponent	0.75	$(0.71 \pm 0.01)^{d}$
Proportionality constant	$3.5 \times 10^{11}\,\mathrm{W}^{-0.75}\mathrm{cm}^{0.5}$	-
Well width	1.6 nm	$(1.3 \pm 0.1)\,\mathrm{nm}^{a}$, $(1.2 \pm 0.2)\,\mathrm{nm}^{c}$
Ge concentration	0.68	$(0.68 \pm 0.01)^{b}$, $(0.69 \pm 0.08)^{c}$

[a] TEM [b] Raman [c] XRD [d] PL

Eigenstates and Band Bending

After we have fully parametrized the effective mass model in the previous section, we calculate the eigenstates and eigenenergies of the Ge multiple-QW structure. In Fig. 5.9, the band diagram for a single QW calculated with an excess carrier density n_{exc} corresponding to the lowest excitation density used in the experiment. Displayed are the six bands that we included into our self-consistent calculation: Γ, L, and Δ bands in the conduction band and HH, LH, and SO bands in the valence band. As a result of the biaxial strain within the SiGe region, we

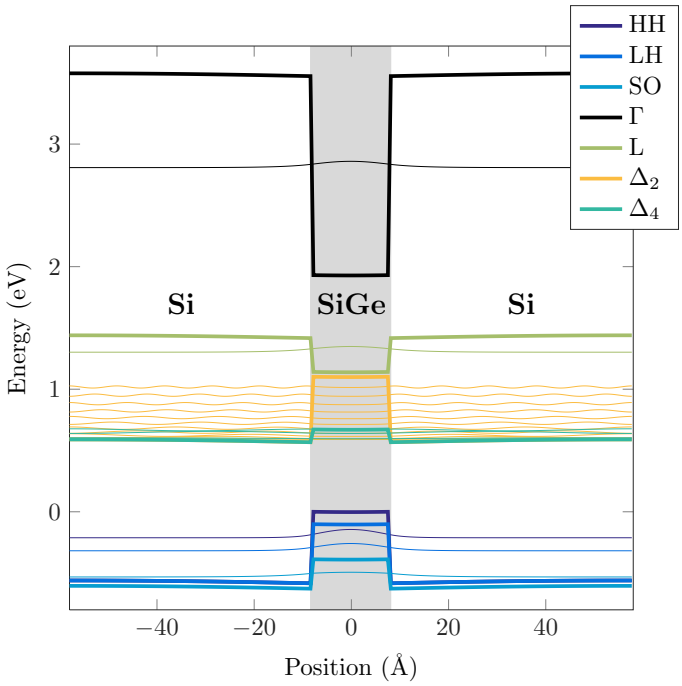

Figure 5.9: *Band diagram of the Ge multiple-QW structure in the low excitation regime. The thick lines indicate the potential term including the electrostatic potential for the Γ, L, and Δ valleys in the conduction band and the HH, LH, and SO holes in the valence band. The thin lines show the squared wavefunction of the confined states in the region with the lowest potential for each band. It can be observed that the holes are confined within the Ge-rich layer, the electrons are located in the Si barrier region in the Δ-valleys.*

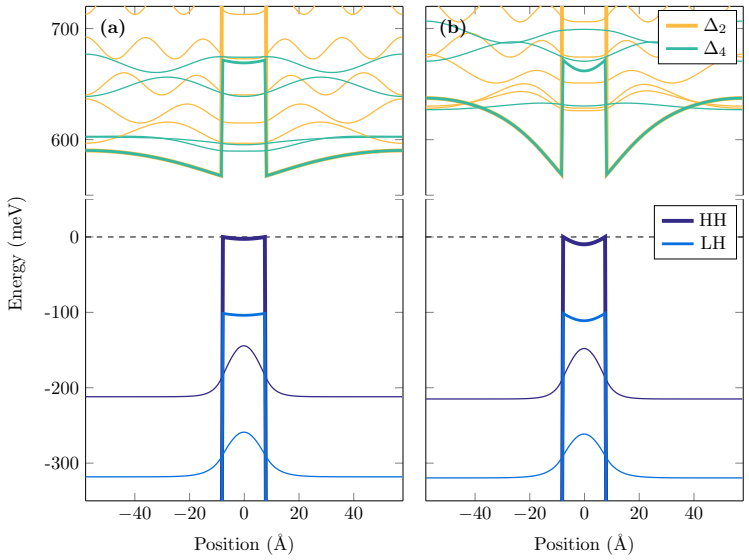

Figure 5.10: *Band diagram of the Ge multiple-QW structure for (a)* $0.03\,\mathrm{MW/cm^2}$ *and (b)* $1.60\,\mathrm{MW/cm^2}$ *excitation density. The thick lines indicate the potential term including the electrostatic potential for the* Δ *valleys in the conduction band and the HH and LH in the valence band. The thin lines show the squared wavefunction of the confined states for each band. For the higher excitation density, a stronger band bending is visible, which affects foremost the energy of the* Δ *conduction band states. Reproduced from T. Wendav* et al., *"Photoluminescence from ultrathin Ge-rich multiple quantum wells observed up to room temperature: Experiments and modeling", Phys. Rev. B* ***94,*** *245304 (24 2016).* ©*2016 by the American Physical Society.*

see that the six-fold degenerate Δ-valley is split into the four in-plane Δ_4-valleys and the two perpendicular Δ_2-valleys. This splitting of bands is also visible for the HH and LH band within the Ge-rich region. Moreover, we have included the squared wave function of the confined eigenstates into the band diagramm. We find that for the Γ, L, HH, LH, and SO band each one confined state exists. For the Δ-valleys, on the other hand, the lowest potential lies within the Si region, which results in the type-II band alignment. We also observe that due to the energy separation between the valleys, only the Δ valleys are of interest for our calculation in the conduction band, and the HH and LH in the valence band. The occupation of the Δ-valleys in the Si region confirm the interpretation of the experimental PL spectra in Sec. 5.2.3. Thus, the deconvolution of the experimental PL spectra into a phonon-assisted and a NP feature is supported by our model.

In Fig. 5.10(a) and Fig. 5.10(b), the band diagrams calculated with an excess carrier density n_{exc} corresponding to the lowest and the high experimentally used excitation density are shown, respectively. The band diagrams focus on those bands that contribute to the PL spectrum. Comparing conduction and valence bands in the interface regions between barrier and well for both cases, we see that the increased excitation density P leads to a greater band bending. How much the charge carriers are affected by the band bending strongly depends on the individual valleys. Due to the strong confinement within the valence band and the small width of the Ge-rich region, the energy levels of the holes remain almost unchanged, shifting by only 3 meV. In contrast, the energy levels of the electrons in the Δ-valleys get shifted upward by approximately 40 meV. Likewise, the probability distribution of the electrons in the Δ-valley is affected. Whereas in the low excitation limit the lowest lying conduction band states are mainly situated in the barrier region, in the high excitation limit they move closer to the well due to the triangular potential landscape at the interface region. The shift of the conduction band states to higher energies as a result of the charge separation at the interface is a typical result for type-II band alignments and has been observed before in the SiGe and other material systems [184, 209].

The shift of the eigenenergies of the confined states in the Δ-valleys is a first indication that our model confirms the experimentally observed blueshift of the PL spectrum when the excitation density is increased. To further investigate this behavior, we use the theory of heterostructure PL developed in Sec. 5.4 and calculate the PL emission based on the results of our effective mass model.

Spectral Shape of the Phonon-Assisted Feature

A comparison of experimental and simulated PL spectra originating from the phonon-assisted recombination evaluated at $T = 80\,\mathrm{K}$ for different excitation densities is shown in Fig. 5.11(a). Despite the fact that experimental spectra are slightly broader, probably due to fluctuations in material composition and QW width, we find that the pump-induced increase of the peak intensity is well reproduced by the model. We stress that this is not *a priori* obvious since the phenomenological relation between excess carrier n_{exc} and pump density P was tuned to reproduce the energy shift and not the PL peak intensity.

Studying the theoretical spectra, we observe that the onset of the PL spectra blueshifts when the excitation density P is increased. The blueshift is a result of the shift of the conduction band states towards higher energies due to the increased band bending when the excitation density P is increased, which we have already discussed above. Yet, we also notice that the spectra become broader. In particular, we find that in addition to the main PL peak a shoulder develops when the excitation density P is increased. The shoulder results from the population

of the confined state of the LH band, which is of higher energy than the confined state of the HH band and only becomes populated at sufficiently high excitation densities. Consequently, the population of the LH band also contributes to the observed blueshift. Due to the broadening of the experimental spectra, we cannot directly verify the existence of the shoulder through the measured PL emission.

Finally, we investigate the PL peak energy as a function of the excitation density. In Fig. 5.11(b), we show the PL peak energy for measurement and simulation for both phonon-assisted and NP line. Notice that the NP curve has been obtained by upshifting numerical data for the phonon-assisted feature by 51 meV. The experimentally phonon-assisted and NP line blueshift by approximately 50 meV over the range of investigated excitation densities. Comparing these relative shifts to our simulation, we find that the blueshift of the phonon-assisted and the NP feature are well reproduced. Only the absolute energies deviate by approximately 20 meV for reasons already discussed in Sec. 5.5.1.

From the comparison of experimental and theoretical PL spectra, we deduce that our theoretical description of the Ge multiple-QW system is quantitatively in agreement with the measurements. In addition, through the investigation of the electronic structure of the Ge multiple-QW sample, we gained a deeper understanding of the origin of the investigated blueshift. While the blueshift due to an increased excess carrier density has already been investigated elsewhere, we now move on to the investigation of the temperature-dependent measurements that have been studied to a lesser extend.

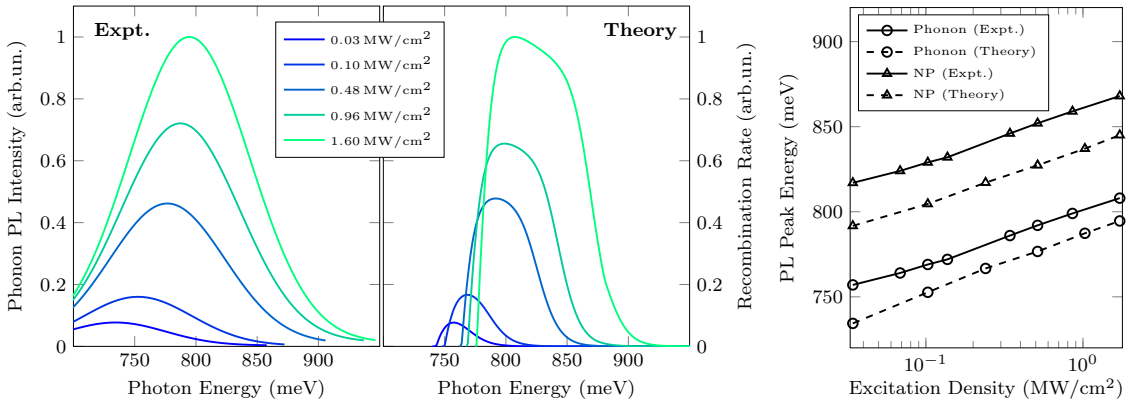

(a) Phonon PL Intensity **(b)** PL Peak Energy

Figure 5.11: *(a) Comparison between experimental and simulated phonon-assisted PL spectra at $T = 80$ K for different excitation densities. Even though the experimental spectra are broader, probably due to fluctuations in the QW thickness and composition, the relative intensities for the different excitation densities are in good agreement between simulation and measurement. (b) PL peak energy of the phonon-assisted and NP line according to theory and experiment as a function of the excitation density. Even though there is a mismatch in absolute energy between measurement and simulation, the relative change in the peak energy for different excitation densities is in good agreement between both. Points are connected for clarity. Reproduced from T. Wendav* et al., *"Photoluminescence from ultrathin Ge-rich multiple quantum wells observed up to room temperature: Experiments and modeling", Phys. Rev. B* ***94,*** *245304 (24 2016).* ©*2016 by the American Physical Society.*

5.5.2 Temperature Dependent Measurements

Choosing the Charge Density

To calculate the phonon-assisted PL luminescence, we need to determine the excess carrier density as a function of the lattice temperature. For this, we make use of the fact that our measurements of the PL intensity as a function of excitation density and temperature have an intercept for the parameters $T = 80\,\mathrm{K}$ and $P = 9.6 \times 10^4\,\mathrm{Wcm}^{-2}$, for which we already know the excess carrier density from the investigation of the excitation density measurements. To determine the excess carrier density for simulations with $T' > 80\,\mathrm{K}$ and $P = 9.6 \times 10^4\,\mathrm{W\,cm}^{-2}$, we tune the excess carrier density in our simulations so that the ratio between the integrated phonon-assisted PL for temperature T' and $T = 80\,\mathrm{K}$ matches that of the PL measurements. From this calibration procedure, we estimate a decrease of the excess carrier density by a factor of 0.3 over the temperature range from $80 - 200\,\mathrm{K}$.

Spectral Shape of the Phonon-Assisted Feature

The Gaussian fits of the phonon-assisted PL feature at different temperatures are compared with numerical data in Fig. 5.12(a). Although the experimental spectra are broader, presumably due to multiple-QW thickness fluctuation in our samples, the ratios among different peak intensities are in good agreement with experiment, which is not obvious *a priori* since in the calibration procedure the integrated intensities were targeted. The good agreement between the peak intensities indicates that the thermal contributions to the broadening are correctly reproduced by our model. We notice that even though the spectral width of the PL signal increases with temperature, the peak energy redshifts nevertheless. From these results, we conclude that the temperature dependence of the phonon-assisted PL peak energy is dominated by the temperature-dependent decrease of the band-gap while the thermal excitation of higher energy states, which in principle could drive a blueshift, plays only a minor role. Furthermore, comparing the temperature dependence of the PL peak energy as obtained from measurement and simulation, we find that our calculations correctly model the monotonic decrease of roughly 30 meV for phonon-assisted and NP line observed in the experiment (see Fig. 5.12(b)). As a result, the observed blueshift in the total PL spectrum visible in Fig. 5.5(a) then has to be attributed to a spectral weight shift from the phonon-assisted feature, dominating at low temperature, to the higher energy NP contribution which becomes dominant at higher temperature. This effect overcompensates the band-gap shrinkage. In fact, considering the 30 meV redshift of the phonon-assisted and NP peak predicted by our model and their energy separated by about 50.0 meV, we estimate a blueshift of the total PL spectrum of about 20 meV, which matches with the measured value of 20 meV between $80\,K$ and $200\,K$. This interpretation is confirmed by the measured ratio between the phonon-assisted and NP integrated PL signals, which is approx. 10 for $T = 80\,\mathrm{K}$ and decreases down to approx. 0.15 for $T = 200\,\mathrm{K}$ (see Fig. 5.13). The thermal quenching of the PL is therefore hindered by a strong increase of the NP intensity at higher T.

We try to explain the change the the relative intensity of phonon-assisted and NP feature by analyzing the temperature-dependence of the phonon-assisted and NP feature separately. For the phonon-assisted feature, the coupling between electrons and phonons is determined through the number of phonons in the system, which is given by the Bose-Einstein statistic. Due to the large phonon energy with respect to $k_\mathrm{B}T$, the electron-phonon coupling can be approximately described as temperature-independent over the investigated temperature range. Therefore, the phonon-assisted signal intensity is mainly governed by the decreasing excess

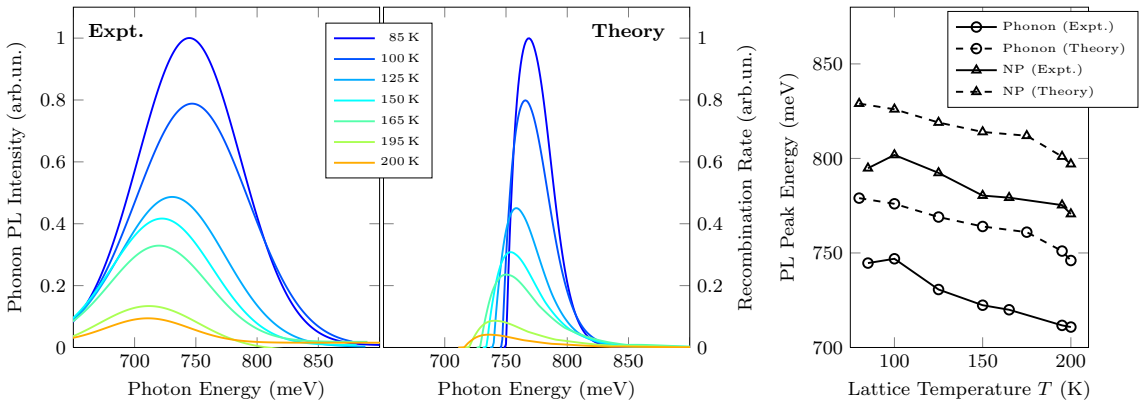

(a) Phonon PL Intensity **(b)** PL Peak Energy

Figure 5.12: *(a) Comparison between phonon-assisted peaks extracted from experiment and theory for different lattice temperatures T and a fixed excitation density of $P = 0.10\,\mathrm{Wcm}^{-2}$. While we find again a broadening of the measured spectra, the relative peak intensity for different lattice temperatures is well reproduced by the simulation. (b) PL peak energy of the phonon-assisted and NP line according to theory and experiment as a function of lattice temperature T. While the absolute energies between experiment and simulation differ, the redshift of the phonon-assisted and NP feature in the experiment can also be identified in the simulation. Points are connected for clarity. Reproduced from T. Wendav* et al., *"Photoluminescence from ultrathin Ge-rich multiple quantum wells observed up to room temperature: Experiments and modeling", Phys. Rev. B* ***94,*** *245304 (24 2016).* ©*2016 by the American Physical Society.*

electron density, which must be related to a faster non-radiative recombination dynamics with increasing temperature. While the NP mechanism must also be affected by the faster non-radiative recombination dynamics, from Fig. 5.13, we infer that the electron-hole coupling of the NP recombination also strongly increases with T to overcompensate for the lower excess carrier density. As our theoretical model does not describe the NP recombination processes, we can only speculate about the origin of the strong increase. Two mechanisms may be responsible for this behavior. At higher temperatures, holes and electrons occupy states with higher in-plane momentum. These larger momenta increase the rate at which charge carriers encounter interface defects. Since these elastic scattering events can provide the missing momentum for indirect transitions, an increased NP recombination rate is to be expected. An alternative explanation for the temperature-driven increase of the NP electron-hole coupling is that at higher temperature conduction electrons populate higher excited sub-bands whose wavefunction penetrate deeper into the SiGe region (see Fig. 5.9). The increased overlap of the wavefunctions with the interface region may enhance the interface roughness scattering rate contributing to the NP PL feature. Note that in this case the enhanced contribution from excited conduction sub-bands will slightly blueshift the NP feature resulting in an increase in energy separation with the phonon-assisted peak. This effect could explain the increase of the energy separation between phonon-assisted and NP peak with increasing temperature shown in Fig. 5.5(b).

Even though the increase of the energy separation between phonon-assisted and NP peak

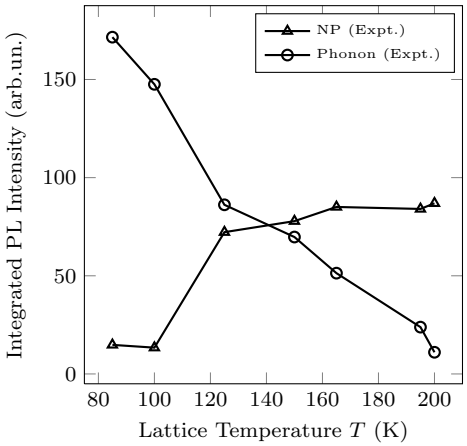

Figure 5.13: *Measured integrated PL intensity for phonon-assisted and NP line as a function of the lattice temperature T. While the phonon-assisted recombination is the dominating process at low temperatures, the NP recombination dominates at high temperatures. Points are connected for clarity. Reproduced from T. Wendav* et al., *"Photoluminescence from ultrathin Ge-rich multiple quantum wells observed up to room temperature: Experiments and modeling", Phys. Rev. B* ***94,*** *245304 (24 2016).* ©*2016 by the American Physical Society.*

with increasing temperature might be an indication that the temperature-driven excitation of higher electronic states causes the increase of the NP recombination rate, due to the limitations of our theoretical model, we cannot draw any further conclusions at this point. Further experimental and theoretical investigations that explicitly investigate the NP radiative recombination are required to validate our hypotheses. This topic will be discussed in more detail in the next section concerning the summary and outlook of our work.

5.6 Summary and Outlook

In our theoretical study, we investigated a Ge multiple-QW consisting of a less than 1.5 nm thick well region with a Ge concentration larger than 60 % and pure Si barrier regions. Investigations of the sample's PL emission revealed that the PL emission of the structure is unusually robust against thermal quenching. Furthermore, the PL spectra show a blueshift of the peak energy when the temperature is increased, which is in conflict with the temperature-related band-gap shrinkage.

To gain a better understanding of the mechanisms leading the PL spectra, we developed a multivalley effective mass model, which included the Γ-band, L-band, and the Δ-valley in the conduction band and the HH, LH, and SO band in the valence band. Geometric structure and material composition for our model were extracted from TEM, Raman, and XRD measurements of the Ge multiple-QW sample. Relevant effects of strain on the band edge energies and effective masses were included into the model. Using experimental data on the integrated PL emission, we formulated an empirical relationship for the number of excited charge carriers inside the structure as a function of excitation density and lattice temperature. We included the effects of charge separation at the interface through a coupling of the effective mass Schrödinger equation with the Poisson equation and a scheme to solve the coupled equations self-consistently.

Based on the eigenstates and energy eigenvalues obtained from our self-consistent multivalley effective mass model, we developed a perturbative approach to calculate those parts of the PL spectra that resulted from phonon-assisted radiative recombination mechanisms. For the NP recombination, we calculated the peak energy of NP related PL features.

Testing our model on the excitation-dependent PL measurements, we could reproduce the blueshift of the measured PL spectra when the excitation density is increased. The blueshift is a result of the increased band bending due to the larger number of charge carriers inside the system, which has been found in other studies as well. In addition, we found that the occupation of higher valence band states also contributes to the blueshift. Employing our model to the lesser studied case of the temperature-dependent PL measurements, we found that both the phonon-assisted and the NP peaks shift towards smaller energies for increasing temperatures as a result of the temperature-related shrinkage of the band-gap. The occupation of higher excited states with increasing temperatures cannot offset the shrinkage of the band-gap. The blueshift of the total PL spectrum is a result of the difference in the temperature-dependence of the phonon-assisted and NP related radiative recombination mechanisms. While the phonon-related PL intensity decreases when the temperature is increased, due to the increase of the non-radiative recombination rate and as a result of the reduced charge carrier density, the NP-related PL intensity increases. This increase of the NP intensity overcompensates the decrease in intensity related to the phonon-assisted transitions and leads to a shift in spectral weight from the phonon-assisted to the NP feature, effectively blueshifting the total PL peak energy. We conjecture that the increase in the NP-related recombination rate is due to the higher in-plane momenta of the charge carriers at higher temperatures, which increases the rate at which charge carriers encounter elastic scattering centers. Alternatively, this effect might also be related to an enhanced interface scattering rate as a result of the occupation of higher energy levels by the optically excited electrons. The wavefunctions related to those higher energy levels penetrate deeper into the interface region between Si and Ge-rich region, enhancing the contribution of the interface roughness scattering rate to the NP signal.

To further investigate these processes, we propose the conduction of experiments investigating in more detail the no-phonon related recombination processes. Those information can then be used to further parameterize our model to estimate the ratio between phonon-assisted and no-phonon recombination rate. From the current state of our investigation, we suspect that the mechanism that limits the effect of thermal quenching is associated to the type-II confinement typical for SiGe/Si QWs. For further clarity, we propose to investigate similar layer structures also in other material systems that exhibit a type-II confinement.

Chapter 6
6 Conclusion

In the final chapter of this thesis, we want to summarize the results of the three investigations presented so far and draw more general conclusions regarding the topic of this thesis - the modeling of SiGeSn-based heterostructures for optoelectronic applications. Moreover, we propose the quantum well infrared photodetector as a medium-term goal and a first possible device application to be realized in the SiGeSn material system.

6.1 Achievements of this Thesis

We can group the investigations presented in this thesis into two categories. First, the investigation of the electronic structure of the SiGeSn material system. Here, we studied the compositional dependence of the direct band-gap of $Ge_{1-x-y}Si_xSn_y$ alloys as well as the band alignment between the Si, Ge, and Sn elemental semiconductors. Secondly, based on the understanding of the electronic structure, we investigated the optoelectronic properties of heterostructures. Here, we analyzed the photoluminescence (PL) of an ultrathin Ge multiple quantum well (multiple-QW) structure. In the following, we highlight the most interesting outcomes of those investigations and draw conclusions for the required future work in the development of SiGeSn heterostructures for optoelectronic applications.

In our first study, we investigated the compositional dependence of the direct band-gap of $Ge_{1-x-y}Si_xSn_y$ alloys. From experimental data on two $Ge_{1-x-y}Si_xSn_y$ alloys of different composition closely lattice-matched to Ge, we extracted the direct band-gap energy. Using this information, we parametrized an empirical equation relating composition and direct band-gap size. Comparing the results of experimental and theoretical studies (including ours) on the compositional dependence of the direct band-gap of $Ge_{1-x-y}Si_xSn_y$ alloys lattice-matched to Ge, we found disagreement between the studies. A key point for discussion still is whether $Ge_{1-x-y}Si_xSn_y$ alloys lattice-matched to Ge become a direct-band-gap semiconductor for large concentrations of Sn, which our study predicts but has not been found by others so far. Moreover, it is not yet clear whether the compositional dependence of the direct band-gap can indeed be described by a bowing equation based on the bowing parameters of the SiGe, GeSn, and SiSn binary alloys. Therefore, in this thesis we showed the need for further experimental and theoretical investigations to overcome this lack of information. In particular, experimental investigations with a greater number of samples covering a wider range of compositions are

required. Also, we suggest a review of the existing theoretical studies based on the empirical pseudopotential method (EPM). The results of the EPM calculations vary considerably as a result of the different pseudopotentials used for the SiGeSn material system. Besides the compositional dependence of direct and indirect band-gaps, also the compositional dependence of the Luttinger parameters required for including the effects of strain on the valence bands within an effective mass model has not been investigated so far for the SiGeSn material system. The EPM can also be used to study these parameters.

Concerning the band alignment calculations between Si, Ge, and Sn, we showed that the currently available density functional theory (DFT) calculations in the Kohn-Sham approach predict a false broken-gap band alignment at the interface between Ge and Sn. As a result, valence band electrons from the Sn region occupy conduction band states in the Ge region. This leads to strong electric fields even within the bulklike regions, which inhibit the convergence of the interface calculations. With our calculations, we showed that the correct band-gap sizes are a key prerequisite in the calculation of the band alignment. We outlined how this can be achieved by using high-level exchange-correlation functionals beyond the standard approximation. Moreover, we showed in an exemplary fashion for the case of Si that nonlinear effects of strain influence the band-offset calculations. These effects are negligible for the band-offset calculations between Si and Ge, but need to be taken into account when calculating the band offset between Ge and Sn.

From our investigation of the PL spectra of an ultrathin Ge multiple-QW structure using a self-consistent multivalley effective mass model, we gained understanding in how far an empirical effective mass approach can be used to model the PL emission of a heterostructure. For the investigated structure, the PL is a result of the indirect phonon-assisted and no-phonon (NP) spontaneous radiative recombination of charge carriers. We found that we are able to fully calculate the spectral shape of the phonon-assisted feature including its temperature and excitation-density dependence. For the calculation of the NP PL spectrum, we encountered two challenges. First, the theoretical description of the NP processes requires a detailed knowledge of the structural features of the sample, like surface roughness and alloy fluctuations. This information can only be obtained through a more detailed experimental analysis of the sample. Secondly, the surface roughness scattering, which is the dominant NP process in our sample, is commonly treated theoretically in a perturbative approach. While this is a valid approach for quantum wells (QWs) where the surface roughness is orders of magnitude smaller than the well width itself, perturbation theory cannot be used for our ultrathin multiple-QWs. Nevertheless, we showed that while we cannot calculate the entire NP spectrum, we can estimate the energy of the peak NP intensity. Combining the NP PL peak energy together with the phonon-assisted PL spectrum, we were able to gain a better understanding of the PL processes within this sample than we would have been from experimental data alone. Moreover, a key strength of our approach is that it is not limited to only the investigated heterostructure, but that it can be adapted for the investigation of other heterostructures as well. Another interesting finding of our study was that using the standard parameters for the SiGe material system, the absolute values of the calculated transition energies deviated from those measured in the experiment. We had to introduce an effective well width to compensate for uncertainties related to material and geometric parameters of our model and reproduce the experimental data. While the effective material parameter is a viable approach to reproduce experimental results, it does not provide any information on which material parameters contribute to the discrepancy between theory and experiment. Indeed, this is an intrinsic difficulty of the effective mass model in which multiple parameters can be used to shift the theoretical predictions in the same direction. Particularly in view of the SiGeSn material system, this is a relevant finding. The material

parameters for the SiGeSn material system are far less understood than for the SiGe material system. While there have been plenty of effective mass models on SiGeSn-based devices, these models are only as good as the set of material parameters used. Therefore, we believe that before formulating effective mass models of complex devices, first the basic properties of the SiGeSn material system need to be investigated more thoroughly.

Combining the findings of all three studies, we conclude that the investigation of the fundamental properties of the SiGeSn material system should be the prime focus of future work. Using an effective mass model to analyze experimental data of complex SiGeSn-based structures and fit unknown material parameters is feasible if only very few material parameters are unknown. Therefore, we suggest to focus future efforts on theoretical and experimental investigations that determine individual material parameters of the SiGeSn material system.

6.2 Future Application: Quantum Well Infrared Photodetectors

When we first introduced the SiGeSn material system in Chap. 1, we motivated our work by referring to the need for optical interconnects that can be monolithically integrated into integrated circuits. While the research for optical interconnects is important, it is also a long-term endeavor. To build SiGeSn-based optical interconnects, devices have to be developed that do not only fulfill specific optoelectronic functionalities, but that are at the same time small enough to be added into integrated circuits and that are fully compatible with current complementary metal–oxide–semiconductor (CMOS) processes. However, the SiGeSn material system can also be used for other devices that are less challenging to build and, therefore, can serve as a medium-term goal. In the following, we want to propose the quantum well infrared photodetector (QWIP) for such a medium-term goal.

The QWIP is used for the detection of infrared radiation. Aside from telecommunication purposes, infrared photo detection plays a crucial role in the detection of chemical substances. Infrared spectroscopy can be used to probe molecular vibrational and rotational degrees of freedom in the 6 µm to 16 µm wavelength region, which provide a characteristic fingerprint for chemical substances and can be used for their identification [210]. A fast and sensitive detection of infrared radiation can be achieved using quantum detectors. Quantum detectors are based on the excitation of charge carriers through the absorption of thermal radiation, which leads to a measurable photocurrent. In order to detect radiation in the fingerprint region, which corresponds to energies between 80 meV to 200 meV, semiconductors like HgCdTe can be used that exhibit a small direct band-band. However, HgCdTe is technologically difficult to fabricate [211]. An alternative are QWIPs. They consist of a stack of identical, doped QWs. Through intersubband absorption of the infrared radiation, the free charge carriers are excited to continuum states which causes a photocurrent [212]. As a result, the detectable wavelength range is decoupled from the band-gap size of the semiconductor alloy. QWIPs based on group-III/V semiconductors are already commercially available. However, the disadvantage of group-III/V-based photodetectors is that the detector has to be bonded to the readout electronic. This increases manufacturing costs and can lead to thermal mismatch problems. Using the SiGeSn material system, it would be possible to manufacture photodetector and readout electronic monolithically and, consequently, develop compact integrated sensing solutions for a wide range of applications. Moreover, the SiGeSn material system provides a large design space for the fabrication of devices with specific optical transitions due to the decoupling of band-gap size and lattice constant. Developing a QWIP requires both experimental and theoretical efforts. The work presented in this thesis can be used as a first step toward this goal.

Appendix A

A "Species" Files for the exciting Calculations

Below, we included the "species" files of Si, Ge, and Sn used for the **exciting** calculations described in Chap. 4. The species files define the basis set used for the description of the wavefunction of the core and valence electrons of each atom. Default species files for each atom are provided with the **exciting** code. However, certain calculations require the adjustment of the species files. For the supercell calculations of interfaces between different elements, a redistribution of charges at the interface can be observed (interface dipole). As a result of this redistribution of charges, electrons that are closely bound to the nuclei in a bulk calculation now partially occupy the interstitial region between the nuclei[1]. Using the default species files, the redistribution of charges is not properly accounted for by the basis functions. Therefore, we amended the default species files by adding additional basis functions. The adapted species files are included below.

```
<?xml version="1.0" encoding="UTF-8"?>
<spdb xsi:noNamespaceSchemaLocation="../../xml/species.xsd"
      xmlns:xsi="http://www.w3.org/2001/XMLSchema-instance">
  <sp chemicalSymbol="Si" name="silicon" z="-14.0000" mass="51196.73454">
    <muffinTin rmin="0.100000E-04" radius="2.20000" rinf="24.9760" radialmeshPoints="300"
        />
    <atomicState n="1" l="0" kappa="1" occ="2.00000" core="true"/>
    <atomicState n="2" l="0" kappa="1" occ="2.00000" core="false"/>
    <atomicState n="2" l="1" kappa="1" occ="2.00000" core="false"/>
    <atomicState n="2" l="1" kappa="2" occ="4.00000" core="false"/>
    <atomicState n="3" l="0" kappa="1" occ="2.00000" core="false"/>
    <atomicState n="3" l="1" kappa="1" occ="1.00000" core="false"/>
    <atomicState n="3" l="1" kappa="2" occ="1.00000" core="false"/>
    <basis>
      <default type="lapw" trialEnergy="0.1500" searchE="false"/>
      <custom l="0" type="apw+lo" trialEnergy="0.1500" searchE="false"/>
      <custom l="1" type="apw+lo" trialEnergy="0.1500" searchE="false"/>
      <lo l="0">
        <wf matchingOrder="0" trialEnergy="0.1500" searchE="false"/>
        <wf matchingOrder="0" trialEnergy="-4.9275" searchE="false"/>
      </lo>
      <lo l="0">
```

[1] The redistribution of charges from the muffin-tin into the interstitial region is referred to as "core leakage".

```
      <wf matchingOrder="0" trialEnergy="-4.9275" searchE="false"/>
      <wf matchingOrder="1" trialEnergy="-4.9275" searchE="false"/>
    </lo>
    <lo l="1">
      <wf matchingOrder="0" trialEnergy="0.1500" searchE="false"/>
      <wf matchingOrder="0" trialEnergy="-3.3487" searchE="false"/>
    </lo>
    <lo l="1">
      <wf matchingOrder="0" trialEnergy="-3.3487" searchE="false"/>
      <wf matchingOrder="1" trialEnergy="-3.3487" searchE="false"/>
    </lo>
  </basis>
 </sp>
</spdb>
```

Listing A.1: *Si species file*

```
<?xml version="1.0" encoding="UTF-8"?>
<spdb xsi:noNamespaceSchemaLocation="../../xml/species.xsd"
     xmlns:xsi="http://www.w3.org/2001/XMLSchema-instance">
 <sp chemicalSymbol="Ge" name="germanium" z="-32.0000" mass="132359.9329">
  <muffinTin rmin="0.100000E-05" radius="2.20000" rinf="25.3660" radialmeshPoints="800"
      />
  <atomicState n="1" l="0" kappa="1" occ="2.00000" core="true"/>
  <atomicState n="2" l="0" kappa="1" occ="2.00000" core="true"/>
  <atomicState n="2" l="1" kappa="1" occ="2.00000" core="true"/>
  <atomicState n="2" l="1" kappa="2" occ="4.00000" core="true"/>
  <atomicState n="3" l="0" kappa="1" occ="2.00000" core="false"/>
  <atomicState n="3" l="1" kappa="1" occ="2.00000" core="false"/>
  <atomicState n="3" l="1" kappa="2" occ="4.00000" core="false"/>
  <atomicState n="3" l="2" kappa="2" occ="4.00000" core="false"/>
  <atomicState n="3" l="2" kappa="3" occ="6.00000" core="false"/>
  <atomicState n="4" l="0" kappa="1" occ="2.00000" core="false"/>
  <atomicState n="4" l="1" kappa="1" occ="1.00000" core="false"/>
  <atomicState n="4" l="1" kappa="2" occ="1.00000" core="false"/>
  <basis>
    <default type="lapw" trialEnergy="0.00" searchE="false"/>
    <custom l="0" type="lapw" trialEnergy="-0.43" searchE="false"/>
    <lo l="0">
      <wf matchingOrder="0" trialEnergy="-6.18" searchE="false"/>
      <wf matchingOrder="1" trialEnergy="-6.18" searchE="false"/>
    </lo>
    <lo l="0">
      <wf matchingOrder="1" trialEnergy="-6.18" searchE="false"/>
      <wf matchingOrder="2" trialEnergy="-6.18" searchE="false"/>
    </lo>
    <lo l="0">
      <wf matchingOrder="2" trialEnergy="-6.18" searchE="false"/>
      <wf matchingOrder="0" trialEnergy="-0.43" searchE="false"/>
    </lo>
    <lo l="0">
      <wf matchingOrder="0" trialEnergy="-0.43" searchE="false"/>
      <wf matchingOrder="1" trialEnergy="-0.43" searchE="false"/>
    </lo>
    <custom l="1" type="lapw" trialEnergy="0.0" searchE="false"/>
    <lo l="1">
      <wf matchingOrder="0" trialEnergy="-4.25" searchE="false"/>
      <wf matchingOrder="1" trialEnergy="-4.25" searchE="false"/>
    </lo>
```

```
      <lo l="1">
        <wf matchingOrder="1" trialEnergy="-4.25" searchE="false"/>
        <wf matchingOrder="2" trialEnergy="-4.25" searchE="false"/>
      </lo>
      <lo l="1">
        <wf matchingOrder="2" trialEnergy="-4.25" searchE="false"/>
        <wf matchingOrder="0" trialEnergy="0.0" searchE="false"/>
      </lo>
      <lo l="1">
        <wf matchingOrder="0" trialEnergy="0.0" searchE="false"/>
        <wf matchingOrder="1" trialEnergy="0.0" searchE="false"/>
      </lo>

      <custom l="2" type="lapw" trialEnergy="-1.07" searchE="false"/>
      <lo l="2">
        <wf matchingOrder="0" trialEnergy="-1.07" searchE="false"/>
        <wf matchingOrder="1" trialEnergy="-1.07" searchE="false"/>
      </lo>
      <lo l="2">
        <wf matchingOrder="1" trialEnergy="-1.07" searchE="false"/>
        <wf matchingOrder="2" trialEnergy="-1.07" searchE="false"/>
      </lo>
    </basis>
  </sp>
</spdb>
```

Listing A.2: *Ge species file*

```
<?xml version="1.0" encoding="UTF-8"?>
<spdb xsi:noNamespaceSchemaLocation="../../xml/species.xsd"
      xmlns:xsi="http://www.w3.org/2001/XMLSchema-instance">
  <sp chemicalSymbol="Sn" name="tin" z="-50.0000" mass="216395.0920">
    <muffinTin rmin="0.100000E-06" radius="2.40000" rinf="26.3269" radialmeshPoints="800"
        />
    <atomicState n="1" l="0" kappa="1" occ="2.00000" core="true"/>
    <atomicState n="2" l="0" kappa="1" occ="2.00000" core="true"/>
    <atomicState n="2" l="1" kappa="1" occ="2.00000" core="true"/>
    <atomicState n="2" l="1" kappa="2" occ="4.00000" core="true"/>
    <atomicState n="3" l="0" kappa="1" occ="2.00000" core="true"/>
    <atomicState n="3" l="1" kappa="1" occ="2.00000" core="true"/>
    <atomicState n="3" l="1" kappa="2" occ="4.00000" core="true"/>
    <atomicState n="3" l="2" kappa="2" occ="4.00000" core="true"/>
    <atomicState n="3" l="2" kappa="3" occ="6.00000" core="true"/>
    <atomicState n="4" l="0" kappa="1" occ="2.00000" core="false"/>
    <atomicState n="4" l="1" kappa="1" occ="2.00000" core="false"/>
    <atomicState n="4" l="1" kappa="2" occ="4.00000" core="false"/>
    <atomicState n="4" l="2" kappa="2" occ="4.00000" core="false"/>
    <atomicState n="4" l="2" kappa="3" occ="6.00000" core="false"/>
    <atomicState n="5" l="0" kappa="1" occ="2.00000" core="false"/>
    <atomicState n="5" l="1" kappa="1" occ="1.00000" core="false"/>
    <atomicState n="5" l="1" kappa="2" occ="1.00000" core="false"/>
    <basis>
      <default type="lapw" trialEnergy="0.0" searchE="false"/>
      <custom l="0" type="lapw" trialEnergy="-0.40" searchE="false"/>
      <lo l="0">
        <wf matchingOrder="0" trialEnergy="-0.40" searchE="false"/>
        <wf matchingOrder="1" trialEnergy="-0.40" searchE="false"/>
      </lo>
      <lo l="0">
```

```
        <wf matchingOrder="1" trialEnergy="-0.40" searchE="false"/>
        <wf matchingOrder="0" trialEnergy="-4.91" searchE="false"/>
      </lo>
      <lo l="0">
        <wf matchingOrder="0" trialEnergy="-4.91" searchE="false"/>
        <wf matchingOrder="1" trialEnergy="-4.91" searchE="false"/>
      </lo>
      <lo l="0">
        <wf matchingOrder="1" trialEnergy="-4.91" searchE="false"/>
        <wf matchingOrder="2" trialEnergy="-4.91" searchE="false"/>
      </lo>
      <custom l="1" type="lapw" trialEnergy="0.0" searchE="false"/>
      <lo l="1">
        <wf matchingOrder="0" trialEnergy="-3.30" searchE="false"/>
        <wf matchingOrder="1" trialEnergy="-3.30" searchE="false"/>
      </lo>
      <lo l="1">
        <wf matchingOrder="1" trialEnergy="-3.30" searchE="false"/>
        <wf matchingOrder="2" trialEnergy="-3.30" searchE="false"/>
      </lo>
      <lo l="1">
        <wf matchingOrder="2" trialEnergy="-3.30" searchE="false"/>
        <wf matchingOrder="0" trialEnergy="0.0" searchE="false"/>
      </lo>
      <lo l="1">
        <wf matchingOrder="0" trialEnergy="0.0" searchE="false"/>
        <wf matchingOrder="1" trialEnergy="0.0" searchE="false"/>
      </lo>
      <custom l="2" type="lapw" trialEnergy="-0.94" searchE="false"/>
      <lo l="2">
        <wf matchingOrder="0" trialEnergy="-0.94" searchE="false"/>
        <wf matchingOrder="1" trialEnergy="-0.94" searchE="false"/>
      </lo>
      <lo l="2">
        <wf matchingOrder="1" trialEnergy="-0.94" searchE="false"/>
        <wf matchingOrder="2" trialEnergy="-0.94" searchE="false"/>
      </lo>
    </basis>
  </sp>
</spdb>
```

Listing A.3: *Sn species file*

B Appendix B

Material Parameters for the Strain Correction

In Tab. B.1, we summarize the material parameters of Si, Ge, and Sn that were used for the analysis of the x-ray diffraction (XRD) measurements and for the strain correction of the PL data in Chap. 3. The material parameters were averaged linearly according to the composition for the description of $Ge_{1-x-y}Si_xSn_y$ alloys.

Table B.1: *Material parameters used for the XRD analysis and removal of the effects of strain on the band gap size.*

Parameter	Si	Ge	Sn
Lattice constant[a] (Å)	5.4310	5.6579	6.4892
Poisson's ratio[a]	0.28	0.27	0.30
Deformation potential VB (eV)[b]	2.38	2.23	1.58
Deformation potential CB (eV)[c]	-10.06	-7.83	-6.00
Shear deformation potential (eV)[d]	-2.1	-2.9	-2.3
Spin-Orbit splitting (eV)[a]	0.04	0.29	0.80

[a] [[22]], [b] [[131]], [c] [[213]], [d] [[214]], [[215]], [[216]]

Bibliography

1. S. E. Thompson and S. Parthasarathy, "Moore's law: the future of Si microelectronics", Mater. Today **9,** 20 (2006).
2. D. A. B. Miller and H. M. Ozaktas, "Limit to the bit-rate capacity of electrical interconnects from the aspect ratio of the system architecture", J. Parallel Distrib. Comput. **41,** 42 (1997).
3. D. A. Miller, "Optical interconnects to electronic chips", Appl. Opt. **49,** F59 (2010).
4. D. Miller, "Device requirements for optical interconnects to silicon chips", Proc. IEEE **97,** 1166 (2009).
5. D. A. Miller, "Energy consumption in optical modulators for interconnects", Opt. Express **20,** A293 (2012).
6. G. Chen *et al.,* "Predictions of CMOS compatible on-chip optical interconnect", INTEGRATION, the VLSI journal **40,** 434 (2007).
7. G. A. Keeler *et al.,* "Optical pump-probe measurements of the latency of silicon CMOS optical interconnects", IEEE Photonics Technol. Lett. **14,** 1214 (2002).
8. M. J. Kobrinsky *et al.,* "On-Chip Optical Interconnects.", Intel Technol. J. **8** (2004).
9. S. Mokkapati and C. Jagadish, "III-V compound SC for optoelectronic devices", Mater. Today **12,** 22 (2009).
10. H. Wada, H. Sasaki and T. Kamijoh, "Wafer bonding technology for optoelectronic integrated devices", Solid State Electron. **43,** 1655 (1999).
11. D. Liang, G. Roelkens, R. Baets and J. E. Bowers, "Hybrid integrated platforms for silicon photonics", Materials **3,** 1782 (2010).
12. Y. Urino *et al.,* "High-density and wide-bandwidth optical interconnects with silicon optical interposers [Invited]", Photonics Res. **2,** A1 (2014).
13. R. Soref and B. Bennett, "Electrooptical effects in silicon", IEEE J. Quantum Electron. **23,** 123 (1987).
14. G. T. Reed, G. Mashanovich, F. Gardes and D. Thomson, "Silicon optical modulators", Nat. Photonics **4,** 518 (2010).
15. P. Moontragoon, PhD thesis (University of Leeds, 2009).
16. M. Süess *et al.,* "Analysis of enhanced light emission from highly strained germanium microbridges", Nat. Photonics **7,** 466 (2013).
17. R. Koerner *et al.,* "Electrically pumped lasing from Ge Fabry-Perot resonators on Si", Opt. Express **23,** 14815 (2015).
18. Y.-H. Kuo *et al.,* "Strong quantum-confined Stark effect in germanium quantum-well structures on silicon", Nature **437,** 1334 (2005).
19. L. Colace *et al.,* "Metal–semiconductor–metal near-infrared light detector based on epitaxial Ge/Si", Appl. Phys. Lett. **72,** 3175 (1998).

20. M. Rouviere *et al.,* "Integration of germanium waveguide photodetectors for intrachip optical interconnects", Opt. Eng. **44,** 075402 (2005).
21. P. Moontragoon, R. Soref and Z. Ikonic, "The direct and indirect bandgaps of unstrained $Si_xGe_{1-x-y}Sn_y$ and their photonic device applications", J. Appl. Phys. **112,** 073106 (2012).
22. O. Madelung, *Semiconductors: data handbook* (Springer Science & Business Media, 2004).
23. S. Groves and W. Paul, "Band structure of gray tin", Phys. Rev. Lett. **11,** 194 (1963).
24. E. Kane. *Narrow Gap Semiconductors Physics and Applications* 13 (Springer, 1980).
25. S. Wirths *et al.,* "Lasing in direct-bandgap GeSn alloy grown on Si", Nat. Photonics **9,** 88 (2015).
26. G. Sun and S.-Q. Yu, "The SiGeSn approach towards Si-based lasers", Solid-State Electron. **83,** 76 (2013).
27. T. Yamaha *et al.,* "Experimental observation of type-I energy band alignment in lattice-matched $Ge_{1-x-y}Si_xSn_y$/Ge heterostructures", Appl. Phys. Lett. **108,** 061909 (2016).
28. G.-E. Chang, S.-W. Chang and S. L. Chuang, "Theory for n-type doped, tensile-strained Ge–$Si_xGe_ySn_{1-x-y}$ quantum-well lasers at telecom wavelength", Opt. Express **17,** 11246 (2009).
29. Y.-H. Zhu, Q. Xu, W.-J. Fan and J.-W. Wang, "Theoretical gain of strained $GeSn_{0.02}$/ $Ge_{1-x-y'}Si_xSn_{y'}$ quantum well laser", J. Appl. Phys. **107,** 073108 (2010).
30. X. Sun, J. Liu, L. C. Kimerling and J. Michel, "Direct gap photoluminescence of n-type tensile-strained Ge-on-Si", (2009).
31. R. People, "Physics and applications of Ge_xSi_{1-x}/Si strained-layer heterostructures", IEEE J. Quantum. Electron. **22,** 1696 (1986).
32. M. M. Rieger and P. Vogl, "Electronic-band parameters in strained $Si_{1-x}Ge_x$ alloys on $Si_{1-y}Ge_y$ substrates", Phys. Rev. B **48,** 14276 (1993).
33. S. Ridene, K. Boujdaria, H. Bouchriha and G. Fishman, "Infrared absorption in Si/ $Si_{1-x}Ge_x$/Si quantum wells", Phys. Rev. B **64,** 085329 (2001).
34. K. L. Low, Y. Yang, G. Han, W. Fan and Y.-C. Yeo, "Electronic band structure and effective mass parameters of $Ge_{1-x}Sn_x$ alloys", J. Appl. Phys. **112,** 103715 (2012).
35. S. Gupta, B. Magyari-Köpe, Y. Nishi and K. C. Saraswat, "Band structure and ballistic electron transport simulations in GeSn alloys", Proc. Simul. Semicond. Processes Devices, 3 (2012).
36. J. Gallagher, C. Senaratne, J. Kouvetakis and J. Menéndez, "Compositional dependence of the bowing parameter for the direct and indirect band gaps in $Ge_{1-y}Sn_y$ alloys", Appl. Phys. Lett. **105,** 142102 (2014).
37. A. A. Tonkikh *et al.,* "Pseudomorphic GeSn/Ge (001) quantum wells: Examining indirect band gap bowing", Appl. Phys. Lett. **103,** 032106 (2013).
38. P. Hohenberg and W. Kohn, "Inhomogeneous electron gas", Phys. Rev. **136,** B864 (1964).
39. R. M. Martin, *Electronic structure: basic theory and practical methods* (Cambridge university press, 2004).
40. J. P. Perdew and K. Schmidt, *Jacob's ladder of density functional approximations for the exchange-correlation energy AIP Conference Proceedings* (2001), 1.

41. M. E. Casida, *Jacob's ladder for time-dependent density-functional theory: Some rungs on the way to photochemical heaven ACS Symposium Series* **828** (2002), 199.

42. E. N. Economou, *The physics of solids: essentials and beyond* (Springer Science & Business Media, 2010).

43. J. P. Perdew and A. Zunger, "Self-interaction correction to density-functional approximations for many-electron systems", Phys. Rev. B **23,** 5048 (1981).

44. M. van Schilfgaarde, T. Kotani and S. Faleev, "Quasiparticle Self-Consistent GW Theory", Phys. Rev. Lett. **96,** 226402 (2006).

45. F. Giustino, *Materials modelling using density functional theory: properties and predictions* (Oxford University Press, 2014).

46. J. P. Perdew, "Density functional theory and the band gap problem", Int. J. Quantum Chem. **28,** 497 (1985).

47. J. P. Perdew, K. Burke and M. Ernzerhof, "Generalized gradient approximation made simple", Phys. Rev. Lett. **77,** 3865 (1996).

48. J. P. Perdew *et al.,* "Prescription for the design and selection of density functional approximations: More constraint satisfaction with fewer fits", The Journal of chemical physics **123,** 062201 (2005).

49. L. C. L. Y. Voon and M. Willatzen, *The kp method: electronic properties of semiconductors* (Springer, 2009).

50. S. L. Altmann, *Band theory of solids: an introduction from the point of view of symmetry* (Clarendon Press Oxford, 1991).

51. M. Tinkham, *Group theory and quantum mechanics* (Courier Corporation, 2003).

52. G. Dresselhaus, A. Kip and C. Kittel, "Cyclotron resonance of electrons and holes in silicon and germanium crystals", Phys. Rev. **98,** 368 (1955).

53. M. A. Green, "Intrinsic concentration, effective densities of states, and effective mass in silicon", J. Appl. Phys. **67,** 2944 (1990).

54. Y. Sun, S. E. Thompson and T. Nishida, *Strain effect in semiconductors: theory and device applications* (Springer Science & Business Media, 2010).

55. G. Grosso and G. P. Parravicini, *Solid state physics* (Elsevier, 2014).

56. E. O. Kane, "Energy band structure in p-type Germanium and Silicon", J. Phys. Chem. Solids **1,** 82 (1956).

57. S. L. Chuang, *Physics of optoelectronic devices* (Wiley New York, 1995).

58. J. M. Luttinger and W. Kohn, "Motion of electrons and holes in perturbed periodic fields", Phys. Rev. **97,** 869 (1955).

59. *Handbook of semiconductors* (ed W. Paul) (North-Holland Publishing Company, 1982).

60. M. Cardona and F. H. Pollak, "Energy-band structure of germanium and silicon: The k·p method", Phys. Rev. **142,** 530 (1966).

61. G. Bastard, "Superlattice band structure in the envelope-function approximation", Phys. Rev. B **24,** 5693 (1981).

62. O. von Roos, "Position-dependent effective masses in semiconductor theory", Phys. Rev. B **27,** 7547 (1983).

63. J. Thomsen, G. Einevoll and P. Hemmer, "Operator ordering in effective-mass theory", Phys. Rev. B **39,** 12783 (1989).

64. M. Burt, "An exact formulation of the envelope function method for the determination of electronic states in semiconductor microstructures", Semicond. Sci. Technol. **3,** 739 (1988).

65. M. Burt, "The justification for applying the effective-mass approximation to microstructures", J. Phys.: Condens. Matter **4,** 6651 (1992).

66. M. Burt, "Fundamentals of envelope function theory for electronic states and photonic modes in nanostructures", J. Phys.: Condens. Matter **11,** 53 (1999).

67. B. A. Foreman, "Effective-mass Hamiltonian and boundary conditions for the valence bands of semiconductor microstructures", Phys. Rev. B **48,** 4964 (1993).

68. B. A. Foreman, "Elimination of spurious solutions from eight-band kp theory", Phys. Rev. B **56,** 1209487 (1997).

69. D. BenDaniel and C. Duke, "Space-charge effects on electron tunneling", Phys. Rev. **152,** 683 (1966).

70. J. R. Chelikowsky and M. L. Cohen, "Nonlocal pseudopotential calculations for the electronic structure of eleven diamond and zinc-blende semiconductors", Phys. Rev. B **14,** 556 (1976).

71. S. Gonzalez, D. Vasileska and A. A. Demkov, "Empirical Pseudopotential Method for the Band Structure Calculation of Strained-Silicon Germanium Materials", J. Comput. Electron. **1,** 179 (2002).

72. A. Canning, L. Wang, A. Williamson and A. Zunger, "Parallel empirical pseudopotential electronic structure calculations for million atom systems", J. Comput. Phys. **160,** 29 (2000).

73. P. Vogl, H. P. Hjalmarson and J. D. Dow, "A Semi-empirical tight-binding theory of the electronic structure of semiconductors†", J. Phys. Chem. Solids **44,** 365 (1983).

74. J.-M. Jancu, R. Scholz, F. Beltram and F. Bassani, "Empirical spds* tight-binding calculation for cubic semiconductors: General method and material parameters", Phys. Rev. B **57,** 6493 (1998).

75. S. Schulz and G. Czycholl, "Tight-binding model for semiconductor nanostructures", Phys. Rev. B **72,** 165317 (2005).

76. Y. Niquet *et al.,* "Electronic structure of semiconductor nanowires", Phys. Rev. B **73,** 165319 (2006).

77. G. Pizzi, M. Virgilio and G. Grosso, "Tight-binding calculation of optical gain in tensile strained [001]-Ge/SiGe quantum wells", Nanotechnology **21,** 055202 (2009).

78. S. Adachi, *Properties of semiconductor alloys: group-IV, III-V and II-VI semiconductors* (John Wiley & Sons, 2009).

79. V. R. D'Costa *et al.,* "Optical critical points of thin-film $Ge_{1-y}Sn_y$ alloys: A comparative $Ge_{1-y}Sn_y/Ge_{1-x}Si_x$ study", Phys. Rev. B **73,** 125207 (2006).

80. J. Weber and M. Alonso, "Near-band-gap photoluminescence of Si-Ge alloys", Phys. Rev. B **40,** 5683 (1989).

81. P. Moontragoon, Z. Ikonić and P. Harrison, "Band structure calculations of Si–Ge–Sn alloys: achieving direct band gap materials", Semicond. Sci. Technol. **22,** 742 (2007).

82. L. Jiang *et al.,* "Compositional dependence of the direct and indirect band gaps in $Ge_{1-y}Sn_y$ alloys from room temperature photoluminescence: implications for the indirect to direct gap crossover in intrinsic and n-type materials", Semicond. Sci. Technol. **29,** 115028 (2014).

83. W.-J. Yin, X.-G. Gong and S.-H. Wei, "Origin of the unusually large band-gap bowing and the breakdown of the band-edge distribution rule in the Sn_xGe_{1-x} alloys", Phys. Rev. B **78,** 161203 (2008).

84. J. Gallagher, C. Xu, L. Jiang, J. Kouvetakis and J. Menéndez, "Fundamental band gap and direct-indirect crossover in $Ge_{1-x-y}Si_xSn_y$ alloys", Appl. Phys. Lett. **103,** 202104 (2013).

85. V. D'Costa, Y.-Y. Fang, J. Tolle, J. Kouvetakis and J. Menéndez, "Ternary GeSiSn alloys: New opportunities for strain and band gap engineering using group-IV semiconductors", Thin Solid Films **518,** 2531 (2010).

86. J. Tolle *et al.,* "Low temperature chemical vapor deposition of Si-based compounds via SiH_3 SiH_2 SiH_3: Metastable SiSn/GeSn/Si (100) heteroepitaxial structures", Appl. Phys. Lett. **89,** 231924 (2006).

87. H. Lin *et al.,* "Structural and optical characterization of $Si_xGe_{1-x-y}Sn_y$ alloys grown by molecular beam epitaxy", Appl. Phys. Lett. **100,** 141908 (2012).

88. S. Sant and A. Schenk, "Pseudopotential calculations of strained-GeSn/SiGeSn heterostructures", Appl. Phys. Lett. **105,** 162101 (2014).

89. C. Hamaguchi, *Basic semiconductor physics* (Springer Science & Business Media, 2010).

90. P. K. Basu, *Theory of optical processes in semiconductors: bulk and microstructures* (Clarendon press, 1997).

91. A. Rouabah, J. Bernardini and A. Rolland, "Structural aspects of tin surface segregation on Ge (Sn)(111) alloy single crystals", Surf. Sci. **315,** 119 (1994).

92. E. Bauer and J. H. van der Merwe, "Structure and growth of crystalline superlattices: From monolayer to superlattice", Phys. Rev. B **33,** 3657 (1986).

93. D. J. Eaglesham and M. Cerullo, "Dislocation-free Stranski-Krastanow growth of Ge on Si(100)", Phys. Rev. Lett. **64,** 1943 (1990).

94. G. Pikus and G. Bir, *Symmetry and strain-Induced effects in semiconductors* (Wiley New York, 1974).

95. T. B. Bahder, "Eight-band k.p model of strained zinc-blende crystals", Phys. Rev. B **41,** 11992 (1990).

96. P. Enders, A. Bärwolff, M. Woerner and D. Suisky, "k.p theory of energy bands, wave functions, and optical selection rules in strained tetrahedral semiconductors", Phys. Rev. B **51,** 16695 (1995).

97. D. Aspnes and M. Cardona, "Piezoresistance and the conduction-band minima of GaAs", Phys. Rev. B **17,** 741 (1978).

98. C. Herring and E. Vogt, "Transport and deformation-potential theory for many-valley semiconductors with anisotropic scattering", Phys. Rev. **101,** 944 (1956).

99. A. Giorgioni *et al.,* "Photoluminescence decay of direct and indirect transitions in Ge/SiGe multiple quantum wells", J. Appl. Phys. **111,** 013501 (2012).
100. M. Virgilio, T. Schroeder, Y. Yamamoto and G. Capellini, "Radiative and non-radiative recombinations in tensile strained Ge microstrips: Photoluminescence experiments and modeling", J. Appl. Phys. **118,** 233110 (2015).
101. M. J. Deen and P. K. Basu, *Silicon photonics: fundamentals and devices* (John Wiley & Sons, 2012).
102. A. Haug, "Band-to-band Auger recombination in semiconductors", J. Phys. Chem. Solids **49,** 599 (1988).
103. M. O. Scully and M. S. Zubairy, *Quantum optics* (Cambridge university press, 1997).
104. W. T. Wenckebach, *Essentials of semiconductor physics* (Wiley, 1999).
105. W. A. Harrison, *Solid state theory* (Courier Corporation, 1980).
106. C. Jacoboni, F. Nava, C. Canali and G. Ottaviani, "Electron drift velocity and diffusivity in germanium", Phys. Rev. B **24,** 1014 (1981).
107. R. Schaevitz, D. Ly-Gagnon, J. Roth, E. Edwards and D. Miller, "Indirect absorption in germanium quantum wells", AIP Adv. **1,** 032164 (2011).
108. B. K. Ridley, *Quantum processes in semiconductors* (Oxford University Press, 2013).
109. L. R. Doolittle, "A semiautomatic algorithm for Rutherford backscattering analysis", Nucl. Instrum. Methods Phys. Res., Sect. B **15,** 227 (1986).
110. B. E. Warren, *X-ray Diffraction* (Courier Corporation, 1969).
111. L. Vegard, "Die Konstitution der Mischkristalle und die Raumfüllung der Atome", Z. Phys. A **5,** 17 (1921).
112. P. Aella *et al.,* "Optical and structural properties of $Si_xSn_yGe_{1-x-y}$ alloys", Appl. Phys. Lett. **84,** 888 (2004).
113. J. Zheng *et al.,* "Single-crystalline $Ge_{1-x-y}Si_xSn_y$ alloys on Si (100) grown by magnetron sputtering", Opt. Mater. Express **5,** 287 (2015).
114. J. Dismukes, L. Ekstrom, E. Steigmeier, I. Kudman and D. Beers, "Thermal and electrical properties of heavily doped Ge-Si alloys up to 1300 K", J. Appl. Phys. **35,** 2899 (1964).
115. A. Chizmeshya, M. Bauer and J. Kouvetakis, "Experimental and theoretical study of deviations from Vegard's law in the Sn_xGe_{1-x} system", Chem. Mater. **15,** 2511 (2003).
116. L. Jiang *et al.,* "Development of Light Emitting Group IV Ternary Alloys on Si Platforms for Long Wavelength Optoelectronic Applications", Chem. Mater. **26,** 2522 (2014).
117. V. D'Costa, Y.-Y. Fang, J. Tolle, J. Kouvetakis and J. Menendez, "Tunable optical gap at a fixed lattice constant in group-IV semiconductor alloys", Phys. Rev. Lett. **102,** 107403 (2009).
118. R. Beeler *et al.,* "Compositional dependence of the absorption edge and dark currents in $Ge_{1-x-y}Si_xSn_y$/Ge (100) photodetectors grown via ultra-low-temperature epitaxy of Ge4H10, Si4H10, and SnD4", Appl. Phys. Lett. **101,** 221111 (2012).
119. M. H. Zoellner *et al.,* "Imaging structure and composition homogeneity of 300 mm SiGe virtual substrates for advanced CMOS applications by scanning X-ray diffraction microscopy", ACS Appl. Mater. Interfaces **7,** 9031 (2015).

120. C. G. Van de Walle and R. M. Martin, "Theoretical study of Si/Ge interfaces", J. Vac. Sci. Technol., B **3,** 1256 (1985).

121. C. G. Van de Walle and R. M. Martin, "Theoretical calculations of heterojunction discontinuities in the Si/Ge system", Phys. Rev. B **34,** 5621 (1986).

122. L. Colombo, R. Resta and S. Baroni, "Valence-band offsets at strained Si/Ge interfaces", Phys. Rev. B **44,** 5572 (1991).

123. G. Schwartz *et al.,* "Core-level photoemission measurements of valence-band offsets in highly strained heterojunctions: Si-Ge system", Phys. Rev. B **39,** 1235 (1989).

124. E. Yu, E. Croke, T. McGill and R. Miles, "Measurement of the valence-band offset in strained Si/Ge (100) heterojunctions by x-ray photoelectron spectroscopy", Appl. Phys. Lett. **56,** 569 (1990).

125. *Properties of strained and relaxed SiGe* (ed E. Kasper) (INSPEC/IEE, 1995).

126. L. Di Gaspare, G. Capellini, C. Chudoba, M. Sebastiani and F. Evangelisti, "Low-energy yield spectroscopy determination of band offsets: application to the epitaxial GeSi (100) heterostructure", Appl. Surf. Sci. **104,** 595 (1996).

127. L. J. Brillson, *An essential guide to electronic material surfaces and interfaces* (Wiley, 2016).

128. M. Jaros, "Simple analytic model for heterojunction band offsets", Phys. Rev. B **37,** 7112 (1988).

129. Y.-H. Li *et al.,* "Revised ab initio natural band offsets of all group IV, II-VI, and III-V semiconductors", Appl. Phys. Lett. **94,** 212109 (2009).

130. A. Franceschetti, S.-H. Wei and A. Zunger, "Absolute deformation potentials of Al, Si, and NaCl", Phys. Rev. B **50,** 17797 (1994).

131. Y.-H. Li, X. Gong and S.-H. Wei, "Ab initio all-electron calculation of absolute volume deformation potentials of IV-IV, III-V, and II-VI semiconductors: The chemical trends", Phys. Rev. B **73,** 245206 (2006).

132. R. Resta, S. Baroni and A. Baldereschi, "Theory of band offsets at semiconductor heterojunctions: An ab-initio linear response approach", Superlattices Microstruct. **6,** 31 (1989).

133. R. Perez, A. Munoz and F. Flores, "The effect of a metal intralayer on the heterojunction band offset: Extrinsic and intrinsic charge neutrality levels", Surf. Sci. **226,** 371 (1990).

134. J. C. Conesa, "Modeling with hybrid density functional theory the electronic band alignment at the zinc oxide–anatase interface", J. Phys. Chem. C **116,** 18884 (2012).

135. M. Di Ventra, M. Peressi and A. Baldereschi, "Chemical and structural contributions to the valence-band offset at GaP/GaAs heterojunctions", Phys. Rev. B **54,** 5691 (1996).

136. Y. Hinuma, A. Grüneis, G. Kresse and F. Oba, "Band alignment of semiconductors from density-functional theory and many-body perturbation theory", Phys. Rev. B **90,** 155405 (2014).

137. A. Franciosi and C. G. Van de Walle, "Heterojunction band offset engineering", Surf. Sci. Rep. **25,** 1 (1996).

138. R. Anderson, "Germanium-gallium arsenide heterojunctions", IBM J. Res. Dev. **4,** 283 (1960).

139. W. Frensley and H. Kroemer, "Theory of the energy-band lineup at an abrupt semiconductor heterojunction", Phys. Rev. B **16,** 2642 (1977).

140. J. Tersoff, "Theory of semiconductor heterojunctions: The role of quantum dipoles", Phys. Rev. B **30,** 4874 (1984).

141. C. G. Van de Walle, "Band lineups and deformation potentials in the model-solid theory", Phys. Rev. B **39,** 1871 (1989).

142. F. Capasso and G. Margaritondo, *Heterojunction band discontinuities: physics and device applications* (North-Holland, 1987).

143. J. M. Ziman, *Prinzipien der Festkörpertheorie* (Verlag Harri Deutsch, 1992).

144. J. Phillips, *Bonds and bands in semiconductors* (Academic Press, 1973).

145. L. Kleinman, "Comment on the average potential of a Wigner solid", Phys. Rev. B **24,** 7412 (1981).

146. A. Baldereschi, S. Baroni and R. Resta, "Band offsets in lattice-matched heterojunctions: a model and first-principles calculations for GaAs/AlAs", Phys. Rev. Lett. **61,** 734 (1988).

147. J. Vergés, D. Glötzel, M. Cardona and O. Andersen, "Absolute hydrostatic deformation potentials of tetrahedral semiconductors", Phys. Status Solidi B **113,** 519 (1982).

148. C. G. Van de Walle and R. M. Martin, ""Absolute"deformation potentials: Formulation and ab initio calculations for semiconductors", Phys. Rev. Lett. **62,** 2028 (1989).

149. Y.-H. Li, X. Gong and S.-H. Wei, "Ab initio calculation of hydrostatic absolute deformation potential of semiconductors", Appl. Phys. Lett. **88,** 042104 (2006).

150. A. Gulans *et al.,* "exciting: A full-potential all-electron package implementing density-functional theory and many-body perturbation theory", J. Phys.: Condens. Matter **26,** 363202 (2014).

151. C. Ambrosch-Draxl, "Augmented planewave methods", Phys. Scr. **2004,** 48 (2004).

152. E. Sjöstedt, L. Nordström and D. Singh, "An alternative way of linearizing the augmented plane-wave method", Solid State Commun. **114,** 15 (2000).

153. M. Methfessel and A. Paxton, "High-precision sampling for Brillouin-zone integration in metals", Phys. Rev. B **40,** 3616 (1989).

154. C. G. van de Walle and R. M. Martin, "Theoretical study of band offsets at semiconductor interfaces", Phys. Rev. B **35,** 8154 (1987).

155. S. Satpathy, R. M. Martin and C. G. Van de Walle, "Electronic properties of the (100)(Si)/(Ge) strained-layer superlattices", Phys. Rev. B **38,** 13237 (1988).

156. C. Tserbak, H. Polatoglou and G. Theodorou, "Unified approach to the electronic structure of strained Si/Ge superlattices", Phys. Rev. B **47,** 7104 (1993).

157. M. Virgilio, G. Pizzi and G. Grosso, "Optical gain in short period Si/Ge superlattices on [001]-SiGe substrates", J. Appl. Phys. **110,** 083105 (2011).

158. H. Mathieu *et al.,* "Deformation potentials of the direct and indirect absorption edges of GaP", Phys. Rev. B **19,** 2209 (1979).

159. K. Guilloy *et al.,* "Germanium under High Tensile Stress: Nonlinear Dependence of Direct Band Gap vs Strain", ACS Photonics **3,** 1907 (2016).

160. M. Lazzouni, M. Peressi and A. Baldereschi, "Valence-band offset at the Si/GaP (110) interface", Appl. Phys. Lett. **68,** 75 (1996).

161. R. Resta, L. Colombo and S. Baroni, "Absolute deformation potentials in semiconductors", Phys. Rev. B **41,** 12358 (1990).

162. A. D. Becke, "A new mixing of Hartree–Fock and local density-functional theories", The Journal of chemical physics **98,** 1372 (1993).

163. J. Muscat, A. Wander and N. Harrison, "On the prediction of band gaps from hybrid functional theory", Chem. Phys. Lett. **342,** 397 (2001).

164. L. G. Ferreira, M. Marques and L. K. Teles, "Approximation to density functional theory for the calculation of band gaps of semiconductors", Phys. Rev. B **78,** 125116 (2008).

165. L. G. Ferreira, M. Marques and L. K. Teles, "Slater half-occupation technique revisited: the LDA-1/2 and GGA-1/2 approaches for atomic ionization energies and band gaps in semiconductors", AIP Adv. **1,** 032119 (2011).

166. F. Freitas, J. Furthmüller, F. Bechstedt, M. Marques and L. Teles, "Influence of the composition fluctuations and decomposition on the tunable direct gap and oscillator strength of $Ge_{1-x}Sn_x$ alloys", Appl. Phys. Lett. **108,** 092101 (2016).

167. A. Wadehra, J. W. Nicklas and J. W. Wilkins, "Band offsets of semiconductor heterostructures: A hybrid density functional study", Appl. Phys. Lett. **97,** 092119 (2010).

168. A. Zunger, S.-H. Wei, L. Ferreira and J. E. Bernard, "Special quasirandom structures", Phys. Rev. Lett. **65,** 353 (1990).

169. U. Denker, M. Stoffel, O. Schmidt and H. Sigg, "Ge hut cluster luminescence below bulk Ge band gap", Appl. Phys. Lett. **82,** 454 (2003).

170. M. Brehm *et al.,* "Quantitative determination of Ge profiles across SiGe wetting layers on Si (001)", Appl. Phys. Lett. **93,** 121901 (2008).

171. L. Tsybeskov and D. J. Lockwood, "Silicon-germanium nanostructures for light emitters and on-chip optical interconnects", Proc. IEEE **97,** 1284 (2009).

172. A. Karmous *et al.,* "Recent developments in Ge dots grown on pit-patterned surfaces", physica status solidi (b) **249,** 764 (2012).

173. Y.-H. Kuo *et al.,* "Quantum-confined Stark effect in Ge/SiGe quantum wells on Si for optical modulators", IEEE J. Sel. Top. Quantum Electron. **12,** 1503 (2006).

174. R. Karunasiri, J. Park, Y. Mii and K. Wang, "Intersubband absorption in $Si_{1-x}Ge_x$/Si multiple quantum wells", Appl. Phys. Lett. **57,** 2585 (1990).

175. K. Gallacher *et al.,* "Mid-infrared intersubband absorption from p-Ge quantum wells grown on Si substrates", Appl. Phys. Lett. **108,** 091114 (2016).

176. M. De Seta *et al.,* "Narrow intersubband transitions in n-type Ge/SiGe multi-quantum wells: control of the terahertz absorption energy trough the temperature dependent depolarization shift", Nanotechnology **23,** 465708 (2012).

177. Y. Busby *et al.,* "Near-and far-infrared absorption and electronic structure of Ge-SiGe multiple quantum wells", Phys. Rev. B **82,** 205317 (2010).

178. R. Bates *et al.,* "Interwell intersubband electroluminescence from Si/SiGe quantum cascade emitters", Appl. Phys. Lett. **83,** 4092 (2003).

179. I. Buyanova *et al.,* "Mechanism for thermal quenching of luminescence in SiGe/Si structures grown by molecular beam epitaxy: Role of nonradiative defects", Appl. Phys. Lett. **71,** 3676 (1997).

180. D. J. Lockwood *et al.,* "Si/SiGe heterointerfaces in one-, two-, and three-dimensional nanostructures: their impact on SiGe light emission", Front. Mater. **3,** 12 (2016).

181. Y. Shiraki, H. Sunamura, N. Usami and S. Fukatsu, "Formation and optical properties of SiGe/Si quantum structures", Appl. Surf. Sci. **102,** 263 (1996).

182. Y. Shiraki and A. Sakai, "Fabrication technology of SiGe hetero-structures and their properties", Surf. Sci. Rep. **59,** 153 (2005).

183. E. Gatti *et al.,* "Room temperature photoluminescence of Ge multiple quantum wells with Ge-rich barriers", Appl. Phys. Lett. **98,** 031106 (2011).

184. T. Baier *et al.,* "Type-II band alignment in $Si/Si_{1-x}Ge_x$ quantum wells from photoluminescence line shifts due to optically induced band-bending effects: experiment and theory", Phys. Rev. B **50,** 15191 (1994).

185. M. Virgilio, R. Farchioni and G. Grosso, "Theoretical investigation of near gap electronic states of Si/SiGe multiple quantum wells on (001)-Si or SiGe substrates", J. Appl. Phys. **99,** 3710 (2006).

186. R. Bergamaschini *et al.,* "Temperature-dependent evolution of the wetting layer thickness during Ge deposition on Si (001)", Nanotechnology **22,** 285704 (2011).

187. G. Capellini, M. De Seta and F. Evangelisti, "SiGe intermixing in Ge/Si (100) islands", Appl. Phys. Lett. **78,** 303 (2001).

188. P. Tan, K. Brunner, D. Bougeard and G. Abstreiter, "Raman characterization of strain and composition in small-sized self-assembled Si/Ge dots", Phys. Rev. B **68,** 125302 (2003).

189. M. Alonso, M. De la Calle, J. Ossó, M. Garriga and A. Goni, "Strain and composition profiles of self-assembled Ge/Si (001) islands", J. Appl. Phys. **98,** 033530 (2005).

190. J. Reparaz, A. Bernardi, A. Goni, M. Alonso and M. Garriga, "Composition dependence of the phonon strain shift coefficients of SiGe alloys revisited", Appl. Phys. Lett. **92,** 081909 (2008).

191. J. Sturm *et al.,* "Well-resolved band-edge photoluminescence of excitons confined in strained $Si_{1-x}Ge_x$ quantum wells", Phys. Rev. Lett. **66,** 1362 (1991).

192. M. Grydlik *et al.,* "Inverted Ge islands in {111} faceted Si pits—a novel approach towards SiGe islands with higher aspect ratio", New J. Phys. **12,** 063002 (2010).

193. S.-W. Chang and S. L. Chuang, "Theory of Optical Gain of Ge-$Si_xGe_ySn_{1-x-y}$ Quantum-Well Lasers", IEEE J. Quantum. Electron. **43,** 249 (2007).

194. Y. Varshni, "Temperature dependence of the energy gap in semiconductors", Physica **34,** 149 (1967).

195. C. Y.-P. Chao and S. L. Chuang, "Spin-orbit-coupling effects on the valence-band structure of strained semiconductor quantum wells", Phys. Rev. B **46,** 4110 (1992).

196. *Semiconductor physics: group IV elements and III-V compounds* (ed O. Madelung) (Springer Verlag, 1982).

197. G. Pizzi, PhD thesis (Scuola Normale Superiore di Pisa, 2011).

198. F. Stern and W. Howard, "Properties of semiconductor surface inversion layers in the electric quantum limit", Phys. Rev. **163,** 816 (1967).

199. J. D. Jackson, *Classical electrodynamics* (Wiley, 1999).

200. X.-X. Liang and X. Wang, "Electron-phonon interaction in a quantum well", Phys. Rev. B **43,** 5155 (1991).

201. M. V. Fischetti, "Monte Carlo simulation of transport in technologically significant semiconductors of the diamond and zinc-blende structures. I. Homogeneous transport", IEEE Trans. Electron Devices **38,** 634 (1991).

202. M. Virgilio, C. Manganelli, G. Grosso, G. Pizzi and G. Capellini, "Radiative recombination and optical gain spectra in biaxially strained n-type germanium", Phys. Rev. B **87,** 235313 (2013).

203. T. Unuma, M. Yoshita, T. Noda, H. Sakaki and H. Akiyama, "Intersubband absorption linewidth in GaAs quantum wells due to scattering by interface roughness, phonons, alloy disorder, and impurities", J. Appl. Phys. **93,** 1586 (2003).

204. S. Fukatsu, H. Akiyama, Y. Shiraki and H. Sakaki, "Quantitative analysis of light emission from SiGe quantum wells", J. Cryst. Growth **157,** 1 (1995).

205. U. Penner, H. Rücker and I. Yassievich, "Theory of interface roughness scattering in quantum wells", Semicond. Sci. Technol. **13,** 709 (1998).

206. A. Valavanis, PhD thesis (The University of Leeds, 2009).

207. H. Wang, X. Liu and Z. M. Zhang, "Absorption Coefficients of Crystalline Silicon at Wavelengths from 500 nm to 1000 nm", Int. J. Thermophys. **34,** 213 (2013).

208. E. F. Schubert, T. Gessmann and J. K. Kim, *Light emitting diodes* (Wiley Online Library, 2005).

209. M. Jo *et al.,* "Origin of the blueshift of photoluminescence in a type-II heterostructure", Nanoscale Res. Lett. **7,** 1 (2012).

210. H. Hu *et al.,* "Far-field nanoscale infrared spectroscopy of vibrational fingerprints of molecules with graphene plasmons", Nature Communications **7** (2016).

211. A. Rogalski, "Infrared detectors: status and trends", Progress in quantum electronics **27,** 59 (2003).

212. E. R. Weber, R. Willardson, H. Liu and F. Capasso, *Intersubband transitions in quantum wells: physics and device applications* (Academic press, 1999).

213. S.-H. Wei and A. Zunger, "Predicted band-gap pressure coefficients of all diamond and zinc-blende semiconductors: Chemical trends", Phys. Rev. B **60,** 5404 (1999).

214. L. D. Laude, F. H. Pollak and M. Cardona, "Effects of uniaxial stress on the indirect exciton spectrum of silicon", Phys. Rev. B **3,** 2623 (1971).

215. M. Chandrasekhar and F. H. Pollak, "Effects of uniaxial stress on the electroreflectance spectrum of Ge and GaAs", Phys. Rev. B **15,** 2127 (1977).

216. B. J. Roman and A. Ewald, "Stress-Induced Band Gap and Related Phenomena in Gray Tin", Phys. Rev. B **5,** 3914 (1972).

Publication List

W1. T. Wendav *et al.,* "Compositional dependence of the band-gap of $Ge_{1-x-y}Si_xSn_y$ alloys", Appl. Phys. Lett. **108,** 242104 (2016).

W2. T. Wendav *et al.,* "Photoluminescence from ultrathin Ge-rich multiple quantum wells observed up to room temperature: Experiments and modeling", Phys. Rev. B **94,** 245304 (2016).

W3. I. A. Fischer *et al.,* "Growth and characterization of SiGeSn quantum well photodiodes", Opt. Express **23,** 25048 (2015).

W4. B. Schwartz *et al.,* "Electroluminescence of GeSn/Ge MQW LEDs on Si substrate", Opt. Lett. **40,** 3209 (2015).